



EFEITO DA TEMPERATURA NO COMPORTAMENTO MECÂNICO DE
COMPÓSITOS REFRAATÓRIOS REFORÇADOS COM TECIDOS DE BASALTO E
CARBONO

Dimas Alan Strauss Rambo

Tese de Doutorado apresentada ao Programa de Pós-graduação em Engenharia Civil, COPPE, da Universidade Federal do Rio de Janeiro, como parte dos requisitos necessários à obtenção do título de Doutor em Engenharia Civil.

Orientadores: Romildo Dias Toledo Filho
Flávio de Andrade Silva

Rio de Janeiro
Março de 2016

EFEITO DA TEMPERATURA NO COMPORTAMENTO MECÂNICO DE
COMPÓSITOS REFRAATÓRIOS REFORÇADOS COM TECIDOS DE BASALTO E
CARBONO

Dimas Alan Strauss Rambo

TESE SUBMETIDA AO CORPO DOCENTE DO INSTITUTO ALBERTO LUIZ
COIMBRA DE PÓS-GRADUAÇÃO E PESQUISA DE ENGENHARIA (COPPE) DA
UNIVERSIDADE FEDERAL DO RIO DE JANEIRO COMO PARTE DOS
REQUISITOS NECESSÁRIOS PARA A OBTENÇÃO DO GRAU DE DOUTOR EM
CIÊNCIAS EM ENGENHARIA CIVIL.

Examinada por:

Prof. Romildo Dias Toledo Filho, D.Sc.

Prof. Flávio de Andrade Silva, D.Sc.

Dr. Otávio da Fonseca Martins Gomes, D.Sc.

Prof. Fernando Gomes de Souza Junior, D.Sc.

Prof. Antonio Domingues de Figueiredo, D.Sc.

RIO DE JANEIRO, RJ - BRASIL

MARÇO DE 2016

Rambo, Dimas Alan Strauss

Efeito da temperatura no comportamento mecânico de compósitos refratários reforçados com tecidos de basalto e carbono/ Dimas Alan Strauss Rambo. – Rio de Janeiro: UFRJ/COPPE, 2016.

XII, 215 p.: il.; 29,7 cm.

Orientadores: Romildo Dias Toledo Filho

Flávio de Andrade Silva

Tese (doutorado) – UFRJ/ COPPE/ Programa de Engenharia Civil, 2016.

Referências Bibliográficas: p. 47-51.

1. Compósitos cimentícios. 2. Fibras de basalto e carbono. 3. Temperaturas elevadas. 4. Propriedades mecânicas. I. Toledo Filho, Romildo Dias *et al.* II. Universidade Federal do Rio de Janeiro, COPPE, Programa de Engenharia Civil. III. Título.

AGRADECIMENTOS

Primeiramente agradeço a Deus, por tudo! Graças a ele tive forças para vencer todos os desafios e aproveitar todas as oportunidades que apareceram em minha vida. Só através dele pude me manter firme quando as dificuldades apareceram. Agora, após mais uma etapa vencida, só tenho a comemorar e agradecer a ele pelas graças recebidas!

Agradeço a meus pais, Valzir Rambo e Marisa Rambo, por toda a paciência, apoio, dedicação e amor investidos em mim ao longo de toda a minha existência. Vocês são o maior presente que Deus poderia ter me dado. Não tenho palavras para descrever o quão feliz me sinto por poder partilhar mais esta conquista com vocês. O mérito também é de vocês! Agradeço também a minha irmã Fabiana que me incentivou a estudar engenharia. Muito obrigado por me apoiar sempre!

Agradeço a minha noiva Isabel, pela paciência, amor, companheirismo e carinho. Por caminhar ao meu lado sempre, independente da situação. Por acreditar em mim e me impulsionar sempre em frente. Por ouvir milhares de vezes as minhas apresentações “teste”. Por ler meus textos. Por me medicar toda vez que surge uma “apresentação oral” onde bate aquela tremenda dor de estômago. Enfim, obrigado por tudo meu amor!

Agradeço aos meus orientadores, Romildo Dias Toledo Filho e Flávio de Andrade Silva, pelos ensinamentos, pelo companheirismo, pela confiança no meu potencial e por todo apoio fornecido ao longo dos últimos 6 anos. Tenho grande respeito e admiração pelos dois. Seu constante incentivo me fez crescer muito academicamente e pessoalmente, por isso, sinto-me muito grato por ter sido orientado por esta dupla de “*experts*”. Agradeço também por terem confiado a mim a execução de muitos projetos, nos quais pude aprender e pôr em prática meus conhecimentos em ciência dos materiais.

Agradeço muito ao Dr. Otávio Gomes, pela participação ativa na construção deste trabalho, através de inúmeras microscopias, tratamento de imagens, TGs e análises de DRX.

Agradeço muito aos colegas do exterior com os quais tive o prazer de aprender e de compartilhar conhecimentos. Foi um prazer trabalhar com estes excelentes profissionais. Agradeço aos meus amigos e colegas Neven Ukrainczyk (Technical universität Darmstadt, Alemanha) e Eduardus Koenders (Technical universität

Darmstadt, Alemanha) por toda a colaboração na elaboração dos artigos referentes à hidratação/desidratação da matriz refratária. E por fim, ao professor Barzin Mobasher (Arizona State University, USA) e ao doutorando Yiming Yao (Arizona State University, USA) pela colaboração com as modelagens numéricas e análises de imagem.

Agradeço muito aos companheiros de percurso, pessoas sensacionais com as quais convivi: João Augusto, Diego, Tamile, Jaelson, Joãozinho, Alfredo, Ederli, Carlos R., Marcela, Karyne, Javier, Eduardo Peldoza, Maosheng, Tina, Adriana, Andrielli, Ana, Samantha, Otávio, Camila, Fabrício, Saulo, Alex, Marco, Thiago, Oscar e Iolanda.

Agradeço as funcionárias Luzidelle e Sandra por todo apoio e carinho durante todos estes anos de muitas viagens e compra de materiais.

Sou muito grato aos técnicos: Renam, Adailton, Alessandro, Clodoaldo, Flávio, Márcio, Rodrigo, Rosangela, Júlio, Thales, Anderson, Índio, Paulinho (*in memorian*) e aos funcionários Josimar, Claudia e Skol.

Agradeço de forma muito especial aos meus familiares que sempre me apoiaram e que me proporcionam muitas alegrias quando estamos juntos. São eles: meu cunhado Eduardo, meu sobrinho Samuel, minha avó Leonia, meu avô Narcí, meus primos Débora e Gelson, meu tio Adeli, minha tia Marcia e minha futura sogra Elisabete.

Agradeço ao CNPq e à Capes, pelo suporte financeiro para realização dessa pesquisa.

Resumo da Tese apresentada à COPPE/UFRJ como parte dos requisitos necessários para a obtenção do grau de Doutor em Ciências (D.Sc.)

EFEITO DA TEMPERATURA NO COMPORTAMENTO MECÂNICO DE
COMPÓSITOS REFRAATÓRIOS REFORÇADOS COM TECIDOS DE BASALTO E
CARBONO

Dimas Alan Strauss Rambo

Março/2016

Orientadores: Romildo Dias Toledo Filho

Flávio de Andrade Silva

Programa: Engenharia Civil

Neste estudo foram desenvolvidos e caracterizados mecanicamente, sob temperaturas elevadas, compósitos cimentícios reforçados com tecido de basalto e carbono. Os ensaios mecânicos foram divididos em: residuais (após aquecimento e resfriamento) e à quente. Visando garantir a resistência mecânica dos compósitos sob temperaturas elevadas, os mesmos foram produzidos com concreto refratário elaborado a partir de cimento de aluminato de cálcio e agregado sintético de aluminato de cálcio. Ambos os tecidos, de basalto e de carbono, deram origem a compósitos com comportamento *strain-hardening*. Os mecanismos de plastificação, enrijecimento e degradação dos revestimentos empregados nas fibras mostraram forte impacto no desempenho mecânico dos compósitos têxteis tanto nos ensaios residuais quanto nos ensaios à quente. Esta interferência se mostrou clara para temperaturas de até 400°C, faixa na qual ocorre a degradação total dos revestimentos. A transformação/desidratação de fases da matriz e a estabilidade térmica das fibras também mostraram ser fatores limitantes quanto a resistência e capacidade de deformação dos compósitos. Mesmo frente a severidade dos ensaios de tração à quente, a resistência dos compósitos testados nesta condição foi de aproximadamente 50% da resistência observada na condição residual.

Abstract of Thesis presented to COPPE/UFRJ as a partial fulfillment of the requirements for the degree of Doctor of Science (D.Sc.)

TEMPERATURE EFFECT ON THE MECHANICAL BEHAVIOR OF
REFRACTORY COMPOSITES REINFORCED WITH BASALT AND CARBON
TEXTILE

Dimas Alan Strauss Rambo

March/2016

Advisors: Romildo Dias Toledo Filho

Flávio de Andrade Silva

Department: Civil Engineering

In the present work the development and mechanical characterization, under elevated temperatures, of textile reinforced cementitious composites reinforced with basalt and carbon textiles were carried out. The mechanical tests were divided in: residual (after heating and cooling process) and in-situ (hot condition). Aiming to ensure the composites mechanical strength under elevated temperature, a refractory concrete was developed from calcium aluminous cement and synthetic calcium aluminous aggregate. Both textiles, basalt and carbon, were able to ensure strain hardening behavior when combined to the refractory matrix. The plastification, stiffening and degradation of the used coatings showed strong impact on the hot and residual mechanical performance of the textile reinforced composites. This interference is clear for temperatures up to 400°C, where the total coating degradation occurs. The transformation/dehydration reaction and the fibers thermal stability also proved to be limiting factors regarding the tensile strength and strain capacity of the composites. Even facing the severity of the hot tests, the composites tested in this condition presented tensile strength approximately 50% lower than that obtained at the residual condition.

SUMÁRIO

1	INTRODUÇÃO	1
2	OBJETIVOS	3
3	REVISÃO BIBLIOGRÁFICA	5
4	METODOLOGIAS E RESULTADOS	14
4.1	DOSAGEM E CARACTERIZAÇÃO BÁSICA DA MATRIZ REFRAATÁRIA	15
4.2	INFLUÊNCIA DA TEMPERATURA NO COMPORTAMENTO QUÍMICO E MECÂNICO DA MATRIZ REFRAATÁRIA (ARTIGO A)	30
4.3	PROPRIEDADES MECÂNICAS DO TECIDO DE BASALTO	31
4.4	INFLUÊNCIA DA TEMPERATURA NO COMPORTAMENTO MECÂNICO DE COMPÓSITOS REFRAATÁRIOS REFORÇADOS COM TECIDO DE BASALTO (ARTIGOS B E C).....	41
4.5	SIMULAÇÃO DO COMPORTAMENTO MECÂNICO DE COMPÓSITOS REFRAATÁRIOS REFORÇADOS COM TECIDO DE BASALTO (ARTIGO D)	42
4.6	INFLUÊNCIA DA TEMPERATURA NO COMPORTAMENTO MECÂNICO DE COMPÓSITOS REFRAATÁRIOS REFORÇADOS COM TECIDO DE CARBONO (ARTIGO E)	43
5	CONCLUSÕES E SUGESTÕES PARA TRABALHOS FUTUROS	44
6	REFERÊNCIAS BIBLIOGRÁFICAS	47
	ANEXOS	52

ARTIGO A – RAMBO DAS, UKRAINCZYK N, SILVA FA, TOLEDO RD, KOENDERS E AND GOMES OFM. EXPOSING CALCIUM ALUMINATE MORTAR TO HIGH TEMPERATURES: OVERCOMING ADVERSE

CONVERSION EFFECTS USING CALCIUM ALUMINATE AGGREGATES. SUBMITTED TO CEMENT AND CONCRETE RESEARCH (2016).....	53
ARTIGO B – RAMBO DAS, SILVA FA, TOLEDO RD AND GOMES OFM. EFFECT OF ELEVATED TEMPERATURES ON THE MECHANICAL BEHAVIOR OF BASALT TEXTILE REINFORCED REFRACTORY CONCRETE. PUBLISHED IN THE JOURNAL OF MATERIALS AND DESIGN (2014). VOLUME 65, JANUARY 2015, PAGES 24–33, DOI:10.1016/J.MATDES.2014.08.060.....	93
ARTIGO C – RAMBO DAS, SILVA FA, TOLEDO RD, UKRAINCZYK N AND KOENDERS E. TENSILE STRENGTH OF A CALCIUM-ALUMINATE CEMENTITIOUS COMPOSITE REINFORCED WITH BASALT TEXTILE IN A HIGH-TEMPERATURE ENVIRONMENT. SUBMITTED TO CEMENT AND CONCRETE COMPOSITES (2015). UNDER REVIEW.....	122
ARTIGO D – RAMBO DAS, YAO Y, SILVA FA, TOLEDO RD AND MOBASHER B. EXPERIMENTAL INVESTIGATION AND MODELLING OF THE TEMPERATURE EFFECTS ON THE TENSILE BEHAVIOR OF TEXTILE REINFORCED REFRACTORY CONCRETES. SUBMITTED TO CEMENT AND CONCRETE COMPOSITES (2016). PENDING REVIEW.....	154
ARTIGO E – RAMBO DAS, SILVA FA, TOLEDO RD AND GOMES OFM. EFFECT OF ELEVATED TEMPERATURES ON THE IN-SITU TENSILE STRENGTH OF COATED AND UNCOATED CARBON TEXTILE REINFORCED REFRACTORY COMPOSITES. SUBMITTED TO CONSTRUCTION AND BUILDING MATERIALS (2015). PENDING REVIEW.....	187

LISTA DE FIGURAS

Figura 3.1 – Processos de fabricação de TRCs: (a) Moldagem manual e (b) bombeamento (Adaptado de: BRAMESHUBER <i>et al.</i> , 2006)	5
Figura 3.2 – Diferentes tipos de têxteis produzidos para aplicação em TRCs.	6
Figura 3.3 – Comparação entre compósitos produzidos a partir de diferentes tipos de têxteis.	7
Figura 3.4 – Aplicação de diferentes tipos de têxteis em elementos de concreto.	8
Figura 3.5 - Representação esquemática da resposta típica de um TRC submetido à tração (BARHUM e MECHTCHERINE, 2014).	8
Figura 3.6 – Efeito da temperatura na resistência á tração de vários tipos de fibras (KRUGER e REINHARDT, 2006 citado por KLEINEBERG, 2004).	9
Figura 3.7 – Aplicações de fibras e tecidos de basalto.	10
Figura 3.8 – Representação geral da formação de hidratos a partir do CA em cimentos de aluminato de cálcio (Adaptado de PENA e DE AZA, 1999).	11
Figura 4.1 – Curva granulométrica e micrografia do cimento aluminoso.	16
Figura 4.2 – Agregado com diâmetro inferior a 1,18mm.	17
Figura 4.3 – Curva granulométrica e micrografia do agregado.	18
Figura 4.4 – Ensaio de compacidade experimental.	22
Figura 4.5 – Detalhes e dimensões dos equipamentos utilizados no ensaio de compacidade experimental (Fonte: Adaptado de FORMAGINI, 2005).	23
Figura 4.6 – Instrumentos necessários ao ensaio de compatibilidade e ponto de saturação.	25
Figura 4.7 – Curvas de escoamento em cone de Marsh para pastas com diferentes dosagens de aditivo superplastificante.	26
Figura 4.8 – Evolução da compacidade do esqueleto granular sólido (binário) da matriz refratária.	27
Figura 4.9 – Curvas típicas de resistência à compressão do concreto refratário aos 7, 14 e 28 dias de idade.	29

Figura 4.10 – Detalhes do tecido de basalto: direções adotadas e dimensões da malha.	32
Figura 4.11 – Aspecto do tecido utilizado nos ensaios de resistência à tração direta.	32
Figura 4.12 – Determinação da área da seção transversal dos cordões de basalto utilizando o software Image J.	33
Figura 4.13 – Regime de aquecimento aplicado às amostras de tecido de basalto.	34
Figura 4.14 – Configuração utilizada no ensaio de tração direta do tecido de basalto.	35
Figura 4.15 – Curvas típicas de resistência à tração direta do tecido de basalto (a) na direção principal e (b) na direção secundária.	36
Figura 4.16 – (a) Curvas típicas de resistência à tração direta residual do tecido de basalto após aquecimento em diversas temperaturas. (b) Evolução do módulo e da resistência à tração residual do tecido com o aumento da temperatura.	37
Figura 4.17 – Tecido de basalto (a) na condição natural e após exposição à (b) 75°, (c) 150°C, (d) 200°C, (e) 300°C, (f) 400°C, (g) 600°C e (h) 1000°C.	38
Figura 4.18 – Cordão de basalto (a) na condição natural e após exposição à (b) 75°C, (c) 150°C, (d) 200°C, (e) 300°C, (f) 400°C, (g) 600°C e (h) 1000°C.	39
Figura 4.19 – Microscopia da seção de um filamento de basalto tratado termicamente a 750°C.	40

LISTA DE TABELAS

Tabela 4.1 – Composição química do cimento aluminoso.	17
--	----

Tabela 4.2 – Diâmetro do agregado (D80 e D50).	18
Tabela 4.3 – Composição química do agregado.....	19
Tabela 4.4 – Características do aditivo superplastificante.	19
Tabela 4.5 – Compacidade dos materiais com dimensões inferiores a 100µm..	24
Tabela 4.6 – Compacidade dos materiais com dimensões superiores a 100 µm.	25
Tabela 4.7 – Composição da matriz de concreto refratário.	28
Tabela 4.8 – Resultados dos ensaios de resistência à compressão uniaxial da matriz para diferentes idades.	29
Tabela 4.9 – Especificações do tecido de basalto fornecidas pelo fabricante. ...	32
Tabela 4.10 – Influência da orientação na resposta à tração do tecido de basalto.	36
Tabela 4.11 – Resultados dos ensaios de resistência à tração residual do tecido de basalto para diferentes temperaturas de aquecimento.....	38

1 INTRODUÇÃO

O uso de reforço têxtil em concretos ou argamassas pode trazer várias vantagens com relação ao reforço convencional (aço) (KRÜGER, 2004) e ainda, com relação a outras variedades de reforços fibrosos (PELED e MOBASHER, 2005). Dada a flexibilidade e a leveza deste tipo de material, sua aplicação em estruturas ou elementos de concreto tem sido cada vez mais frequente, possibilitando avanços no âmbito da construção civil. Quando empregados como reforço principal, permitem que as seções de concreto sejam reduzidas, diminuindo o desperdício de material e tornando as estruturas de concreto mais leves.

Compósitos têxteis, também conhecidos como TRCs (*Textile reinforced concretes*), apresentam usualmente comportamento *strain-hardening*, alcançando valores de tenacidade, resistência à tração e capacidade de deformação superiores àqueles normalmente obtidos em compósitos reforçados com fibras longas alinhadas ou randomicamente distribuídas (PELED e MOBASHER, 2005). Sua utilização possui grande potencial na produção de produtos laminados/finos (elementos de proteção, elementos de fachada, revestimento de túneis, paredes), na reabilitação de estruturas e na concepção de estruturas leves e de forma livre (pontes, obras de arte, mobiliário) (SIM *et al.*, 2005, PELED e MOBASHER, 2005, KRÜGER e REINHARDT, 2006).

É importante considerar, no entanto, que em muitas dessas aplicações, tanto o concreto como o reforço têxtil sofrem efeitos térmicos, tornando o estudo do desempenho mecânico dos TRCs sob temperaturas elevadas absolutamente indispensável (SILVA *et al.*, 2014, KRÜGER e REINHARDT, 2006, REINHARDT, 1976, BUTTNER *et al.*, 2007). Tal vertente, tema principal do presente estudo, foi caracterizada como “lacuna do

conhecimento” por vários pesquisadores presentes na mais recente Conferência Internacional sobre TRCs realizada na Alemanha em 2015.

O presente estudo engloba o desenvolvimento de uma metodologia diferenciada de caracterização mecânica de TRCs em temperatura, baseada não apenas em ensaios residuais (após aquecimento e resfriamento), como também em testes à quente, realizados em uma ampla gama de temperaturas alvo (25°C até 1000°C). Tal metodologia possibilita tanto a avaliação, quanto a otimização dos TRCs em termos de segurança frente a temperaturas elevadas. Analogamente, a modelagem proposta no estudo, permite a previsão da resposta mecânica dos TRCs em condições residuais.

Os avanços deste trabalho em comparação às demais pesquisas presentes atualmente na literatura estão relacionados aos seguintes tópicos: utilização de matriz refratária (com agregados reativos) na produção de TRCs; utilização de tecido de basalto na produção de TRCs; e utilização de ensaios de tração à quente para avaliação do comportamento mecânico de TRCs sob temperaturas elevadas.

2 OBJETIVOS

Esta pesquisa tem por objetivo o desenvolvimento e a caracterização mecânica em temperaturas elevadas de dois tipos de TRCs, sendo o primeiro reforçado com basalto e o segundo reforçado com carbono. Ambos os compósitos foram produzidos a partir de uma mesma matriz de concreto refratário, visando sua aplicação em condições extremas, tais como temperaturas elevadas.

O presente trabalho foi escrito na forma de artigos dentre os quais alguns já foram publicados em periódicos internacionais indexados. Outros, no entanto, passaram pelo processo de submissão e aguardam aceitação por parte dos revisores. Os referidos artigos encontram-se no anexo do documento. Alguns estudos, não incluídos nos artigos, estão dispostos como capítulos independentes no corpo do trabalho (em português). O capítulo sobre metodologia e resultados resume as metodologias utilizadas para atingir os objetivos da presente pesquisa fazendo dessa forma uma ponte para os artigos. O estudo contempla ainda uma revisão bibliográfica, a qual apresenta uma visão geral das pesquisas encontradas na literatura que tratam da produção de TRCs, dos tipos de fibras empregados neste estudo (basalto e carbono) e do efeito da temperatura nas propriedades mecânicas da matriz e das fibras. A estrutura do trabalho foi definida da seguinte maneira:

1.0 – Introdução

2.0 – Objetivos

3.0 – Revisão Bibliográfica

4.0 – Metodologias e resultados

4.1 – Dosagem da matriz refratária;

4.2 – Influência da temperatura no comportamento químico e mecânico da matriz refratária (Artigo A);

4.3 – Propriedades mecânicas do tecido basalto;

4.4 – Influência da temperatura no comportamento mecânico de compósitos refratários reforçados com tecido de basalto (Artigos B e C);

4.5 – Simulação do comportamento mecânico de compósitos refratários reforçados com tecido de basalto (Artigo D);

4.6 – Influência da temperatura no comportamento mecânico de compósitos refratários reforçados com tecido de carbono (Artigo E);

5.0 – Conclusões e sugestões para trabalhos futuros.

Os artigos produzidos contemplam diferentes lacunas do conhecimento. Sendo assim, cada artigo abordará introduções, metodologias, conclusões e revisões bibliográficas específicas sobre o assunto ao qual faz referência.

3 REVISÃO BIBLIOGRÁFICA

Os primeiros TRCs (*Textile reinforced concretes*) surgiram no início da década de 80, tendo, como principal característica, a substituição do reforço convencional de aço por reforço têxtil (SCHEERER and SCHLADITZ, 2015). Compósitos têxteis são produzidos a partir de matrizes finas, com agregados de diâmetros máximos tipicamente inferiores a 2 mm. Sendo assim, é comum encontrar pesquisas tratando do material como “Argamassa reforçada com têxtil”, ou em inglês, TRM (*Textile reinforced mortar*).

TRCs podem ser fabricados através de diferentes técnicas, partindo da simples moldagem manual (*hand lay-up*) (Figura 3.1 - a), até processos mais complexos como a laminação, pultrusão, extrusão ou até injeção/bombeamento (Figura 3.1 - b).

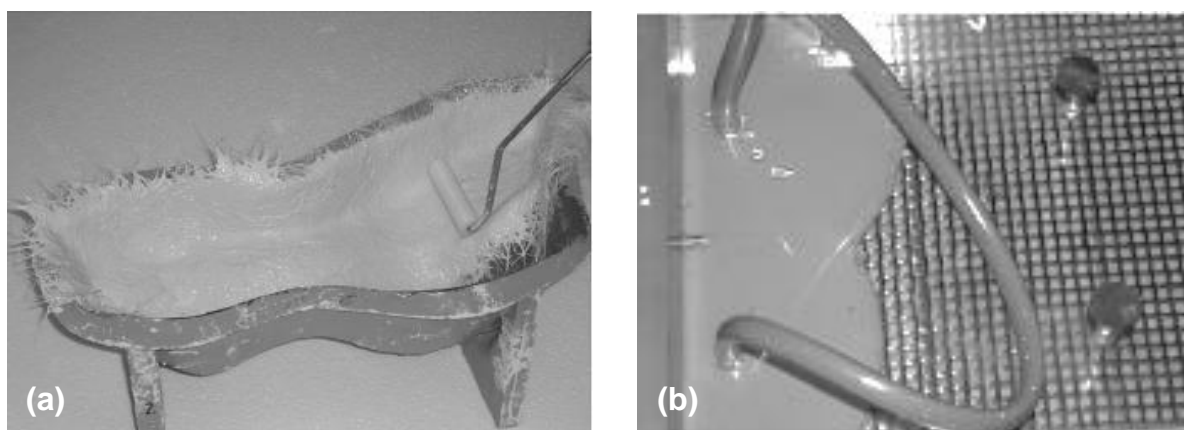


Figura 3.1 – Processos de fabricação de TRCs: (a) Moldagem manual e (b) bombeamento
(Adaptado de: BRAMESHUBER *et al.*, 2006)

A resposta mecânica de um compósito têxtil varia de acordo com as características da matriz (resistência, módulo de elasticidade, reologia), do tecido empregado como reforço

(tipo de fibra, arranjo espacial, volume de fibras, presença de revestimento) e da interação entre ambos. Alguns exemplos de reforço têxtil com diferentes configurações espaciais empregados em matrizes cimentícias são apresentados na Figura 3.2.

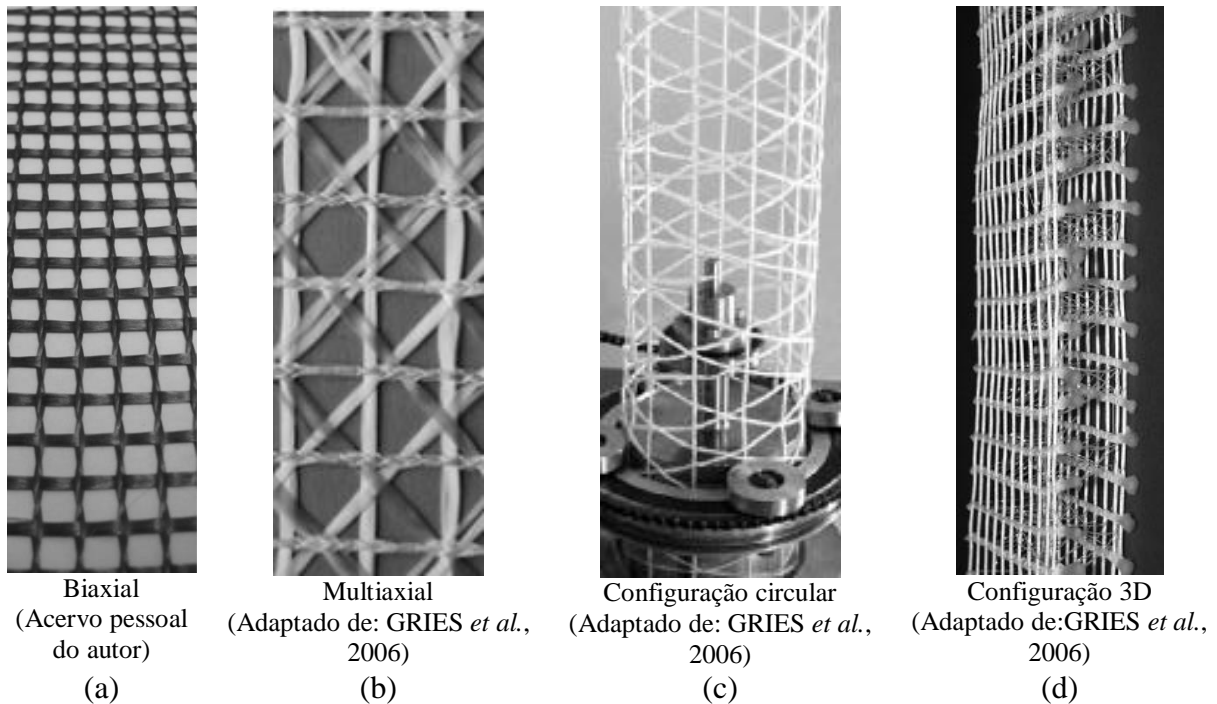
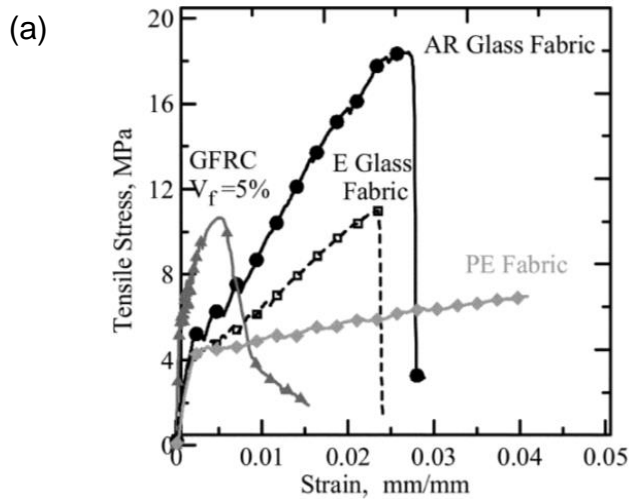
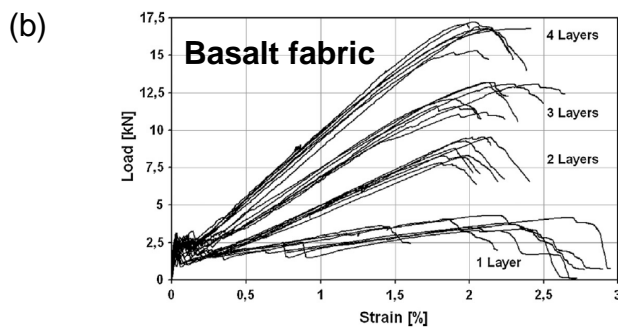


Figura 3.2 – Diferentes tipos de têxteis produzidos para aplicação em TRCs.

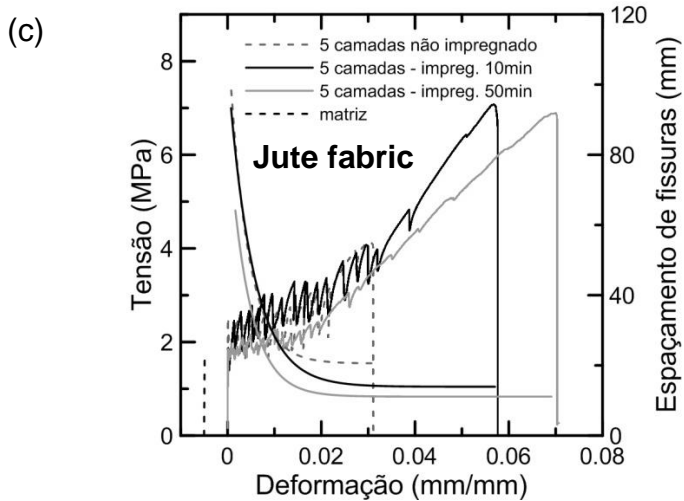
Dentre os tipos de reforço mais utilizados na produção de TRC estão tecidos de fibra de vidro, carbono e aramida. Entre os menos comuns, podem ser citados tecidos de basalto (LARRINAGA *et al.*, 2014), polietileno (PELED, 2007) e tecidos produzidos a partir de fibras naturais (SILVA *et al.*, 2007). Na Figura 3.3 são apresentados exemplos de respostas mecânicas de diferentes tipos de compósitos têxteis extraídos das referências bibliográficas deste estudo. Observando a Figura 3.3-b, por exemplo, é possível verificar a influência da fração volumétrica de fibras no desempenho de um compósito laminado produzido com tecido de basalto. Do mesmo modo, através da Figura 3.3-c, é possível observar a influência da impregnação com polímero em compósitos reforçados com tecido de juta.



Adaptado de:
PELED e MOBASHER,
2005



Adaptado de:
LARRINAGA *et al.* (2014)



Adaptado de:
FIDELIS *et al.* (2014)

Figura 3.3 – Comparação entre compósitos produzidos a partir de diferentes tipos de têxteis.

O tipo de tecido e sua configuração variam de acordo com o tipo de aplicação e com as condições as quais o compósito será submetido. Tecidos planos reforçados em duas ou mais direções são tipicamente empregados na produção de laminados finos, ou ainda no reforço/reparo de estruturas (Figura 3.4 – a b). Tecidos 3D são produzidos com a finalidade de reforçar elementos estruturais como vigas de diferentes seções, pilares e placas (Figura 3.4 – c).



Adaptado de:
TOMOSCHEIT *et al.* (2015)

Adaptado de:
SIM *et al.* (2002)

Adaptado de:
REMPPEL e HEGGER, 2015

Figura 3.4 – Aplicação de diferentes tipos de têxteis em elementos de concreto.

Conforme observado anteriormente na Figura 3.3, em geral, TRCs apresentam comportamento *strain-hardening*, o qual pode ser subdividido em três fases principais: fase elástica, formação de múltiplas fissuras e localização de fissuras (ver Figura 3.5). A primeira fase é composta pela resposta elástica do compósito, predominantemente governada pela matriz. O fim desta fase é alcançado quando o nível de tensão imposto ao compósito supera a resistência à tração do concreto. Após a formação da primeira fissura, inicia-se o processo de múltipla-fissuração do compósito, o qual caracteriza a segunda fase apresentada na ilustração. A terceira e última fase é caracterizada pela abertura das fissuras, bem como, pela localização de uma das fissuras, a qual passa a abrir mais que as demais fissuras, levando ao colapso do compósito.

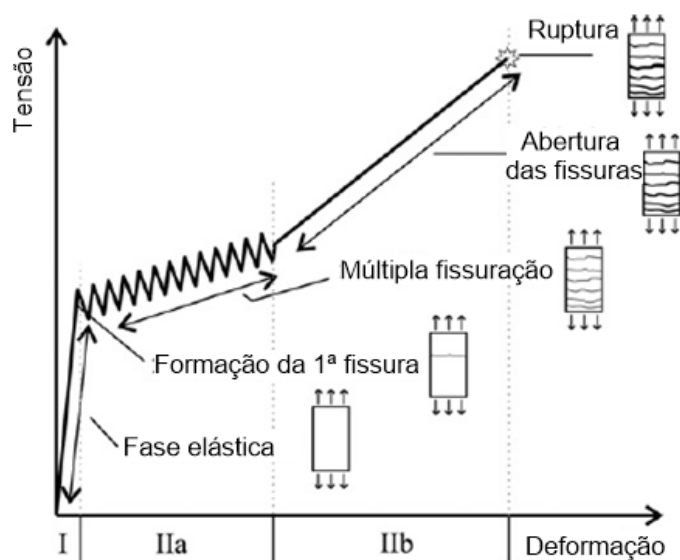


Figura 3.5 - Representação esquemática da resposta típica de um TRC submetido à tração (BARHUM e MECHTCHERINE, 2014).

Um dos principais aspectos a serem considerados em elementos de concreto, além da capacidade de suporte e da durabilidade, é a resistência a temperaturas elevadas. Esta lacuna, em termos de conhecimento científico (principalmente relativa a segurança das estruturas), é tida atualmente como um dos limitantes, que barram a entrada de artefatos de concreto reforçados com têxteis no mercado da construção civil. Em se tratando de compósitos têxteis, tanto o concreto quanto o reforço empregado sofrem efeitos deletérios provenientes das ações térmicas. Deste modo, assim como descrito por BÜTTNER *et al.* (2007), para o caso de TRCs, o efeito da temperatura deve ser investigado separadamente em todos os materiais envolvidos na produção do compósito (matriz, fibras e revestimentos).

Visando a manutenção da resistência mecânica do TRC sob temperaturas elevadas, o mesmo pode ser produzido utilizando matérias primas resistentes a efeitos térmicos. Matrizes de concreto refratário (CONCRETE SOCIETY, 1973), ou ainda geopoliméricas (ARIOZ *et al.*, 2012), podem ser empregadas com esta finalidade. Com relação ao tipo de reforço, é necessário que a estabilidade térmica das fibras seja compatível com o tipo de aplicação ou temperatura aos quais o compósito será submetido. Na Figura 3.6 pode-se visualizar o efeito da temperatura na resistência mecânica de alguns dos tipos de reforço empregados em TRCs.

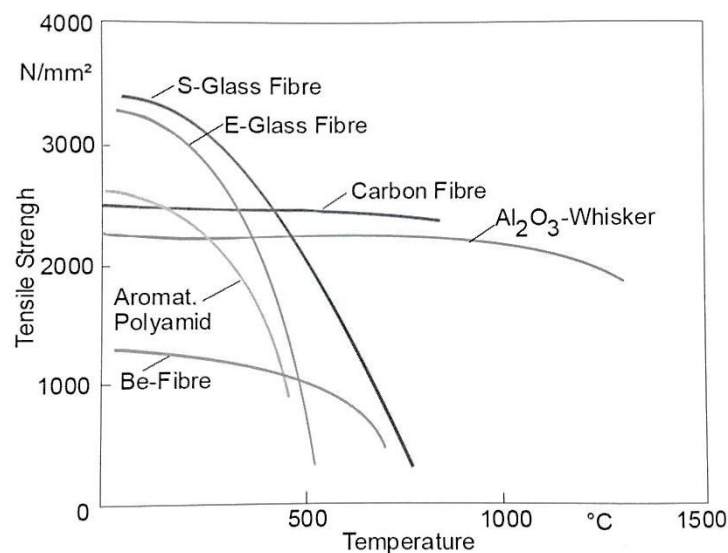
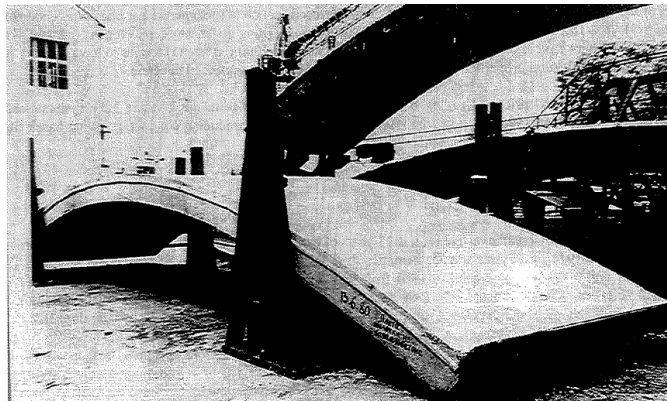


Figura 3.6 – Efeito da temperatura na resistência á tração de vários tipos de fibras (KRUGER e REINHARDT, 2006 citado por KLEINEBERG, 2004).

Embora incomuns no mercado brasileiro, fibras de basalto, objeto de estudo desta pesquisa, possuem boa estabilidade térmica, comparável a fibras com desempenho mecânico similar (ex: vidro e carbono). Além disso, o baixo custo de produção e a grande quantidade de matéria prima disponível tornam-nas normalmente mais baratas que fibras de vidro e de

carbono (LARRINAGA *et al.*, 2014, SINGHA, 2012, DI LUDOVICO *et al.*, 2010). Além da elevada resistência à tração ($\sim 2000\text{MPa}$), e módulo de elasticidade ($\sim 70\text{GPa}$), fibras de basalto não são combustíveis e possuem alta estabilidade química. São fibras inorgânicas produzidas a partir da fusão de rochas de basalto em temperaturas de aproximadamente 1500°C . Sob esta temperatura o material se liquidifica, possibilitando a fabricação de filamentos com diâmetros muito reduzidos (ex: $7\text{-}15\mu\text{m}$) (DIAS e THAUMATURGO, 2005, SIM *et al.*, 2002, *et al.*, 2003, SINGHA, 2012). Na maioria das vezes, tecidos produzidos a partir de fibras de basalto são empregadas como reforço em materiais poliméricos (WANG *et al.*, 2008, WANGA *et al.*, 2013), no entanto, possuem alto potencial mecânico/econômico para aplicações em compósitos cimentícios (Figura 3.7), incluindo a substituição de vergalhões de aço, ou de outros tipos de fibras (ex: kevlar, vidro e carbono) (BRIK, 1997).



Confinamento de elementos estruturais.
Adaptado de: DI LUDOVICO *et al.*(2010)

Reforço em núcleos de edifícios agrícolas.
Adaptado de: BRIK, 1997

Figura 3.7 – Aplicações de fibras e tecidos de basalto.

Fibras de carbono, também presentes no escopo do trabalho, possuem elevada estabilidade térmica (400 a 900°C), resistência à tração (2500 a 4000MPa), módulo de elasticidade ($\sim 250\text{GPa}$), resistência à corrosão e resistência à fadiga. Entretanto, são normalmente mais caras que as demais fibras dado seu complexo processo de produção. Quando expostas a altas temperaturas em atmosfera oxidante, as fibras de carbono se decompõem por oxidação.

Ambas as fibras, basalto e carbono, podem ser empregadas como reforço em matrizes refratárias produzidas a partir de cimento de aluminato de cálcio (CAC), uma vez que este tipo de cimento possui baixo teor de álcalis (LEA's, 2003), favorecendo assim a durabilidade das fibras. O mesmo não ocorre em matrizes de cimento Portland, onde a alcalinidade pode vir a degradar o reforço, diminuindo assim o desempenho final do compósito. A velocidade de hidratação dos cimentos com alto teor de alumina (utilizados em concretos refratários) é

normalmente superior àquelas observadas nos cimentos Portland comuns. Deste modo, concretos refratários podem alcançar cerca de 80% da resistência máxima nas primeiras 24 horas (BAZANT e KAPLAN, 1996). Tal característica favorece a produção de elementos pré-fabricados sendo, portanto, uma excelente vantagem em relação à produção de compósitos têxteis em larga escala.

Os CACs se distinguem do cimento Portland comum por possuírem maior teor de alumina (Al_2O_3) e apresentarem como característica comum, aluminatos de cálcio como fases reativas e hidratos formados (LEA's, 2004, BAŽANT *et al.*, 1996). O processo de formação dos hidratos provenientes do CAC depende fundamentalmente da temperatura na qual ocorre (Figura 3.8).

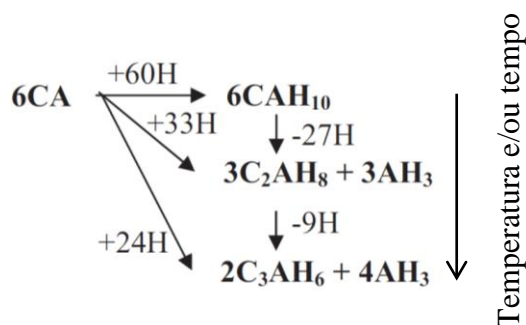


Figura 3.8 – Representação geral da formação de hidratos a partir do CA em cimentos de aluminato de cálcio (Adaptado de PENA e DE AZA, 1999).

Dentre os hidratos mais comumente encontrados em concretos refratários estão: o CAH_{10} ($\text{CaO} \cdot \text{Al}_2\text{O}_3 \cdot 10\text{H}_2\text{O}$), C_2AH_8 ($2\text{CaO} \cdot \text{Al}_2\text{O}_3 \cdot 8\text{H}_2\text{O}$), C_3AH_6 ($3\text{CaO} \cdot \text{Al}_2\text{O}_3 \cdot 6\text{H}_2\text{O}$) e AH_3 ($\text{Al}_2\text{O}_3 \cdot 3\text{H}_2\text{O}$) (TURRIZIANI, 1984, GUIRADO *et al.*, 1998, LEA's, 2004).

O hidrato CAH_{10} é um hidrato metaestável de baixa densidade ($\sim 1,72 \text{ g/cm}^3$) cuja formação é favorecida em temperaturas baixas (ex: $5\text{-}20^\circ\text{C}$) (GUIRADO *et al.*, 1998, RAMACHANDRAN *et al.*, 2002). Como reportado por TURRIZIANI (1984), os cristais de CAH_{10} são hexagonais prismáticos. Em sua estrutura, o CAH_{10} possui moléculas de água as quais podem ser subtraídas facilmente pelo aquecimento, dando origem a hidratos mais estáveis como o C_2AH_8 e o C_3AH_6 . Este fenômeno é altamente dependente da temperatura (RAMACHANDRAN *et al.*, 2002).

O hidrato C_2AH_8 , com estrutura cristalina também hexagonal, é mais estável que o CAH_{10} a temperaturas em torno de 25°C e apresenta densidade de $1,92 \text{ g/cm}^3$. Sua formação é favorecida pelo aumento da temperatura durante a hidratação (ex: $21\text{-}35^\circ\text{C}$). Em conjunto,

CAH₁₀ e C₂AH₈ constituem o principal grupo de hidratos responsáveis pela resistência inicial dos concretos produzidos a partir de CAC's. Ambos sofrem o fenômeno conhecido como "conversão" (que resulta na formação de C₃AH₆ e AH₃), o qual só ocorre em detrimento do tempo, ou da temperatura à qual o concreto for submetido, sendo sempre necessária a presença de água livre (RAMACHANDRAN *et al.*, 2002).

A formação dos hidratos C₃AH₆ e AH₃ acontece devido ao processo de conversão dos hidratos metaestáveis CAH₁₀ e C₂AH₈. No entanto, sob elevadas temperaturas e na presença de água, ambos podem ser formados diretamente a partir do monoaluminato de cálcio (CA) ou ainda do C₁₂A₇, fases presentes na maioria dos CAC's.

De acordo com a literatura (RAMACHANDRAN *et al.*, 2002, LEA's, 2004), a conversão dos hidratos metaestáveis em C₃AH₆ e AH₃ é acompanhada por uma marcante redução da resistência mecânica. Isto porque, a conversão das fases hexagonais (CAH₁₀ e C₂AH₈) para a fase cúbica (C₃AH₆) resulta em decréscimos de volume sólido de mais de 50% para ambos os hidratos, aumentando assim o volume de vazios da pasta. Por essa razão muitos colapsos em estruturas ocorreram na década de 70 no Reino Unido. Sua utilização, no entanto, não diminuiu e continua sendo recomendada para aplicações específicas onde suas vantagens únicas desempenham papel importante.

Um dado interessante relacionado à combinação entre as matrizes de CAC e ambas as fibras empregadas neste estudo (basalto e carbono) está nas propriedades térmicas destes materiais. Fibras de basalto e carbono possuem coeficientes de expansão térmica (sentido radial) de, respectivamente, $8 \times 10^{-6}/K$ (DHAND *et al.*, 2015) e $12 \times 10^{-6}/K$ (XIA *et al.*, 2015), enquanto matrizes refratárias possuem coeficientes da ordem de $2,5 \times 10^{-6}/K$ a $5 \times 10^{-6}/K$ (BAZANT e KAPLAN, 1996). Este fato contribui para o aumento da área de interface entre fibras e matriz quando da ocorrência do acréscimo da temperatura, resultando assim em melhorias no desempenho mecânico do compósito.

Estudos sobre o comportamento mecânico de TRCs submetidos a temperatura elevada são escassos na literatura disponível. Na maioria dos casos, são desenvolvidos por grupos de pesquisa financiados por empresas produtoras de artefatos de concreto reforçados com têxteis que mantêm os dados sob sigilo até patentear o produto e colocá-lo no mercado. Tal fato mostra-se muito presente na Alemanha, país expoente na fabricação e utilização de têxteis como reforço em concreto.

SILVA *et al.*, (2014) desenvolveram testes residuais de arrancamento em compósitos têxteis reforçados com fibras de carbono revestidas por polímero SBR. Os resultados revelaram que o aquecimento/resfriamento do polímero presente no tecido, na temperatura de 150°C, gera um eficiente mecanismo de intertravamento entre os filamentos. Tal mecanismo resultou em acréscimos significativos na resistência ao arrancamento dos cordões de carbono.

KRÜGER e REINHARDT, (2006) realizaram testes de fogo direto em quatro diferentes vigas (tipo I) produzidas a partir de argamassa reforçada com têxteis de fibras de vidro (resistentes a ataque alcalino) e carbono. A investigação centrou-se na capacidade de carga dos compósitos durante um teste a fogo sob carga constante. Em um dos tecidos de carbono, uma resina SBR foi utilizada como revestimento. Os resultados mostraram-se extremamente dependentes da resistência mecânica das fibras utilizadas quando submetidas à temperatura. Devido à perda de rigidez do revestimento SBR (a cerca de 90°C) a interface fibra-matriz foi rapidamente prejudicada, resultando no arrancamento das fibras e, subsequente, colapso do compósito.

O presente estudo contribui para o avanço do conhecimento referente ao comportamento mecânico à tração sob temperaturas elevadas de compósitos reforçados com tecido de basalto e carbono. A pesquisa contempla ensaios realizados em tecidos revestidos e não revestidos, em temperaturas alvo pré-determinadas, em duas diferentes condições: à quente e residuais (após aquecimento e resfriamento).

4 METODOLOGIAS E RESULTADOS

Assim como abordado nos objetivos, o capítulo 4 foi subdividido em 6 diferentes itens. Em sua fase inicial, o capítulo tratou da dosagem da matriz refratária (item 4.1), realizada de modo a combinar alta compacidade e reologia adequada à produção de TRCs. Posteriormente, no item 4.2, a matriz foi caracterizada química e mecanicamente (em testes residuais) entre as temperaturas de 25°C e 1000°C. Neste item, buscou-se determinar a influência da temperatura na microestrutura da matriz (formação/transformação/desidratação de fases), bem como no comportamento mecânico da mesma. Este estudo deu origem ao primeiro artigo científico da tese, Artigo A (ver anexos). Dando continuidade a pesquisa (item 4.3), o tecido de basalto, assim como a matriz refratária, teve suas propriedades mecânicas investigadas, tanto na temperatura ambiente quanto em testes residuais (25°C à 1000°C). Este item, assim como o item 4.2, teve como objetivo a caracterização “individual” dos materiais que deram origem aos primeiros TRCs produzidos no estudo (item 4.4).

O item 4.4 aborda a influência da temperatura no comportamento mecânico de compósitos produzidos a partir da matriz refratária e do tecido de basalto caracterizados respectivamente nos itens 4.2 e 4.3. Com base neste estudo, dois diferentes artigos científicos foram produzidos, Artigo B e Artigo C (ver anexos). O primeiro, remete principalmente ao desenvolvimento do TRC e seu desempenho em ensaios de tração residuais. O segundo, no entanto, compara o comportamento mecânico residual do compósito com o comportamento à quente.

No item 4.5 uma simulação do comportamento mecânico residual dos compósitos reforçados com tecido de basalto foi desenvolvida através de um modelo de diferenças finitas

(Artigo D). Por fim, objetivando o desenvolvimento de compósitos de alta performance em ambientes de temperatura elevada, compósitos refratários reforçados com tecido de carbono foram produzidos e testados sob tração à quente, resultando assim no último artigo do estudo, Artigo E.

4.1 DOSAGEM E CARACTERIZAÇÃO BÁSICA DA MATRIZ REFROTÁRIA

4.1.1 INTRODUÇÃO

Matrizes cimentícias utilizadas na produção de compósitos têxteis devem atender exigências especiais em relação à reologia, resistência e afinidade com o reforço fibroso. Fibras de basalto e carbono podem sofrer degradação em matrizes alcalinas, perdendo assim parte da resistência mecânica. Neste contexto, este capítulo aborda o desenvolvimento de uma matriz quimicamente compatível com reforço fibroso empregado no estudo (basalto e carbono), de alta compactidade e com propriedades reológicas satisfatórias à produção de compósitos têxteis.

O capítulo se inicia com a caracterização dos materiais que constituem a matriz, seguida da dosagem da mistura binária de grãos (cimento + agregado). O software *Betonlab Pro3*[®] foi empregado de modo a otimizar a mistura granular seca visando a obtenção de uma matriz compacta e de alta resistência. A matriz obtida foi caracterizada mecanicamente aos 7, 14 e 28 dias de idade.

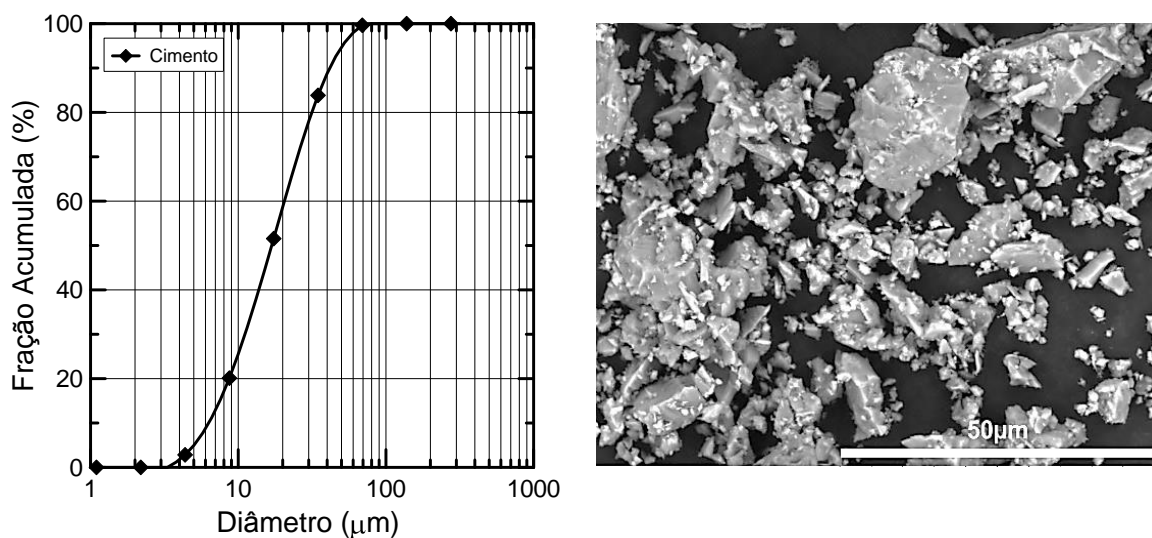
4.1.2 MATERIAIS E MÉTODOS

Os materiais selecionados para a confecção da matriz refratária foram cimento de aluminato de cálcio (Secar 51), agregado sintético denso de aluminatos de cálcio (Alag Fino), aditivo modificador de viscosidade (VMA), superplastificante em pó a base de policarboxilatos (Peramin[®]CONPAC 500) e água. Neste estudo, a formulação da matriz refratária foi obtida com o auxílio do software *Betonlab Pro3*[®], o qual se utiliza do modelo do empacotamento compressível (MEC) como ferramenta de dosagem. Através dele, é realizada a otimização dos constituintes do concreto, visando não apenas o aumento da compactidade das misturas granulares, como também a diminuição da porosidade e do risco

de segregação. Este software permite simular diferentes composições ou esqueletos granulares para uma determinada mistura visando atender propriedades pré-definidas, sejam elas no estado fresco ou endurecido. Mais detalhes sobre o MEC podem ser obtidos nos estudos de DE LARRARD (1999), SEDRAN (1999) e FORMAGINI (2005). A caracterização dos constituintes da matriz refratária serviu como base de dados para as simulações geradas no software *Betonlab Pro3*®.

4.1.2.1 Cimento

Dentre os vários cimentos aluminosos existentes, optou-se neste estudo pela utilização do cimento de aluminato de cálcio Secar 51, comercializado no Brasil pela empresa Kerneos. O cimento apresentou massa específica de $3,035 \text{ kg/m}^3$, determinada através de picnômetro a gás (hélio), modelo Accupyc da Micromeritics, disponível no laboratório de físico-química do LabEST. A Figura 4.1 – a apresenta a curva granulométrica do cimento. Através da Figura 4.1 - b é possível visualizar a ampla faixa de tamanhos de partículas do cimento, obtida por microscopia eletrônica de varredura com detecção por elétrons retroespalhados.



a) Curva granulométrica do cimento

b) Morfologia das partículas de cimento

Figura 4.1 – Curva granulométrica e micrografia do cimento aluminoso.

A determinação da composição química do cimento aluminoso Secar 51 (Tabela 4.1) foi realizada por meio de espectroscopia por fluorescência de energia dispersiva de raios-X. O equipamento utilizado foi o EDX 800, da marca Shimadzu, pertencente ao Laboratório de Estruturas e Materiais da COPPE/UFRJ, com tubo de ródio e detector de Silício (Lítio), resfriado com nitrogênio líquido.

Tabela 4.1 – Composição química do cimento aluminoso.

Cimento	
Composto	Quantidade (% em massa)
Al ₂ O ₃	51,45
CaO	38,51
SiO ₂	3,07
Fe ₂ O ₃	1,76
TiO ₂	1,89
SO ₃	0,61
K ₂ O	0,42
ZrO ₂	0,12
Cr ₂ O ₃	0,07
SrO	0,05
Ta ₂ O ₅	0,03
MnO	0,02
Ga ₂ O ₃	0,01
Y ₂ O ₃	0,01
NbO	0,01
Perda ao fogo	1,96

4.1.2.1 Agregado

Neste estudo optou-se pela utilização de um agregado sintético à base de aluminatos de cálcio, obtido por fusão, comercializado no Brasil pela empresa KERNEOS com a denominação (Alag fino). Este agregado, segundo dados fornecidos pelo fabricante, é resistente a choques térmicos e indicado para utilização em temperaturas na faixa dos -180°C a 1100°C. O agregado foi peneirado de modo que fossem utilizadas na produção dos concretos apenas partículas com diâmetros inferiores a 1,18mm.

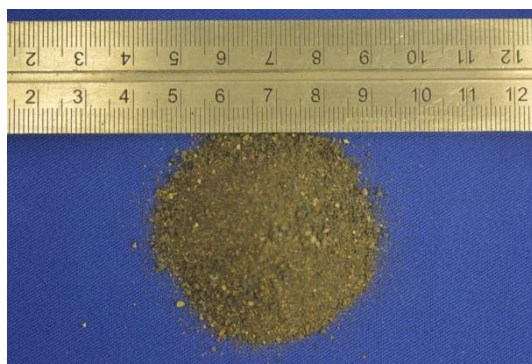


Figura 4.2 – Agregado com diâmetro inferior a 1,18mm.

A Figura 4.3 - a apresenta a curva de distribuição granulométrica do agregado utilizado na preparação dos concretos refratários. A distribuição granulométrica das partículas com diâmetros entre 1,18mm e de 300µm foi determinada através de

peneiramento, de acordo com os procedimentos estabelecidos na NBR NM 248 (2003). A composição granulométrica do material passante na malha com abertura de $300\mu\text{m}$ foi determinada por granulometria a laser, utilizando o equipamento MALVERN disponível no laboratório de físico-química do LabEST. Juntamente com a curva granulométrica, é apresentada uma imagem do agregado (Figura 4.3 - b) obtida por microscopia eletrônica de varredura.

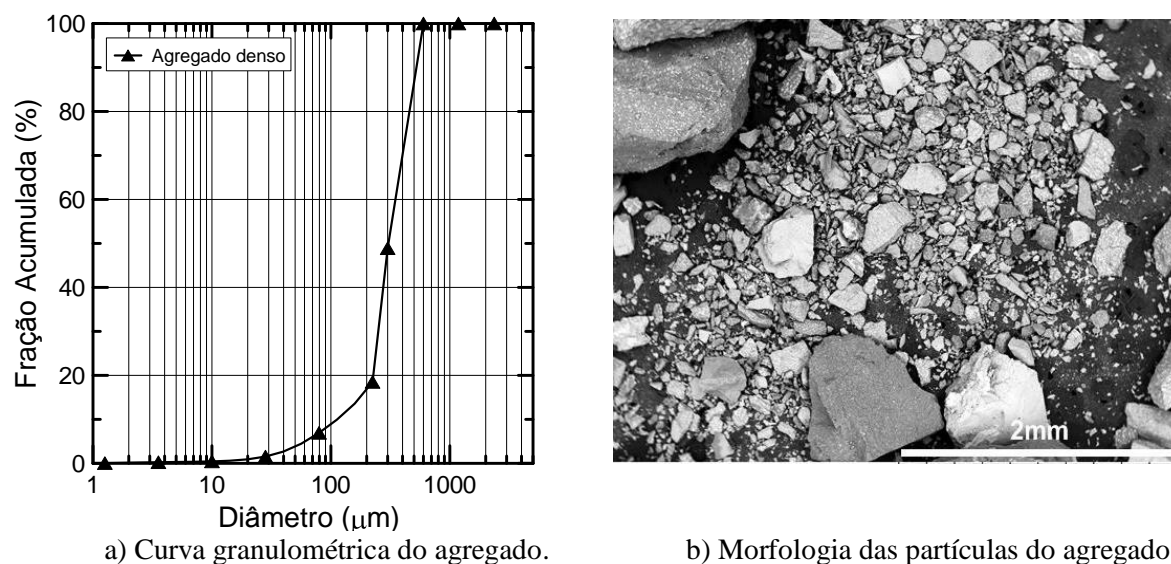


Figura 4.3 – Curva granulométrica e micrografia do agregado.

Os parâmetros característicos D_{80} e D_{50} os quais se referem respectivamente aos tamanhos de partículas abaixo do qual se encontram 80% e 50% da massa do material, também foram determinados.

Tabela 4.2 – Diâmetro do agregado (D_{80} e D_{50}).

Diâmetro	
D_{80}	482,58 μm
D_{50}	306,45 μm

O valor de massa específica do agregado foi determinado através de picnômetro a gás (hélio), modelo Accupyc da Micromeritics, disponível no laboratório de físico-química do LabEST. A picnometria a hélio consiste na determinação do volume de uma amostra, cuja massa é conhecida, através da variação de pressão do gás em um volume calibrado. O resultado da determinação foi de $3,18 \text{ g/cm}^3$, obtido a partir da média aritmética de três determinações.

O resultado da composição química do agregado, utilizando o equipamento EDX 800, encontra-se na Tabela 4.3.

Tabela 4.3 – Composição química do agregado

Agregado	
Composto	Quantidade (% em massa)
Al ₂ O ₃	39,88
CaO	36,02
Fe ₂ O ₃	14,48
SiO ₂	2,79
P ₂ O ₅	1,77
TiO ₂	1,61
SO ₃	1,05
K ₂ O	0,19
MnO	0,19
Ga ₂ O ₃	0,15
ZrO ₂	0,09
V ₂ O ₅	0,06
SrO	0,03
Y ₂ O ₃	0,01
Perda ao fogo	1,68

4.1.2.2 *Agente modificador de viscosidade (VMA)*

Visando evitar a exsudação, segregação e manter a coesividade dos concretos refratários, foi empregado na mistura um agente modificador de viscosidade (Rheomac UW 410), fabricado pela empresa BASF. O Rheomac UW 410 é um produto com base química de polímeros de celulose de alto peso molecular em forma de pó e de cor branca.

4.1.2.3 *Superplastificante*

Tendo em vista a importância da dispersão das partículas no desempenho reológico e mecânico da matriz refratária, neste estudo fez-se uso de um aditivo superplastificante em pó como constituinte da mistura. As principais características do aditivo encontram-se descritas na Tabela 4.4.

Tabela 4.4 – Características do aditivo superplastificante.

Características	Peramin®CONPAC 500
Base	policarboxilatos (PCE)
Aparência	pó
Massa específica (g/cm ³)	0,45

*Dados fornecidos pelo fabricante

4.1.2.4 *Determinação da compacidade experimental dos materiais*

A determinação da compacidade experimental, propriedade indispensável para o processo de dosagem por meio do MEC (Modelo do empacotamento compressível) foi

realizada de duas diferentes maneiras: ensaio de demanda d'água (em materiais compostos por partículas < 100µm) e ensaio de compressão e vibração (em materiais compostos por partículas > 100µm).

- **Ensaio de demanda d'água**

Este ensaio consiste em adicionar progressivamente água a uma mistura granular seca visando à obtenção de uma pasta homogênea com máximo empacotamento das partículas. Neste caso, a massa de água empregada para alcançar a mistura homogênea é definida como “demanda de água do material”. Mais detalhes podem ser obtidos em FORMAGINI (2005) e SEDRAN (1999).

O ensaio de demanda d'água é realizado em um misturador planetário de 2 L de capacidade. Durante o processo de adição de água ao material seco, são criadas pontes líquidas entre as partículas, são originadas pela tensão superficial da água. Como resultado, reduz-se o índice de vazios da mistura, fase denominada “estado pendular”. Dando continuidade a adição de água, o material atinge outro estado conhecido como “estado funicular” onde as partículas encontram-se envoltas por água ao longo de toda a superfície. Neste estado, também é possível observar a presença de bolhas de ar em meio à pasta. A última e mais importante fase é denominada “capilar” e resulta do preenchimento total dos vazios da pasta por água. O início desta fase é caracterizado como o “ponto de demanda de água” do material.

Os ensaios de demanda d'água (com e sem superplastificante) foram realizados a 24°C ± 1°C. O tempo médio de ensaio foi de 10 min. O valor de compacidade real de empacotamento foi determinado pela equação (1).

$$c = \frac{1}{1 + \delta \frac{m_a}{m}} \quad (1)$$

Onde:

c: Compacidade experimental;

m_a: Massa de água;

m: Massa de material seco;

δ : Massa específica do material;

- **Ensaio de compressão e vibração**

Em seus estudos DE LARRARD (1999) propõe que o ensaio de compacidade utilizando energia de prensagem e vibração seja realizado com o material dividido em classes de monotamanhos, formados pelos grãos compreendidos entre as peneiras da série normal. SILVA (2004), entretanto, avaliou os valores de compacidade de cada classe monotamanho de uma areia e obteve variação pouco significativa, inferior a 5%. Desta forma, no presente estudo, optou-se por não dividir o agregado sintético de aluminato de cálcio em classes de monotamanhos durante a determinação da compacidade experimental. Como resultado, apenas um valor de compacidade foi obtido para o material como um todo (as várias classes monotamanho que compõe o agregado).

Na Figura 4.4 são apresentadas etapas do ensaio de compacidade realizado para o agregado denso em estudo. As etapas do ensaio foram as seguintes:

- Posicionamento e fixação do cilindro metálico na região central da mesa vibratória;
- Colocação da massa de material seco (3 kg) no cilindro metálico (Figura 4.4 – a);
- Colocação do pistão maciço de aço (com peso aproximado de 200 N) sobre a amostra, já depositada no interior do cilindro metálico (Figura 4.4 – b)¹;
- Inicialização do processo de vibração da mesa (a uma frequência de 68 Hz) com duração de 3 min.
- Determinação das posições inicial (sem amostra) e final do pistão (amostra compactada) realizadas com o auxílio de um catetômetro (Figura 4.4 – c) nivelado e posicionado à frente da mesa vibratória.

¹ A finalidade de dispor o maciço de aço sobre a amostra durante a vibração é provocar uma pressão constante de 10 kPa sobre o material seco ao longo de todo o ensaio.



a) Agregado denso depositado no interior do cilindro metálico.



b) Cilindro metálico portando a amostra e o pistão maciço de aço.



c) Catetômetro utilizado para a determinação do parâmetro “h”.

Figura 4.4 – Ensaio de compactação experimental.

Depois de finalizado o ensaio, a compactação real de empacotamento “ C ” foi determinada pela equação (2).

$$C = \frac{4M_s}{\pi D_c^2 h \rho_s} \quad (2)$$

Onde:

ρ_s : Densidade do material;

M_s : Massa do material seco;

D_c : Diâmetro interno do cilindro metálico;

h : Altura final da camada do material seco compactado.

Os detalhes e as dimensões do conjunto de aparatos utilizados no ensaio de compactação encontram-se na Figura 4.5 juntamente com um esquema indicando a localização do parâmetro h .

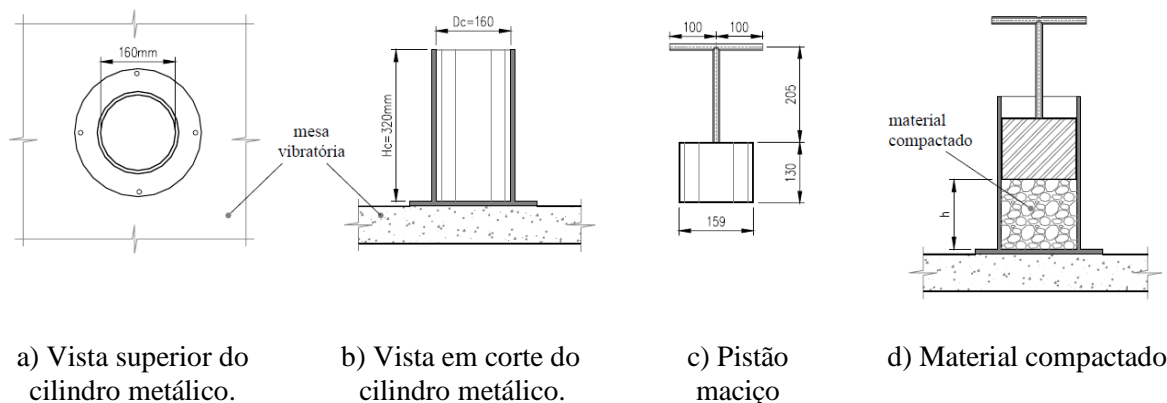


Figura 4.5 – Detalhes e dimensões dos equipamentos utilizados no ensaio de compacidade experimental (Fonte: Adaptado de FORMAGINI, 2005).

- **Determinação do ponto de saturação (Ensaio de Cone de Marsh)**

A compatibilidade entre o cimento aluminoso Secar 51 e o superplastificante Peramin[®]CONPAC 500 foi avaliada através do ensaio de escoamento utilizando o funil de Marsh (AİTCIN, 1998). O método baseia-se em medir o tempo necessário para que 1 L de pasta escoe através de um funil de um dado diâmetro (para diferentes teores de superplastificante). As medições do tempo de escoamento são feitas em intervalos de tempo pré-determinados (5, 15 e 30 min), de modo a verificar variações das propriedades reológicas da pasta com o tempo.

O ponto de saturação é determinado a partir da análise das curvas de tempo de escoamento *versus* teor de superplastificante. Sua obtenção é feita observando-se o ponto, a partir do qual, a adição de superplastificante não acarreta reduções significativas no tempo de escoamento da pasta. Assim como descrito por AİTCIN (1998), a compatibilidade entre o cimento e o superplastificante só se estabelece, quando os diferentes tempos de escoamento analisados apresentam valores próximos (para um mesmo teor de superplastificante). Caso o oposto ocorra, e o intervalo entre os tempos de escoamento do fluido forem significativamente diferentes, diz-se então que o dispersante possui “baixa eficiência” para com o cimento empregado.

4.1.3 RESULTADOS

4.1.3.1 *Empacotamento de materiais compostos por partículas < 100µm (procedimento de demanda de água)*

A compacidade real do cimento aluminoso (com e sem dispersante) foi obtida experimentalmente através de um ensaio denominado “método de demanda de água”, proposto por De LARRARD (1999). Para esta e as demais análises foram empregados 350 g de material seco em misturador planetário de 5 L.

Os resultados de compacidade experimental (C) dos materiais com dimensões inferiores a 100 µm, determinados pelo procedimento de demanda de água são apresentados na Tabela 4.5. Cada valor foi obtido a partir da média aritmética de três determinações.

Tabela 4.5 – Compacidade dos materiais com dimensões inferiores a 100µm.

Material	Sem dispersante	Com dispersante (Peramin®CONPAC 500)	
	Compacidade (C)	Teor de dispersante (%)	Compacidade (C)
Cimento Secar 51	0,547	0,5	0,634

A compacidade experimental (C) do cimento Secar 51 aumentou de 0,547 sem dispersante, para 0,634 com dispersante tipo Peramin®CONPAC 500. Observa-se deste modo, um aumento de 15,9 % no valor da compacidade. Este acréscimo se dá em função do efeito de repulsão das partículas de cimento e da redução da água de amassamento, ambos promovidos pelo dispersante em pó. Uma vez que o ensaio de demanda de água se baseia no reconhecimento visual do ponto em que a mistura atinge o estado “capilar”, quando da utilização do superplastificante, menor será a quantidade de água necessária para que a mistura atinja este estado e, portanto, maior será a compacidade alcançada para uma mesma quantidade de cimento.

4.1.3.2 *Empacotamento de materiais compostos por partículas > 100µm (procedimento utilizando energia de prensagem e vibração)*

O valor experimental de compacidade, obtido através do procedimento utilizando energia de prensagem e vibração, para o agregado sintético de aluminato de cálcio é apresentado na Tabela 4.6, juntamente com o valor da altura final da camada compactada (*h*).

Tabela 4.6 – Compacidade dos materiais com dimensões superiores a 100 μm .

Parâmetros	Material
	Agregado sintético de aluminato de cálcio
Camada compactada – h (mm)	68,73
Compacidade real – C	0,682

4.1.3.3 Determinação do ponto de saturação (Ensaio de Cone de Marsh)

Neste estudo, utilizou-se um funil de Marsh com abertura diametral de 5 mm (Figura 4.6). Para cada análise dos tempos de escoamento, 1000 mL de material foram produzidos. As pastas empregadas para os ensaios de compatibilidade e ponto de saturação utilizaram relação água/cimento constante de 0,35.



a) Funil de Marsh e proveta graduada (1,2 L).



c) Misturador industrial.

Figura 4.6 – Instrumentos necessários ao ensaio de compatibilidade e ponto de saturação.

Na Figura 4.7 são apresentados os resultados obtidos do ensaio com o cone de Marsh para os tempos de escoamento de 5, 15 e 30 min. O ponto de saturação observado para o aditivo foi de 0,5% da massa de cimento. Dada a proximidade entre os diferentes valores de escoamento mensurados, o aditivo superplastificante foi considerado compatível com o cimento aluminoso.

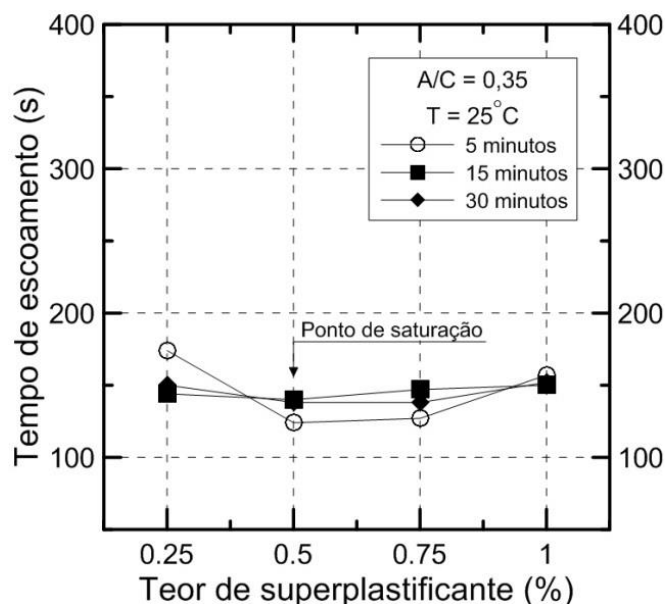


Figura 4.7 – Curvas de escoamento em cone de Marsh para pastas com diferentes dosagens de aditivo superplastificante.

4.1.3.4 Aplicação do MEC ao caso da matriz refratária

Na Figura 4.8 está apresentada a evolução da compacidade do esqueleto granular sólido (ϕ^*) do concreto refratário, obtida no *software Betonlab Pro3®* a partir da variação da relação entre cimento (C) e agregado (A) para um fator água/cimento fixo de 0,35. Assim como descrito no início do capítulo, a dosagem foi realizada visando a obtenção da maior compacidade possível para a mistura binária em estudo, mantendo reologia adequada para utilização de reforços têxteis.

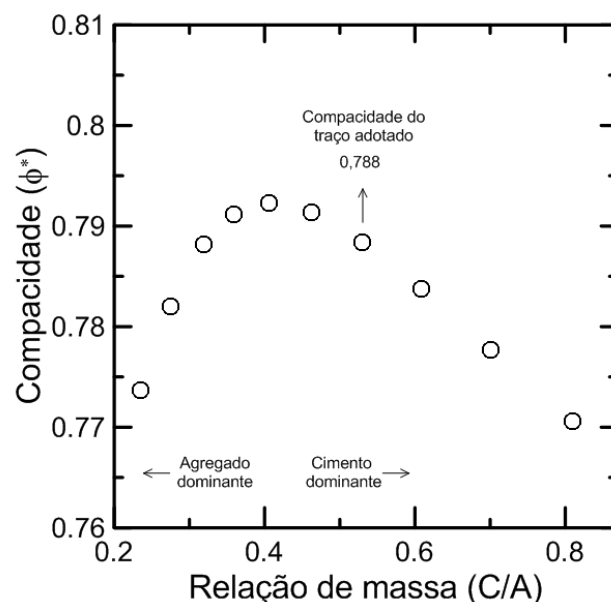


Figura 4.8 – Evolução da compacidade do esqueleto granular sólido (binário) da matriz refratária.

Para a mistura investigada (Figura 4.8), a maior compacidade (0,792) foi atingida para uma relação cimento/agregado igual a 0,405 (massa de cimento: 650 kg; massa de agregado “A1”:1602,1 kg). No entanto, quando reproduzida em laboratório a mistura não apresentou fluidez necessária à produção dos compósitos têxteis. Visando priorizar a compacidade, mas ao mesmo tempo garantir uma reologia adequada à produção de TRCs, outro traço gerado pelo *software* com relação cimento/agregado igual a 0,529 (massa de cimento: 750 kg; massa de agregado: 1416,2 kg) foi reproduzido em laboratório (compacidade 0,788). Este último satisfaz os critérios almejados, uma vez que apresentou compacidade próxima da máxima (ver Figura 4.8) e capacidade de fluir através das malhas de reforço sem sinais de segregação ou exsudação. O traço adotado no estudo, gerado pelo *software Betonlab Pro3®*, com reologia adequada à confecção dos compósitos têxteis, encontra-se na Tabela 4.7. É importante ressaltar que o traço utilizado na produção dos TRCs utiliza um teor de superplastificante de 0,65%, superior ao ponto de saturação determinado anteriormente através do ensaio com Cone de Marsh. Esta otimização é proveniente do próprio *software* e se dá em função da maior quantidade de finos (cimento) empregada no referido traço (750kg/m³).

Tabela 4.7 – Composição da matriz de concreto refratário.

Composição	
Agregado (kg/m ³)	1416,2
Cimento (kg/m ³)	750
Superplastificante (kg/m ³)	4,87
Modificador de Viscosidade (kg/m ³)	0,562
Água (kg/m ³)	262,6
Teor de superplastificante (%)	0,65
Água/cimento	0,35

4.1.3.5 Caracterização mecânica da matriz

A produção da matriz de concreto foi realizada em sala climatizada a $24^{\circ}\text{C} \pm 1^{\circ}\text{C}$, utilizando um misturador planetário com capacidade para 5 L de concreto. Durante a produção, os materiais secos (incluindo o superplastificante em pó) foram adicionados à cuba do misturador e homogeneizados em velocidade baixa durante um minuto. Após esta etapa, foi realizada a adição da água da mistura seguida de um período de homogeneização de 3 minutos em velocidade média e, por fim, adição do VMA seguida de 1 min de homogeneização. Para os ensaios de resistência à compressão e módulo de elasticidade foram confeccionados corpos-de-prova cilíndricos de 50 mm de diâmetro e 100 mm de altura. Todos os corpos-de-prova foram faceados em torno mecânico de forma a garantir planicidade e paralelismo entre as faces.

A matriz refratária foi submetida a ensaios de resistência à compressão aos 7, 14 e 28 dias de idade. A Figura 4.9 apresenta as curvas típicas de tensão *versus* deformação obtidas dos ensaios compressão para as idades investigadas. Do mesmo modo, na Tabela 4.8 são apresentados os resultados de carga de ruptura (ou carga crítica) “ P_{cr} ”, tensão de pico (ou tensão crítica) “ σ_{cr} ”, deformação de ruptura (ou deformação crítica) “ ϵ_{cr} ” e módulo de elasticidade (referentes à média aritmética de 4 amostras). O módulo de elasticidade foi obtido no trecho linear das curvas, até 40% da carga máxima. Através da Tabela 4.8 é possível verificar que com apenas 7 dias de cura, a matriz refratária alcança cerca de 90% da resistência e 80% do módulo de elasticidade alcançados aos 28 dias. Sendo assim, visando acelerar o processo de caracterização tanto da matriz quanto dos compósitos, a idade de 7 dias foi definida como idade padrão para todos os ensaios mecânicos realizados no presente estudo (incluindo os ensaios realizados nos demais capítulos).

Acredita-se que a escolha de uma idade padrão mais elevada (ex: 28 dias) acarretaria em diferenças nos resultados obtidos para os compósitos testados em temperatura. Tal fato é

provável, uma vez que processo de conversão induzido pelo tempo altera a microestrutura da matriz (ver item 4.2).

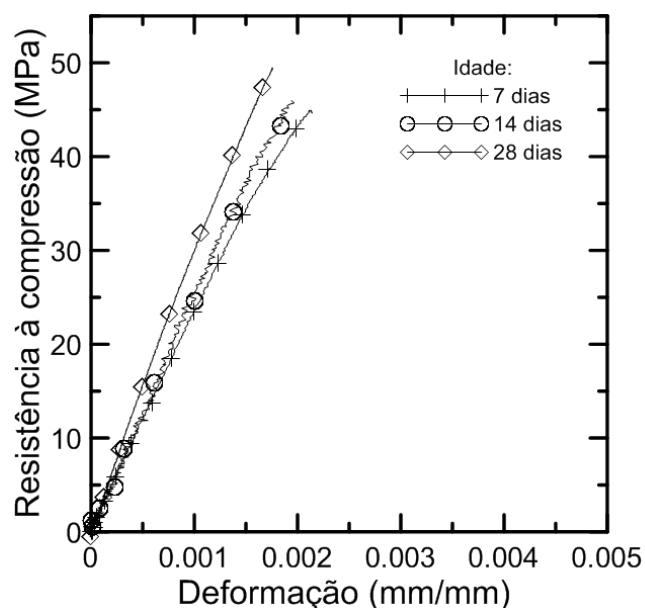


Figura 4.9 – Curvas típicas de resistência à compressão do concreto refratário aos 7, 14 e 28 dias de idade.

Tabela 4.8 – Resultados dos ensaios de resistência à compressão uniaxial da matriz para diferentes idades.

Idade (dias)	Valores experimentais			
	P_{cr} (kN)	σ_c (MPa)	ϵ_{cr} (mm/mm)	E_c (GPa)
7	89,78	45,72	0,00217	25,05
	(6,55)	(3,33)	(0,000195)	(1,09)
14	96,19	48,98	0,00212	23,25
	(12,62)	(6,43)	(0,000223)	(4,17)
28	100,80	51,34	0,00177	31,25
	(3,42)	(1,74)	(0,000067)	(1,25)

4.1.4 CONCLUSÃO

No item 4.1 foi apresentado o desenvolvimento da matriz de concreto refratário, a qual foi empregada na produção dos compósitos têxteis reforçados com basalto (item 4.4) e carbono (item 4.6). A matriz escolhida para o estudo apresentou compacidade igual a 0,788. A caracterização mecânica da matriz foi realizada através de ensaios de compressão uniaxial aos 7, 14 e 28 dias. A matriz apresentou resistência à compressão aos 7 dias (idade padrão escolhida para todos os ensaios mecânicos deste estudo) de 45,72 MPa e módulo de elasticidade de 25,05 GPa.

4.2 INFLUÊNCIA DA TEMPERATURA NO COMPORTAMENTO QUÍMICO E MECÂNICO DA MATRIZ REFROTÁRIA (Artigo A)

O ítem 4.2 merece destaque entre os demais apresentados neste trabalho tendo em vista que trata da caracterização mecânica, em temperaturas elevadas, de uma matriz de concreto refratário não-convencional produzida com agregado reativo (clinker). O capítulo visa correlacionar a evolução da composição da pasta de cimento (hidratação, desidratação, transformações de fases) quando submetida a temperaturas pré-determinadas, com o desempenho mecânico residual da matriz em tais condições. Para isso, foram empregados no estudo ensaios de resistência à compressão e módulo de elasticidade, bem como, um modelo matemático simplificado baseado nas reações químicas dos principais minerais presentes na matriz. Posteriormente no estudo, a matriz refratária foi empregada para a fabricação de TRCs (itens 4.4, 4.5 e 4.6).

Os resultados indicam que a utilização de agregado sintético de aluminato de cálcio (reativo) pode contribuir para com o desempenho mecânico da matriz (resistência à compressão e módulo de elasticidade) tanto durante sua hidratação (investigada até 28 dias), quanto em casos de exposição a temperaturas elevadas. Isso acontece devido a processos de dissolução e re-precipitação que alteram o tipo e a quantidade de fases hidratadas presentes na matriz. Além disso, a natureza poli-mineral dos agregados de aluminato de cálcio resulta na dissolução seletiva de sua superfície, o que beneficia a zona de interface agregado-pasta. Tal fato não ocorre quando da utilização de agregados convencionais (não reativos), o que resulta em zonas de transição interfaciais (agregado x pasta) menos resistentes.

Boa concordância foi estabelecida entre o modelo e valores experimentais de água combinada e água perdida por evaporação. O mesmo pôde ser observado para os valores experimentais e simulados de porosidade. As discrepâncias observadas entre os os valores experimentais e simulados a 400°C, para água combinada, água evaporada e porosidade (a partir da densidade dos sólidos), podem ser explicadas pela decomposição incompleta dos produtos de hidratação estáveis e/ou processos de carbonatação durante o aquecimento das amostras. Assim, em se tratando de valores experimentais, tais processos resultam numa maior quantidade de água combinada, acompanhada de menor quantidade de água evaporada e menor porosidade em relação aos valores previstos pelo modelo.

4.3 PROPRIEDADES MECÂNICAS DO TECIDO DE BASALTO

4.3.1 INTRODUÇÃO

O comportamento mecânico de um têxtil é exclusivamente dependente das características dos materiais utilizados e do processo de produção. Fatores como a resistência mecânica das fibras, rigidez, orientação da malha e utilização de revestimentos (*coatings*) resultarão em têxteis com características mecânicas distintas. Neste contexto, este item trata de ensaios de tração direta realizados de modo a investigar a influência da orientação na resposta mecânica do tecido de basalto. Esta investigação possibilitou a escolha da direção do reforço à ser empregada posteriormente na produção dos TRCs (ver item 4.4). A escolha da orientação foi realizada tendo como prioridade a resistência à tração alcançada. Dando sequência a pesquisa, foram realizados ensaios de tração direta visando avaliar a resistência residual do tecido de basalto após pré-aquecimento em temperaturas na faixa de 25°C a 1000°C. Para os ensaios residuais utilizou-se a mesma orientação escolhida para a produção dos TRCs. Microscopia eletrônica de varredura (MEV) foi empregada a fim de estudar a degradação do revestimento e das fibras de basalto após o processo de aquecimento.

A caracterização do tecido foi realizada de modo a contribuir para o entendimento do comportamento global dos compósitos reforçados com tecido de basalto produzidos e testados em altas temperaturas no item 4.4. Analogamente, tal caracterização serviu para a obtenção de dados não disponibilizados pelo fabricante, bem como, para a comparação com dados por ele fornecidos.

4.3.2 Materiais e métodos

O tecido de basalto (Figura 4.10) empregado no presente estudo é comercializado pela empresa chinesa Zhejiang GBF Basalt Fiber Co. Ltd em rolos de (1m x 50m). As propriedades do tecido de basalto são apresentadas na (Tabela 4.9).

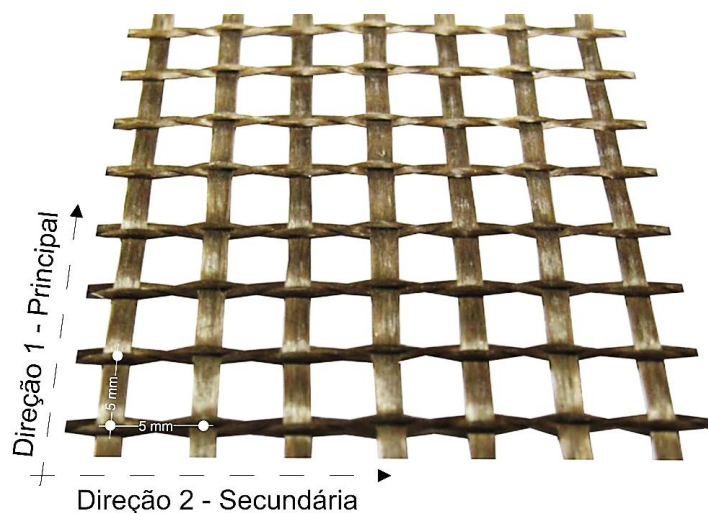
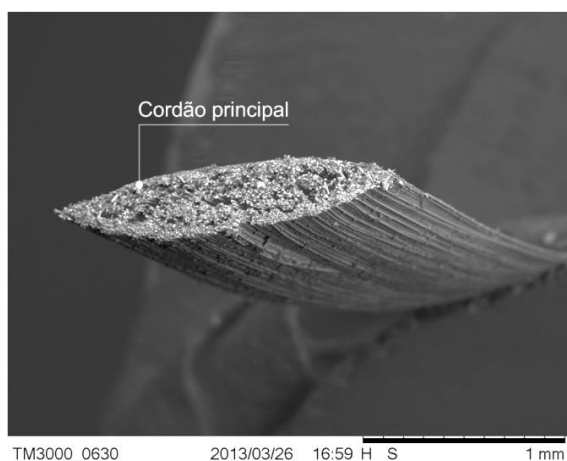


Figura 4.10 – Detalhes do tecido de basalto: direções adotadas e dimensões da malha.

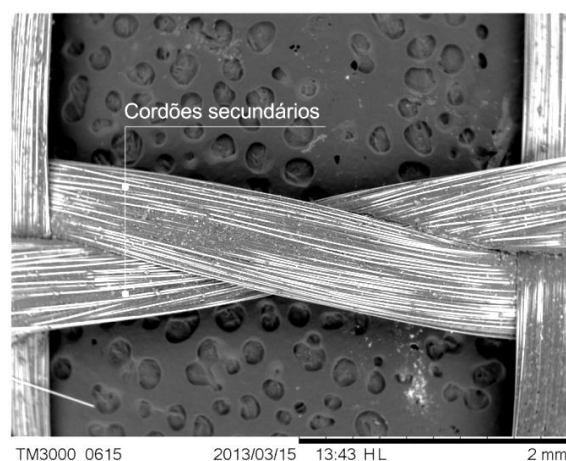
Tabela 4.9 – Especificações do tecido de basalto fornecidas pelo fabricante.

Propriedade	Valor
Densidade (g/cm ³)	2,70
Ponto de fusão (°C)	1350
Abertura da malha (mm x mm)	5 x 5
Quantidade de “coating” (g/m ²)	43

Conforme ilustrado na Figura 4.11, os cordões principais que compõe o tecido de basalto possuem seção transversal em forma de elipse, bem achatada, com cerca de 0,28 mm x 1,72 mm. Os cordões secundários também apresentam seção elíptica (0,32 mm x 0,67 mm), porém, menos achatada.



a) Seção transversal de um cordão principal.



b) Cordões secundários.

Figura 4.11 – Aspecto do tecido utilizado nos ensaios de resistência à tração direta.

Visando uma interpretação precisa dos resultados mecânicos obtidos nos ensaios de tração direta descritos neste capítulo, a área da seção transversal dos cordões principais e

secundários foi determinada através de análises de imagem utilizando o software Image J. Para isso, foram preparadas amostras contendo tecido de basalto embutido em resina transparente, as quais foram serradas e polidas mecanicamente de modo a revelar a seção transversal dos cordões nas duas direções. O procedimento de análise baseou-se em transformar imagens digitais da seção transversal dos cordões (obtidas por MEV) em imagens binárias, nas quais apenas dois valores (ou cores) são possíveis para cada pixel (Figura 4.12). A partir da escala das micrografias (convertidas em imagens binárias) e da contagem dos pixels referentes à área de cada fibra, pôde-se então determinar o “somatório de áreas das fibras” presentes nas seções transversais dos cordões de basalto. Os resultados da determinação da “área de fibras” para os cordões principais e secundários foram de, respectivamente, 0,194 mm² e 0,097 mm², obtidos a partir da média aritmética de dez determinações.

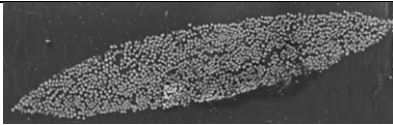



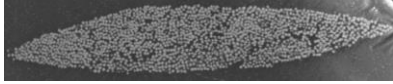



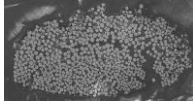

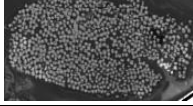

Direção	Recorte da imagem original	Imagem binária	Área (mm ²)
Principal			0,190
Principal			0,186
Principal			0,216
Secundária			0,076
Secundária			0,111
Secundária			0,104

Figura 4.12 – Determinação da área da seção transversal dos cordões de basalto utilizando o software Image J.

A investigação sobre o comportamento mecânico do tecido de basalto incluiu ensaios de resistência à tração direta em ambas as direções do tecido em temperatura ambiente e ainda ensaios de tração direta residuais na direção principal. Os ensaios residuais foram realizados após aquecimento controlado a 75, 150, 200, 300, 400, 600 e 1000°C. Ao todo, cinco amostras de tecido foram avaliadas para cada uma das condições estudadas. O regime de aquecimento aplicado às amostras é apresentado na Figura 4.13. Um forno elétrico (tipo

mufla) com aquecimento por radiação (liga metálica Kanthal "A1") foi utilizado para o aquecimento das amostras. O resfriamento das amostras ocorreu de forma natural no interior do forno. A taxa de aquecimento empregada no processo de aquecimento foi de 10°C/min. O nível de temperatura foi mantido constante durante 60 min em cada uma das temperaturas alvo.

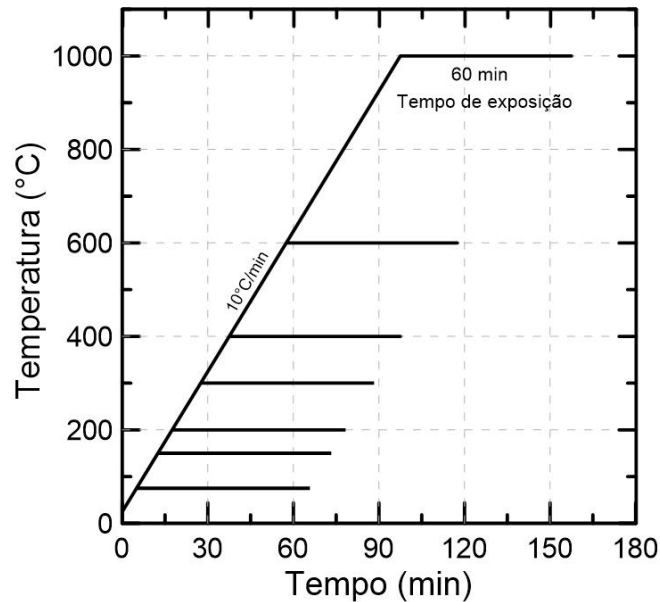


Figura 4.13 – Regime de aquecimento aplicado às amostras de tecido de basalto.

Os testes foram conduzidos em amostras retangulares de 50 x 360 mm (largura x comprimento). Na Figura 4.14 - a são apresentados os detalhes do arranjo experimental empregado no estudo. Para este ensaio utilizou-se uma máquina Shimadzu, servo-elétrica, com capacidade de carga de 100 kN e velocidade de carregamento de 0,4 mm/min para ambas as direções do tecido. A determinação dos deslocamentos axiais foi feita através de um *clip-gauge* adaptado a um aparato metálico fixo à região central das amostras. Um comprimento de medida (*“gage-length”*) de 200 mm foi utilizado. Tanto o carregamento, quanto as deformações foram registradas através do software TRAPEZIUM (versão 1.3.0) produzido pela Shimadzu *company*. A pressão das garras sobre as amostras de tecido foi imposta manualmente com o auxílio de uma chave-de-boca. Nas extremidades de cada amostra, foram coladas fitas adesivas resistentes de modo a proteger o tecido do contato direto com as garras (Figura 4.14 - b).

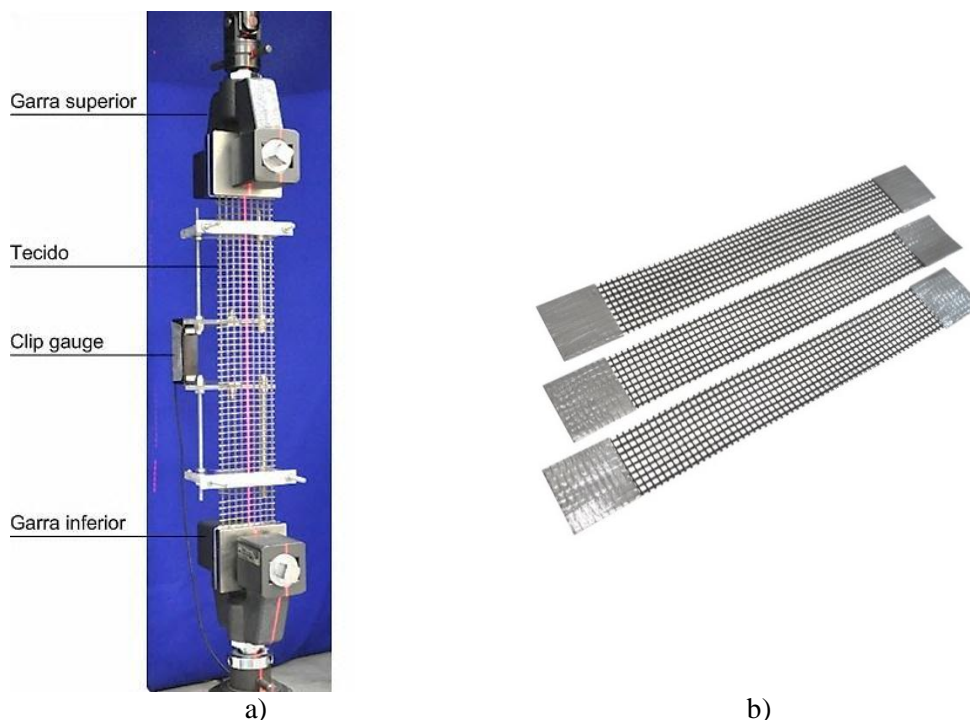


Figura 4.14 – Configuração utilizada no ensaio de tração direta do tecido de basalto.

4.3.3 RESULTADOS

4.3.3.1 *Influência da orientação na resposta mecânica à tração do tecido de basalto*

Os resultados obtidos dos ensaios de tração direta foram representados graficamente sob a forma de curvas tensão *versus* deformação e força *versus* deformação. O cálculo da tensão foi determinado com base na área da seção transversal (ver Figura 4.12) e no número de cordões dispostos na direção principal (9 cordões) e secundária (18 cordões). A Figura 4.15 ilustra, o comportamento mecânico sob tração direta do tecido de basalto na direção principal e na direção secundária. Os resultados referentes à determinação das tensões, deformações máximas e do módulo de elasticidade do tecido nas duas direções foram obtidos a partir da média aritmética de cinco determinações (Tabela 4.10). É importante ressaltar que, para o cálculo do módulo de elasticidade do tecido na direção principal, foi desconsiderada a fase ascendente da curva compreendida entre 0 e 300N. Isto porque, trata-se de uma fase na qual ocorre o alinhamento das fibras (em inglês: “*crimp effect*”) que devido a processo de produção do tecido, apresentam padrão ondulatório. O valor médio de resistência à tração do tecido de basalto tracionado na direção principal superou em 9,6% o valor médio obtido para o tecido tracionado na direção secundária. Quanto ao módulo de elasticidade, o tecido de basalto tracionado na direção secundária apresentou valor médio 45,5% inferior ao obtido nos

ensaios realizados na direção principal. As curvas de resistência à tração obtidas para a direção secundária não apresentaram padrão curvo relativo a fase de alinhamento das fibras (*crimp effect*). Sendo assim, neste caso, os valores de módulo de elasticidade foram determinados utilizando todo o trecho linear das curvas tensão-deformação.

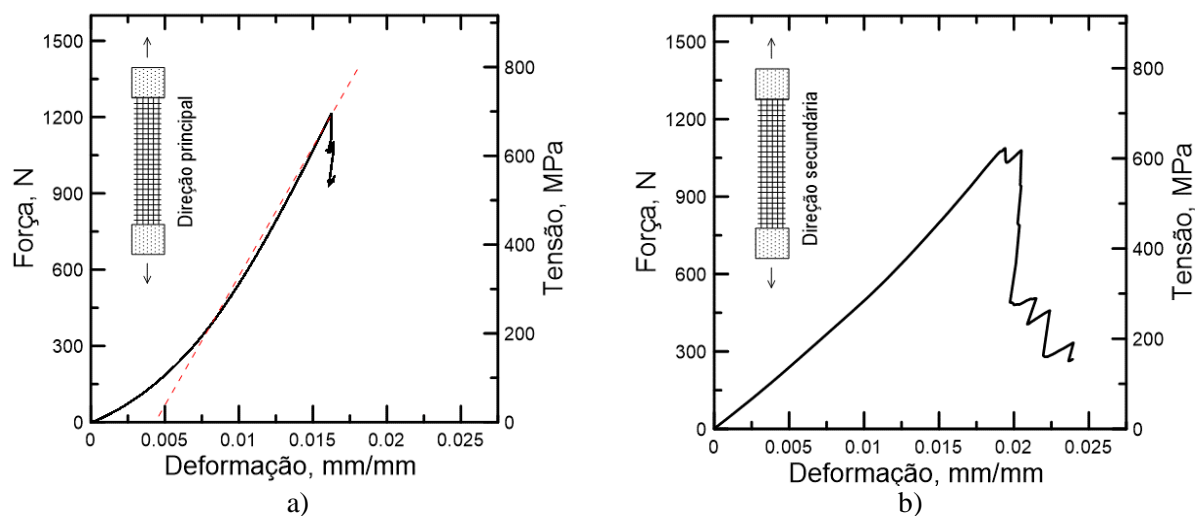


Figura 4.15 – Curvas típicas de resistência à tração direta do tecido de basalto (a) na direção principal e (b) na direção secundária.

Tabela 4.10 – Influência da orientação na resposta à tração do tecido de basalto.

Direção	Valores experimentais			
	P_{cr} (N)	σ_{cr} (MPa)	ϵ_{cr} (mm/mm)	E_{tec} (GPa)
Principal	1207,1 (160,8)	691,4 (92,09)	0,0153 (0,0018)	60,50 (8,96)
Secundária	1100,4 (54,25)	630,29 (31,07)	0,0184 (0,0011)	32,94 (1,91)

4.3.3.2 Efeito da temperatura na resistência residual do tecido de basalto (direção principal)

Conforme apresentado na Figura 4.16, o comportamento mecânico do tecido de basalto (utilizado neste estudo para a produção de TRCs, ver item 4.4) mostrou ser fortemente afetado pelo tratamento térmico. Os resultados da avaliação de todas as curvas são apresentados na Tabela 4.11. Através dos resultados obtidos é possível perceber que o pré-aquecimento das amostras nas temperaturas de 75°C e 150°C acarretou melhorias no desempenho mecânico do tecido de basalto (Figura 4.16 (a) e (b)). Conforme apresentado na Tabela 4.11, os acréscimos na resistência à tração para as temperaturas de aquecimento de 75°C e 150°C foram de, respectivamente, 13% e 49% em relação ao tecido testado na

temperatura ambiente. Analisando a Figura 4.16-b, é possível perceber que houve acréscimos também no módulo de elasticidade do tecido, os quais foram de, respectivamente, 23% e 31% para as temperaturas 75°C e 150°C. Nesta faixa de temperatura, o comportamento do polímero passa de visco-elástico para plástico. Nesta condição, o polímero acaba impregnando zonas mais internas dos cordões, estendendo assim as regiões de interface entre filamentos. Após o resfriamento, o polímero volta à condição original (rígida). Este mecanismo permite uma distribuição mais uniforme dos esforços de tração entre os filamentos impregnados, melhorando assim o desempenho à tração dos cordões e, conseqüentemente, do tecido como um todo. Conforme ilustrado na Figura 4.16, a partir de 150°C, iniciou-se um processo gradual de perda de resistência mecânica do tecido o qual se estendeu até 600°C onde os valores de tensão se mostraram insignificantes perante os valores obtidos à temperatura ambiente. Os valores de módulo também apresentaram redução com o aumento da temperatura, no entanto, isto só ocorreu a partir de 200°C (maior valor de módulo obtido). No presente estudo, as reduções da resistência à tração e do módulo de elasticidade residual na temperatura de 400°C foram de, respectivamente, 65% e 32% em comparação aos resultados obtidos em temperatura ambiente. Tal comportamento reflete não apenas as mudanças na estrutura dos filamentos de basalto, como também, a etapa final do processo de degradação do polímero presente no tecido.

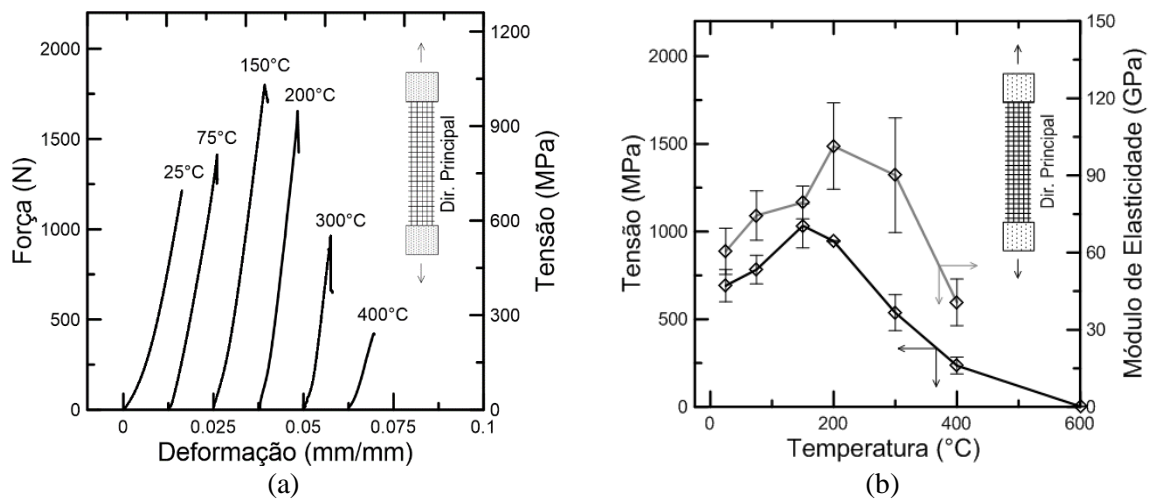


Figura 4.16 – (a) Curvas típicas de resistência à tração direta residual do tecido de basalto após aquecimento em diversas temperaturas. (b) Evolução do módulo e da resistência à tração residual do tecido com o aumento da temperatura.

Tabela 4.11 – Resultados dos ensaios de resistência à tração residual do tecido de basalto para diferentes temperaturas de aquecimento.

Direção	Temperatura de aquecimento	Valores experimentais			
		P_{cr} (N)	σ_{cr} (MPa)	ϵ_{cr} (mm/mm)	E_{tec} (GPa)
Principal	25°C	1207,1 (160,80)	691,4 (92,09)	0,0153 (0,0018)	60,50 (8,96)
Principal	75°C	1303,8 (144,79)	783,4 (109,01)	0,0112 (0,0019)	74,44 (9,59)
Principal	150°C	1803,8 (220,52)	1033,1 (126,30)	0,0148 (0,0013)	79,51 (6,40)
Principal	200°C	1650,6 (5,60)	945,37 (3,21)	0,0102 (0,0018)	101,41 (16,81)
Principal	300°C	938,2 (181,49)	537,3 (103,94)	0,0081 (0,0013)	90,07 (22,31)
Principal	400°C	411,6 (82,84)	235,7 (47,45)	0,0067 (0,002)	40,66 (9,07)
Principal	600°C	4,56 (3,12)	2,61 (1,78)	*	*
Principal	1000°C	**	**	**	**

*Não foi possível a instalação do clip-gauge.

** Ruptura ao toque.

As superfícies do tecido e dos cordões de basalto foram avaliadas antes e depois do processo de aquecimento, utilizando um microscópio eletrônico de varredura (MEV) FEI Quanta 400. Amostras de tecido com dimensões de 20 x 20 mm (comprimento x largura) foram revestidas com 20 nm de ouro para se tornarem condutoras e adequadas para análise no MEV convencional. Na Figura 4.17 são apresentadas as micrografias do tecido bi-direcional de basalto em sua condição natural e após a exposição às temperaturas estudadas. Do mesmo modo, na Figura 4.18 são apresentadas as micrografias das superfícies dos cordões de basalto, nas mesmas condições.

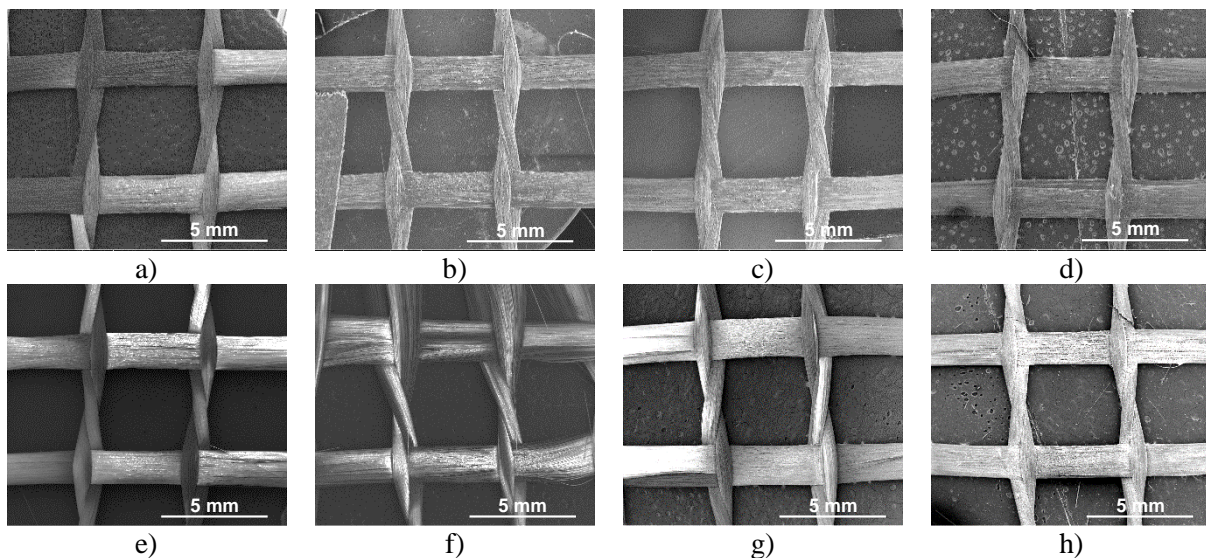


Figura 4.17 – Tecido de basalto (a) na condição natural e após exposição à (b) 75°, (c) 150°C, (d) 200°C, (e) 300°C, (f) 400°C, (g) 600°C e (h) 1000°C.

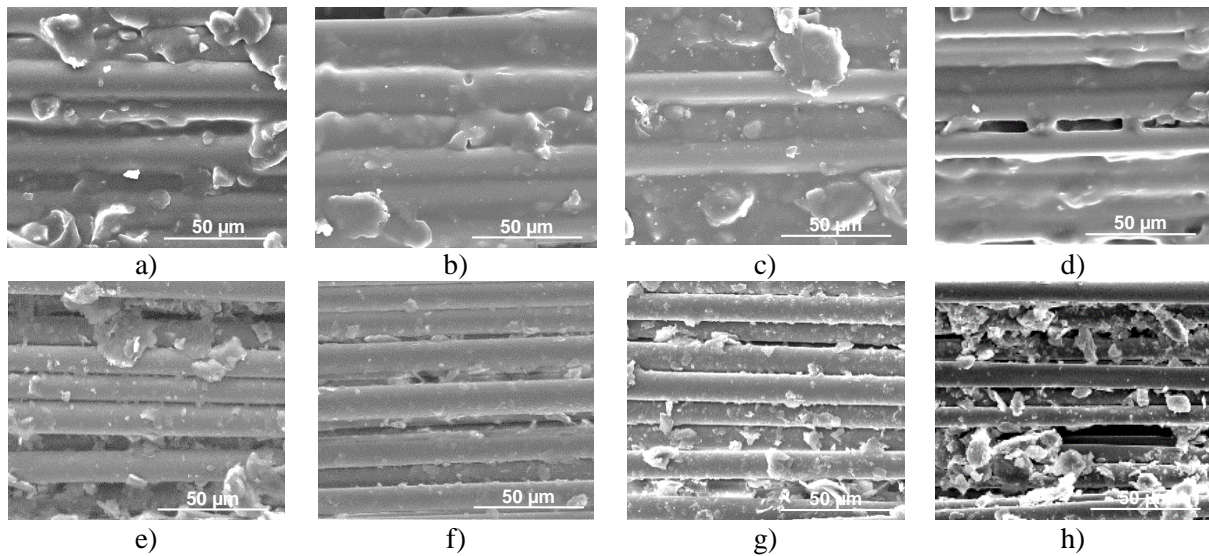


Figura 4.18 – Cordão de basalto (a) na condição natural e após exposição à (b) 75°C, (c) 150°C, (d) 200°C, (e) 300°C, (f) 400°C, (g) 600°C e (h) 1000°C.

Diferentemente das amostras extraídas dos compósitos (ver item 4.4), as amostras extraídas do tecido de basalto só apresentaram sinais visíveis de degradação do polímero (estireno acrílico látex) depois de aquecidas a 300°C. Nesta temperatura, a parcela de polímero remanescente permanece entre as fibras, assumindo a forma de pequenas lâminas finas semelhantes a escamas de peixe depositadas na interface dos filamentos (Figura 4.18 - e). Este processo de deterioração da zona de interface entre filamentos está diretamente associado às reduções de resistência e de módulo residuais (Tabela 4.11) ocorridas entre as temperaturas alvo de 200°C a 300°C, as quais podem ser observadas claramente nas curvas apresentadas na Figura 4.16. Estas reduções foram de, respectivamente, 43% e 11%.

Através da Figura 4.18 é possível perceber que o polímero em torno das fibras foi completamente perdido a 400°C, afetando assim os valores de resistência à tração e módulo residuais. Os resultados apresentados na Tabela 4.11 revelam que a resistência do tecido após o pré-aquecimento a 400°C representa aproximadamente 1/3 daquela obtida na temperatura ambiente. Com relação ao módulo de elasticidade, a relação é de 2/3. Não foi possível a obtenção dos valores de deformação para o tecido submetido a 600°C, uma vez que a amostra apresentou comportamento extremamente frágil. O mesmo ocorreu para a temperatura de 1000°C, inviabilizando assim os ensaios de tração nestas temperaturas. Isto ocorre devido a degradação dos filamentos de basalto, que, assim como apresentado por ČERNÝ *et al.* (2007), se fragmentam em altas temperaturas (~750°C) apresentando superfície com aspecto “granular” ou “craquelado” (Figura 4.19).

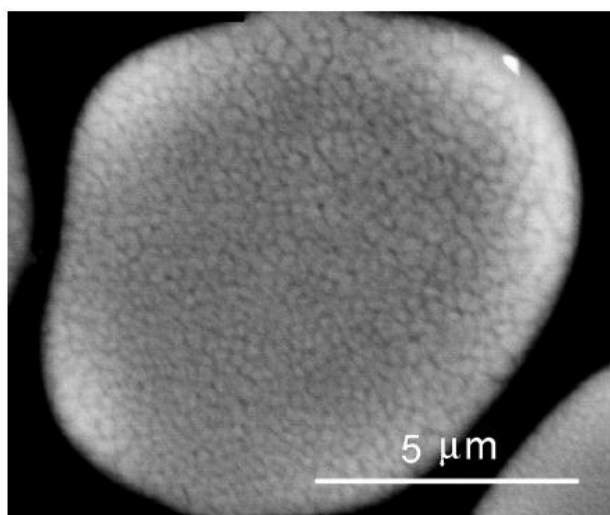


Figura 4.19 – Microscopia da seção de um filamento de basalto tratado termicamente a 750°C.
Fonte: ČERNÝ *et al.* (2007).

4.3.4 CONCLUSÃO

No item 4.3 foi apresentado o estudo da influência da orientação no comportamento mecânico a tração do tecido de basalto. Além disso, o tecido foi pré-aquecido em diferentes temperaturas de modo a se investigar a evolução de suas propriedades mecânicas após o tratamento térmico.

Quanto à comparação mecânica realizada entre as duas direções do reforço, observou-se que o tecido tracionado na direção secundária alcança níveis de deformação 20% superiores àqueles obtidos na direção principal. Tal característica pode ser tomada como uma vantagem interessante na produção de compósitos têxteis, uma vez que, dependendo da aplicação, materiais com maior capacidade de deformação e menor módulo de elasticidade são necessários.

O tratamento térmico até 150°C melhorou o desempenho mecânico do tecido de basalto no tocante à resistência e ao módulo de elasticidade. A aderência mecânica entre filamentos, oriunda do processo de plastificação e enrigecimento do polímero, foi responsável por este fenômeno. Uma vez que a impregnação dos cordões promove uma melhor redistribuição de carga entre os filamentos, significativos acréscimos são percebidos na resistência do tecido como um todo.

O pré-aquecimento em temperaturas superiores a 150°C (temperatura na qual o compósito apresentou melhor performance) resultou em decréscimos da resistência à tração do tecido de basalto em comparação a resposta mecânica obtida na referida temperatura. A

deterioração das propriedades mecânicas se mostrou significativa na temperatura de 400°C onde a redução de resistência em comparação à temperatura ambiente supera 65%.

4.4 INFLUÊNCIA DA TEMPERATURA NO COMPORTAMENTO MECÂNICO DE COMPÓSITOS REFROTÁRIOS REFORÇADOS COM TECIDO DE BASALTO (Artigos B e C)

Este capítulo apresenta uma investigação experimental sobre a influência da fração volumétrica de fibras e da temperatura (condições: à quente e residual) no desempenho mecânico à tração de um compósito refratário reforçado com tecido de basalto. Ensaio de tração foram realizados em compósitos reforçados com 1, 3 e 5 camadas de tecido de basalto. Os compósitos reforçados com 3 e 5 camadas apresentaram comportamento *strain-hardening*, com múltipla fissuração. A utilização de 5 camadas de tecido de basalto levou o compósito a alcançar mais de 13 MPa de resistência a tração e 1,58% de deformação (aos 7 dias de idade).

Com relação aos testes residuais (25°C a 1000°C), os regimes de aquecimento e resfriamento utilizados no presente trabalho, mostraram afetar a resposta à tração do TRC. O pré-aquecimento das amostras até 150°C teve impacto positivo sobre a resistência à tração do compósito, dado o mecanismo de intertravamento entre fibras e matriz gerado pelo revestimento polimérico. O desempenho à tração dos compósitos apresentou tendência de queda para temperaturas superiores a 150°C. Tal comportamento reflete a degradação do revestimento, a desidratação da matriz e a já discutida perda de resistência do reforço têxtil (ver item 4.3). O comportamento à tração dos compósitos, quando submetidos a 200°C por diferentes períodos de tempo (1, 3 e 6 h) também foi investigado. No entanto, não foram observadas diferenças significativas na relação tensão-deformação dos TRCs para os períodos de tempo estudados.

Dada a severidade dos ensaios de tração à quente (realizados sob temperatura constante entre 25°C e 400°C), os valores de resistência obtidos foram praticamente a metade daqueles referentes à condição residual. Sob elevadas temperaturas, o revestimento no entorno e no interior dos cordões plastifica, reduzindo a adesão entre filamentos, a ancoragem entre cordões principais e secundários e ainda, a ancoragem entre cordões e matriz.

4.5 SIMULAÇÃO DO COMPORTAMENTO MECÂNICO DE COMPÓSITOS REFRAATÓRIOS REFORÇADOS COM TECIDO DE BASALTO (Artigo D)

Este capítulo aborda a modelagem das leis constitutivas de tração dos compósitos produzidos e testados anteriormente no item 4.4. Um modelo de diferenças finitas desenvolvido anteriormente por Soranakom e Mobasher (2010) foi utilizado para simular o comportamento *strain-hardening* e o espaçamento entre fissuras dos TRCs.

O estudo também contempla análises de imagem aplicadas ao processo de fissuração das amostras. Por meio da correlação digital de imagem, ou em inglês, *digital image correlation* (DIC), foi possível visualizar a evolução da largura e espaçamento das fissuras, os quais foram posteriormente correlacionados com a resposta mecânica dos compósitos testados nas temperaturas alvo do estudo. Microscopia eletrônica de varredura (SEM) foi empregada a fim de investigar o processo de degradação da interface fibra-matriz após exposição a temperaturas elevadas.

A correlação digital de imagem revelou padrões não uniformes de deformação longitudinal nos TRCs, os quais foram divididos em três zonas características: de localização, de cisalhamento e de tensão uniforme. Através desta abordagem foi possível determinar parâmetros importantes relativos à fissuração do TRCs, tais como: abertura de fissuras, espaçamento de fissuras e dimensão da zona de cisalhamento.

O modelo empregado foi capaz de simular as respostas experimentais dos TRCs submetidos aos testes de tração residuais, abordando os comportamentos mecânicos da matriz, do tecido e da interface entre ambos. O acréscimo da força adesional no modelo resultou num padrão mais refinado de fissuras, o qual é confirmado nos testes experimentais e no DIC.

4.6 INFLUÊNCIA DA TEMPERATURA NO COMPORTAMENTO MECÂNICO DE COMPÓSITOS REFRAATÓRIOS REFORÇADOS COM TECIDO DE CARBONO (Artigo E)

Neste item, buscou-se produzir TRCs com propriedades térmicas e mecânicas superiores às obtidas com os compósitos reforçados com tecido de basalto. Este estudo surgiu após a constatação da reduzida estabilidade térmica das fibras de basalto (item 4.3.3.2) e da perda de resistência dos compósitos devido à decomposição do revestimento (*coating*) presente no tecido (item 4.4). Assim, optou-se pela produção de TRCs reforçados com tecido de carbono. A escolha do tipo de fibras foi baseada em dados da literatura relacionados à resistência mecânica e ao processo de degradação do carbono sob temperaturas elevadas (YIN *et al.*, 1994, PARK, 2014). A avaliação dos compósitos reforçados com tecido de carbono foi realizada através de ensaios de tração à quente, visando obter a performance do material em condições extremas.

Os compósitos refratários produzidos neste item foram reforçados com dois diferentes tecidos de carbono: com revestimento (tratamento superficial com resina epóxi) e sem revestimento. A faixa de temperatura empregada foi de 25 a 600°C, tendo em vista os principais processos de desidratação ocorridos da matriz refratária em estudo, bem como, o processo de oxidação das fibras de carbono. Análises termogravimétricas e DRX foram utilizadas na identificação de fases da matriz para todas as temperaturas alvo. Analogamente, microscopia eletrônica de varredura foi empregada na visualização da degradação do revestimento e da oxidação das fibras de carbono.

Dada a estabilidade térmica das fibras de carbono e a impregnação parcial da matriz no tecido, os compósitos produzidos com carbono sem revestimento foram capazes de resistir a temperaturas de 400°C mantendo a mesma resistência à tração e o dobro da deformação apresentada em temperatura ambiente. Uma vez que o revestimento à base de epóxi se decompõe sob temperaturas moderadas, o acréscimo de temperatura de 25 para 600°C gerou uma clara tendência de redução de resistência à tração nos compósitos reforçados com tecido revestido.

5 CONCLUSÕES E SUGESTÕES PARA TRABALHOS FUTUROS

Compósitos refratários reforçados com tecidos de basalto (com revestimento) e de carbono (com e sem revestimento) foram caracterizados mecanicamente em diferentes temperaturas através de ensaios à quente e residuais. O tecido de basalto e a matriz refratária também foram caracterizados individualmente, todavia, apenas na condição residual.

A investigação química/mecânica da matriz refratária revelou que a utilização de agregado sintético de aluminato de cálcio (reativo) pode contribuir para com o desempenho mecânico da matriz tanto durante sua hidratação (investigada até 28 dias), quanto em casos de exposição a temperaturas elevadas. A melhoria das propriedades mecânicas da matriz é atribuída ao aumento da reação de hidratação (hidratação adicional associada ao fenômeno da conversão) e a natureza mais densa dos produtos de hidratação estáveis em comparação aos metaestáveis.

O tecido de basalto apresentou resistência à tração de 691 MPa e módulo de elasticidade superior a 60 GPa quando testado na direção principal a 25°C. A caracterização mecânica do tecido de basalto realizada nas duas direções do reforço revelou que o tecido tracionado na direção secundária alcança níveis de deformação 20% superiores aqueles obtidos na direção principal. Quando caracterizado mecanicamente na condição residual (25 a 1000°C), o tecido de basalto atingiu sua máxima resistência à tração na temperatura de 150°C. A aderência mecânica entre filamentos, oriunda do processo de plastificação e enrijecimento do polímero, foi responsável por este fenômeno.

Em linha com os resultados obtidos para o tecido pleno, os TRCs reforçados com tecido de basalto e testados à tração na condição residual apresentaram máxima resistência na temperatura de 150°C (15,30 MPa). Até esta temperatura, a resistência dos cordões é impactada positivamente pela plastificação do revestimento polimérico das fibras o qual, depois de resfriado, promove uma melhor distribuição de carga entre os filamentos e uma melhor adesão com a matriz. O modelo de diferenças finitas empregado neste estudo foi capaz de simular o comportamento residual de enrijecimento na tração (*strain hardening*) observado nos TRCs reforçados com basalto.

Os valores máximos de resistência à tração obtidos para os compósitos reforçados com basalto na condição quente foram em média 50% menores do que os obtidos na condição residual. Este efeito negativo foi atribuído principalmente à ineficiência do reforço fibroso gerada pela perda de rigidez do revestimento quando submetido a altas temperaturas.

Compósitos reforçados com tecidos de carbono (revestidos e não revestidos) foram testados à tração em ensaio à quente na faixa de 25°C a 400°C. Uma vez que o revestimento plastifica e se decompõem em temperaturas baixas e moderadas, respectivamente, uma tendência clara de redução de resistência à tração pôde ser observada nos TRCs reforçados com tecido revestido. Dada a impregnação da matriz refratária no tecido e a estabilidade térmica das fibras de carbono, o TRC produzido a partir do tecido não revestido exposto a 400°C, mostrou uma capacidade de carga igual àquela observada em temperatura ambiente. A deformação, por outro lado, aumentou em aproximadamente 100%.

Do ponto de vista da aplicabilidade dos TRCs em estudo, no âmbito da construção civil, acredita-se que o compósito reforçado com basalto tem potencial desde que empregado em baixas temperaturas, não superiores a 150°C (temperatura na qual apresenta seu melhor desempenho na condição residual). A partir deste limite o desempenho mecânico do TRC reforçado com basalto passa a ser comprometido pelas transformações ocorridas no revestimento das fibras, bem como, pela gradual perda de resistência do tecido. Cabe ressaltar no entanto, que mesmo após aquecimento a 400°C o compósito apresentou resistência última de 5 MPa, a qual pode ser adequada para alguns tipos de aplicação (ex: proteção de estruturas de aço, ou revestimento de túneis).

O compósito produzido com tecido de carbono sem revestimento se mostrou mais indicado para aplicações em temperaturas elevadas ($\leq 400^{\circ}\text{C}$), mesmo quando submetido à condição quente (apontada como a mais agressiva).

A metodologia de caracterização mecânica em temperatura (residual e à quente) utilizada no presente estudo não é restrita a compósitos têxteis, deste modo, poderá ser aplicada também a outros tipos de compósitos. O modelo de diferenças finitas, todavia, foi concebido especificamente para compósitos com reforço bidirecional.

Pouquíssimos estudos abordando manufatura, caracterização mecânica e utilização de TRCs podem ser encontrados na literatura Brasileira. Claramente, um maior número de pesquisas é necessário para que as potencialidades deste tipo de compósito possam ser determinadas e tomadas como soluções para as demandas atuais da indústria da construção civil e de artefatos cimentícios.

6 REFERÊNCIAS BIBLIOGRÁFICAS

AİTCIN, P.C., **High performance concrete**, London, E&F Spon, 1998, 591 p.

ARIOZ, E., ARIOS, O, KOCKAR, O.M. “Leaching of F-type fly ash based geopolymers”. **Procedia Engineering**, v. 42, pp.1114 – 1120, 2012.

BARHUM, R., MECHTCHERINE, V. “Effect of short, dispersed glass and carbon fibres on the behaviour of textile-reinforced concrete under tensile loading”. **Engineering Fracture Mechanics**, v. 92, pp. 56–71, 2012.

BAŽANT, Z. P., KAPLAN, M. F. **Concrete at High Temperatures: Material Properties and Mathematical Models**. London: Longman (Addison-Wesley), p. 412, 1996.

BRAMESHUBER, W., PACHOW, U., PELED, A., REINHARDT, H.W., WASTIELS, J. *Chapter 5: Production Technologies*. In: Report 36: Textile Reinforced Concrete - State-of-the-Art Report of RILEM Technical Committee 201-TRC. Ed: Wolfgang Brameshuber. 2006.

BRIK, V.B. *Basalt fiber composite reinforcement for concrete*. NCHR-IDEA Program Project 25, Transportation Research Board, Washington, D.C., 1997.

BÜTTNER, T., ORLOWSKY, J., RAUPACH, M. “Fire resistance tests of textile reinforced concrete under static loading - results and future developments”. In: *Fifth International RILEM Workshop on High Performance Fiber Reinforced Cement Composites (HPFRCC5)*. Editor(s): H.W. Reinhardt, A.E. Naaman, pp. 361 – 370, 2007.

ČERNÝ, M., GLOGAR, P., GOLIÁŠ, V., HRUŠKA, J., JAKEŠ, P., SUCHARDA, Z., VÁVROVÁ, I. “Comparison of mechanical properties and structural changes of continuous basalt and glass fibres at elevated temperatures”. **Ceramics – Silikáty**, v. 51, n. 2, pp. 82–88, 2007.

CONCRETE SOCIETY. *Fibre-Reinforced Cement Composites*. Technical Report 51.067. London; 1973.

DE LARRARD, F. **Concrete Mixture Proportioning: A Scientific Approach**, Modern Concrete Technology Series, vol. 9, E&FN SPON, London, 1999, 421 pages.

DHAND, V., MITTAL, G., RHE, K.Y., PARK S., HUI, D. “A short review on basalt fiber reinforced polymer composites”. **Composites: Part B**, v. 73, pp. 166–180, 2015.

DIAS, D.P., THAUMATURGO, C. “Fracture toughness of geopolymeric concretes reinforced with basalt fibers”. **Cement & Concrete Composites**, vol. 27, 2005, pp. 49-54.

DI LUDOVICO, M., PROTA, A., MANFREDI, G. “Structural upgrade using basalt fibers for concrete confinement”. **Journal of composites for construction, ASCE**, v. 14, n. 5, pp. 541-552, 2010.

FIDELIS, M.E.A. *Desenvolvimento e caracterização mecânica de compósitos cimentícios têxteis reforçados com fibras de juta*. Tese de D.Sc., Universidade Federal do Rio de Janeiro, Rio de Janeiro, Brasil, 2014.

FORMAGINI, S. *Dosagem científica e caracterização mecânica de concretos de altíssimo desempenho*. Tese de D.Sc., Universidade Federal do Rio de Janeiro, Rio de Janeiro, RJ, Brasil, 2005.

GRIES T, OFFERMANN P, PELED A. “Chapter 3: Textiles”. In: *Report 36: Textile Reinforced Concrete - State-of-the-Art*. Report of RILEM Technical Committee 201-TRC. Ed: Wolfgang Brameshuber. 2006.

GUIRADO, F., GALÍ, S., CHINCHÓN, J.S. “Thermal Decomposition of Hydrated Alumina Cernent (CAH₁₀)”. **Cement and Concrete Research**, v. 28, n. 3, p. 381-390, 1998.

KLEINEBERG, M., HERBECK, L., BROSINGER, A. **CFRP APU INTAKE DUCT for MEGALINER**. SAMPE Europe Conference & Exhibition, 2004.

KRÜGER, M., REINHARDT, H.W. *Fire resistance*. In: W. Brameshuber (Eds.), *Textile Reinforced Concrete. State-of-the-Art Report of RILEM Technical Committee 201 – TRC: Textile Reinforced Concrete (Report 36)*, RILEM Publications S.A.R.L., Aachen, pp. 211-219, 2006.

KRÜGER, M., 2004, *Vorgespannter textildbewehrter beton*, MSc Dissertation, Institut für Werkstoffe im Bauwesen der Universität Stuttgart, Germany.

LARRINAGA, P., CHASTRE, C., BISCAIA, H.C., SAN-JOSÉ, J.T. “Experimental and numerical modeling of basalt textile reinforced mortar behavior under uniaxial tensile stress”. *Materials and Design*, v. 55, pp. 66–74, 2014.

LEA’s. **Chemistry of Cement and Concrete**, Publisher: Elsevier Science & Technology Books,. Chapter 13 - *Calcium Aluminate Cements*. Karen L. Scrivener and Alain Capmas, 2004.

PELED A. “Textiles as reinforcements for cement composites under impact loading”. In: *Fifth International RILEM Workshop on High Performance Fiber Reinforced Cement Composites (HPFRCC5)*, pp. 455-462, 2007.

PELED, A., MOBASHER, B. “Pultruded fabric–cement composites”. *ACI Materials Journal*, v. 102, pp. 15–23, 2005.

PENA, P. DE AZA, A.H. “Cementos de aluminatos cálcicos”. **Constitución, características y aplicaciones**. pp. 85-106, 1999.

RAMACHANDRAN, V. S., PAROLI, R. M., BEAUDOIN, J. J., DELGADO, A. H. **Handbook of thermal analysis of construction materials**. Institute for Research in Construction. National Research Council of Canada, Ottawa, Ontario, Canada, 2002.

REMPEL, S., HEGGER, J. “Slender facade structures made of textile-reinforced high performance concrete”. In: *Proceedings of: FERRO-11 – 11th International Symposium on Ferrocement and 3rd ICTRC - International Conference on Textile Reinforced Concrete*. Editor: Wolfgang Brameshuber. RILEM Publications SARL, p. 337-346, 2015.

SEDRAN, T., 1999, *Rheologie et rheometrie des betons. Application aux betons autonivelants*. These de Doctorat, École Nationale des Ponts et Chaussées, Paris, France, p. 220.

SEDRAN, T., DE LARRARD, F., 2000, *Betonlab Pro3®* – Logiciel de formulation de bétons. École Nationale des Ponts et Chaussées, Paris, France, CD-Rom. .

SILVA, A.S.M. *Dosagem de Concreto Pelos Métodos de Empacotamento Compressível e Aïtcin-Faury Modificado*. Dissertação de Mestrado, Universidade Federal do Rio de Janeiro, Rio de Janeiro, Março, 2004.

SILVA, F.A., BUTLER, M., HEMPEL, S., TOLEDO, R.D., MECHTCHERINE, V. “Effects of elevated temperatures on the interface properties of carbon textile-reinforced concrete”. **Cement & Concrete Composites**, v. 48, pp. 26–34, 2014.

SIM, J., PARK, C., MOON, D.Y. “Characteristics of basalt fiber as a strengthening material for concrete structures”. **Composites: Part B**, v. 36, pp. 504-512, 2005.

SINGHA, K. “A Short Review on Basalt Fiber”. **International Journal of Textile Science**, v. 1, n. 7, pp. 19-28, 2012.

SORANAKOM, C., MOBASHER, B. “Geometrical and mechanical aspects of fabric bonding and pullout in cement composites”. **Materials and Structures**, v. 42, n. 6, pp. 765-777, 2009.

SORANAKOM, C., MOBASHER, B. “Modeling of tension stiffening in reinforced cement composites: part I - Theoretical modeling”. **Materials and Structures**, v. 43, pp. 1217-1230, 2010.

TOMOSCHEIT, S., GRIES, T., HORSTMANN, M., HEGGER, J. “Project Life Insu-Shell Reducing the Carbon Footprint in Concrete Construction”. *European Conference Sustainable Building: Towards 0-Impact Building and Environment*, Maastricht, Heusden-Zolder, Aachen, Liege, p. 11-13, 2010.

TURRIZIANI, R. “The Calcium Aluminate Hydrates and Related Compounds”. In: TAYLOR, H. F. W (eds). *The Chemistry of Cements*. London: Academic Press, v. 2. p. 233-286, 1964.

WANGA, X, WUA, Z., WUA, G., ZHUA, H., ZENA, F. “Enhancement of basalt FRP by hybridization for long-span cable-stayed bridge”. **Composites: Part B**, v. 44, pp. 184–192, 2013.

XIA, L., ZHONG, B., ZHANG, T., HU, X., WU, S., YANG, J. “Effect of boron doping on the thermal properties of carbon fibers reinforced lithium aluminosilicate matrix composites”. **Journal of the European Ceramic Society**, v. 35, n. 9, pp: 2555-2562, 2015.

ANEXOS

Artigo A – Rambo DAS, Ukrainczyk N, Silva FA, Toledo RD, Koenders E and Gomes OFM. Exposing Calcium aluminate mortar to high temperatures: Overcoming adverse conversion effects using calcium aluminate aggregates. Submitted to Cement and Concrete Research (2016).

**Exposing Calcium aluminate mortar to high temperatures:
Overcoming adverse conversion effects using calcium aluminate aggregates**

Dimas Alan Strauss Rambo^{a*}, Neven Ukrainczyk^b, Flávio de Andrade Silva^c, Eddie Koenders^b, Romildo Dias Toledo Filho^a and Otávio da Fonseca Martins Gomes^d

^a Civil Engineering Department, COPPE, Universidade Federal do Rio de Janeiro, P.O. Box 68506, CEP 21941-972, Rio de Janeiro – RJ, Brazil.

^b Institute of Construction and Building Materials, Faculty of Civil and Environmental Engineering, TU Darmstadt, Franziska-Braun-Straße 3, 64287 Darmstadt, Germany.

^c Civil Engineering Department, Pontifícia Universidade Católica do Rio de Janeiro (PUC-Rio), Rua Marques de São Vicente 225, 22451-900 - Rio de Janeiro - RJ, Brazil.

^d Centre for Mineral Technology (CETEM), Rio de Janeiro – RJ, Brazil.

February, 2016

Abstract

The effect of elevated temperatures on a calcium aluminate mortar with clinker aggregates is studied. After an exposure period of 3h at temperatures ranging from 25 to 1000°C, specimens were tested for mechanical and microstructural properties. Thermogravimetry, Scanning Electron Microscopy, X-ray diffraction analysis and porosimetry were used to study microstructural changes as a function of temperature. A simplified hydration model based on the main chemical reaction scheme of the principal minerals was proposed to predict the evolution of the matrix composition during the early age hydration, transformation and dehydration reactions of the calcium aluminate mortar at different temperatures. The model predictions showed good agreements with experimental results. Improvements of the mechanical properties with altering conversion reactions, cured at room temperature and when exposed to 200°C, is attributed to an increased hydration reaction. Besides this, when compared to the metastable reactions, an improved interlocking effect at the reactive aggregate interface, and a more dense nature of the stable hydration products, was observed. This compensated for the adverse effects conversion reactions have on mechanical properties.

Keyword: high temperatures, compressive strength, microstructure, calcium aluminate cement.

*Corresponding author: e-mail: fsilva@puc-rio.br, Tel: +55(21) 3527-1188. Fax: +55 (21) 3527-1195.

Notation:

C= CaO

A= Al₂O₃

F= Fe₂O₃

S= SiO₂

H= H₂O

T=TiO₂

QXRD= Quantitative X-ray Diffraction

MIP= Mercury Intrusion Porosimetry

1. Introduction

Calcium Aluminate Cement (CAC) is used in versatile high performance applications [1,2,3,4,5]. In particular, the type of aggregate, and associated development of a highly porous interfacial transition zone (ITZ), has been strongly related to the degradation of concrete. In some types of high performance CAC based concretes, calcium aluminate clinker is also used as a synthetic aggregate [5,6,7,8]. Moreover, calcium aluminate clinker, typically made by fusion of bauxite and limestone, has a high density, almost no porosity and has a polymineral composition that is resulting in a strong compatibility with CAC. This participation of aggregates in the reaction with a cementitious material creates a special “bridge effect”, which excels the concrete resistance to chemical [9,10,11,12,13], abrasion [5,7] and thermal [6,7,8] attacks. In addition, CAC based materials may exhibit a rapid setting and hardening process [16,17], thus, can be placed into service much faster than an ordinary Portland cement type of concrete.

In general, use of CAC based matrixes is limited to high performance applications because of its high price and its well known adverse effects such as a reduction of strength, caused by conversion reactions. However, in certain cases the distinct behaviour of CAC based matrixes make them economically competitive. Heerden [14] showed practical applications of CAC cements combined with reactive aggregates in fiber reinforced shotcretes used by the mining industry in South Africa. As reported by the author, despite the high cost of CAC based matrixes, the choice for reactive aggregates (f.e.: Alag and andesite) can represent the best

cost-benefit when resistance to impact, abrasion, corrosion and heat are required. This because, in the case of tunnel linings, the long-term durability of a well designed CAC based lining overcomes the life time of the same structure made with OPC shotcrete. Thus, the rehabilitation costs of the OPC structure makes impracticable its use in comparison to CAC based lining.

The use of reactive aggregate was also reported by Wöhrmeyer et al. [15] which evaluated the influence of calcium aluminate aggregates on refractory castable properties in comparison to bauxite. The obtained results indicate very little open porosity for the matrix containing calcium aluminate aggregate when compared to bauxite, even after firing at 1400°C. Despite the lower density, the matrix produced with reactive aggregates presented higher CMOR (cold modulus of rupture) due to the better bonding (chemical affinity) between the cement paste and aggregates.

Hydration of CAC is highly temperature dependent, yielding in different morphologies and hydration products that continuously alter the material properties. Setting and hardening of CAC is primarily driven by the hydration of CA which is highly temperature dependent [1-16], yielding into the following main hydration products at approximated temperature ranges:



At ambient temperatures, the metastable hydrates CAH_{10} , C_2AH_8 and AH_x convert to a more stable C_3AH_6 and AH_3 (eqs. (4-6)) with release of water and consequent impairment of the material porosity, permeability and mechanical properties. The conversion is accelerated by temperature increase and moisture availability enhancing the dissolution and re-precipitation processes to take place.



This adverse conversion effect has to be taken into account since collapsing CAC concretes have led to disasters in several countries, causing significant strength regression, which is also why its use is often forbidden for structural applications. Earlier construction failures in the history of CAC concrete emphasised that a design must be on the basis of the transformed properties, primarily strength, and the water/cement mass ratio (w/c) should be below 0.4 and must be respected in practice. New generations of superplasticisers offer novel possibilities to improve workability and lower the w/c ratio as well [17], which could aid the long-term performance of CAC-based materials. However, it is well known that in CAC mortars, with conventional (non-reactive) aggregates, the transformed material always show a low compressive strength, owed to the transformation process. Most interesting finding reported in this paper is the improvement of the mechanical properties with ongoing conversion reactions, which occur in both conditions, i.e. cured at room temperature and when the mortar is exposed to 200°C. Overruling the adverse conversion effects is related to the employment of both Alag aggregates and a low w/c ratio.

Conventional, high cement castables [18] are used in high temperature applications up to about 1000°C [1]. They exhibit a characteristic drop in strength at intermediate temperatures due to the conversion hydration reactions as well as sluggish sintering which does not allow for the development of ceramic bonds after breaking down the hydraulic bonds. A sufficient cement content is essential to maintain an adequate minimum strength at 1000°C limit; above that temperature stronger ceramic bonds result again in an increase in strength. The phases crystalized under higher temperatures depend highly on the composition of CAC and

aggregates. The high lime content of conventional castables favors the formation of low melting phases like mayenite ($C_{12}A_7$ and CA), which are known to degrade the refractoriness at higher temperatures (above 1000°C). Advanced refractories, for applications above 1100°C, are made with low and ultra-low cement contents (with the overall CaO content less than 2.5%), containing micron-sized mineral additives [18,19], which are increasingly being researched but are out of scope of the current paper. Aggregates used in CAC refractory castables include a dense packing of fused alumina, chromite, sintered bauxite, chamotte and exfoliated vermiculite [1,6,7,8].

Studies in the field of CAC based refractory castables with clinker aggregates are scarce and mostly insufficient. Therefore, this paper investigates the effect of elevated temperatures on microstructural properties, synergetic ITZ bond, and resulting mechanical strength evolution of CAC mortar with clinker aggregates. The compressive strength of CAC mortar was measured in two different conditions, i.e. specimens cured at room temperature (7, 14 and 28 days) and exposed to elevated temperatures (from 25 to 1000°C). The transformation hydration reactions and dehydration process of the mortar were investigated using TGA, SEM, XRD and Hg porosimetry analysis. A simple hydration model based on the main chemical reaction scheme of the principal minerals was employed to predict the evolution of the cement paste composition during early age hydration at room temperature, and the transformation and dehydration reactions of CAC at higher temperatures. The model was used to predict the evolution of the solid volume fraction, porosity, chemically bond and released (evaporated) water. In order to compare the cement paste model predictions with the experimental results obtained at mortar level, they were related (normalized) to the mass or volume of the cement paste component. For this, the mortar was represented as a homogenous mixture of air bubbles, aggregates and evolving cement paste microstructure,

which further consisted of reacting cement and water, and forming hydration products and internal porosity resulting from chemical shrinkage [20].

2. Materials and Methods

2.1 CAC mortar

The materials used in the CAC mortar composition were commercially available calcium aluminate cement (Secar 51 from Kerneos Inc.) and synthetic calcium aluminate aggregate (Alag from Kerneos Inc.), polycarboxylate superplasticizer in powder (Peramin CONPAC 500 from Kerneos Inc.) and methyl-cellulose as viscosity modifier agent to avoid segregation. Oxide composition of the CAC and aggregates as obtained by XRF (EDX 720, Shimadzu Co. with rhodium tube and SiLi detector) is given in Table 1.

Table 1 – Chemical composition of the calcium aluminate cement and of the synthetic calcium aluminate aggregate.

Cement		Aggregate	
Compound	Content/%	Compound	Content/%
Al ₂ O ₃	51.45	Al ₂ O ₃	39.88
CaO	38.51	CaO	36.02
SiO ₂	3.07	SiO ₂	2.79
Fe ₂ O ₃	1.76	Fe ₂ O ₃	14.48
TiO ₂	1.89	TiO ₂	1.61
SO ₃	0.61	SO ₃	1.05
K ₂ O	0.42	K ₂ O	0.19
ZrO ₂	0.12	ZrO ₂	0.09
MnO	0.02	MnO	0.19
SrO	0.05	SrO	0.03
Ga ₂ O ₃	0.01	Ga ₂ O ₃	0.15
Y ₂ O ₃	0.01	Y ₂ O ₃	0.01
Ta ₂ O ₅	0.03	P ₂ O ₅	1.77
Cr ₂ O ₃	0.07	V ₂ O ₅	0.06
NbO	0.01	LOI	1.68
LOI	1.96		

The mineralogical composition of the CAC and Alag obtained by QXRD (section 2.4.1) is: 60% CA, 22% C₂AS, 4% C₁₂A₇ with CT, iron perovskite and pleocroite as remaining phases, and 45% CA, 16% C₂AS, 11% C₁₂A₇ with C₂A_xF_{1-x}, C₂S, respectively. Alag has particle diameters ranging from 0.001 mm to 1.18 mm. The water/cement mass ratio of the refractory

concrete was 0.35. Fig. 1 shows the grain size distribution of the used cement and aggregate determined by mechanical sieving [21] (diameter > 300 μm) and laser granulometry (diameter < 300 μm).

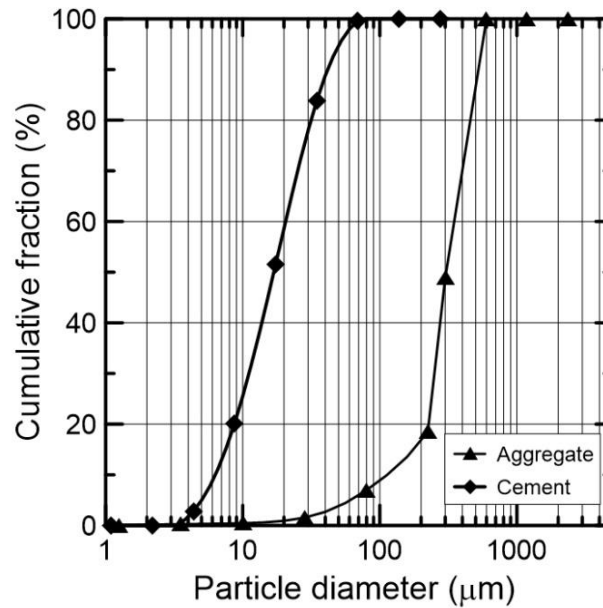


Fig. 1 – Particle size distribution of the used aluminous cement and aggregate.

Table 2 gives the composition of the concrete matrix. To achieve elevated compressive strength values, the CAC mortar used in this research was designed following the compressible packing model (CPM) routine [22,23]. The model was optimized for experimental compactness, size grading distributions and specific gravity of the constituents (cement and synthetic aggregate) as well as for the saturation dosage of the powder chemical additives.

Table 2 – Mix composition.

Composition	
Synthetic calcium aluminate aggregate (kg/m^3)	1264.4
Calcium Aluminate Cement (kg/m^3)	670
Powder polycarboxilate superplasticizer (kg/m^3)	4.35
Viscosity modifier agent - VMA (kg/m^3)	0.502
Water (kg/m^3)	234.5
Superplasticizer content (%)	0.65
Water/cementitious mass ratio	0.35

2.2 Heating and drying regime

Specimens were cured for 7, 14 and 28 days at 25°C in sealed conditions (without water exchange with environment). The specimens cured for 7 days were heated to 200, 400, and 1000°C and subsequently cooled by a natural process inside the furnace. An electric furnace with radiant heating (metal alloy type Kanthal "A1" in alumina tubes) internally protected by perforated ceramic plates was used. The applied heating rate was set to 10°C/min. The temperature level was kept constant for 1h at each targeted temperature. The furnace was cooled down before the specimens were removed in order to avoid a thermal shock. The rate of cooling was not controlled but followed a natural equilibrating thermal process.

Experiments on specimens stored at room temperature, without additional heating, were also carried out. Drying of these specimens (labeled 25°C) was achieved by using a vacuum pump for 30 days. Drying of specimens by heating was not done because of the effect of the transformation reactions [1] that significantly modifies the pore microstructure of CAC based materials.

Release of water (RW , in vol.% of the mortar) due to exposure of the specimens to high temperatures (200, 400 and 1000°C) or vacuum drying at 25°C is obtained from weight measurements before exposure to heat (W_{before}), the dry weight after exposure (W_{after}), and the sample volume (obtained by Archimedes method) W_{Arch} , according to the following equation:

$$RW = \frac{W_{\text{before}} - W_{\text{after}}}{W_{\text{Arch}}} \times 100 \quad (7)$$

2.3 Compressive strength test

Compression tests were performed in a Shimadzu universal testing machine model UH-F1000kN with a computer-controlled hydraulic servo system. Three cylindrical specimens measuring 50 mm x 100 mm (diameter x height) were tested in each of the studied ages (7,

14 and 28 days). The tests were carried out at a rate of 0.1 mm/min. Before testing, the cylinder faces were regularized by means of a lathe. The axial strain of the cylinders was measured using two LVDT's attached to the sample by steel rings (gage length of 50 mm).

2.4 Materials characterization

The mortar matrix was investigated using a scanning electron microscope (SEM) FEI Quanta 400. For this, matrix samples (tested under compression) were sectioned, from specimens, with dimensions of 20 x 20 mm (length x width). The samples were coated with a 20 nm gold layer to become conductive and suitable for conventional SEM analysis. The SEM was operated using 25 kV of acceleration tension and 30 mm of working distance.

TGA analyses were carried out using the powder obtained from crushed fragments of the specimens tested under compressive loading. The thermal analyses were performed in a TA Instruments, SDT Q600 model TGA/DTA/DSC simultaneous apparatus with temperatures ranging between 35 and 1000°C using 100 mL/min of nitrogen flow, corundum sample holders and a reference material. In order to eliminate the residual non-bonded free water, an isothermal step at 35°C for 1 hour was applied before commencing the analyses. Bond water in the dried specimens was obtained from a mass loss between 35 and 550°C and related to the mass of the anhydrous solid mortar material obtained after firing at 1000°C.

2.4.1 Powder X-ray diffraction

The composition of CAC cement, Alag aggregates and mortars were investigated by powder X-ray diffraction (XRD). Operating conditions for qualitative analysis of the Bruker D8 advance instrument were set to 40 kV and 40 mA using $\text{CuK}\alpha_{1,2}$ radiation 2θ value between 3 to 55°. For quantitative analysis, operating conditions of the Bruker-AXS D4 ENDEAVOR diffractometer were set to 40 kV and 40 mA, using Fe-filtered $\text{CoK}\alpha_{1,2}$ radiation ($\lambda_1=0.1789$ nm, $\lambda_2=0.1793$ nm). Cobalt radiation was selected over copper in order to minimize micro-

absorption (i.e. in general larger absorptions by Fe of $\text{CuK}\alpha$ radiation) [24] and fluorescent background as well as better angular dispersion of the diffraction lines due to longer wavelength. Diffractograms were recorded from 4° to 105° 2θ , in 0.02° 2θ increments. A LYNXEYE linear Si-strip-type detector was used with an opening of 3.8° 2θ , being equivalent to 188 active channels. A counting time of 1.85 s per increment and channel was used, resulting in a total measurement time per scan of about 2.6 h. Only qualitative diffractograms (with standard $\text{CuK}\alpha_{1,2}$ radiation) are shown here. In order to enable a qualitative and quantitative analysis, samples were prepared using crushed mortar material. For quantitative analysis ten percent of corundum in mass was added as internal standard to samples (> 3 g for mortars) and then further grounded to enhance the number of particles analysed, to improve powder homogeneity and packing characteristics, and to minimize micro-absorption related problems. Corundum was a reasonable choice as it was assured by preliminary qualitative XRD analyse that no traces of corundum were detected in original samples (detailed further in the Discussion section). Quantitative XRD analysis of specimens was done using the adiabatic principle with auto flushing [25] as a proven method [26]. Here, the matrix-flushing method was applied as it enables to directly quantify relative mineral portions in samples including both the crystalline and amorphous components by analyzing for only those components of interest. Here only CA and C_{12}A_7 (and C_2AS only in CAC cement and Alag as raw materials but not in hydrated mortar specimens), while quantification of other minerals (e.g. pleochroite, C_2S , FeO, CT, iron perovskite and $\text{C}_2\text{A}_x\text{F}_{1-x}$) and amorphous phases were and can be omitted. The criterion for this method is that the reference material (here corundum) should have close level of crystallinity, i.e. very similar level of perfection or imperfection in a crystal structure, as the quantified component in the sample. The Full-Width at Half-Maximum of reflections in an X-ray diffraction pattern was compared as an indication of the crystallinity of the components, showing no significant differences. It

is important to note that the possible effect of the difference in crystallinity is lowered by using peak areas instead of peak heights to define and quantify the diffraction peak intensity. In the matrix-flushing method the relationship between intensity (peak area) of the characteristic X-ray reflection I_m is directly proportional to the weight fraction of the component by a factor k_m which contains the mass absorption coefficient of the total sample. The k_m values were determined by mixing the pure phase, whose syntheses is described in [27], with standard corundum in a 50:50 weight ratio. Appropriate corrections for peak overlaps were meticulously applied by inference to diffraction peak areas of the pattern due to pure synthetic phases. Mass fraction of mineral w_{m_XRD} in XRD sample is calculated according to:

$$w_{m_XRD} = k_m w_A I_m / I_A \quad (8)$$

It is difficult to separate CA reactivity coming from cement or from the Alag aggregates. Therefore, a new procedure was developed to enable this analysis where Alag reactivity is considered as an additional ‘virtual’ reactivity of cement. Such a degree of reacted CA is obtained by normalizing it to the initial amount of CA in cement which is then easily calculated according to:

$$\alpha_{CA} = (w_{CA,0} - w_{CA,t}) / w_{CA,0} \quad (9)$$

where $w_{CA,0}$ is the initial mass fraction of CA in anhydrous CAC (i.e. before hydration) and $w_{CA,t}$ represents the mass fraction of CA after hydration reactions, also normalized to the mass of anhydrous CAC, which is calculated as:

$$w_{CA,t} = w_{CA_XRD} (1 + BW M_{cem}) - M_{Alag} w_{CA_Alag} \quad (10)$$

where w_{CA_XRD} is the mass fraction of CA in the sample undergone XRD analysis that comprises cement, Alag aggregates and chemically bond water, BW expressed in g/g of

cement; M_{cem} is the mass fraction of cement in anhydrous mortar (0.346, Table 2), M_{Alag} is the mass fraction of Alag aggregates in anhydrous mortar (0.654) and $w_{\text{CA_Alag}}$ is the initial amount of CA in Alag. The degree of reacted CA obtained by eq. (9) can thus have values greater than 1, meaning that all CA from cement is consumed, but also an additional CA from Alag has reacted. In other words, the results were normalized to cement, but the overall CA coming from both cement and Alag is considered in eqs 9 and 10.

2.4.2 Porosimetry

The mercury intrusion porosimetry (MIP) measurements were carried out with Pascal 440 from Thermo-Scientific, in accordance with the procedure described in the ISO 15901-1 / 2005 standard. The volume of mercury, which penetrates the sample, is a function of the applied hydrostatic pressure (up to 400 MPa). The pore diameter is determined with the Washburn equation. Mercury properties are: density 13.53 g/cm^3 , surface tension 0.485 N/m , and contact angle 130° . The measurements were performed with gradual reading for each applied pressure (increase speed of about 10 MPa/min), on the previously dried sample with an evacuation pressure of $50 \text{ }\mu\text{m Hg}$ during 5 min.

Apparent density and air content of mortars were determined following ASTM C185-08 (2008). The volume and mass of the hardened mortar specimens, cured in sealed conditions, was measured as well. The air content (14%) is calculated from the measured apparent density of the mortar specimens, from the known densities of the constituents (Table 2), and the mixture proportions.

Density of the powdered mortar specimens was measured using Pycnomatic ATC (Thermo-Scientific) instrument with Helium as a working gas medium. Based on this density, a new procedure is presented here to calculate the theoretical porosity of cement paste:

$$P_{\text{paste}} = 1 - \frac{v_{\text{solid}}}{v_{\text{paste}}} \quad (11)$$

where v_{solid} is the volume of cement paste solids comprising of the remaining cement and formed hydration products, and v_{paste} is the volume of cement paste which adds also the remaining unreacted capillary water but without considering the volume of air bubbles. Normalizing these volumes to 1 g of cement, they are calculated as:

$$v_{\text{paste}} = \frac{1}{\rho_{\text{cem}}} + \frac{w/c}{\rho_{\text{H}_2\text{O}}} \quad (12)$$

$$v_{\text{solid}} = \frac{1 + BW}{\rho_{\text{solid}}} \quad (13)$$

where w/c is the water to cement mass ratio (0.35), BW is chemically bond water in g/g of cement, ρ_{cem} and $\rho_{\text{H}_2\text{O}}$ are the densities of cement and water, respectively, and ρ_{solid} is the density of the solids in the paste, which can be measured when working with pastes (without aggregates), but here for mortars it is obtained by combining eq (13) with following equation (14) for the theoretical density of the mortar:

$$\rho_{\text{mort, s}} = \frac{1 + BW + m_{\text{alag}}}{v_{\text{solid}} + \frac{m_{\text{alag}}}{\rho_{\text{alag}}}} \quad (14)$$

where $\rho_{\text{mort, s}}$ is the measured density of the solids in the mortar, m_{Alag} is mass of Alag per 1 g of cement (=1265/750, from Table 2) and ρ_{Alag} is density of Alag. The solid paste volume, v_{solid} can be calculated by extracting from eq. 14 where it is the only unknown value.

2.5 Modeling

Modeling CAC hydration requires knowledge on the stoichiometry and kinetics of the hydration reactions. This information is not yet fully available due to the complexity of the commercial cement hydration process. However, in a first approximation only principal (congruent) hydration reactions in their pure form can be considered. In the case of both iron-rich (Alag) aggregates and low-iron (Secar 51) cement, most hydraulic phases are CA and $C_{12}A_7$, while the rest of the phases (C_2S , C_2AS , C_4AF , perovskite and pleocroite) may be considered to have no significant reactivity. The main effects of $C_{12}A_7$ are on the dissolution rate, which is accelerated, and on the occurrence of a small quantity of C_2AH_8 even at low temperature hydration when eq. (1) is dominant. Moreover, $C_{12}A_7$ is present in much smaller quantities (generally 2-7%) than CA (40-70%) and gives similar products as CA hydration, predominantly CAH_{10} and C_2AH_8 (which transform at elevated temperatures) [1,28]. The evolution of chemically bond water (BW) during hydration can be expressed as:

$$BW = \sum_m (H/m)_{tot} w_m \alpha_m \quad (15)$$

where the sum is done over all reactive minerals m , in order to generalize the model, but in this paper only equations (2 and 3) for CA are considered, α_m is the degree of reaction for mineral m , w is the mass fraction of mineral in cement, and

$$(H / m)_{tot} = \frac{M_H \nu_H}{M_m \nu_m} \quad (16)$$

$(H / m)_{tot}$ is the stoichiometric water to cement mass ratio for complete hydration of mineral m calculated from molar masses M , and stoichiometric coefficients in the reaction scheme ν . For the case when all $\alpha_m = 1$ the value for BW corresponds to the stoichiometric water requirement in g per g of CAC.

During setting and hardening, the microstructure of material and amounts of certain phases are changing. During hydration, both volume fractions of the non-reacted cement and free water decrease, while the fractions of formed hydration products increase. The solid fraction comprises the formed hydration products and fraction of non-reacted cement. The paste solid volume content (in cm^3/g CAC) can be formulated as:

$$v_{\text{solid}} = v_{\text{CAC},0} + \sum_m (v_{\text{hydrates}} - v_{m,0}) w_m \alpha_m \quad (17)$$

where $v_{\text{CAC},0}$ and $v_{m,0}$ is the initial (non-hydrated) specific volume of cement ($v_{\text{CAC},0}$ is in cm^3/g) and mineral m ($v_{\text{CA},0}$ in cm^3/g of CA mineral), respectively, and v_{hydrates} is the volume of formed hydration products per 1 g of completely reacted mineral m (f.e. CA) calculated as:

$$v_{\text{hydrates}} = \sum_h \left(\frac{M_h v_h}{M_m v_m \rho_h} \right)_{\text{hydrates}} \quad (18)$$

Volume fractions are obtained by normalizing/dividing eq. (17) with the volume of cement paste (v_{paste} , eq. (12)) containing 1 g of cement. In eq. (18) the sum is over all hydration products (e.g. $h = \text{C}_2\text{AH}_8 + \text{AH}_3$ for reaction eq. (2)), v_h and M are the stoichiometric coefficient and molar masses of the reaction components, respectively, and ρ_h is the density of a hydration product [29,30] (Table 3).

Table 3 – Densities [29,30] and molar masses of the hydration reactants and products.

Component	$\rho / \text{g cm}^{-3}$	$M / \text{g mol}^{-1}$
CA	2.98	158.1
C_{12}A_7	2.85	138.7
CAH_{10}	1.72	338.1
C_2AH_8	1.96	358.2
C_3AH_6	2.52	378.3
AH_3	2.44	156.0

Note that for reaction (2) AH_x is approximated as AH_3 gibbsite, because it is difficult to separate reactions eqs. (2), (5) and (6), and furthermore C_2AH_8 and AH_x are sensitive to drying due to releases of their loosely bond water (up to C_2AH_5 [31]).

Depending on the water to cement mass ratio, H/CAC and initial amount of reactive minerals in CAC the reaction of hydration can be stopped by insufficiencies of ‘free’ water or by a ceasing of the reactive cement minerals. Another possibility to terminate hydration, in the case of water saturated conditions, is an insufficient free space for the growth of reaction products. Thus, the model eqs. (15) and (17) are valid for:

$$0 \leq BW \leq (H/CA)_{\text{tot}} \quad (19)$$

and for

$$v_{\text{CAC},0} \leq v_{\text{solid}} \leq v_{\text{paste}} \quad (20)$$

Note that in eq. (20) the right hand side is the volume of cement paste (eq. 12) which is considered here not to change during hydration. The cement paste model presented here does not contain entrained air bubbles. The mortar level model represents a homogenous mixture with air bubbles, aggregates and cement paste. Due to calibration/validation and experimental difficulties, the individual reactivity of aggregate and cement was not considered separately. The effect of aggregate reactivity was simplified via an additional virtual increase in the degree of cement reaction.

3. Results

3.1 Mechanical tests

3.1.1 Influence of age on compressive strength of CAC mortar

Fig. 2 shows representative stress–strain curves obtained from compression tests (at room temperature) performed with the CAC mortar at an age of 7, 14 and 28 days. All specimens showed a brittle behavior under compression load since the first micro-cracks propagate throughout the specimens creating an interconnected network of micro-cracks that result in large macro-cracks and consequently into failure.

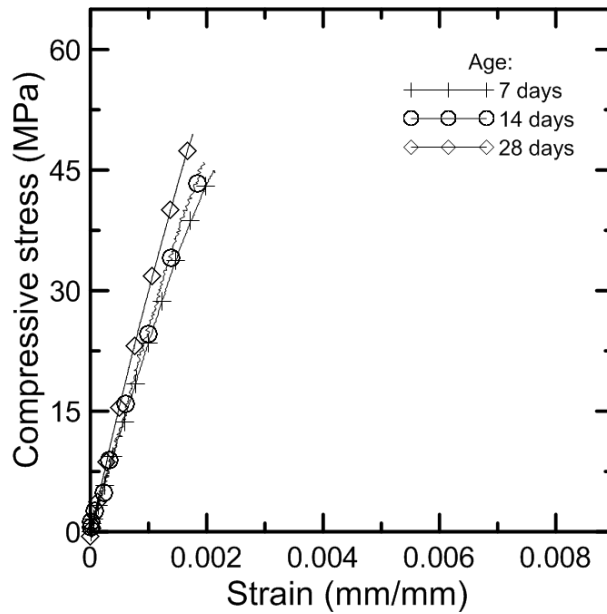


Fig. 2 – Compressive strength - strain curves of CAC mortar at 7, 14 and 28 days of age.

As expected, the average stress levels achieved by specimens at the target ages were very close, given the short setting time and high mechanical strength of the CAC mortar. With respect to the ultimate compressive strength (σ_{UCS}), enhanced curing times to 14 and 28 days showed increases of, respectively, 7% and 12% in comparison to the CAC matrix with 7 days of age. Table 4 provides the corresponding values. This continuous increase in strength up to 28 days (at 25°C) is contrary to the well-known conversion process during CAC hydration which decreases the mechanical properties of conventional CAC based materials. Main reason for this new finding is related to the incorporation of reactive Alag aggregates and a low w/c ratio, which will be discussed later in this paper. Since at 7 days of age the CAC mortar reached 90% of the 28 days compressive strength, this period (7 days) was established as a reference for the mechanical tests performed to study the temperature effect.

Table 4 – Mechanical properties for different ages.

Age (days)	Experimental values			
	P_{UCS} (kN)	σ_{UCS} (MPa)	ϵ (mm/mm)	E_c (GPa)
7	89.78	45.72	0.00217	25.05
	(6.55)	(3.33)	(0.000195)	(1.09)
14	96.19	48.98	0.00212	23.25
	(12.62)	(6.43)	(0.000223)	(4.17)
28	100.80	51.34	0.00177	31.25
	(3.42)	(1.74)	(0.000067)	(1.25)

3.1.2 Effect of temperature on compressive strength of CAC mortar

Fig. 3 shows the mechanical strength evolution of CAC mortar submitted to elevated temperatures. Results obtained from the specimens are given in Table 5. The CAC mortar showed to be strongly affected by thermal impact when submitted to a compressive loading.

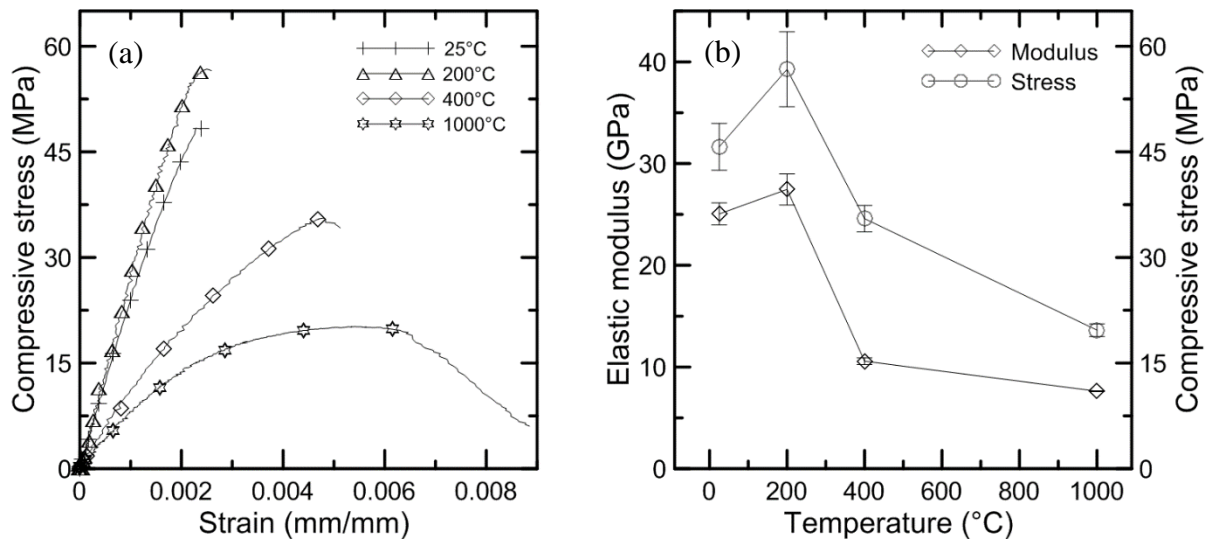


Fig. 3 – Effect of temperature on the residual compressive strength (a) and elastic modulus (b) of CAC mortar (7 days of age).

Table 5 – Effect of temperature on mechanical properties (7 days of age).

Temperature	Experimental values			
	P_{UCS} (kN)	σ_{UCS} (MPa)	ϵ (mm/mm)	E_c (GPa)
25°C	89.78	45.72	0.00217	25.05
	(6.55)	(3.33)	(0.00019)	(1.09)
200°C	111.36	56.72	0.00234	27.46
	(10.42)	(5.31)	(0.00033)	(1.53)
400°C	69.72	35.51	0.00481	10.57
	(3.66)	(1.87)	(0.00029)	(0.34)
1000°C	38.63	19.67	0.00537	7.62
	(1.77)	(0.90)	(0.00011)	(0.41)

When preheated up to 200°C the CAC mortar showed a substantial increase in compressive strength of 24%. From this temperature and above, the compressive strength values decreased gradually with increasing temperature. In comparison with the results obtained at room temperature, the decreases in compressive strength for 400°C and 1000°C were, respectively, 22% and 57%. Similar trend as observed for the compressive strength was reflected by the elastic modulus (see Fig. 3). When preheated up to 200°C, the CAC mortar showed a slight increase in the elastic modulus of 8%. At temperatures between 200°C and 1000°C, severe loss was observed in the elastic modulus. In comparison with CAC mortar tested at room temperature, the decreases in elastic modulus (E_C) for mortars heated at 400°C and 1000°C were 58% and 70%, respectively. As well as the influence of age, the effect of temperature will be further addressed in the discussion section, where mechanical results are correlated with the physical and chemical changes occurring in the microstructure of CAC mortar.

3.2 Microstructural analysis

The TG curves in Fig. 4 are plotted starting from the end of the aforementioned isothermal stage at 35°C. The DTG peaks presented by the unheated sample (25°C), comprehended between 35 and 200°C, are related to different process which include: loss of free and loosely held structural water of the AH_x gel and dehydration of the metastable C_2AH_8 [31]. As shown in Fig. 5 the crystalline structure of metastable hydrate C_2AH_8 was also detected by XRD. The same DTG peaks (between 35 and 200°C) are not visible in the other curves given the heating process applied to both (200 and 400°C) specimens. Between 200 and ~350°C, both the unheated sample (25°C) and samples heated up to 200°C, presented significant mass losses. These losses correspond primarily [31] to dehydration of the stable phases C_3AH_6 and AH_3 , which persist after heating and drying of the CAC mortar. These phases are also detected by XRD (see Fig. 5). Since main hydration products presented by the CAC matrix decompose under temperatures below 400°C, the samples 400 and 1000°C did not show

significant mass losses. This mass loss can be attributed to some remaining crystalline water in $C_{12}A_7H$ [32] and $AlOOH$ [33,34], but also to a decomposition of the carbonate phases after about $600^{\circ}C$, as heating of the specimens could be accompanied by some degree of carbonation.

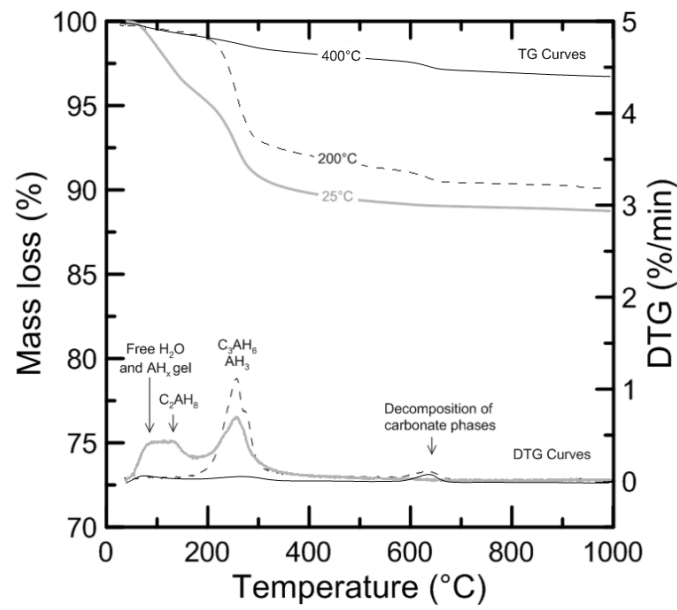


Fig. 4 – Thermal analysis of CAC mortar at 7 days of age and after exposure to 200 and $400^{\circ}C$.

XRD analysis on specimens obtained from hydrated specimens cured at different conditions, shown in Fig. 5, confirmed the hydrate compositions expected from literature [1,29]. The main hydration products observed on $25^{\circ}C$ samples was C_2AH_8 with traces of AH_3 and C_3AH_6 . The sample heated up to $200^{\circ}C$ presented a substantial increase in diffraction peaks for C_3AH_6 and AH_3 , accompanied by a decrease in diffraction peaks for CA. This process is related to a conversion process accompanied by further hydration of reactive CA minerals. Diffraction peaks of metastable hydration products and aluminium hydroxide are fairly broadened, indicating poor crystallinity, while that of C_3AH_6 showed a good crystallinity.

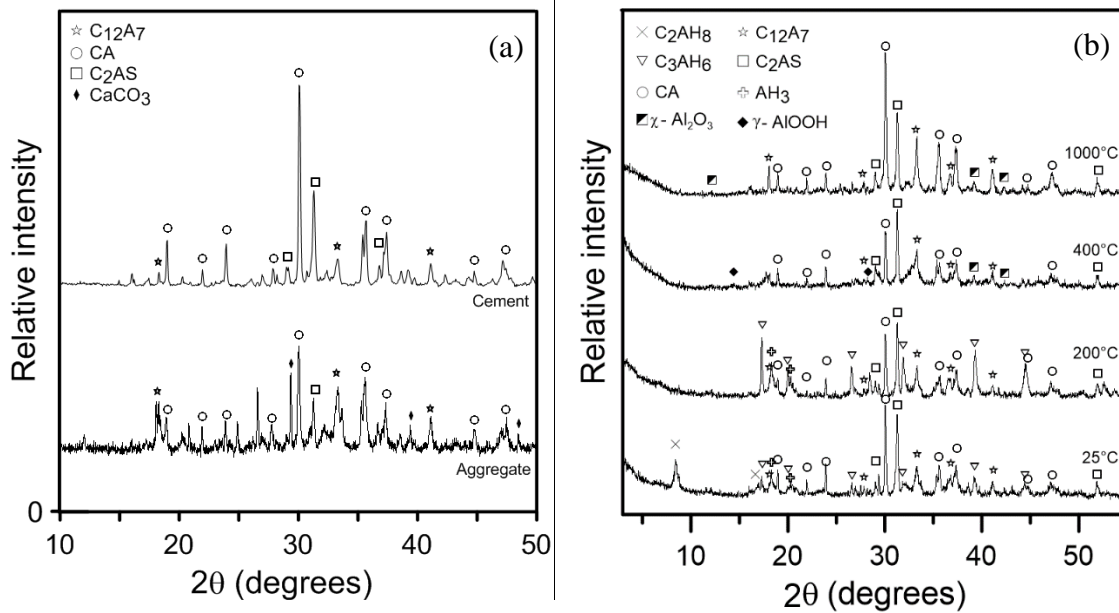


Fig. 5 – XRD profiles for cement and aggregate (a) and for CAC mortar at room temperature and preheated at 200, 400 and 1000°C (b).

At 400°C XRD results show traces of amorphous diffraction peaks for C₃AH₆ and an increase in the amount of C₁₂A₇ accompanied by loss of its crystallinity as observed by its peak widening. At 1000°C XRD reveals an increase in the level of C₁₂A₇ crystallinity and a strong increase in CA diffraction lines, demonstrating crystallization of CA and C₁₂A₇. The amount of reacted and re-crystallized CA and C₁₂A₇ phases as a function of temperature is quantified as well (in discussion section).

Table 6 shows further experimental results performed on CAC mortar specimens and samples. Release of water (*RW*) due to the drying effect, expressed in vol. % of mortar specimen, indicates an increased evaporation of ‘free’ water from the specimens, with increasing exposure temperature.

Table 6 – Experimental results performed on CAC mortars: release of water due to high temperatures (200, 400 and 1000°C) or vacuum drying at 25°C (in vol. % of mortar); chemically bonded water remained after high temperature or vacuum treatment (in g/g of anhydrous solids, i.e. normalized to the mass of fired mortar which comprises cement and aggregate); density of mortar solids, i.e. skeleton density g/cm³, measured on grinded samples; MIP porosity (in vol. % of mortar).

Specimen	Water release (<i>RW</i>), vol. % mortar	Bond water (<i>BW</i>), g/g dry solids	Mortar solids density, g/cm ³	MIP porosity, vol. % mortar
25°C*	3.6	0.1044	2.799	21.9
200°C	8.9	0.0780	2.906	26.1
400°C	20.9	0.0283	3.034	33.5
1000°C	26.3	0.0023	3.172	38.8

*Vacuum dried

At 25°C upon vacuum drying, mass loss of the samples is due to evaporation of ‘free’ water but also because of the loosely held structural water in C₂AH₈ (->C₂AH₅ [31]) and AH_x metastable hydration products. At 200°C the specimen loses 145% more water than during vacuuming at the 25°C specimen. This increase can be attributed to conversion reactions which occur under hydrothermal conditions within the specimen, i.e. combined high temperature and water availability due to a low vapor diffusion process through the material. Such a conversion reaction results in a production of more ‘free’ water (eq. (4-6)). Eventually, at time of exposure in the furnace, this free water could be evaporated from the specimen. At 400°C, the amount of water release is 136% higher than at 200°C, due to decomposition of stable hydration products. At 1000°C, the specimen exhibits 25% higher water release than at 400°C due to a more complete decomposition of hydration products, as well as carbonates formed by the carbonation process during the heating regime.

Chemically bonded water that remained in the specimens, was obtained from TG measurements and expressed in g/g of anhydrous solids, i.e. normalized to mass of fired mortar solids (at 1000°C) which comprises anhydrous cement and aggregate. As expected from the conversion reactions (eq. (4-6)), the results show a decrease in bonded water (*BW*), and an increase in mercury intrusion porosity (MIP), with enhancing temperature. Mortar

solids density, measured on powdered specimens, increases with temperature in agreement with a simultaneous decrease of the chemically bonded water.

Effect of temperature on the cumulative pore size distribution (MIP, Fig. 6) shows a coarsening of the pore sizes at 400 and 1000°C.

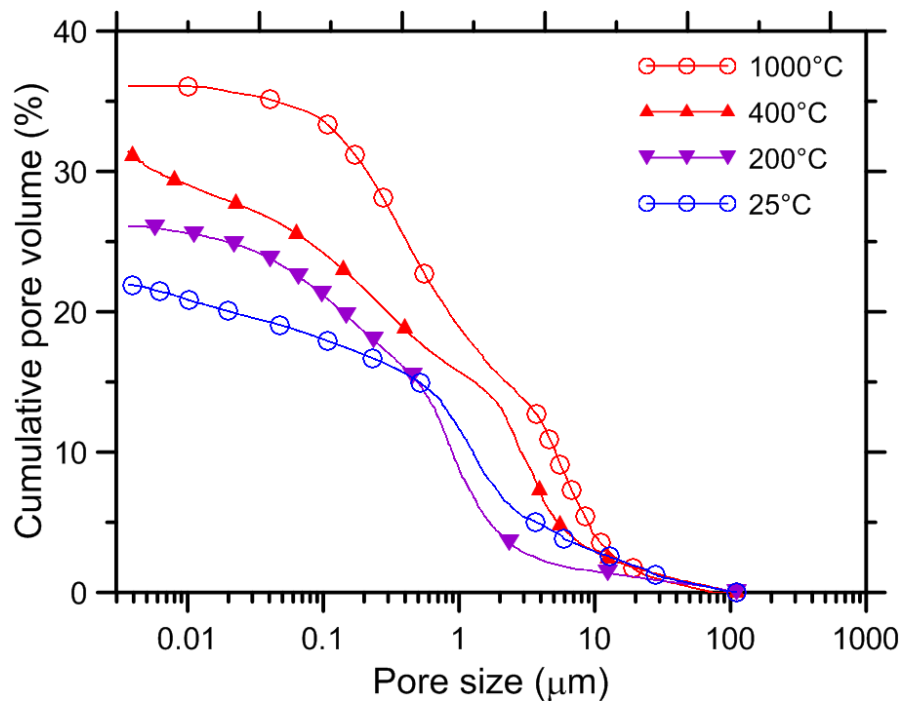


Fig. 6 – Cumulative pore size distribution curve (MIP): effect of temperature.

However, interestingly, metastable samples at 25°C exhibits a coarser pore size distribution than the converted sample at 200°C. This can be attributed to the sensitivity of loosely held structural water in C_2AH_8 and AH_x gel to drying [31] (Fig. 7 and Fig. 8), but could indicate a possible change in pore morphology due to a re-distribution of hydration products within the pore space during conversion reactions as well. Unfortunately it is difficult to separate this two effects.

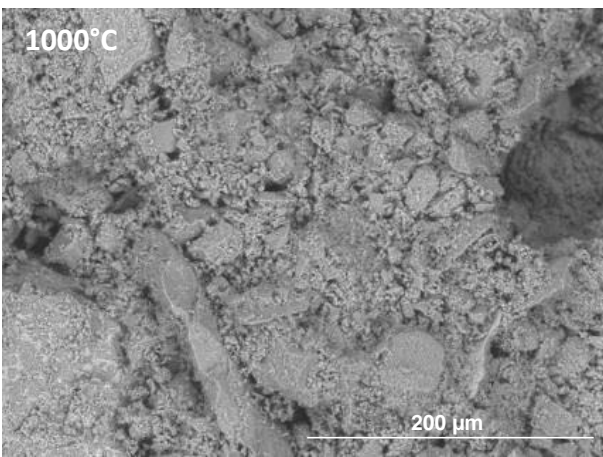
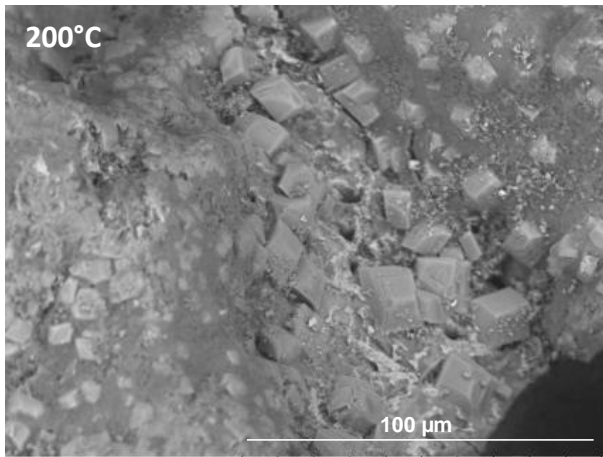
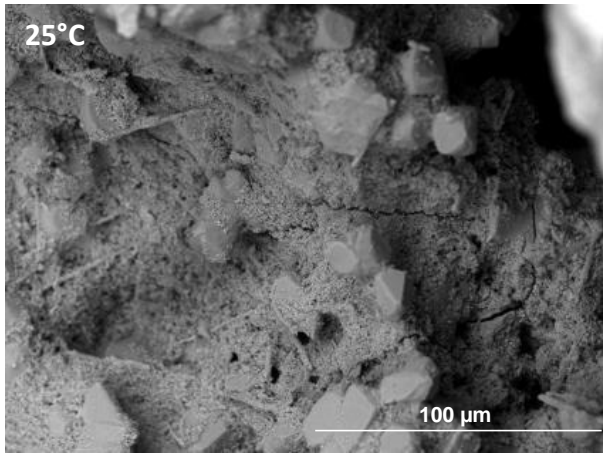


Fig. 7 – SEM secondary electrons mode images.

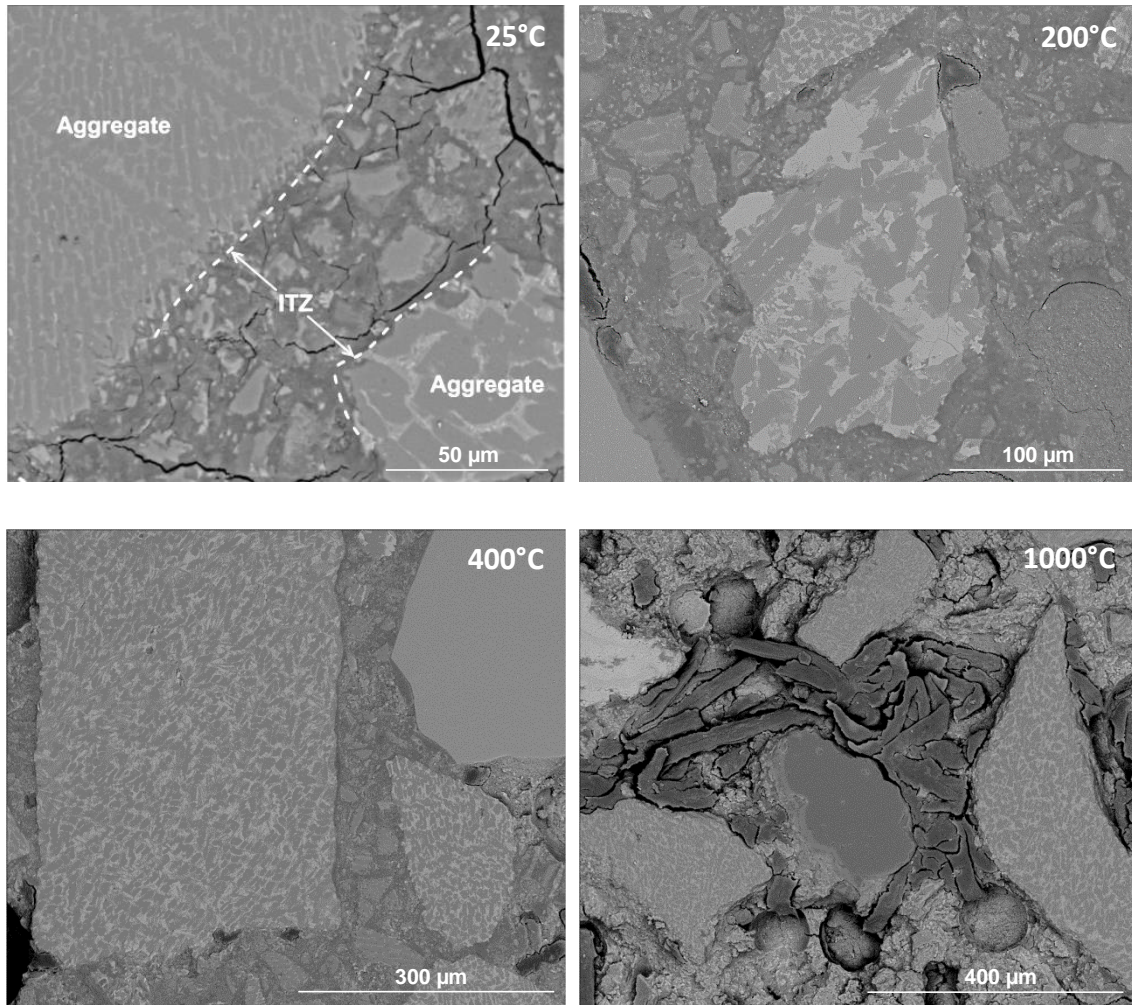


Fig. 8 – SEM back scattered electrons (*bse*) images of CAC polished mortar samples at room temperature and after heating process up to 200, 400 and 1000°C. The *bse* grey scaling depends on the atomic number averaged density, where bright areas represent slow reacting phases containing atoms with larger atomic numbers: C_4AF , CT, C_2AS .

Specimens cured at 25°C, formed plate-shaped C_2AH_8 crystals and AH_x amorphous gel in the CAC matrix (Fig. 7 a). In the structure of those specimens cured at 200°C (Fig. 7 b), irregular cubic C_3AH_6 crystals, completely or partially covered by AH_3 crystalline material, are observed. The samples were also contaminated by carbonation and re-hydration due to difficulties in preparations. Considerable changes in structure of CAC matrices were found after heating at 1000°C (Fig. 6). The contours of the cubic and irregular cube crystals has significantly diminished (remainings are probably due to rehydration of the specimens), replaced by the increased amount of small pores.

3.3 Discussion

The proposed model for hydration reactions rests on the following assumptions: a) only reaction eq. (2) for hydration at 25°C, where AH_3 is used for AH_x gel, justified by difficulty to separate hydration reactions eqs. (2), (5) and (6), and also by drying sensitivity of metastable hydration products; b) only reaction eq. (3) for converted samples at 200°C; c) the only reactive minerals are CA and $C_{12}A_7$; and d) their hydration is congruent, i.e. exhibit same rates, $\alpha_{CA}=\alpha_{C_{12}A_7}$ during hydration. The hydration of $C_{12}A_7$ was treated together with CA hydration by simply increasing the CA quantity by the amount of $C_{12}A_7$ in CAC. The assumption of their congruent hydration and similar reaction stoichiometry is justified by the small amount of $C_{12}A_7$ in the CAC (4% $C_{12}A_7$ and 60% CA, based on QXRD results).

The volume of formed hydration products per 1 g of completely reacted mineral calculated by eq. (18), according to reaction eqs. (1), (2) and (3), are 1.243 cm³/g, 0.780 cm³/g and 0.586 cm³/g, respectively. Furthermore, by reference to eq. (16), the $(H/CA)_{tot}$ for the individual CA hydration reaction (1), (2), and (3) is 1.1385, 0.6262, and 0.4557, respectively.

Bond water (*BW*) and released water (*RW*, in vol % of paste) for the CAC mortars plotted in Fig. 9 as a function of temperature show good agreement between model and experimental results. Good agreement can be also observed, Fig. 10, between predicted and measured (obtained from solid density) paste porosities. Fig. 10 plots also the MIP porosities normalized to cement pastes, which are obtained by subtracting the 14 vol. % of air bubbles from the mortar MIP porosities (Table 6), and then dividing by the volume fraction of paste (0.4551, calculated from cement and water amount from Table 2) in the mortar, i.e. $P_{paste} = (P_{mortar} - 14)/0.4551$. The air content of 14% is calculated from the measured apparent density of the mortar specimens. One can observe, on Fig. 10, that MIP paste porosities are always significantly lower than the ones obtained from the measured densities of solid mortar

powders. This can be attributed to the distribution of air bubbles in the specimens, which is not ideally homogenous. Relatively small samples (2cm^3) for MIP analysis, taken from the center of the specimen, thus may not be fully representative as they may contain different amounts of air bubbles than the rest of the specimen. It can be expected that more air bubbles are located more at the top of the specimen than at the bottom, due to segregation effects. However, considering the small w/c and addition of viscosity modifying agent for improving the cohesion of fresh mortar that avoids segregation of the components, a relatively good stability of the air bubbles is expected.

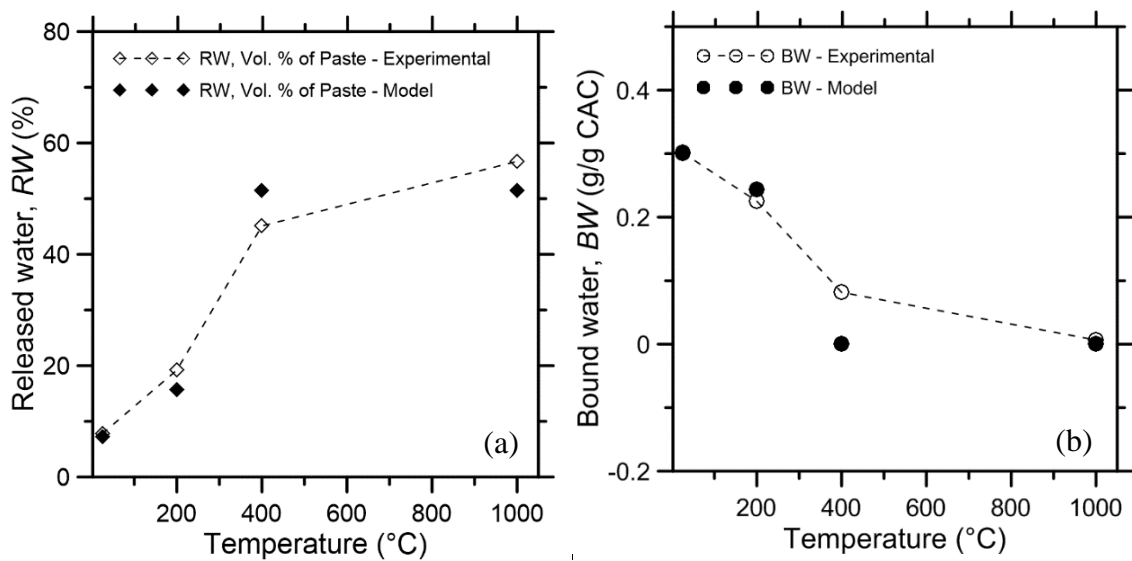


Fig. 9 – Released water (RW , vol % of paste) (a) and bond water (BW) (b) for CAC mortars as a function of temperature: comparison of model and experimental values.

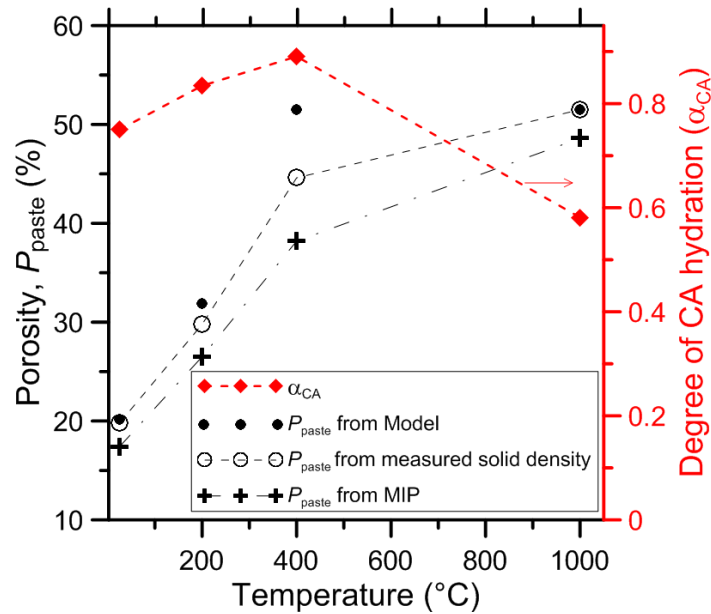


Fig. 10 – Evolution of porosity obtained from measured mortar solids density (Table 6) and eqs. (11), (12) and (14) and mortar MIP results (Table 6): comparison of model and experimental porosity normalized to paste volume without air bubbles. Right ordinate shows CA hydration reactivity up to 400°C, and crystallization reactivity at 1000°C.

Higher discrepancy at 400°C, for *BW*, *RW* (Fig. 9) and porosity (from solid density, Fig. 10), can be explained by incomplete decomposition of the stable hydration products (addressed further in the last paragraph) and/or carbonation processes during heating of the specimens, which results in a higher amount of bond water, accompanied by lower amount of released water and porosity, in the measured values rather than in the predicted ones.

Predicted values for both 400°C and 1000°C samples are the same as they both assume (as a first simplification) that a complete dehydration process has occurred: $BW_{model} = 0$ g/g CAC, porosity and $RW = 51.5\%$. Predicted amounts of released water (*RW*) is 7.3 % and 15.7%, for 25°C and 200°C samples, respectively, while the predicted bond water is 0.3006 g/g CAC and 0.2432 g/g (Fig 9), and predicted porosity is 20.1% and 31.8% (Fig 10).

CA hydration reactivity, Fig. 10 - right ordinate, increases up to 400°C due to hydration reactions taking place at 25°C which is then further stimulated by conversion reactions taking place during heating to 200 and 400°C. A higher degree of reacted CA at 400°C rather than at

200°C could be attributed to a higher reaction temperatures under wet, i.e. hydro-thermal conditions assured by a slow transport of moisture within the specimen that gradually reaches the drying-out equilibrium with respect to the evaporated water content. At 1000°C the degree of reacted CA is significantly lower, which can be explained by crystallization of CA around 1000°C [35], also corroborated by an exothermal peak observed in the DSC curve around 990°C (not shown here). Evolution of $C_{12}A_7$ mass fraction in anhydrous mortar as a function of temperature is presented in Fig. 11.

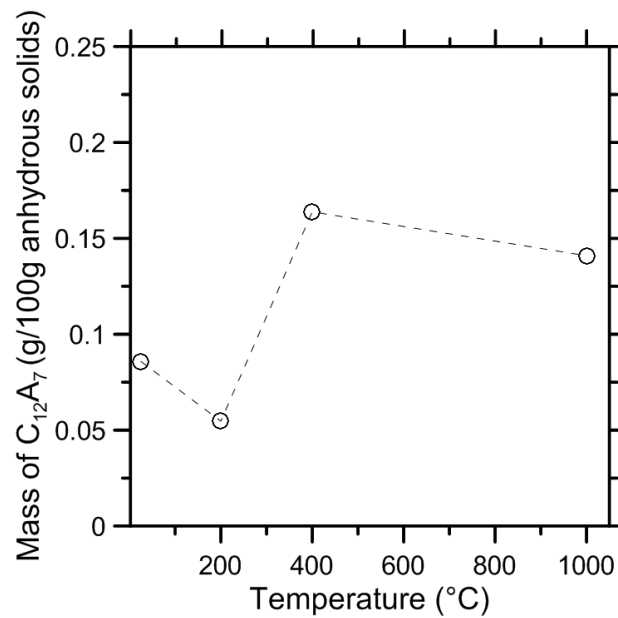


Fig. 11 – Evolution of $C_{12}A_7$ mass fraction as a function of temperature, results are normalized to anhydrous solids, i.e. mass of fired (at 1000°C) mixture of cement and aggregates.

Initial $C_{12}A_7$ reactivity at 25°C was not possible to discern because of very small amounts of $C_{12}A_7$ in cement (4%) compared to larger amounts of it (11%) in Alag aggregates. However, semi-quantitative results in Fig. 11 could show a relatively higher reactivity due to transformation reactions at 200°C, followed by crystallization of $C_{12}A_7$ at 400 and 1000°C. This crystallization of $C_{12}A_7$, already at 400°C, as well as CA at 1000°C, at such relatively low temperatures can be ascribed to high chemical affinity of a well homogenized mixture of

amorphous dehydrated precursors whose CaO and Al₂O₃ parts are already well mixed at the molecular level according to their stoichiometric mass ratios [35].

The w/c and the amount of main active minerals in CAC are the principal variables governing the porosity and strength development during the transformation reactions [1]. This is because free water is released by transformation reactions (eqs. (4-6)), as metastable hydration products contain more structural water than stable ones, which contributes to a further hydration of non-hydrated cement that further fills the porosity. Thus, the deleterious effect transformation reactions have on the properties of CAC-based materials could be reduced by lowering the w/c ratio. Recently this improvement in material properties was demonstrated by usage of a PCE superplasticiser [17]. That study demonstrated that lowering the w/c ratio from 0.470 to 0.291, by superplasticiser addition while fixing the workability, compressive strengths were improved up to 41% for mortars with mainly metastable hydration products and by up to 90% for the specimens with transformed hydration products. Conversion of CAH₁₀ and C₂AH₈ to C₃AH₆ theoretically results in 75% and 47% volume reduction, relative to the original volume of hydration products, normally leading to strength retrogression. For our mortar systems, with clinker aggregates, the predicted increase in paste porosity is 58%, i.e. from 20.1% to 31.8% (Fig 10). Although the converted strength of conventional CAC based materials (without clinker aggregates) is lower than the initial metastable strength, in relative terms, the converted strength is greater than at higher w/c ratios [5]. This could be attributed to the fact that C₃AH₆ and gibbsite are expected to be stronger than metastable (amorphous and layered [31]) hydration products, which results in stronger bonding [1]. However, in conventional CAC based materials the adverse effect of an increase in porosity prevails over a better bonding of stable hydration products.

Without reactive clinker aggregates, the transformation process was always documented to impair compressive strength, in reference with the maximal metastable one, indicating that the increase of material porosity prevails the effect of further increase in degree of hydration. Moreover, the stable hydration products contain more crystalline OH⁻ bonds, and a higher crystalline level. The stable hydration products have a much lower capacity for filling the capillary porosity in CAC paste than the metastable ones. This results in lower porosity (and hence better performances) for metastable phase although the hydration degree is lower. Chemically bond water for complete hydration of considered active minerals (in this paper CA and C₁₂A₇ in the investigated cement), the (H/CAC)_{tot} upon reaction eq. (1), (2) and (3) is calculated by (H/CA w_{CA}), where the CA content is increased by the C₁₂A₇ content, to be 0.73 g/g CAC, 0.40 g/g CAC and 0.30 g/g CAC, respectively.

The polymineral nature of aggregates results in selective dissolution of its surface leaving the slow reactive iron-containing minerals (brighter areas in SEM-bse images, Fig 8) sticking out into the hydration products of the surrounding cement paste's interfacial zone. This enables the mechanical interlocking effect between Alag aggregate and paste. SEM micrographs (Fig 8) show excellent bonding between aggregates and cement paste, and an even more compact matrix (Fig 7) for 200°C than 25°C. This paper shows that in spite of the increased cement paste porosity from 21% to 32% upon heating the specimens at 200°C, the induced conversion reactions resulted in improved mechanical properties. This was attributed to a better bonding within the interfacial zone, and by a stronger nature of the stable hydration products, compared to weaker amorphous and layered metastable products (with high amount of loosely held water molecules), which is further stimulated by an increased degree of cement and aggregate hydration that improves the mechanical interlocking effect between Alag aggregate and the paste components.

As no portlandite was observed at 400°C (nor CaO at 1000°C), following sintering reaction can describe the crystallisation of C₁₂A₇ from a decomposition of C₃AH₆ and AH₃:



At 400°C, C₁₂A₇ might also contain some remaining amounts of crystalline water [32]. The stoichiometry of reactants in this dehydration (and re-crystallisation) reaction, molar ratio of $n(\text{AH}_3)/n(\text{C}_3\text{AH}_6)=3/4$, consumes less AH₃ than available, as formed according to hydration reaction eq. (3) where $n(\text{AH}_3)/n(\text{C}_3\text{AH}_6)=2/1$. This may be attributed to the nature of the crystallization process and by the sintering mechanism which occurs preferentially on the boundaries of particles of the dehydrated phases. At 1000°C, CA crystallizes by sintering reaction of C₁₂A₇ with amorphous A:



Both these crystallization processes are formed by sintering reactions where atoms in the material's microstructure diffuse across the boundaries of the particles, fusing the particles together and creating a new solid phase. Therefore, an observed low degree of conversion for these reactions can be explained by their strongly kinetically (diffusion) controlled mechanism. From this, the reaction initially takes place only at boundaries where the two reacting phases meet, i.e. amorphous C₃A, formed by dehydration of C₃AH₆, and amorphous A, from AH₃ dehydration. A better intermixing of these two phases, as a result of (through solution [27]) hydration precipitation reactions, leads to higher reactive surface areas and thus the sintering reaction rate [35]. The dehydration products react to produce new crystalline phases, which create a load bearing capacity via ceramic bonds (Fig 8), largely due to intergrowth of C₁₂A₇ and/or CA crystals with the aggregates. At 400°C gibbsite loses part of its crystalline water, and transforms to boehmite (gamma-AlOOH) [33]. The XRD patterns of gibbsite after heating at 400°C indicate a trace of boehmite (at 14.5 °2θ CuK_{alpha}) along

with the disappearance of gibbsite peaks. Boehmite then further decomposes to amorphous aluminum oxide and semi-crystalline χ -Al₂O₃ [33]. At 400°C and 1000°C, traces of χ -Al₂O₃ phase could be detected (Fig 5 b), which gradually loses water until about 800°C [33, 34]. Therefore, for the 400°C samples, the TG loss (Fig 4) and *BW* discrepancy (Fig 9b) can be attributed, beside carbonation, also to remaining water in C₁₂A₇H [32] and AlOOH [33,34].

4. Conclusions

It was found that inclusion of reactive Alag aggregates in mortars with a low w/c ratio, increased strength by 7% and 12% at room temperature curing for 14 and 28 days, respectively, in comparison to the CAC matrix with 7 days of age. The CAC mortar specimens heated up to 200°C showed a substantial increase in compressive strength of 24%, followed by a decrease of 22% and 57%, for 400°C and 1000°C, respectively. The same trend was reflected in the elastic modulus results: increase in the elastic modulus of 8% at 200°C, and a decreases of 58% and 70% at 400°C and 1000°C, respectively.

This paper shows that in spite of the increase in porosity of the cement paste from 21% to 32% upon heating the specimens at 200°C, the induced conversion reactions resulted in improved mechanical properties. This was attributed to 1) a better bonding within the interfacial zone due to stronger stable hydration products, compared to the weaker metastable products, and 2) an increased degree of aggregate and cement hydration which improves the mechanical interlocking effect between Alag aggregates and paste. The polymineral nature of the aggregates results in a selective dissolution of its surface leaving the slow reactive iron-containing cement minerals sticking out into the hydration products of the surrounding cement paste interfacial zone, contributing also to a reinforced bond.

CA hydration reactivity increases up to 400°C due to hydration reactions (at 25°C) which is further stimulated by conversion reactions taking place during heating to 200 and 400°C. At

1000°C the degree of reacted CA is significantly lower, which can be explained by crystallization of CA around 1000°C. A certain amount of $C_{12}A_7$ shows reactivity due to hydration reactions at 200°C, followed by crystallization of $C_{12}A_7$ at 400 and 1000°C.

The effect of temperature increase on cumulative pore size distribution shows a coarsening of the pore sizes at 400 and 1000°C, and attributes to the decomposition of hydration products. Metastable samples at 25°C exhibits a coarser pore distribution than converted samples at 200°C.

Model predictions, based on the main chemical reaction schemes for CA minerals, show good agreements with experimental values for chemically bonded water, evaporated water and porosity as a function of temperature. Discrepancy at 400°C could be attributed to persisting crystalline water in $C_{12}A_7H$ and $AlOOH$.

Acknowledgements

The authors gratefully acknowledge the Brazilian Agency CNPq and TU Darmstadt for its partial financial support and Kerneos (France) for supplying the cement, superplasticizer and aggregate. The authors would like to thank Dr. Reiner Neumann (CETEM - Centre for Mineral Technology, Rio de Janeiro, Brazil) for help with QXRD measurements.

[1] J. Bensted, Calcium Aluminate Cements, Chapter 4 in Structure and Performance of Cements, 2nd ed., (ed. Bensted J, Barnes P), London, 2002. 114-138. ISBN 0-419-23330-X

[2] R.J. Mangabhai, F.P. Glasser, Ed, Proc. Int. Conf. on CAC, Edinburgh, UK, 2001. ISBN 1-86125-142-4

[3] C.H. Fentiman, R.J. Mangabhai and K.L. Scrivener, (Eds.) Calcium aluminates. Proceedings of the International Conference 2014, Avignon, France, 18–21, May 2014.

[4] C.M. George, Industrial aluminous cements in *Structure and Performance of Cements* (ed. P.Barnes), Applied Science, London, (1983) 415-470.

[5] K.L. Scrivener, J.L. Cabiron, R. Letourneux, High-performance concretes from calcium aluminate cements, *Cem. Concr. Res.* 29 (1999) 1215–1223. doi:10.1016/S0008-8846(99)00103-9.

[6] C. Wöhrmeyer, C. Alt, N. Kreuels, C. Parr and M. Vialle, Calcium Aluminate Aggregates for use in Refractory Castables, TP-GB-RE-LAF-016, 1998, 1-13. (<http://www.secar.net/-Technical-Papers>).

[7] C. Wöhrmeyer, C. Parr, H. Fryda, E. Frier, New calcium aluminate aggregates for refractory castables installed in highly abrasive environments, TP-GB-RE-LAF-092, 2011, 1-13. (<http://www.secar.net/-Technical-Papers>).

[8] C. Wöhrmeyer, C.Parr, H. Fryda, E. Frier, Aggregates for Non-Ferrous Applications, Kerneous, TP-GB-LAF-094, 2011, 1-12. (<http://www.secar.net/-Technical-Papers>).

[9] C. H. Fentiman, R. J. Mangabhai and K. L. Scrivener, (Eds.) Calcium aluminates. Proceedings of the International Conference 2014, Avignon, France, 18–21 May 2014.

[10] A. M. Goyns, M. G. Alexander, Performance of various concretes in the Virginia experimental sewer over 20 years, in Calcium aluminates. Proceedings of the International Conference 2014, Avignon, France, 18–21 May 2014, 573-584.

[11] J. Herisson, E. D. Van Hullebusch, M. Guéguen-minerbe and T. Chaussadent, Biogenic corrosion mechanism: study of parameters explaining calcium aluminate cement durability, in Calcium aluminates. Proceedings of the International Conference 2014, Avignon, France, 18–21 May 2014, 633-644.

[12] M.L. Berndt, Protection of concrete in cooling towers from microbiologically influenced corrosion, *Geotherm. Resour. Counc. Trans.* 25 (2001) 3–7.

[13] S. Lamberet, D. Guinot, E. Lempereur, J. Talley, C. Alt, Field investigations of high performance calcium aluminate mortar for wastewater applications, in *Calcium Aluminate Cements: Proceedings of the Centenary Conference*, Avignon, 30 June-2 July 2008, pp. 269-277.

[14] D.V. Heerden. The use of calcium aluminate cement in shotcrete. In: *Shotcrete: More Engineering Developments: Proceedings of the Second International Conference on Engineering Developments in Shotcrete*, Bernard (ed), October 2004, Cairns, Queensland, Australia.

[15] C. Wöhrmeyer, C. Parr, H. Fryda, E. Frier, New stronger bonds for monolithic castables through surface reactive calcium aluminate aggregates, TP-GB-RE-LAF-085, 2010, 1-9. (<http://www.secar.net/-Technical-Papers>).

[16] C. Gosselin, E. Gallucci, K. Scrivener, Influence of self heating and Li₂SO₄ addition on the microstructural development of calcium aluminate cement, *Cem. Concr. Res.* 40 (2010) 1555–1570. doi:10.1016/j.cemconres.2010.06.012.

[17] N. Ukrainczyk, Effect of Polycarboxylate superplasticizer on properties of Calcium aluminate cement mortar. *Adv. Cem. Res.* (2015) 27(7) 388–398. <http://dx.doi.org/10.1680/adcr.14.00022>

[18] W.E. Lee, W. Vieira, S. Zhang, K.G. Ahari, H. Sarpoolaky, C. Parr, Castable refractory concretes, *Int. Mater. Rev.* 46 (2001) 145–167. doi:10.1179/095066001101528439.

[19] C. Gogtas, H.F. Lopez, K. Sobolev, Role of cement content on the properties of self-flowing Al₂O₃ refractory castables, *J. Eur. Ceram. Soc.* 34 (2014) 1365–1373. doi:10.1016/j.jeurceramsoc.2013.11.004.

[20] N. Ukrainczyk, Chemical Shrinkage During Hydration Reactions of Calcium Aluminate Cement, *Austin J. Chem. Eng.* 1 (2014) 1–7.

[21] Abnt, NBR NM 248: Agregados - Determinação da composição granulométrica, Test. (2003) 6.

[22] De Larrard F. *Concrete mixture proportioning: a scientific approach*. London. E&FN SPON. 1999.

[23] Sedran T. *Rhéologie et rhéométrie des bétons: application aux bétons autonivelants*. Doctoral dissertation. Ecole Nationale des Ponts et Chaussées 1999:484.

[24] J.C. Taylor, L.P. Aldridge, C.E. Matulis and I. Hinczak, Chapter 18 X-ray powder diffraction analysis of cements, in *Structure and Performance of Cements*, 2nd ed., (ed. Bensted J, Barnes P), London, 2002. 420-442. ISBN 0-419-23330-X.

[25] F. Chung, Quantitative interpretation of X-ray diffraction patterns of mixtures. II. Adiabatic principle of X-ray diffraction analysis of mixtures, *J. Appl. Crystallogr.* 7 (1974) 526–531. doi:10.1107/S0021889874010387.

[26] H.G. Midgley, Quantitative determination of phases in high alumina cement clinkers by X-ray diffraction, *Cem. Concr. Res.* 6 (1976) 217–223. doi:10.1016/0008-8846(76)90119-8.

[27] N. Ukrainczyk, Kinetic modeling of calcium aluminate cement hydration, *Chem. Eng. Sci.* 65 (2010) 5605–5614. doi:10.1016/j.ces.2010.08.012.

[28] R.N. Edmonds, A.J. Majumdar, The hydration of $12\text{CaO}\cdot 7\text{Al}_2\text{O}_3$ at different temperatures, *Cem. Concr. Res.* 18 (1988) 473–478. doi:10.1016/0008-8846(88)90082-8.

[29] K.L. Scrivener, A. Capmas, 13 - Calcium Aluminate Cements, in: *Lea's Chem. Cem. Concr.* (Fourth Ed., 2003: pp. 713–782. doi:http://dx.doi.org/10.1016/B978-075066256-7/50025-4.

[30] F.M. Lea, *The Chemistry of Cement and Concrete*, 3rd ed., Edward Arnold, London, (1976) ISBN 0-7131-2277-3.

[31] N. Ukrainczyk, T. Matusinovic, S. Kurajica, B. Zimmermann, J. Sipusic, Dehydration of a layered double hydroxide- C_2AH_8 , *Thermochim. Acta.* 464 (2007) 7–15. doi:10.1016/j.tca.2007.07.022.

[32] M.C. Ball, The thermal dehydroxylation of C_3AH_6 , *Cem. Concr. Res.* 6 (1976) 419–420. doi:10.1016/0008-8846(76)90107-1.

[33] A. Malki, Z. Mekhalif, S. Detriche, G. Fonder, A. Boumaza, A. Djelloul, Calcination products of gibbsite studied by X-ray diffraction, XPS and solid-state NMR, *J. Solid State Chem.* 215 (2014) 8–15. doi:10.1016/j.jssc.2014.03.019.

[34] B. Zhu, B. Fang, X. Li, Dehydration reactions and kinetic parameters of gibbsite, *Ceram. Int.* 36 (2010) 2493–2498. doi:10.1016/j.ceramint.2010.07.007.

[35] A.A. Goktas, M.C. Weinberg, Preparation and Crystallization of Sol-Gel Calcia-Alumina Compositions, *J. Am. Ceram. Soc.* 74 (1991) 1066–1070. doi:10.1111/j.1151-2916.1991.tb04344.x.

Artigo B – Rambo DAS, Silva FA, Toledo RD and Gomes OFM. Effect of elevated temperatures on the mechanical behavior of basalt textile reinforced refractory concrete. Published in the Journal of Materials and Design (2014). Volume 65, January 2015, Pages 24–33, doi:10.1016/j.matdes.2014.08.060

**Effect of elevated temperatures on the mechanical behavior of basalt textile
reinforced refractory concrete**

Dimas Alan Strauss Rambo^a, Flávio de Andrade Silva^{b*}, Romildo Dias Toledo Filho^c
and Otávio da Fonseca Martins Gomes^d

^{a,c} Civil Engineering Department, COPPE, Universidade Federal do Rio de Janeiro, P.O.
Box 68506, CEP 21941-972, Rio de Janeiro – RJ, Brazil.

^bDepartment of Civil Engineering, Pontifícia Universidade Católica do Rio de Janeiro
(PUC-Rio), Rua Marques de São Vicente 225, 22451-900 - Rio de Janeiro - RJ, Brazil

^d Centre for Mineral Technology (CETEM), Rio de Janeiro – RJ, Brazil.

June 2014

*Corresponding author: e-mail: fsilva@puc-rio.br, Tel: +55(21) 3527-1188. Fax: +55 (21) 3527-1195.

Abstract

The work in hand presents the results of an experimental investigation on the thermo-mechanical properties of a textile refractory composite reinforced with polymer coated basalt fibers under tensile loading. The composites were produced as a laminate material using basalt bi-directional fabric layers as reinforcement. A high alumina cement matrix was used in the matrix composition which was designed using the compressible packing method. A series of uniaxial tensile tests was performed under temperatures ranging from 25 to 1000°C. The cracking mechanisms were discussed and compared to that obtained at room temperature. Thermogravimetry and X-ray diffraction analysis were used to study the deterioration/phase changes as a function of the studied temperatures. Scanning electron microscopy (SEM) was used to study the damage processes in the fiber–matrix interfaces after exposure to high temperatures. The obtained results indicated that the presence and the type of coating can become a deterministic factor in the tensile response of the composite submitted to elevated temperatures. A sudden drop in the serviceability limit state of the composite was observed above 400°C, caused by the degradation of the polymer used as a fiber surface coating, the degradation of the basalt fiber and by the dehydration process of the refractory matrix.

Keyword: thermomechanical properties, textile reinforced refractory concrete, basalt fiber, high temperatures.

1. Introduction

Textile reinforced concretes (TRC) are a new generation of cementitious materials with enhanced tensile strength and ductility [1, 2]. With its excellent mechanical properties, the TRC's are used, currently, in a wide range of applications that include: strengthening and repair in structural elements, protective linings, thin-walled elements, facade elements, bridges and also freeform and lightweight structures. In the last two decades significant improvements in the development of TRC have been achieved resulting in high performance composites that can present uniaxial tensile strength up to 50 MPa and tensile strain up to 5% [3, 4]. It is important to consider, however, that in many of these applications the concrete and the textile undergo thermal effects, becoming the study of thermo-mechanical performance of TRC absolutely indispensable [5, 6, 7].

Although there is a growing interest in the use of TRC elements, little is known about their thermo-mechanical performance and even less about applications using refractory concrete as a matrix. Conventional fiber refractory concrete present increased ductility and toughness compared to the plain refractory matrix [8, 9]. In most cases, the use of a fiber reinforcement in refractory concretes is related to the control of cracking during the heating or drying process (bridging the crack and limiting the crack propagation) [8, 10] and as an attempt to reduce the fragmentation process of the concrete when subjected to high temperatures (spalling) [10, 11, 12].

It is known that aluminous cement has alkali content typically less than 0.5% of its weight [13]. Therefore, the risk of alkali attack, common to basalt, glass and natural fibers, decreases substantially in refractory concretes. Taking advantage of these

properties, several researches used aluminous cements in the past to produce fiber reinforced composites (specially using glass fibers) [14].

Basalt it is a low cost material that brings interesting opportunities to the construction industry. Recent researches developed by Larrinaga *et al.*, [15] contributed to explain the mechanical behavior of basalt fabric as a reinforcement in a TRM (textile reinforced mortar). Several basalt layers were used as reinforcement in a non-commercial cement-based mortar containing a redispersable resin to achieve fire-proof properties. The tensile strength showed to be strongly affected by the reinforcement ratio. There were visible differences in the cracking spacing as well as in the crack width and the strain capacity surpassed 2% for the most of the studied TRM specimens. Sim, Park and Moon [16] investigated the applicability of the basalt fiber as a strengthening material for structural concrete members through durability, mechanical, thermo-mechanical and structural tests. The results obtained indicated that, compared to FRP (fiber reinforced polymer) strengthening systems, the basalt fiber strengthening may be a good alternative when characteristics such as moderate structural strengthening and high resistance for fire are simultaneously sought (such as for building structures). When tested under high-temperature (over 600°C) and compared to carbon and S-glass fibers, only the basalt maintained its volumetric integrity and 90% of the strength.

Some types of polymer can benefit from the heating/cooling process until certain temperatures. Recent researches developed by Silva *et al.*, [6] using TRC reinforced with carbon fibers showed that when heating polymer coated carbon fibers TRC under temperatures up to 150°C a polymer interlocking mechanism between filaments and matrix is observed. This mechanism results in significant increases in the maximum pullout load. Krüger and Reinhardt [5] performed fire tests on four different I-shaped

mortar beams reinforced with AR-glass and carbon textiles. The investigation was focused on the load bearing capacity of the composite during a fire test under constant load. In one of the cases a SBR thermoplastic resin was used as coating in the carbon fabric. The results showed to be very dependent on the fire behavior of the used fibers. Due to the softening of the SBR coating (at about 90°C) the fiber-matrix interface was rapidly impaired, resulting in fiber pullout and, subsequent, failure.

The aim of this article is to investigate the effect of elevated temperatures on the mechanical properties of a textile refractory composite reinforced with basalt fabric submitted to tensile loading. At first, the refractory composites were produced with a cementitious matrix, made of calcium aluminate aggregates and calcium aluminate cement (CAC), reinforced with basalt fabrics. The composites were tested under tensile load after being submitted to different temperatures regime ranging from 25 to 1000°C. The studied temperature range has a particular interest due to the decomposition of the fiber coating and the microstructural transformations that occur in the hardened paste as a result of the dehydration process. The influence of the number of textile layers on the tensile behavior of TRC was also addressed. The influence of the exposure time on the tensile behavior of basalt TRC was investigated for the temperature of 200°C. The crack formation was investigated using a high resolution imaging procedure. Crack spacing was measured using image analysis and correlated with the applied strain under tensile loading. Tensile tests on basalt fabric specimens were carried out at room temperature and at 400°C. The identification of the dehydration reactions caused by the heating regime was addressed using thermo-gravimetric analysis (TGA) and X-ray diffraction (XRD). The present study adds an important knowledge to the existing literature on the thermo-mechanical behavior of textile reinforced concrete.

2. Materials and Processing

2.1 Refractory Concrete Matrix

The matrix used in this research (compressive strength of about 45MPa) was designed following the compressible packing model (CPM) routine [17, 18] and then adapted to the rheology necessary to produce laminated TRC's. As a result of the small diameter of the continuous filaments and the small distance between the reinforcement textile layers, the maximum aggregate diameter had to be less than 1.18 mm. The materials used in the TRC composition were a calcium aluminate cement (Secar 51) with alumina content of about 50%, a synthetic calcium aluminate aggregate (with an alumina content of about 40%) with diameter ranging from 0.001mm to 1.18mm and a polycarboxilate superplasticizer in powder. The water/cementitious material ratio of the refractory concrete was 0.35. Table 1 gives the composition of the concrete matrix.

Table 1 – Mix composition.

Composition	
Dense aggregate (kg/m ³)	1416.2
Cement (kg/m ³)	750
Superplasticizer (kg/m ³)	4.87
Viscosity modifier agent - VMA (kg/m ³)	0.562
Water (kg/m ³)	262.6
Superplasticizer content (%)	0.65
Water/cementitious material ratio	0.35

2.2 The basalt fabric

A basalt textile commercialized by the Chinese company Zhejiang GBF Basalt Fiber Co. Ltd. was used as reinforcement for the TRC specimens. The basalt textile was produced with a styrene-acrylic latex coating (43g/m²). The warp as well as the weft is formed by about 800 monofilaments with average diameter of 13 μ m. Table 2 presents the properties of coated basalt textile.

Table 2 – Properties of the basalt fabric.

Density (g/cm ³)	2.70
Melting point (°C)	1350
Warp wire spacing (mm)	5
Type of coating	styrene-acrylic latex
Coating content (g/m ²)	43
Specific surface weight (g/m ²)	250

2.3 Matrix processing and composite manufacturing

The refractory concretes were produced in a room with controlled temperature of 24°C ± 1°C using a planetary mixer (previously moistured) of 5 liters capacity. The cementitious materials were homogenized by dry mixing for 60s prior to the addition of water. The mixture was blended for 5 minutes. The viscosity modifier agent type Rheomac UW 410 (VMA) was added after 4 minutes of mixing.

Rectangular plates measuring 400 mm x 250 mm x 13 mm (length x width x thickness) were produced for direct tensile tests using a lamination technique. For the production of the plates, the concrete mixtures were placed in the acrylic molds. The process started with a thin concrete layer placed on the bottom of the surface mold. The second phase consisted on positioning the first mesh of basalt textile reinforcement over the fresh concrete (Figure 1). The basalt fabric was then pressed and smoothed in order to regularize and align the surface of the layer. After the second phase, the procedure was repeated until reaching the desired number of fabric layers. In this study 1, 3 and 5 fabric layers were used as reinforcement in the TRC's, however, samples without fabric layers were also produced. A manual vibration was applied to the samples. After 7 days, the rectangular plates were cut, resulting in 4 specimens of 400 mm x 60 mm x 13 mm (length x width x thickness). In this study, refractory composites were produced without reinforcement and with 1, 3 and 5 layers of basalt fabric (equally spaced), resulting in

fiber volume fractions of 0%, 0.59%, 1.79% and 2.98%. The tensile stress of TRC was calculated dividing the load values by the cross-sectional area of the samples. The determination of the cross-sectional area was performed by the average of four measurements (width and thickness) at four different points of each sample.

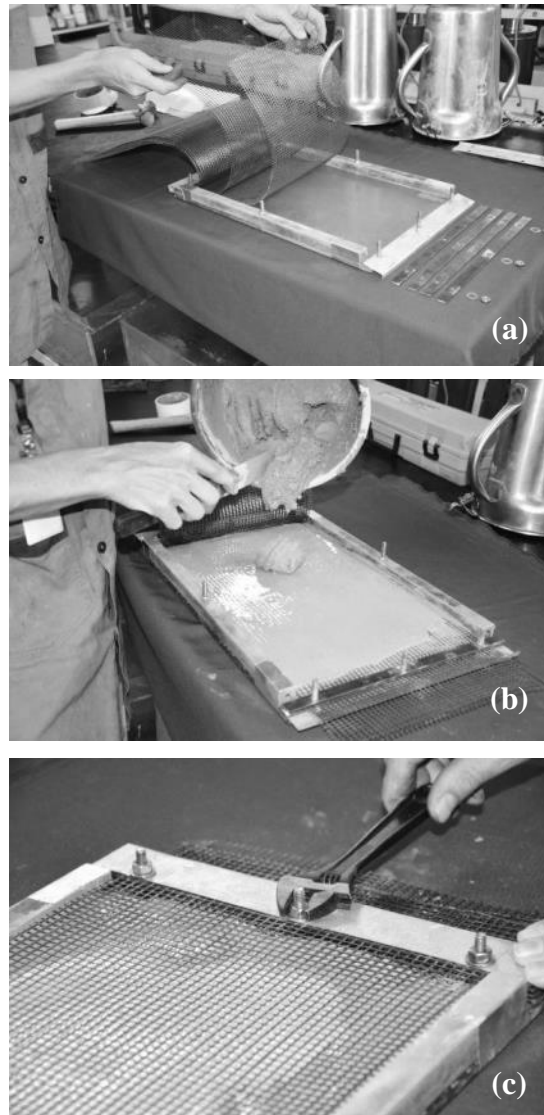


Figure 1 – Production methodology used for fabricating the TRC reinforced with basalt fabrics.

3.0 The heating regime

The TRC specimens were heated up to 75, 150, 200, 300, 400, 600 and 1000°C and subsequently cooled by a natural process inside the furnace. Experiments on specimens

stored at room temperature were also carried out. In order to better understand the mechanical behavior of TRC under elevated temperatures, additional tensile tests using different exposure times (at the target temperature de 200°C) were performed. The thermo-mechanical behavior of basalt fabric was also investigated, but using only specimens stored at room temperature and heated at 400°C. The heating regime applied to the saturated specimens at an age of 7 days is presented in the Figure 2. An electric oven with radiant heating (metal alloy type Kanthal "A1" in alumina tubes) internally protected by perforated ceramic plates was used. All samples were subject to a heating rate of 10°C/min in the furnace. The temperature level was kept constant for 60 min in each target temperature. The furnace was cooled down before the specimens were removed in order to prevent thermal shock. The rate of cooling was not controlled.

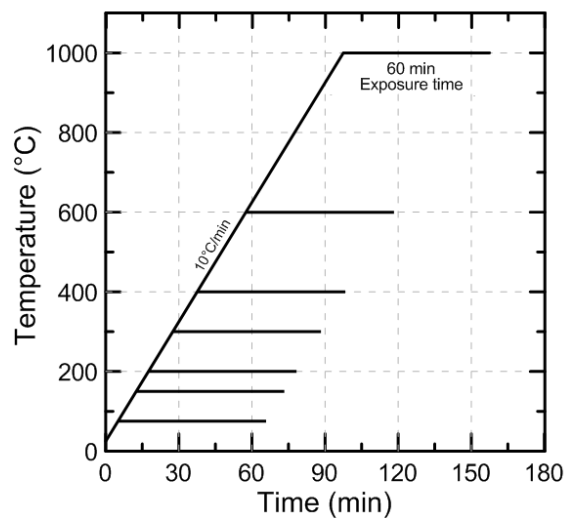


Figure 2 — Heating regime applied to the refractory concrete.

4.0 Mechanical Testing

The direct tensile tests on the TRC plates and on the fabric samples were performed in a Shimadzu universal testing machine model AGX – 100 kN and controlled by the actuator displacement at a rate of 0.4 mm/min. For the composites, the force was

transferred to the specimens via rotatable steel plates screwed to the TRC plates. Four rectangular shaped specimens measuring 400mm x 60mm x 13mm (length x width x thickness) were tested using a gage length of 200mm with fixed–hinged boundary conditions. Deformation of TRC's was measured using two LVDT's. Fabric specimens measuring 360mm x 50mm (length x width) were tested using a gage length of 200mm (same used in the TRC). A clip-gage was used to measure the strain of the fabrics. Fifteen textile specimens were evaluated in the warp direction for each studied condition. The tensile load and actuator displacement were recorded for both direct tensile tests. During the direct tensile tests a Nikon D90 digital camera with an AF Micro Nikkor 60 mm lens (f/2.8D) and frame grabber captured images of 4288 x 2848 pixels in resolution at 30s intervals. The images were used to measure the crack spacing which was correlated to the strain.

5.0 Materials characterization

Before and after the heating process, the fiber–matrix interfaces were investigated using a scanning electron microscope (SEM) FEI Quanta 400. The TRC samples were sectioned in specimens with dimensions of 20 x 20 mm (length x width). The samples were coated with 20nm of gold to become conductive and suitable for conventional SEM analysis. The SEM was operated using 25 kV of acceleration tension and about 30 mm of working distance. The TGA analyses were carried out using fragments of the samples tested under tensile loading. After tested, the extracted samples, were placed in plastic bags to avoid contact with moisture. Samples of about 10 mg were collected and analyzed. The thermal analyses were performed in a TA Instruments, SDT Q600 model TGA/DTA/DSC simultaneous apparatus with temperatures between 35 and 1000°C

using 100 mL/min of nitrogen flow. In order to eliminate the residual non combined free water, an isothermal step at 35°C for 1 hour was carried out before the analyses. The material of reference and sample pans was platinum. Refractory concretes were analyzed by X-ray diffraction (XRD) from a 2θ value of 5 to 50° with a Shimadzu XRD 6000 instrument using a step of 0.05° and C_{uk} radiation. In order to enable a qualitative analysis, the sample preparation used matrix material with particle sizes of less than 75 μm . The analyzes were performed at room temperature and at temperatures of 200°C, 400°C (target temperatures close to the key temperatures in the dehydration process of the used refractory concrete) and 1000°C.

6. Discussion and analyses

6.1. Influence of the number of layers on the TRC tensile behavior (at room temperature)

Figure 3 (a) shows representative stress–strain curves obtained from the tensile tests (at room temperature) performed with the plain matrix and with TRC reinforced with 1, 3 and 5 bi-directional basalt fabric layers. The typical cracking patterns are shown in Figures 5 (b), (c), (d) and (e). The results obtained from the specimens tested at 7 days of age are given in the Table 3. The bend-over point (BOP) of each curve corresponds to the end of the linear elastic region and to the formation of a first matrix crack crossing the entire cross-section. Only one crack was formed in the unreinforced specimens and also in the specimens reinforced with only one fabric layer. In the case of the TRC reinforced with only one fabric layer the stages II and III, typically seen in TRC's, are absent (see Figure 3 (a)). The TRC's produced with 3 and 5 fabric layers showed a strain hardening behavior. For these two composites, the stress-strain curves

were depicted in 3 distinct stages using roman numerals, with one stage prior and two stages after the bend-over point (BOP). The stage I corresponds to the elastic-linear range where both matrix and fiber behave linearly. The post BOP stage is characterized by the formation of distributed cracking (stage II). After the initiation of cracks in the matrix, the load-carrying capacity of TRC does not reduce since the cracks are bridged by the fabrics. Immediately after the initiation of the first matrix crack, other matrix cracks also propagate throughout the specimen at approximately regular intervals (related to the fabric geometry and the fiber-matrix interface). In this phase, as the applied strain increases, more cracks form culminating in a multiple cracking pattern along the sample. The stage III, is characterized by a crack-widening phase, leading to a stretching of the fabric and, posterior, failure of the composite. As expected the average stress levels achieved at the bend-over point (σ_{BOP}) by the matrix and by the TRC's reinforced with 1, 3 and 5 fabric layers were very close. At this point, the contribution of the textile reinforcement to the stiffness is negligible. With relation to the multiple cracking stage (II), the average $\varepsilon_{t, II}$ value for the TRC produced with 3 fabric layers was 66% higher than that for the TRC with 5 fabric layers. In this case, increasing the reinforcement ratio leads to an increase in the stiffness of the second branch ($E_{t, II}$) and a decrease in the cracking distance, thus, maximizing the mechanical performance of the composite. With respect to the ultimate tensile strength (σ_{UTS}), the use of 3 and 5 layers of basalt fabric provided great improvements, representing increases of, respectively, 1.2 and 2.6 times in comparison to the unreinforced matrix. Table 3 provides the corresponding values. The maximum strain capacity ($\varepsilon_{t, III}$) was observed for the TRC reinforced with 5 fabric layers, culminating at 1.58%.

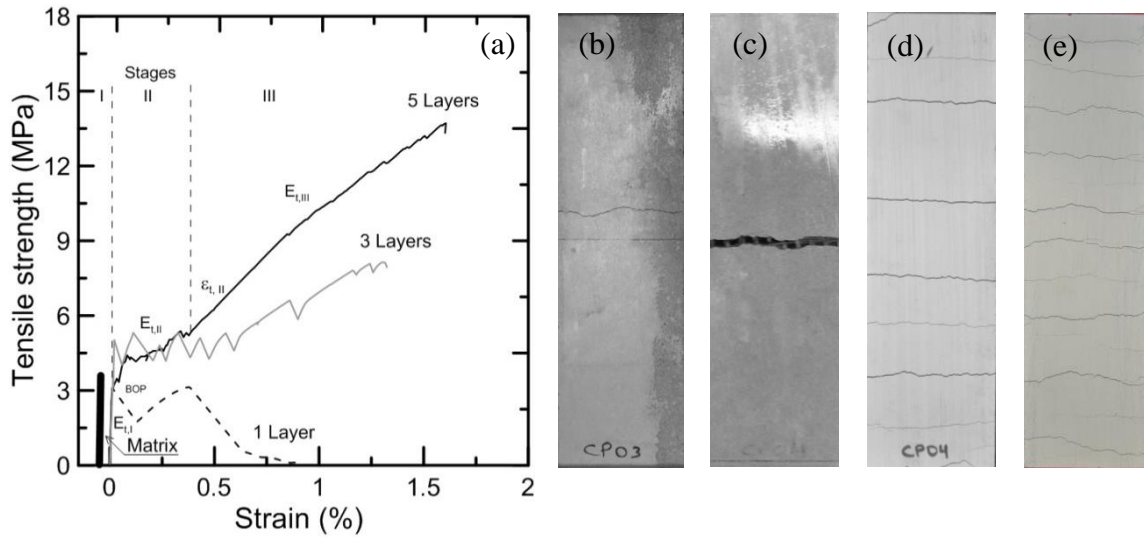


Figure 3 – Effect of basalt fabric reinforcement on the tensile behavior of TRC: (a) stress-strain relation and cracking formation for samples (b) without reinforcement (c) with one fabric layer, (d) with three fabric layers and (e) with five fabric layers.

Table 3 – Influence of the number of reinforcement layers on the tensile properties of TRC. Average values are given and the standard deviation values are presented in parentheses.

Reinforcement	First crack values				Post crack values					
	P _{BOP} (kN)	σ _{BOP} (MPa)	ε _{BOP,I} (%)	E _{t,I} (GPa)	P _{UTS} (kN)	σ _{UTS} (MPa)	E _{t,II} (GPa)	E _{t,III} (GPa)	ε _{t,II} (%)	ε _{UTS,III} (%)
Without reinforcement	2.84 (0.04)	3.74 (0.20)	0.011 (0.0027)	32.40 (1.94)	-	-	-	-	-	-
1 Layer	2.59 (0.56)	3.58 (0.86)	0.016 (0.0034)	28.29 (3.32)	-	-	-	-	-	-
3 Layers	3.29 (0.34)	4.09 (0.44)	0.019 (0.0061)	24.65 (2.09)	6.79 (0.33)	8.44 (0.44)	0.096 (0.05)	0.43 (0.02)	0.70 (0.12)	1.36 (0.17)
5 Layers	2.85 (0.65)	3.45 (0.78)	0.011 (0.0006)	34.64 (2.55)	11.13 (0.38)	13.49 (0.39)	0.45 (0.13)	0.67 (0.01)	0.42 (0.05)	1.58 (0.11)

6.2. Influence of elevated temperatures on the TRC tensile behavior

The produced TRC showed to be strongly affected by thermal processing when submitted to a tensile loading. Likewise, the mechanical properties of the basalt yarn as well as the basalt fabric were influenced. Figure 4 presents one representative curve obtained for the TRC tested under direct tensile loading after being submitted to the different heating regimes investigated in the present work. The results of evaluation of all curves are given in Table 4. A strain-hardening behavior was observed for the TRC's

in the majority of the target temperatures, excluding only 600°C and 1000°C which presented, respectively, strain-softening and brittle behavior. The positive influence of preheating the specimens up to 75°C and 150°C on the mechanical performance of TRC was clearly noticeable along the entire course of the stress–strain curves, but mainly with relation to the tensile strength at the BOP and, specially, to the multiple cracking pattern (Figure 4 b, c, d). This behavior was more pronounced for the temperature of 150°C where the TRC showed σ_{BOP} about 92% greater than the TRC tested at room temperature.

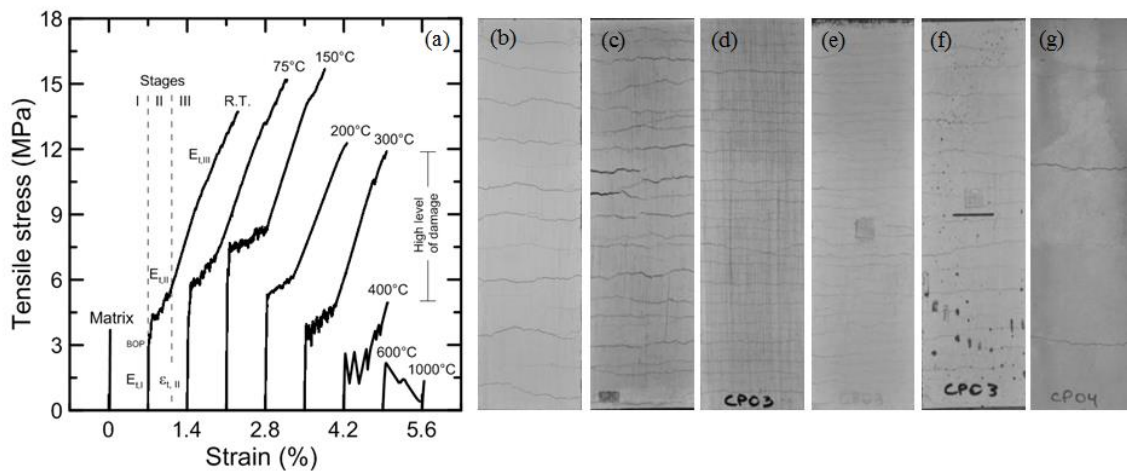


Figure 4 – (a) Influence of temperature on the tensile behavior of basalt TRC's. Cracking patterns obtained during the stage III of the tensile tests for specimens tested at (b) room temperature and after the following heating processes (c) 75°C, (d) 150°C, (e) 200°C, (f) 300°C and (g) 400°C.

Table 4 — Average results of the direct tensile test performed on the basalt TRC.
Standard deviation values are presented in parentheses.

Heating rate	Target temperature	First crack values				Post crack values					
		P _{BOP} (kN)	σ _{BOP} (MPa)	ε _{BOP,I} (%)	E _I (GPa)	P _{UTS} (kN)	σ _{UTS} (MPa)	E _{t,II} (GPa)	E _{t,III} (GPa)	ε _{t,II} (%)	ε _{UTS,III} (%)
-	25°C *	2.85 (0.65)	3.45 (0.78)	0.011 (0.0006)	34.64 (2.55)	11.13 (0.38)	13.49 (0.39)	0.45 (0.13)	0.67 (0.01)	0.42 (0.05)	1.58 (0.11)
10°C/min T.P.: 1h	75°C	3.73 (0.45)	4.85 (0.58)	0.021 (0.0005)	28.57 (5.79)	11.48 (0.48)	14.94 (0.55)	0.31 (0.08)	0.79 (0.11)	0.71 (0.20)	1.66 (0.08)
10°C/min T.P.: 1h	150°C	5.10 (0.13)	6.65 (0.22)	0.024 (0.0024)	31.63 (0.67)	11.74 (0.58)	15.30 (0.58)	0.12 (0.10)	0.73 (0.03)	0.62 (0.14)	1.64 (0.11)
10°C/min T.P.: 1h	200°C	4.19 (0.74)	5.09 (0.92)	0.036 (0.0634)	23.82 (5.37)	10.22 (0.97)	12.40 (1.18)	0.15 (0.06)	0.64 (0.03)	0.39 (0.09)	1.50 (0.21)
10°C/min T.P.: 1h	300°C	3.47 (0.33)	4.31 (0.44)	0.033 (0.0048)	20.52 (1.68)	9.64 (0.56)	11.97 (0.65)	0.19 (0.05)	0.75 (0.06)	0.50 (0.10)	1.59 (0.07)
10°C/min T.P.: 1h	400°C	1.87 (0.13)	2.42 (0.17)	0.025 (0.0025)	10.93 (1.83)	3.79 (0.41)	4.98 (0.55)	0.36 (0.19)	0.90 (0.33)	0.47 (0.05)	0.68 (0.11)
10°C/min T.P.: 1h	600°C	1.56 (0.10)	1.98 (0.16)	0.044 (0.0032)	5.37 (1.41)	-	-	-	-	-	-
10°C/min T.P.: 1h	1000°C	1.10 (0.30)	1.33 (0.36)	0.037 (0.0274)	3.96 (0.39)	-	-	-	-	-	-

T.P.: Time period in which the specimens were kept at the target temperature.

*Room temperature.

With relation to the ultimate tensile strength (σ_{UTS}), the contribution of the preheating process up to 75°C and 150°C was not so significant, generating increases of, respectively, 10.7% and 13.4%. As can be seen in Figure 5, at the temperatures of 75°C and 150°C the main process induced in the matrix by the thermal regime is the evaporation of free water, lost of structural water of the AH_x gel and the dehydration of metastable CAH₁₀ (CaO.Al₂O₃.10H₂O). The XRD data (see Figure 6) obtained from the TRC samples at room temperature and heated at 200°C confirmed this process. As reported by Lea's [13], at ambient temperatures the presence of metastable hydrates may persist for years. However, there is an inevitable thermodynamic force for "conversion" to the stable hydrates (such as AH₃ (Al₂O₃.3H₂O) and C₃AH₆ (3CaO.Al₂O₃.6H₂O)). For temperatures greater than 150°C, the stress level at the BOP and the ultimate tensile strength decreased gradually with increasing temperature. This decrease was accompanied by a significant reduction of the elastic modulus for 200°C. The TRC heated to 200°C showed a multiple cracking pattern, similar to the TRC heated to 150°C, however significant signs of strength deterioration were noticed for

this temperature and above. Studies using thermo-gravimetric analysis (see Figure 5) showed that the loss in strength at this range (150°C to 200°C), can be explained by the end of the dehydration of metastable CAH₁₀ and by the start of dehydration of the stables AH₃ and C₃AH₆ phases.

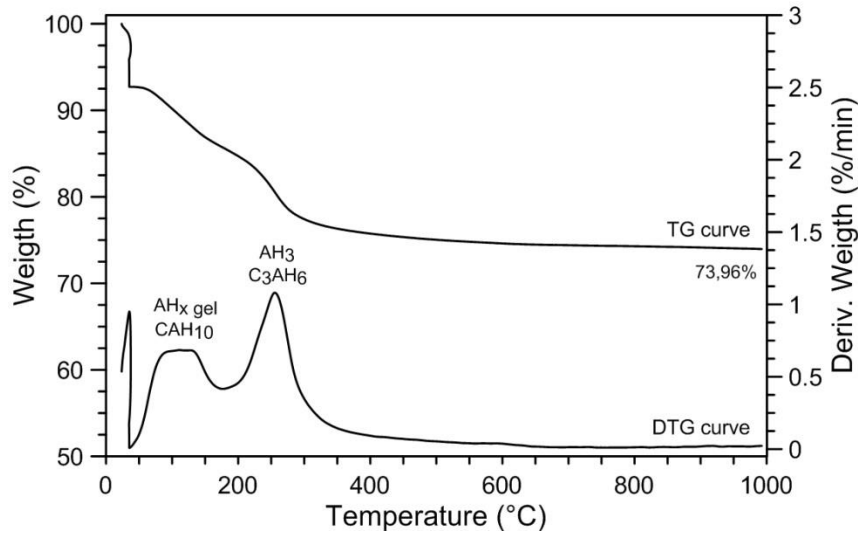


Figure 5 — Thermal analysis of the refractory concrete (7 days of age) on initial sample mass basis.

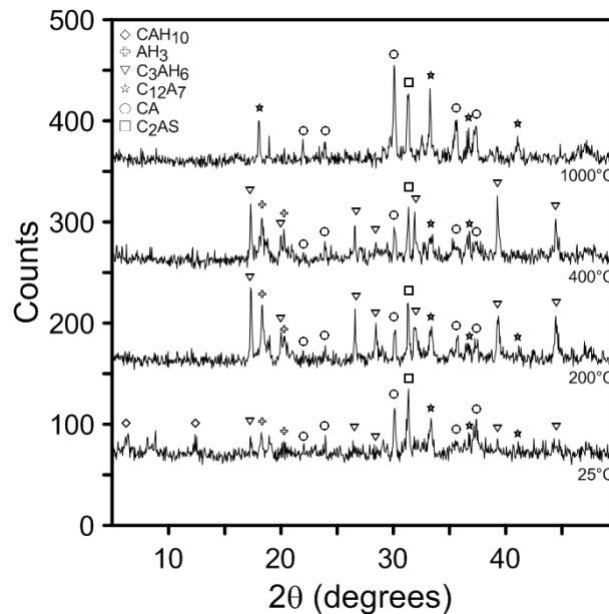


Figure 6 – XRD profiles for the refractory concrete at room temperature and preheated at 200, 400 and 1000°C.

The hydrate CAH₁₀ was not detected by XRD at 200°C and above (see Figure 6). For temperatures between 200°C and 300°C, remaining hydrates AH₃ and C₃AH₆ are almost

completely dehydrated causing more losses in the elastic modulus and in the tensile strength. However, it is still possible to observe the presence of hydrates AH_3 and C_3AH_6 even in the results at $400^\circ C$ obtained by XRD. Between the temperatures of $300^\circ C$ and $400^\circ C$ severe strength loss was observed. In comparison with the TRC heated at $300^\circ C$ the decrease in the ultimate tensile strength (σ_{UTS}) for TRC heated at $400^\circ C$ was 58%. With relation to the tensile strength at the BOP, the reduction was about 43%. For temperatures greater than $400^\circ C$ the specimens failed abruptly and large cracks occurred. At these temperatures, both the refractory matrix and basalt fabric showed significant signs of deterioration causing pronounced brittle behavior beyond the peak stress. The results presented in Figure 7 show that the tensile strength of basalt fibers, as well as similar fibers (S-Glass fibers and E-Glass fibers) [5], decrease rapidly at temperatures greater than $400^\circ C$.

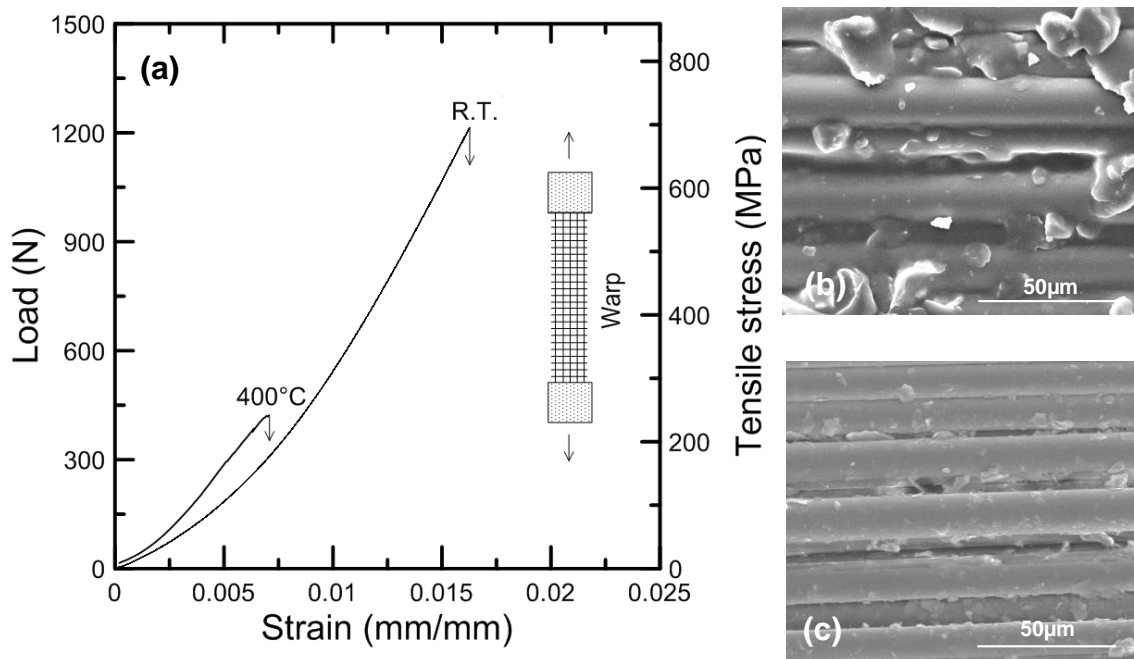


Figure 7 – Temperature effect on the (a) tensile behavior of the basalt fabric and SEM micrographs of the basalt yarn (b) in its natural condition and (c) after exposure to $400^\circ C$.

As a consequence, the thermo-mechanical behavior of the TRC was largely affected for this temperature and above. As reported previously, the TRC heated at 600°C showed a strain softening behavior. At this temperature, the minor crack-bridging action of the fibers could be neglected if compared to the results at the lower target temperatures. The composite heated at 1000°C, however, showed a fragile type of failure. This brittle behavior is attributed, in part, to the melting (see Figure 8) of the basalt filaments that occurred for lower temperatures than those defined by the manufacturer (Table 2). The average tensile strength for the composite heated at 1000°C at the first crack was 1.33MPa, 38.5% of the σ_{BOP} at room temperature. There was no visible concrete spalling for any one of the used temperatures (75, 150, 200, 300, 400, 600 and 1000°C). This can be attributed to the small thickness of the samples and to the presence of the textile reinforcement.

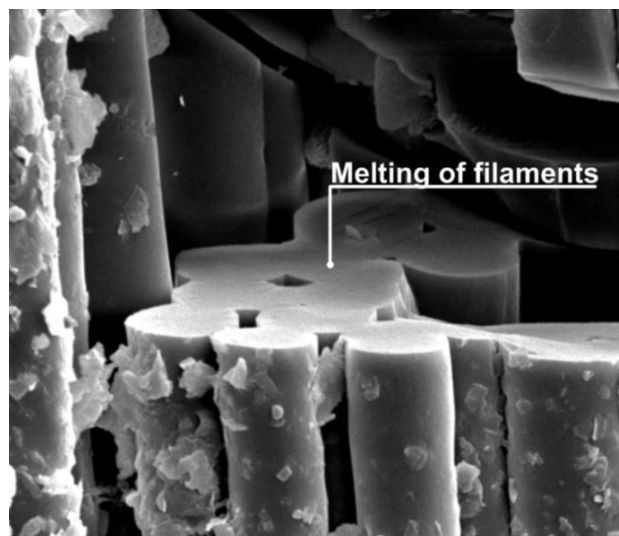


Figure 8 – Fractured basalt yarn after being exposed to 1000°C.

A micro-structural investigation using the SEM was carried out to confirm the damage process on the TRC previously discussed. Figure 9 shows SEM micrographs of the bi-directional TRC's in its natural condition and after exposure to the studied temperatures.

Likewise, Figure 10 shows the fiber–matrix interface micrographs of the basalt yarns at the same conditions.

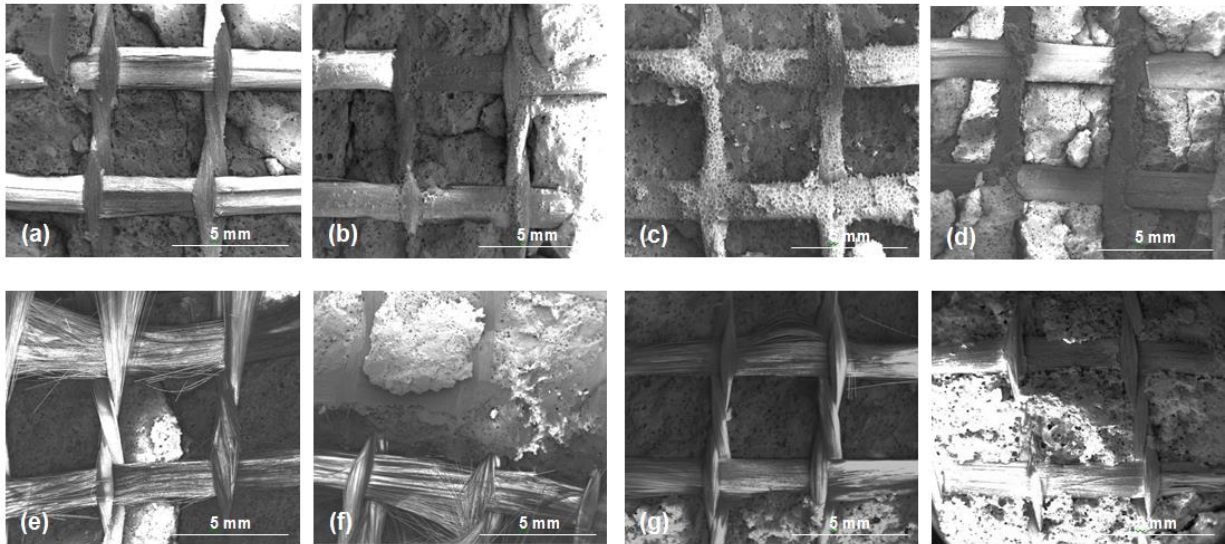


Figure 9 – Scanning electron microscope (SEM) images of basalt TRC (a) in its natural condition and after exposure to temperatures of (b) 75°C, (c) 150°C, (d) 200°C, (e) 300°C, (f) 400°C e (g) 600°C and (h) 1000°C.

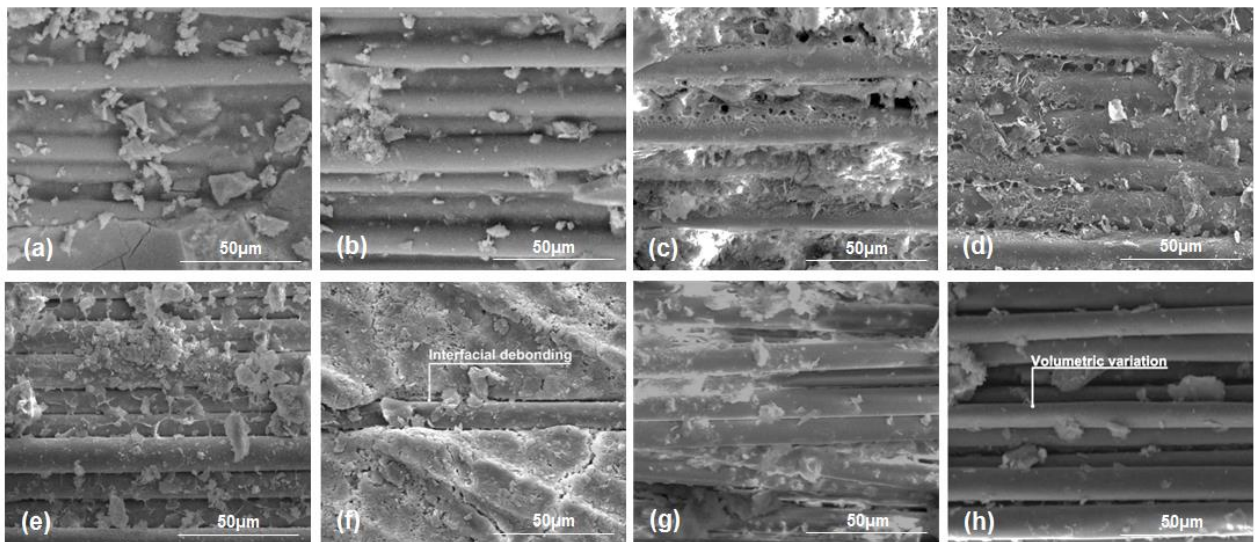


Figure 10 – Basalt TRC fiber-matrix interface: (a) in its natural condition and after exposure to temperatures of (b) 75°C, (c) 150°C, (d) 200°C, (e) 300°C, (f) 400°C, (g) 600°C and (h) 1000°C.

It can be seen that for 75°C the styrene-acrylic latex coating starts to transform from visco-elastic to plastic, thus, impregnating more strongly the matrix and the internal filaments. At this temperature, a pronounced merging of polymer towards the matrix occurs (see Figure 11). Between 75°C and 150°C, as the temperature is not able to decompose the polymer, after cooling, the styrene-acrylic latex becomes stiffer and visco-elastic again. The newly generated polymer interlocks change the interface mechanisms of the TRC, increasing the bond between the fibers and matrix. As reported in previous researches [19, 6], the penetration of coating in the yarn, in this case due to the heating regime, makes pronounced changes in the composite behavior. This occurs because the filaments are stressed more equally, taking part in the load support and, consequently, increasing the tensile stress. Furthermore, the irreversible shrinkage of the hardened paste (between 25°C and ~200°C) [8, 20], that remains after the cooling process of the material, can lead to an improve in the bond between the fibers and the matrix. This microstructure evolution occurs due to the evaporation mechanism of free water and the dehydration of calcium aluminate hydrates and is accompanied by micro-cracking in the paste. The first signs of degradation of the polymer started to appear at 200°C. From Figure 10 (d) (TRC preheated at 200°C) it can be seen that the coating between the fibers is porous and presents less interlocks than the coating at the room temperature and in the temperatures of 75°C (Figure 10 (b)) and 150°C (Figure 10 (c)). At 200°C the polymer take the form of thin-films or scales deposited over the filaments. As a result of the less amount of coating between the fibers and in the fiber–matrix interfaces, significant strength losses were observed. This means that even though the fiber content remains constant, the presence of coating can become a deterministic factor in the tensile response of the composite. Increasing the temperature to 300°C, it is

possible to verify that the polymer is still present, however, the thin layers of polymer almost disappear (see Figure 10 (e)). Figure 10 (f) shows that the coating surrounding the fibers was entirely lost at 400°C. As a consequence, the tensile behavior of the TRC change leading to a reduced crack-widening phase (stage III) and a sudden drop in the serviceability limit state of the composite. Similar interface degradation process was observed at the same temperature in previous investigations reported by Silva *et al.*, [6] in TRC's produced with polymer coated carbon fabrics. Figure 10 (h) shows the fiber–matrix interface micrographs highlighting the volumetric variation caused by the temperature of 1000°C.

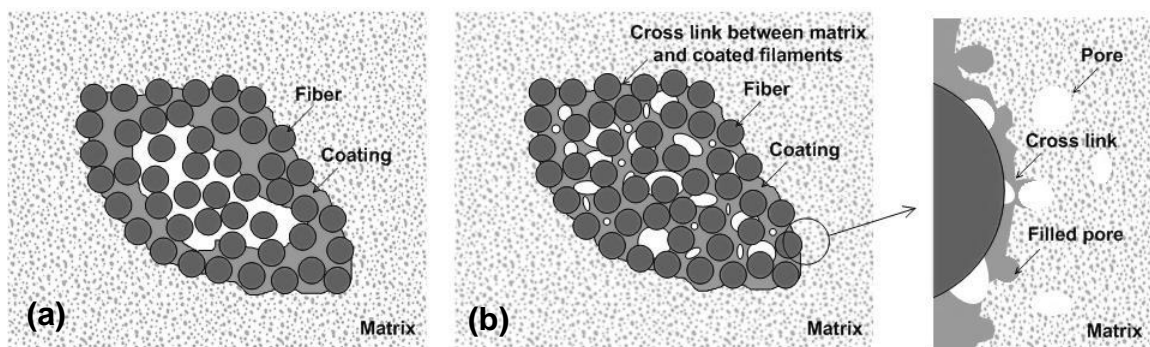


Figure 11 – Bonding mechanisms in a multifilament polymer coated basalt yarn (a) at room temperature and (b) after heating at temperatures below 200°C.

6.2. Influence of elevated temperatures on the crack spacing response

The crack spacing measurements for TRC heated up to 150°C and beyond 150°C are shown, respectively, in the Figure 12 (a) and Figure 12 (b). The crack spacing as a function of applied strain was adjusted using an exponential decay function. Through the curves presented in the Figure 12 (a) it is possible to see that the preheating up to 150°C induced a general reduction in the crack spacing during loading until a steady state condition was reached (strain: ~ 0.7%). This behavior was more pronounced for the TRC tested at 150°C. Figure 12 (a) and (b) shows that, after the first crack, as the

applied strain increases, more cracks form and the spacing decreases in an exponential manner. Up to 150°C, the stiffness of the fibers remained constant causing no effect on the cracking spacing. On the other hand, the improvement in the fiber-matrix interface and the shrinkage of the hardened paste resulted in increases in the number of cracks. For the temperatures of 200, 300 and 400°C an opposite behavior could be observed (see Figure 12 (b)). Beyond 150°C it is possible to note a significant increase in the crack spacing values originated from the gradual degradation of the coating and the dehydration of the main hydrates presents in the concrete matrix. Furthermore, the rate of reduction of crack spacing was also affected, being smaller to the temperatures above 150°C (see Figure 12 (b)). It's important to remember that the decrease in the number of cracks is, in part, due to the deterioration of the basalt fibers when submitted to elevated temperatures, which will be covered with greater depth in future researches. Since only one crack was formed in the TRC tested at 600°C and 1000°C, no crack spacing curves were obtained for these composites.

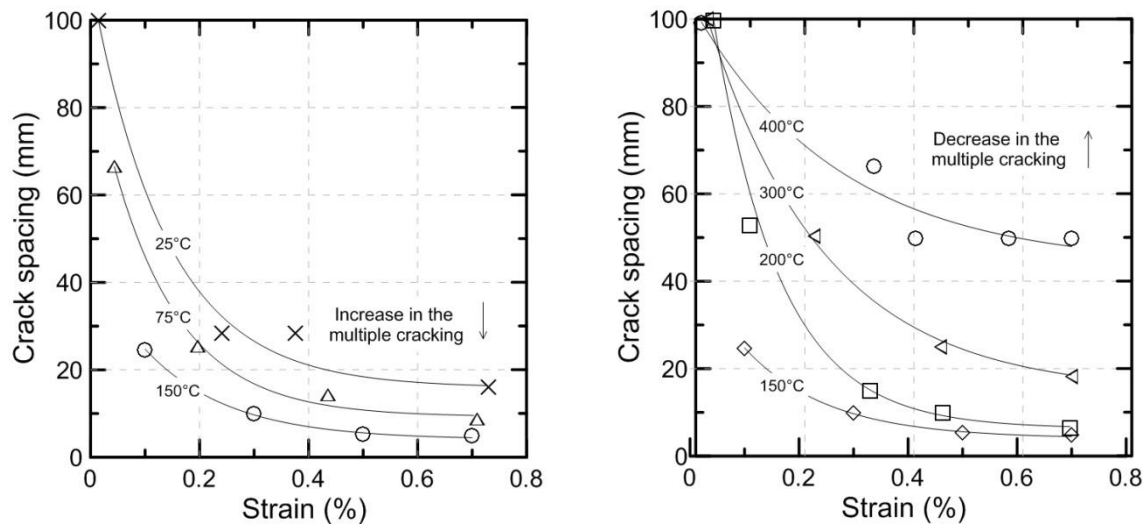


Figure 12 – Temperature effect on the crack spacing of TRC's tested (a) up to 150°C and (b) above 150°C.

6.3. Influence of exposure time (at 200°C)

Figure 13 compares tensile responses of the TRC varying the exposure time inside the furnace after the temperature of 200°C. The results of evaluation of all curves are given in Table 5. The curves (Figure 13 (a)) show that the increase in the exposure time to three and six hours practically had no effect on the tensile behavior of the TRC. The decreases observed at the ultimate tensile strength caused by the increase in the residence time from one to three and six hours was about 7%. As reported previously, the temperature of 200°C (using a residence time of 1 hour) causes partial decomposition of the coating present in the basalt yarns. However, the increase in the residence time at this temperature did not significantly aggravate this process. Since the target temperature of 200°C is intermediate with relation to the main dehydration peaks of the concrete (see Figure 5), the refractory matrix did not suffer weakening originated from the increase in the exposure time.

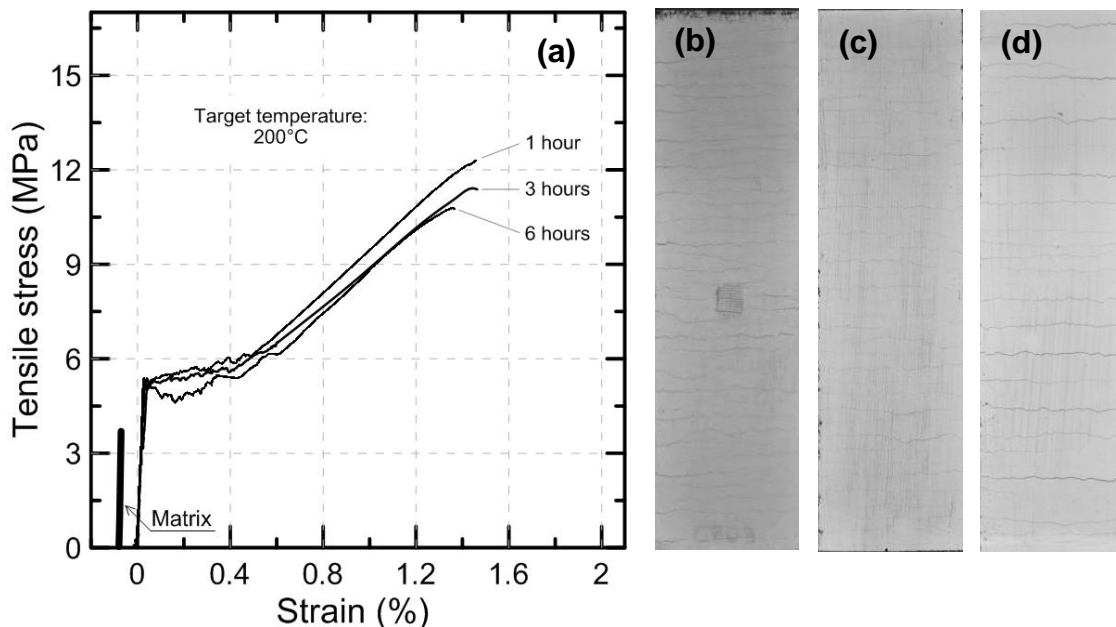


Figure 13 – Effects of exposure time on the (a) tensile behavior of TRC's heated up to 200°C and its cracking pattern after being exposed to a temperature of 200°C for (b) one hour (c) three hours and (d) six hours.

Table 5 — Influence of the exposure time on the tensile properties of TRC tested at 200°C. Standard deviation values are presented in parentheses.

Heating rate	Target temperature	First crack values				Post crack values					
		P _{BOP} (kN)	σ _{BOP} (MPa)	ε _{BOP, I} (%)	E _{t, I} (GPa)	P _{UTS} (kN)	σ _{UTS} (MPa)	E _{t, II} (GPa)	E _{t, III} (GPa)	ε _{t, II} (%)	ε _{UTS, III} (%)
10°C/min T.P.: 1h	200°C	4.19 (0.74)	5.09 (0.92)	0.036 (0.063)	23.82 (5.37)	10.22 (0.97)	12.40 (1.18)	0.15 (0.06)	0.64 (0.03)	0.39 (0.09)	1.50 (0.21)
10°C/min T.P.: 3h	200°C	4.16 (0.30)	5.03 (0.30)	0.037 (0.011)	15.23 (6.61)	9.51 (0.79)	11.46 (0.82)	0.17 (0.13)	0.61 (0.12)	0.45 (0.04)	1.49 (0.20)
10°C/min T.P.: 6h	200°C	4.51 (0.19)	5.61 (0.17)	0.030 (0.003)	21.62 (2.19)	9.19 (1.01)	11.44 (1.20)	0.17 (0.13)	0.65 (0.01)	0.50 (0.07)	1.40 (0.20)

T.P.: Time period in which the specimens were kept at the target temperature.

*Room temperature.

7. Conclusions

The following conclusions can be drawn from the present work:

- The behavior of the TRC is strongly influenced by the reinforcement ratio. The TRC's produced with 3 and 5 fabric layers showed an effective cracking control and, therefore, significant increases on the tensile response and on the overall ductility of the composite system.
- The heating-cooling regimes used in the present work showed to affect the tensile response of the TRC. Preheating up to 150°C had a significant impact on the maximum tensile response of the composite since, up to this temperature level, the matrix-polymer interlocking mechanism helps to create a high bond between filaments and matrix. Furthermore, the yarn strength is impacted by the penetration of coating which, after cooled, promotes a better load redistribution between the filaments.
- After preheating the composite above 150°C a clear drop in the tensile performance was observed, due to the coating's thermal decomposition (starting between 150°C and 200°C) and to the dehydration process of the matrix. After

the exposure to temperatures of 600°C and 1000°C the behavior of TRC's becomes brittle, presenting tensile strength smaller than at room temperature.

- Thermogravimetry and X-ray diffraction analysis allowed accompany the dehydration process of the main hydrated products formed in the used refractory concrete and correlate it with the tensile mechanical response. The major mass decreases occurred between 50 and 200°C and between 200 and 400°C arising, respectively, from the decomposition of the phase CAH_{10} and from both AH_3 and C_3AH_6 . Tensile strength losses agree well with the results obtained from the thermogravimetry and X-ray diffraction analysis.
- When submitted at 200°C (where partial coating's decomposition occurs) for different time periods (1, 3 and 6 hours), no significant differences were observed in the stress-strain relation of the TRC.

Acknowledgements

The authors gratefully acknowledge the Brazilian Agency CNPq for its partial financial support and Kerneos (France) for supplying the cement, superplasticizer and aggregate.

-
- [1] Mechtcherine V. Novel cement-based composites for the strengthening and repair of concrete structures. Review Article. *Construction and Building Materials* 2013;41:365-373.
- [2] C, Mobasher B. Geometrical and mechanical aspects of fabric bonding and pullout in cement composites. 2009; 42:765-777.
- [3] Peled A, Mobasher B. Pultruded fabric–cement composites. *ACI Materials Journal* 2005;102:15–23.
- [4] Verbruggen S, Aggelis DG, Tysmans T, Wastiels J. Bending of beams externally reinforced with TRC and CFRP monitored by DIC and AE. *Composite Structures* 2014;112:113–121.
- [5] Krüger M, Reinhardt HW. In: Wolfgang Brameshuber, editor. Chapter 6: Fire resistance. Report 36: Textile Reinforced Concrete - State-of-the-Art Report of RILEM Technical Committee 201-TRC, Bagnaux: Rilem publications S.A.R.L; 2006, p.83-218.
- [6] Silva FA, Butler M, Hempel S, Toledo RD, Mechtcherine V. Effects of elevated temperatures on the interface properties of carbon textile-reinforced concrete. *Cement & Concrete Composites* 2014;48:26–34.
- [7] Reinhardt HW. On the Biaxial Testing and Strength of Coated Fabrics. *Experimental Mechanics* 1976;16:71-74.

[8] Bazant ZP, Kaplan MF. Concrete at High Temperatures. Material Properties and Mathematical Models. Concrete Design and Construction Series, England: Longman Group; 1996.

[9] Cailleux E, Cutard T, Bernhart G. Pullout of steel fibres from a refractory castable: experiment and modeling. *Mechanics of Materials* 2005;37:427–445.

[10] Montgomery R. 4 - Heat-resisting and refractory concretes. *Advanced Concrete Technology Set*. In: John Newman, Ban Seng Choo and Ban Seng Choo, Butterworth-Heinemann editors. 1st ed. Oxford; 2003.

[11] Collignon B, Moyne C, Guichard JL, Perrot C, Jannot Y. Modelling the pressure dependence and the influence of added polymeric fibers on the permeability of refractory concretes. *Ceramics International* 2011;37:627–634.

[12] Salomão R, Pandolfelli VC. Dryout temperature–vapor pressure profile of polymeric fiber containing refractory castables. *Ceramics International* 2013;39:7217–7222.

[13] Lea's. *Chemistry of Cement and Concrete*. Chapter 13 - Calcium Aluminate Cements. 4th ed. In: Peter C. Hewlett, Butterworth-Heinemann editor. Oxford; 2003.

[14] *Fibre-Reinforced Cement Composites*. Technical Report 51.067. Concrete Society, London; 1973.

[15] Larrinaga P, Chastre C, Biscaia HC, San-José JT. Properties of glass concrete reinforced with short basalt fibre. *Materials and Design* 2014;55:66–74.

-
- [16] Sim J, Park C, Moon DY. Characteristics of basalt fiber as a strengthening material for concrete structures. *Composites: Part B* 2005;36:504-512.
- [17] De Larrard F. *Concrete mixture proportioning: a scientific approach*. London. E&FN SPON. 1999.
- [18] Sedran T. *Rhéologie et rhéométrie des bétons: application aux bétons autonivelants*. Doctoral dissertation. Ecole Nationale des Ponts et Chaussées 1999:484.
- [19] Köckritz U, Offermann P, Jesse F, Curbach M. Influence of textile manufacturing technology on load bearing behavior of textile reinforced concrete. In: *Proceedings of the 13th International Techtexile-Symposium 2005*.
- [20] Innocenti MDM, Cardoso FA, Akyiوشي MM, Pandolfelli VC. Drying Stages during heating of high-alumina. Ultra-low-cement refractory castables. *Journal of the American Ceramic Society* 2003;86:1146–8.

Artigo C – Rambo DAS, Silva FA, Toledo RD, Ukrainczyk N and Koenders E. Tensile strength of a calcium-aluminate cementitious composite reinforced with basalt textile in a high-temperature environment. Submitted to Cement and Concrete Composites (2015). Under review.

**Tensile strength of a calcium-aluminate cementitious composite reinforced with basalt
textile in a high-temperature environment**

Dimas Alan Strauss Rambo^a, Flávio de Andrade Silva^{b,*}, Romildo Dias Toledo Filho^c, Neven
Ukrainczyk^d and Eddie Koenders^d

^{a,c} Civil Engineering Department, COPPE, Universidade Federal do Rio de Janeiro, P.O. Box
68506, CEP 21941-972, Rio de Janeiro – RJ, Brazil.

^b Civil Engineering Department, Pontifícia Universidade Católica do Rio de Janeiro (PUC-Rio),
Rua Marques de São Vicente 225, 22451-900 - Rio de Janeiro - RJ, Brazil.

^d Institute of Construction and Building Materials, Faculty of Civil and Environmental
Engineering, TU Darmstadt, Franziska-Braun-Straße 3, 64287 Darmstadt, Germany.

July 2015

*Corresponding author: e-mail: fsilva@puc-rio.br, Tel: +55(21) 3527-1188. Fax: +55 (21) 3527-1195.

Abstract

The effect of elevated temperatures on basalt textile reinforced calcium aluminate cementitious composite is reported. After being exposed for 1 h at various constant temperature levels, samples were tested in hot as well as after cooling down at room temperature conditions (termed as residual tests). Targeted constant temperatures considered were from 25 up to 400°C, representing the range that affects the main dehydration of hydration products present in the matrix. The residual mechanical response of basalt fabric at similar temperature ranges was also measured. Thermogravimetry and X-ray diffraction analysis were used to study phase changes as a function of temperature. Scanning electron microscopy (SEM) was used to study damage processes in the fiber–matrix interfaces. Results indicate that the tensile strength of composites in residual conditions is higher than that in hot conditions. This traced back the mechanism that the fabric-coating visco-elastic/plastic interface changes with temperature, which affects the textile-cementitious adhesion properties. When the composite was tested in hot conditions, a much more aggressive loss of the load-carrying capacity was observed. With increasing temperature, the hot tests, showed a significant reduction in tensile strength, elastic modulus and strain capacity. Ultimate direct tensile strength values obtained under hot condition were, on average, 50% lower than the residual ones.

Keyword: textile reinforced refractory cementitious composite, basalt fiber, calcium aluminate cement, high temperatures, mechanical properties.

1. Introduction

Textile reinforced concretes (TRC) are a new generation of cementitious materials with enhanced tensile strength and ductility [1,2]. With its excellent mechanical properties, TRC's are used, currently, in a wide range of applications that include: strengthening and repair in structural members, protective linings, thin-walled elements, facade panels, bridges and also freeform and lightweight structures. It is important to consider, however, that in many of these applications both concrete and textile may be effected by thermal effects, which make a thorough study on the thermo-hydro-chemo-mechanical performance of TRC mandatory [3,4,5]. Although there is a growing interest in the use of TRC elements, little is known about their thermo-mechanical performance and even less about TRC applications using refractory concrete/mortar as a matrix [6]. As reported by Colombo et al [7], there are still only a few results available in literature about the fundamental properties of TRC's exposed to extreme conditions such as high temperature and fire conditions.

The response of refractory concrete members when submitted to elevated temperatures largely depends on the thermo-hydro-chemo-mechanical properties of the concrete phase, determined by the multi-scale matrix structure of the cementitious and aggregate composite, as well as on the environmental conditions such as humidity, heating rate, exposure time and presence of gases. The mechanical properties of refractory concrete specimens pre-heated at particular temperature levels do not correspond to the properties of such specimens obtained after being cooled down to room temperature again, and tested under ambient conditions [8,9,10]. Most measurements are generally done at room temperature (past cooling, residual tests), after an accumulation period at a given target temperature. This was to avoid complex assembling's of devices necessary to

carry out tests at high temperature, such as instrumenting LVDT's for high temperature, coupling ovens/thermostatic chambers to a universal testing machine, installing high temperature resistant parts, applying insulated thermocouples and installing advanced cooling systems.

Designing concrete structures to resist elevated temperatures (e.g. tunnel lining, fire barriers, cooling towers and encapsulation elements), requires specific knowledge on the thermo-mechanical properties of the used materials. In this context, parameters such as strength, elastic modulus, toughness and brittleness during and after heat treatment under elevated temperatures are required. Moreover, to gain a fundamental understanding of the degradation mechanism involved, mechanical results should be accompanied by microstructural and chemical analysis.

Studies reported by Soro et al [11] revealed that it is possible to develop refractory composites reinforced with long parallel fibers (e.g. low-cost glass fibers) showing ductile residual behavior even after dehydration of the main hydrated products ($\sim 400^{\circ}\text{C}$). Colombo [12] showed the applicability of TRC's (reinforced with AR-glass fabric) in sandwich panels with the purpose of saving energy in new and existing buildings (energy retrofitting). In this study the durability of TRC when exposed to freezing-thawing cycles was investigated. According to the authors, curing conditions, both heating and cooling, may affect the matrix shrinkage, and consequently the bond strength inside the composite material. In relation to the freeze-and-thaw cycles, mechanical performances of TRC's are directly related to their self-healing and late hydration capacity since matrix cracking may occur during these thermal cycles.

Coatings applied to a textile fabric can improve the durability (e.g. against corrosive alkaline environment or high temperatures). However, when exposed to elevated temperatures, some types of coating change their chemical and mechanical properties, leading to a reduced bond performance between fiber and matrix [6]. Recently, researchers, developed a system (Silva et al.

[8]), that uses TRC reinforcement with carbon fibers and showed that when heating the polymer-coated carbon fibers TRC under temperatures up to 150°C, a polymer-based interlocking mechanism between the filaments and matrix revealed. This mechanism resulted in a significant increase of the maximum pullout load.

Therefore, the aim of this paper is to investigate the effect of elevated temperatures on the mechanical properties of textile refractory composites reinforced with a basalt fabric submitted to tensile loading under different thermal testing conditions, i.e. hot and residual. At first, refractory composites were produced with a cementitious matrix made of synthetic calcium aluminate aggregates and calcium aluminate cement (CAC), then reinforced with basalt fabrics. The composites were tested in tension after being submitted to different temperature regimes, with targeted constant temperature levels ranging from 25 to 400°C. During high-temperature testing, specimens were loaded after having been exposed to the targeted temperature for 1 h, while the residual test specimens were loaded at room temperature, so after having experienced the same thermal exposure time, these specimens were cooled down to room temperature. The microstructure of the composites was characterized by scanning electron microscopy (SEM), thermo-gravimetric analysis (TGA) and powder X-ray diffraction (XRD) and then related to their mechanical properties.

2. Materials and methods

a. Refractory matrix

The matrix used in this research (compressive strength of about 45MPa) was designed according to the compressible packing model (CPM) procedure [13,14] and adjusted to achieve a rheology

necessary to produce the laminated TRC's. Because of the small diameters of the continuous filaments and small distances between the reinforcement textile layers, the maximum aggregate size had to be less than 1.18 mm in diameter. The materials used in the TRC composition were a calcium aluminate cement (Secar 51 from Kerneos Inc.) with an alumina content of about 51%, a synthetic calcium aluminate aggregates (Alag from Kerneos Inc.) with an alumina content of about 40% and diameters ranging from 0.001mm to 1.18 mm, and a powder polycarboxilate superplasticizer (Peramin CONPAC 500 from Kerneos Inc.). Table 1 presents detailed information about the chemical composition of the cement and of the synthetic calcium aluminate aggregate. The water-cement ratio of the refractory matrix was 0.35. Mix-design details of the referred matrix are provided in Table 2.

Table 1 – Chemical composition of the cement and of the synthetic calcium aluminate aggregate.

Cement		Aggregate	
Compound	Content/%	Compound	Content/%
Al ₂ O ₃	51.45	Al ₂ O ₃	39.88
CaO	38.51	CaO	36.02
SiO ₂	3.07	SiO ₂	2.79
Fe ₂ O ₃	1.76	Fe ₂ O ₃	14.48
TiO ₂	1.89	TiO ₂	1.61
SO ₃	0.61	SO ₃	1.05
K ₂ O	0.42	K ₂ O	0.19
ZrO ₂	0.12	ZrO ₂	0.09
MnO	0.02	MnO	0.19
SrO	0.05	SrO	0.03
Ga ₂ O ₃	0.01	Ga ₂ O ₃	0.15
Y ₂ O ₃	0.01	Y ₂ O ₃	0.01
Ta ₂ O ₅	0.03	P ₂ O ₅	1.77
Cr ₂ O ₃	0.07	V ₂ O ₅	0.06
NbO	0.01	LOI	1.68
LOI	1.96		

Table 2 – Mix-design of the concrete matrix.

Composition	
Synthetic calcium aluminate aggregates (kg/m ³)	1416.2
Calcium aluminate cement (kg/m ³)	750
Powder polycarboxilate superplasticizer (kg/m ³)	4.87
Viscosity modifier agent - VMA (kg/m ³)	0.562
Water (kg/m ³)	262.6
Superplasticizer content (%)	0.65
Water/cementitious mass ratio	0.35

b. Basalt fabric

A basalt textile, commercialized by the Zhejiang GBF Basalt Fiber Co. Ltd., China, was used as reinforcement for the TRC specimens. The basalt textile was produced with a styrene-acrylic latex coating (43g/m²). The warp as well as the weft is contains about 800 monofilaments with an average diameter of 13µm. Table 3 presents the properties of the used coated basalt textile.

Table 3 – Properties of basalt fabric.

Density (g/cm ³)	2.70
Melting point (°C)	1350
Warp wire spacing (mm)	5
Type of coating	styrene-acrylic latex
Coating content (g/m ²)	43
Specific surface weight (g/m ²)	250
Fiber volume fraction used to reinforce the TRC (%)	2.98

c. Matrix processing and composite manufacturing

The refractory composites were produced in a temperature controlled room at 24°C ± 1°C using a planetary mixer (moistured in advance) with a 5 liter capacity. The dry cementitious materials were homogenized for 60s, prior to water addition. The mixture was blended for 5 min. The

viscosity modifying agent type Rheomac UW 410 (VMA) was added 4 min later. Rectangular TRC fabric plates, measuring 400 mm x 250 mm x 13 mm (length x width x thickness), were produced for the direct tensile tests using a consistent lamination technique. For preparation of these plates acrylic molds were used. First, a thin refractory matrix layer was placed at the bottom of the mould. After that, the first basalt textile reinforcement fabric layer was placed on top of the fresh matrix (Figure 1).

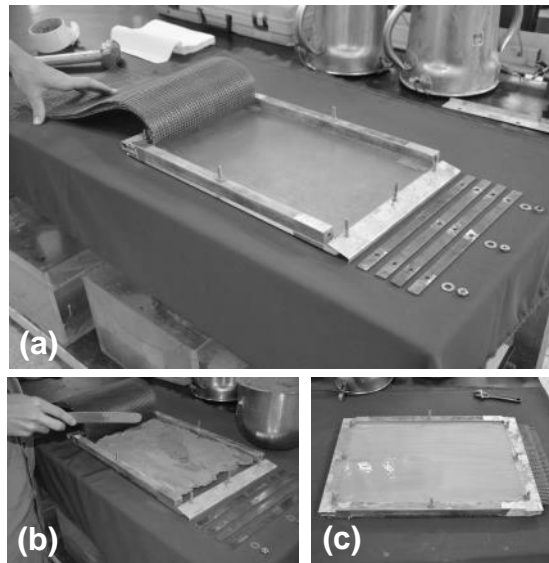


Figure 1– Production methodology used for fabricating the TRC reinforced with basalt fabrics.

The basalt fabric was then stretched and aligned in order to regularize and smoothen the first surface layer. Next, this procedure was repeated until reaching the desired number of 5 equally-spaced fabric layers was reached, resulting in a fiber volume fraction of 2.98%. A manual vibration was applied to the samples. After 7 days, the rectangular plates were de-moulded and cut, resulting in 4 specimens of 400 mm x 60 mm x 13 mm (length x width x thickness). The cross-section used for the stress calculations was obtained by averaging the nominal cross-sectional area (width and thickness) at four different locations for each sample.

3. Test procedure and thermal regimes

a. Tests in residual condition

The TRC fabric specimens that were tested in tension at residual conditions, were preheated at 25 (room temperature), 75, 150, 200 and 400°C, stayed at this temperature level for 1 h, and subsequently cooled down naturally inside the furnace. The heating regime that was applied to the specimens (age 7 days) is presented in Figure 2.

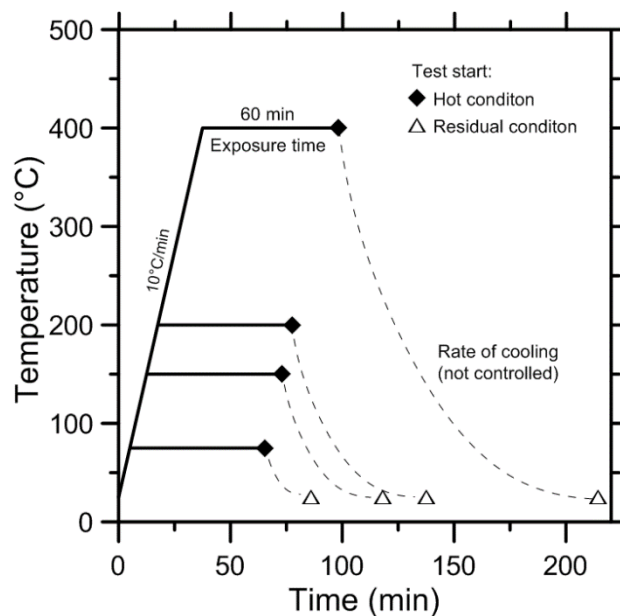


Figure 2 — Heating regimes applied to the refractory matrix under consideration.

For this, an electrical oven with a radiant heating system (metal alloy type Kanthal "A1" in alumina tubes), internally protected by perforated ceramic plates, was used (see Figure 3 b). Specimens were placed in the furnace and subjected to a heating rate of 10°C/min. The furnace was preprogrammed to keep the targeted temperature levels constant for 60 min within an accuracy range of $\pm 2^\circ\text{C}$. After this period, the furnace was switched off to let the specimens cool down naturally to room temperature before they were taken out for tensile testing. This procedure was followed to prevent a thermal shock.

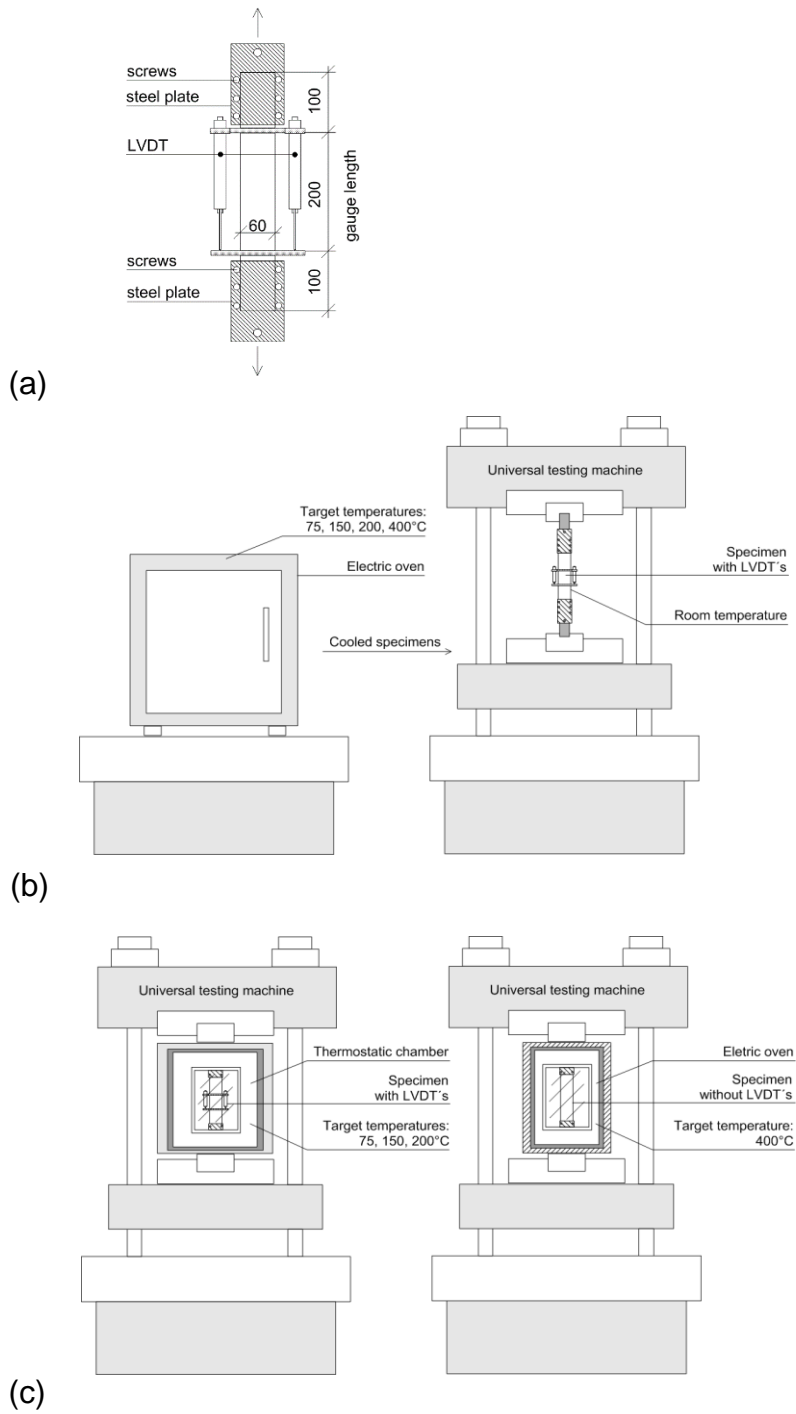


Figure 3 – Direct tensile test set up for the TRC (a) and testing conditions: (b) Residual and (c) Hot. Measurements in millimeters.

b. Tests in hot condition

The specimens tested in hot condition were subjected to the same targeted temperatures, heating rate and exposure times as applied to the specimens tested in residual conditions (see Figure 2). A Shimadzu universal testing machine with a thermostatic chamber was used for those specimens that were tested in tension up to 200°C. The test that were tested at 400°C were heated using an electrical oven with a radiant heating unit that was positioned over the testing area of the universal testing machine. In this case, the tensile tests were carried out without using LVDT's for strain measurements (see Figure 3 c). Also in this case, all specimens were subject to a heating rate of 10°C/min until reaching the targeted temperature level. After that, the temperature was kept constant for 60 min before commencing the loading at hot conditions.

4. Mechanical tests

a. Textile Reinforced Concrete

TRC specimens were tested in direct tension in a Shimadzu universal testing machine model AGX – 100 kN (Figure 3 a), and were displacement controlled using the actuator displacements at a rate of 0.4 mm/min. For each temperature condition, four specimens (400mm x 60mm x 13mm) were tested in uniaxial tension. The tensile force was applied to the specimens by clamping two steel plates at both outer ends of the specimens, which were then bolted together and hinged to the cross head. The elongation of the specimens was measured with two LVDTs over a gauge-length of 200mm (see Figure 3a). Finally, the TRC composites were tested in warped direction, and the tensile load and actuator displacement were recorded for all tests continuously.

b. Basalt fabric

To measure the performance of basalt fabric under direct tension, tests were performed on 50 x 360mm (width x length) rectangular fabric samples. Figure 4 shows the configuration of the tensile test set-up that is used for this study.

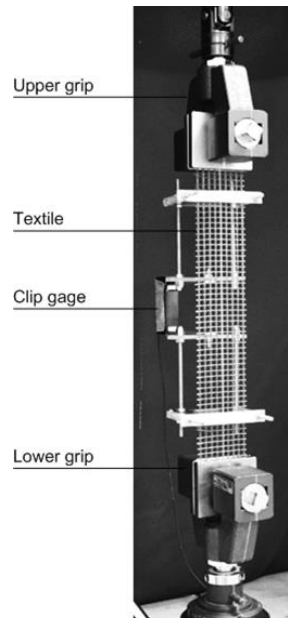


Figure 4 - Direct tensile test set-up for the basalt fabric.

A Shimadzu universal testing machine model AGX – 100 kN controlled by actuator displacement at a rate of 0.4 mm/min was also used here to perform the tensile tests on the fabric oriented in the warp direction (same machine and conditions as used for the TRC testing). The axial strain was measured by a clip gage that was applied to two metallic grips, which were fixed to both ends of the fabric samples. A gauge length of 200mm was used. The pressure applied to the grips was manually introduced. Protective tape was glued at both sides of the fabric samples in order to protect them from direct contact with the grips. To enable a precise interpretation of the mechanical test results, the cross-sectional area of the yarns was examined

by image analysis using SEM micrographs and Image J software. For this, small cubic TRC samples (20mm x 20mm) containing basalt fabric embedded in a transparent resin were prepared and polished manually to reveal the cross-section of the yarns in warp direction. The average cross-section of the warp yarns was 0.194 mm² obtained from 10 independent measurements.

5.0 Materials characterization

Before and after heating, fiber–matrix interfaces were investigated using a scanning electron microscope (SEM) FEI Quanta 400. For this, TRC samples were sectioned in specimens with dimensions of 20 x 20 mm (length x width). The samples were coated with 20 nm gold to become conductive and suitable for conventional SEM analysis. The SEM was operated using 25 kV of acceleration tension with a working distance of about 30 mm. TG analyses were carried out using crushed fragments of the samples tested under tensile loading. After testing, the extracted samples, were directly placed in plastic bags to avoid contact with moisture. Samples of about 10 mg were collected and analyzed. The thermal analyses were performed in a TA Instruments, SDT Q600 model TGA/DTA/DSC simultaneous apparatus with temperatures ranging between 35 and 1000°C using 100 mL/min of nitrogen flow. In order to eliminate the residual non-bounded free water, an isothermal step at 35°C during 1 hour was applied before starting the actual analysis. The reference material and sample pans were platinum. The specimens were also analyzed by X-ray diffraction (XRD) with a 2θ value between 5 to 50° with a Brucker D8 Advance instrument using a step of 0.05° and a CuK $\alpha_{1,2}$ radiation. In order to enable a qualitative analysis, samples were prepared using crushed matrix material with particle sizes less than 75 μ m. The measurements were performed with samples stored at room

temperature and preheated up to 200°C and 400°C (key temperatures in the dehydration process of the used refractory cementitious composite).

6. Discussion and analysis

6.1. Influence of test conditions on TRC tensile behavior

In Figure 5, typical stress-strain curves in tension are shown for the unheated reference specimen ($T = 25^{\circ}\text{C}$) and for specimens that were heating up to 75, 150, 200 and 400°C. The TRC specimens contained 5 bi-directional basalt fabric layers and all were tested in both residual and hot conditions. The crack pattern obtained after loading, in both residual and hot testing conditions, are shown in Figure 5 a, b, c and d, at the right hand side. Numerical data obtained from the specimens tested at 7 days of age are given in Table 4.

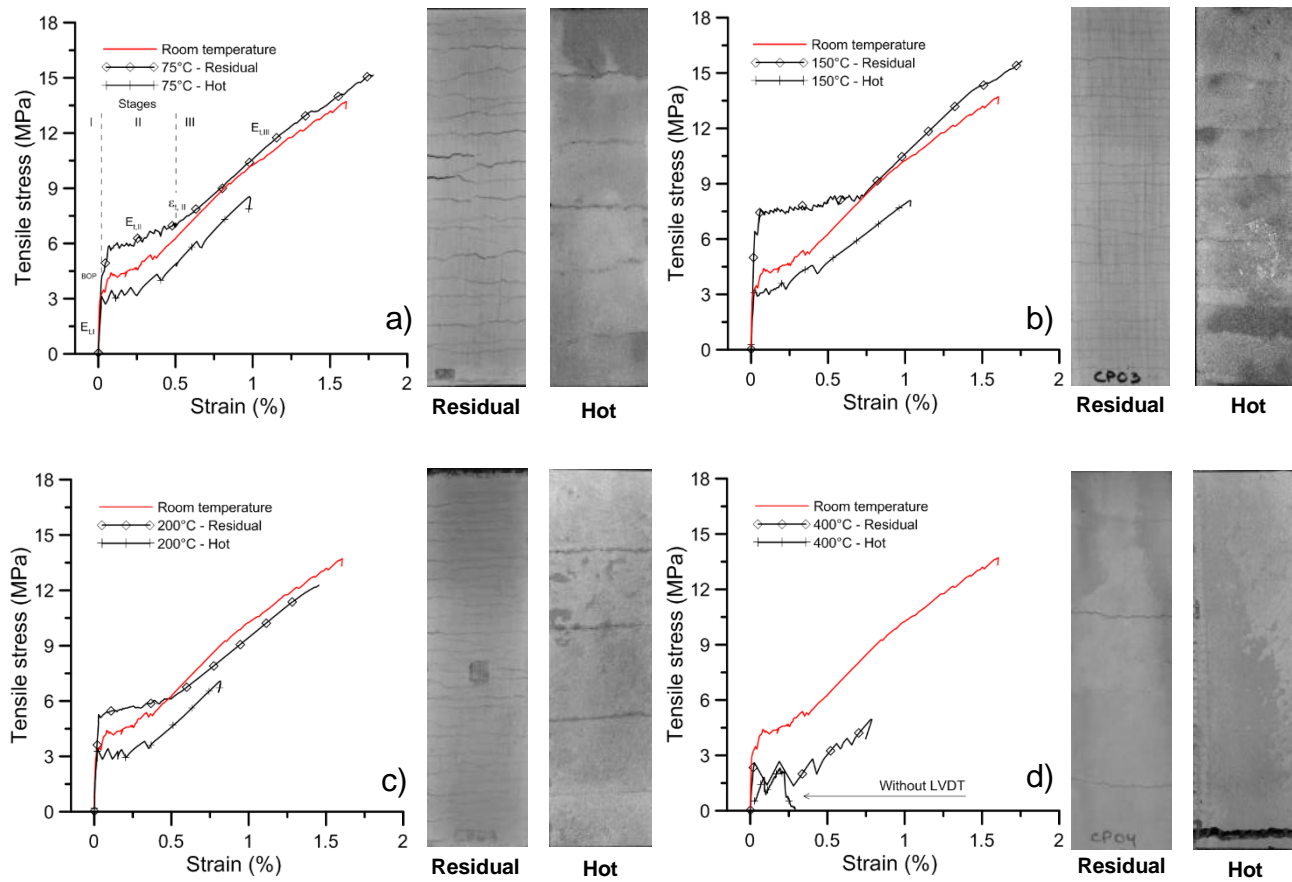


Figure 5 – Influence of temperature and testing conditions on the tensile behavior of basalt TRC’s heated up to (a) 75°C, (b) 150°C, (c) 200°C and (d) 400°C.

Table 4 – Average results of the direct tensile test (residual condition) performed on the basalt TRC. Standard deviation values are presented in parentheses.

Heating rate	Target temperature	First crack values				Post crack values					
		P_{BOP} (kN)	σ_{BOP} (MPa)	$\epsilon_{BOP, I}$ (%)	$E_{t, I}$ (GPa)	P_{UTS} (kN)	σ_{UTS} (MPa)	$E_{t, II}$ (GPa)	$E_{t, III}$ (GPa)	$\epsilon_{t, II}$ (%)	$\epsilon_{UTS, III}$ (%)
-	25°C	2.85 (0.65)	3.45 (0.78)	0.011 (0.0006)	34.64 (2.55)	11.13 (0.38)	13.49 (0.39)	0.45 (0.13)	0.67 (0.01)	0.42 (0.05)	1.58 (0.11)
10°C/min T.P.: 1h	75°C	3.73 (0.45)	4.85 (0.58)	0.021 (0.0005)	28.57 (2.79)	11.48 (0.48)	14.94 (0.55)	0.31 (0.08)	0.79 (0.11)	0.71 (0.20)	1.66 (0.08)
10°C/min T.P.: 1h	150°C	5.10 (0.13)	6.65 (0.22)	0.024 (0.0024)	31.63 (0.67)	11.74 (0.58)	15.30 (0.58)	0.12 (0.10)	0.73 (0.03)	0.62 (0.14)	1.64 (0.11)
10°C/min T.P.: 1h	200°C	4.19 (0.74)	5.09 (0.92)	0.036 (0.0634)	23.82 (5.37)	10.22 (0.97)	12.40 (1.18)	0.15 (0.06)	0.64 (0.03)	0.39 (0.09)	1.50 (0.21)
10°C/min T.P.: 1h	400°C	1.87 (0.13)	2.42 (0.17)	0.025 (0.0025)	10.93 (1.83)	3.79 (0.41)	4.98 (0.55)	0.36 (0.19)	0.90 (0.33)	0.47 (0.05)	0.68 (0.11)

T.P.: Time period in which the specimens were kept at the target temperature.

All values represent the average of four TRC tested specimens. The Bend Over Point (BOP) of each curve corresponds to the end of the linear elastic region and to the initiation of the first

crack crossing the entire matrix cross-section. TRC's mostly showed a strain-hardening behavior, presenting stress-strain curves with 3 distinct stages (see Figure 5 a): one stage prior and two stages after the bend-over point (BOP). Stage I corresponds to the elastic-linear range where both matrix and fiber behave linear. The post-BOP stage is characterized by the formation of multiple distributed cracks (stage II). During this stage of multiple crack development in the matrix, the load-bearing capacity of TRC remains at the same level since the cracks are bridged by the fabrics. Immediately after initiation of the first matrix crack, other cracks also appear throughout the specimen at almost regular intervals (depending on the fabric geometry and fiber-matrix interface). As the applied strain increases, various cracks culminate into a multiple cracking pattern along the sample. The final stage is stage III, which is characterized by crack-widening, leading to a stretching of the fabric and, posterior, failure of the composite.

6.1.1 Residual tests

Current test results have shown that the tensile behavior of TRC is strongly depending on the actual temperature condition. A strain-hardening behavior was observed for all TRC specimens tested after the targeted temperature ranges, under residual conditions. Preheating the specimens up to 75°C and 150°C generated a positive influence on the mechanical performance of TRC along the entire stress-strain curve. This was most pronounced when considering the tensile strength at the BOP (Figure 6) and, especially, when observing the multiple cracking pattern (Figure 5).

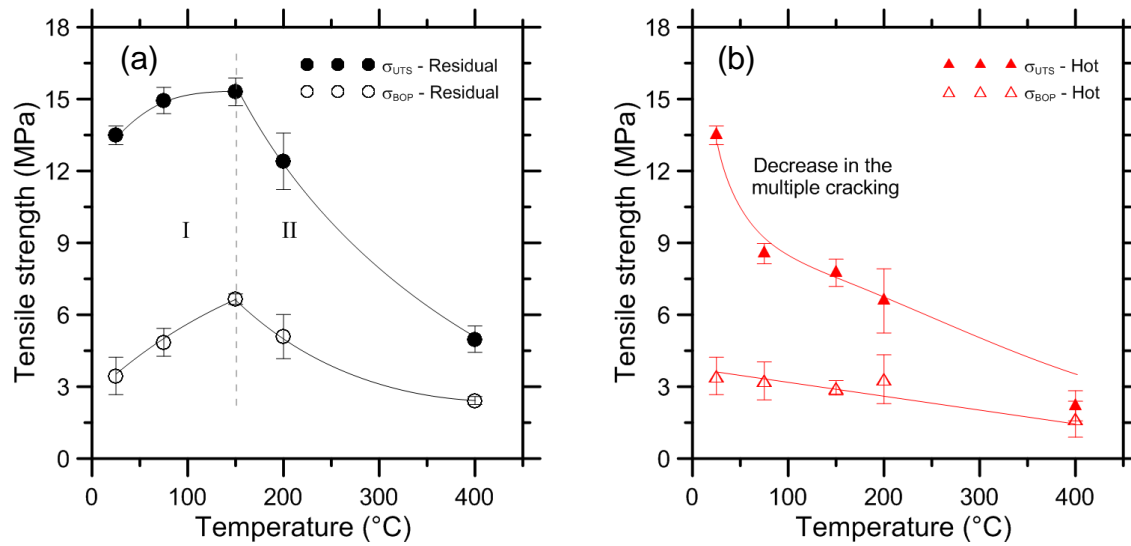


Figure 6 — Response of TRC in tension: (a) in residual, and (b) in hot conditions; UTS = at the end of the crack-widening phase; BOP = at the end of the elastic behavior.

In particular, for the temperature range of 150°C, where the TRC showed a σ_{BOP} that is about 92% higher than the TRC tested at room temperature, this behavior was most explicit. In relation to the ultimate tensile strength (σ_{UTS}), the effect of preheating up to 75°C and 150°C was less significant, i.e. generating improvements close to 11% and 13%, respectively.

As shown in the SEM micrographs presented in Figure 7, at 150°C (an even at 75°C) the styrene-acrylic latex coating, representing the fabric-matrix interface, transforms from a visco-elastic to a plastic one, thus, still able to create a strong bond between matrix and internal filament surfaces.

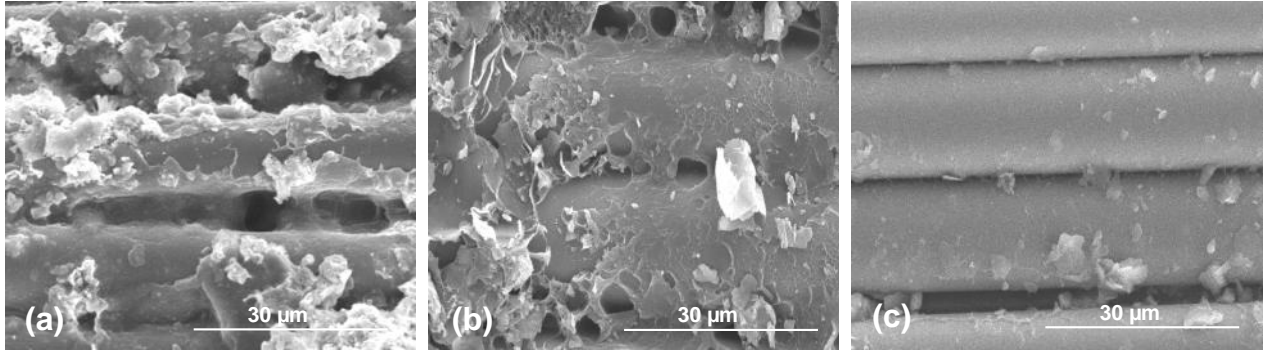


Figure 7 – Basalt TRC fiber-matrix interface after exposure to temperatures of (a) 150°C, (b) 200°C and (c) 400°C.

At this temperature, an intended merging of the polymer towards the matrix starts to occur. Between 75°C and 150°C (see Figure 7 a), as the temperature is still not able to fully decompose the polymer, after cooling to room temperature, the styrene-acrylic latex becomes stiffer and visco-elastic again. Thus, the newly generated polymer interlocks between filaments and matrix increases the bond strength, which is directly reflected by the TRC tensile response. In addition, as also reported by several other researches [15, 8], the penetration of the coating in the yarn, in this case due to the residual testing condition, is causing pronounced enhancements in the composite behavior. This occurs because the filaments now are stressed more uniform, taking more equally part in the load transfer and, consequently, increase the tensile strength. Finally, the irreversible shrinkage of the hardened paste (between 25°C and ~200°C) [18,16], that evolved after cooling the specimen to room conditions, may confine the matrix-fiber interface, and as such, improving the bond.

Figure 8 shows the TG data for a specimen at room temperature (25°C) and another that was measured after having being preheated up to 200°C.

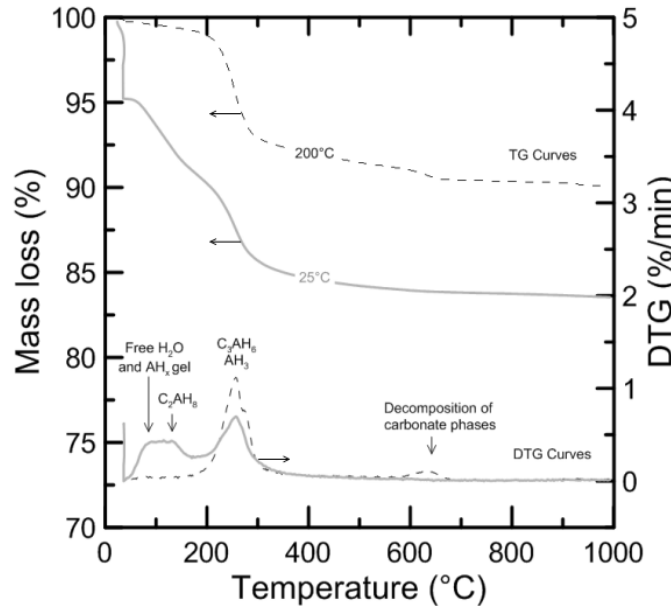


Figure 8 — Thermal analysis of the refractory concrete (7 days of age) on initial sample mass basis.

From these results the following observations could be done for the matrix: evaporation of free water, loss of structural water of the AH_x gel and dehydration of the metastable CAH_{10} ($CaO \cdot Al_2O_3 \cdot 10H_2O$) and C_2AH_8 ($2CaO \cdot Al_2O_3 \cdot 8H_2O$). Such processes normally go along with a reduction of the strength, however, this phenomenon was not explicitly observed in the present study, since the TG testing conditions (for sample 25°C) did not correspond to the heating regimes applied to the TRC specimens. In particular, the TRC specimens showed both hydrothermal and drying behaviour, while in a TG the small powdered samples just show drying (dehydration) in a very low humidity atmosphere (due to 100 mL/min of nitrogen flow). In more detail, from the difference between the specimens that have been heated up to 200°C and the non-heated specimens (25°C), the chemically bonded water that has remained in the matrix can be calculated. For this, TG measurements (25°C and 200°C) are expressed in terms of g/g anhydrous solids, i.e. normalized to the mass of the fired solids (TG results at 1000°C), representing the mass of anhydrous cement and clinker aggregate. The results show a decrease in

bonded water from 0.1044 g/g dry matrix solids to 0.078 g/g. Relating these values to the amount of anhydrous cement (dividing by the mass fraction of cement in anhydrous matrix, 0.3462 calculated from Table 2), yields: 0.3015 g/g cement (for 25°C) and 0.2252 g/g (at 200°C). When assuming no environmental water exchange during the initial 7 days of curing (sealed conditions), the calculated free water in the system (subtracting bond water from w/c) remaining in the specimen at 25°C is 0.0485 g/g cement. From here, the amount of released water evaporating from the specimen by heating up to 200°C, calculated in the same manner, is 0.1248 g/g cement.

In hydrothermal (open moisture and high temperature) conditions the conversion reactions of metastable hydration products (CAH_{10} , AH_x and C_2AH_8) to stable ones (C_3AH_6 and AH_3) is accelerated by thermal activation and the availability of moisture, leading to a dissolution and re-precipitation processes taking place [17,18]. Conversion reactions are accompanied by a simultaneous increase in matrix porosity and associated loss of strength. During this process, the water/cement ratio and the amount of main (active) minerals in CAC are the dominating variables that govern the transformation reactions [17,19]. This is because transformation reactions release free water (metastable hydrates contain more water than the stable ones), but also contribute to a continuing hydration of the unhydrated cement phases as well as the reactive aggregates that further occupies the porosity. Thus, the deleterious effect transformation reactions have on the properties of CAC-based materials could be reduced by lowering the w/c ratio [19]. In the TRC specimens under consideration, the low w/c ratio (w/c=0.35) is below the threshold limit of 0.4 (a stoichiometric water requirement for complete hydration), and thus the porosity increasing conversion effect is compensated for by further hydration of the reactive CA minerals. Moreover, the 0.4 limit is valid for conventional CAC concretes made with non-

reactive aggregates. Thus, the use of reactive (CAC) aggregates is expected to increase this limit (to $w/c > 0.4$), as more reactive CAC is available in the system to further reduce the porosity. XRD data (see Figure 9) obtained from TRC samples at room temperature and heated at 200°C confirmed that there is an increase in diffraction peaks for C_3AH_6 and AH_3 , accompanied by a decrease in diffraction peaks for CA (relative to C_2AS peaks, as a very slow reacting mineral).

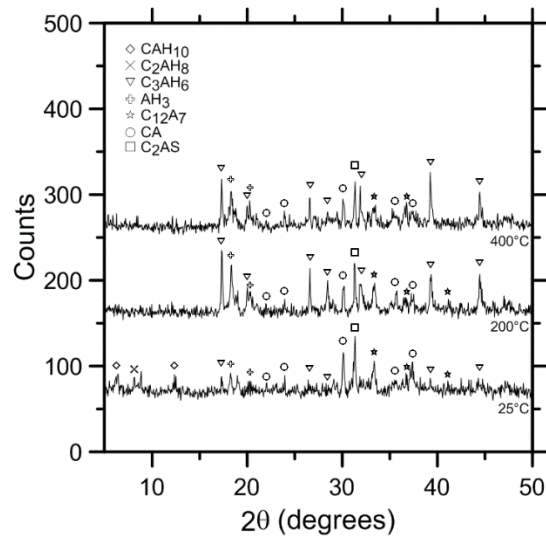


Figure 9 – XRD profiles for the refractory concrete at room temperature and preheated at 200 and 400°C; Counts: X-Ray intensity; 2θ : Angle of diffraction.

When considering the mechanical performance of the TRC tested specimens at residual conditions, up to a temperature of 150°C, the tensile strength increases continuously, after which it is decreasing quite rapidly (see Figure 6). TG studies (Figure 8) showed that loss of strength at this range (150°C to 200°C) can be explained by the end of dehydration of metastable CAH_{10} , C_2AH_8 , and by the start of dehydration of stable AH_3 and C_3AH_6 phases. The same was observed from XRD results, given the fact that CAH_{10} and C_2AH_8 phases were not detected at 200°C and above (see Figure 9). Furthermore, from Figure 7 b (TRC preheated at 200°C) it can be seen that the coating between the fibers at 200°C is porous and presents less interlocks than the coating heated at a temperature of 150°C only. At 200°C the degraded polymer shows more like a thin-

film morphology stretched over the filaments. It is very likely that the reduced amount of coating between the fibers-matrix interface, is the reason for a significant loss of strength associated with a decreased crack formation. This means that even though the fiber content remains constant, the performance of the coating at higher temperatures can become a determining factor for the tensile response of the composite.

At temperatures between 200°C and 400°C, severe strength loss was observed. In comparison with TRC heated at 200°C, the decrease in ultimate tensile strength (σ_{UTS}) for TRC heated at 400°C was about 60%. In relation to the tensile strength at the BOP, this reduction was about 52%. This decrease in tensile capacity is induced by the coating's thermal decomposition which happens between 300°C to 400°C (Figure 7 c). As a consequence, the tensile behavior of the TRC changes dramatically, leading to a reduced crack-widening (stage III) and a sudden drop in the load-carrying capacity of the composite. Similar interface degradation behavior, at the same temperature levels, was observed in previous investigations reported by Silva et al. [8], for TRC's produced with polymer coated carbon fabrics.

Besides the observed coating degradation at the fiber-matrix interface, at temperatures between 200°C and 400°C, the remaining hydration products AH_3 and C_3AH_6 are completely dehydrated (see Figure 8), while causing losses in the tensile strength and elastic modulus. However, it is still possible to observe the presence of hydration products like AH_3 and C_3AH_6 at 400°C, which is due to the presence of hydrothermal conditions in the specimens, as was also discussed before. Data on the elastic modulus of CAC-based materials are rare and insufficient in comparison with similar studies on PC-based materials. CAC hydration products are expected to have the same stiffness [15] as calcium silicate hydrate (C-S-H) gel, which is around 22 GPa, similar to the mean elastic modulus generally found for ettringite. There are no significant differences found

for the stiffness of the unhydrated cement minerals, which is around 117 GPa. Thus, based on this, the evolution of the elastic modulus (as well as strength) of CAC- and PC-based materials is related to the growth of solid volume and to degree of connectivity of the solids. On the other hand, upon heating, the elastic modulus of the matrix decreases (Table 5) due to the thermal degradation caused by the dehydration reactions which increase the porosity and decrease a degree of connectivity of the solids.

It is known that the incompatibility between cement and aggregates may create internal stresses and microcracking in the matrix, which may weaken the refractory concrete when exposed to high temperatures. However, given the fact that in this study the calcium aluminate clinker, used as aggregates, has a strong compatibility with the calcium aluminate cement, it is believed that internal cracking of the matrix for temperatures up to 150°C can be considered a “secondary effect” whenever comparing this effect with the degradation caused by coating during testing.

6.1.2 Hot tests

From Figure 5 (section 6.1) it can be observed that the mechanical performance of TRC’s loaded under hot condition is considerably less than when loaded under residual conditions. Evaluation results of all curves are given in Table 5. Similar to the specimens tested in residual conditions, strain-hardening was clearly observed from the stress-strain curves of all specimens tested under hot temperature conditions. However, with increasing temperature, a significant reduction in tensile strength, elastic modulus and strain capacity was observed, even for the lowest imposed temperatures, i.e. 75°C. This behavior indicates a much more aggressive loss of the load-carrying capacity once TRC is exposed (and tested) to hot conditions.

Table 5 – Average results of the direct tensile test (hot condition) performed on the basalt TRC. Standard deviation values are presented in parentheses.

Heating rate	Target temperature	First crack values				Post crack values					
		P _{BOP} (kN)	σ _{BOP} (MPa)	ε _{BOP, I} (%)	E _{t, I} (GPa)	P _{UTS} (kN)	σ _{UTS} (MPa)	E _{t, II} (GPa)	E _{t, III} (GPa)	ε _{t, II} (%)	ε _{UTS, III} (%)
-	25°C	2.85 (0.65)	3.45 (0.78)	0.011 (0.0006)	34.64 (2.55)	11.13 (0.38)	13.49 (0.39)	0.45 (0.13)	0.67 (0.01)	0.42 (0.05)	1.58 (0.11)
10°C/min T.P.: 1h	75°C	2.77 (0.59)	3.24 (0.79)	0.016 (0.0024)	22.43 (7.62)	7.34 (0.14)	8.54 (0.42)	0.31 (0.37)	0.75 (0.02)	0.31 (0.10)	0.95 (0.08)
10°C/min T.P.: 1h	150°C	2.37 (0.20)	2.95 (0.30)	0.0243 (0.0081)	21.20 (5.98)	6.25 (0.46)	7.75 (0.57)	0.42 (0.03)	0.61 (0.07)	0.42 (0.03)	1.04 (0.01)
10°C/min T.P.: 1h	200°C	2.66 (0.79)	3.31 (1.02)	0.018 (0.0109)	12.76 (7.42)	5.36 (1.16)	6.58 (1.34)	0.13 (0.06)	0.69 (0.10)	0.35 (0.04)	0.78 (0.16)
10°C/min T.P.: 1h	400°C	0.89 (0.73)	1.64 (0.75)	*	*	1.79 (0.56)	2.20 (0.63)	*	*	*	*

T.P.: Time period in which the specimens were kept at the target temperature.

*Unavailable (test without LVDT).

In comparison with the ultimate tensile strength (σ_{UTS}) obtained from specimens tested at room temperature, the decrease under hot conditions was, 37%, 43%, 51% and 83% for temperatures of 75°C, 150°C, 200°C and 400°C, respectively. The decrease in TRC tensile strength observed at the BOP (σ_{BOP}) was, respectively, 6%, 9%, 15% and 52% for temperatures of 75°C, 150°C, 200°C and 400°C. It may be important to notice that with increasing temperature, the decrease observed in σ_{UTS} is proportional to the strain decrease at the same point (ϵ_{UTS}). In comparison with the results obtained at room temperature, the decrease in the elastic modulus for temperatures of 75°C, 150°C, 200°C were 35%, 38% and 63%, respectively. The tests at 400°C were performed without LVDTs (therefore the elastic modulus was not determined).

Through Tables 4 and 5 it is possible to verify that the σ_{UTS} values obtained under residual conditions are, on average, 100% greater than that obtained under hot conditions. Some factors contribute to this behavioral difference. As shown in Figure 5, the lower crack spacing obtained under residual conditions suggests a higher bond strength between the fabric and refractory matrix. At high temperatures, however, the coating's softening behavior reduce the pullout resistance of the yarns and, consequently, the ability of the composite to carry and transfer loads,

and to form new cracks. It is probable that, for the same reason, the anchorage mechanism offered by the transverse yarns under hot condition is significantly lower as well.

Besides coating's changes, it is possible that high pore pressure developments combined with thermal cracking may reduce the mechanical performance of a refractory concrete submitted to high temperature. This phenomenon (pore pressure combined with thermal cracking), which may have occurred in both testing conditions used in this research (hot and residual) was reported for ordinary and high-strength Portland-based concretes before [18,20]. In this study, no explicit tests were performed to measure/distinguish the damage process induced by either pore pressure or thermal cracking, in the used testing conditions. It is believed that the pore pressure is, in a way, responsible for the performance of the TRC's submitted to the hot tests. This is because, under hot conditions, tensile strength capacity is reduced by the internal vapor pressure development, which tends to split the matrix. The opposite effect is quite common whenever compression loadings are applied. On the other hand, the cooling phase is expected to enhance the various dilatancies of the different components resulting in an increase of the residual damage compared to the ones tested in hot conditions. However, since the thickness of the specimens is only 13 mm, it is reasonable to assume that temperature gradients did not significantly degraded the TRC's. Consequently, no extensive thermal cracking is expected to happen. Besides this, no visible concrete spalling was observed for all samples tested under both testing conditions, i.e. 75, 150, 200 and 400°C. This can be attributed to the typical CAC concrete characteristics (conversion reactions), the small thickness of the samples and to the presence of textile reinforcement which promote pore pressure relief inside the heated TRC when exposed to high temperatures. During heating the fabric coating is burning out from the yarns creating micro-channels in the matrix, which facilitate this potential gas relief.

6.1.3 Basalt fabric: Results for residual tests

All TRC's tested in both conditions, hot and residual, presented multiple cracking behavior, excluding only the TRC tested at 400°C under hot condition. This behavior indicates that the textile reinforcement was very effective in limiting the formation of cracks thus increasing the load capacity of the composites.

As shown in Figure 10, the mechanical behavior of basalt fabric used as reinforcement in the TRC showed to be strongly affected by the heating-cooling regime used in the residual tests. Evaluation results of all curves are presented in Table 6.

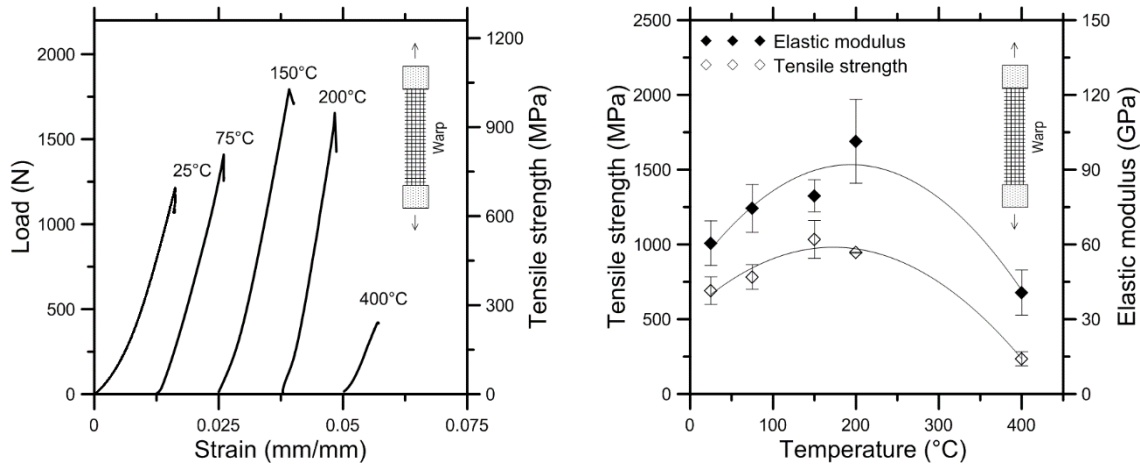


Figure 10 – Influence of temperature on the residual tensile behavior of basalt fabric heated up to 75°C, 150°C, 200°C and 400°C.

Table 6 – Average results of the residual tensile test performed on the basalt fabric. Standard deviation values are presented in parentheses.

Heating rate	Target temperature	Experimental values			
		P_{FAB} (N)	σ_{FAB} (MPa)	ϵ_{FAB} (mm/mm)	E_{FAB} (GPa)
-	25°C	1207.1 (160.80)	691.4 (92.09)	0.0153 (0.0018)	60.50 (8.96)
10°C/min T.P.: 1h	75°C	1303.8 (144.79)	783.45 (109.01)	0.0112 (0.0019)	74.44 (9.59)
10°C/min T.P.: 1h	150°C	1803.8 (220.52)	1033.12 (126.30)	0.0148 (0.0013)	79.51 (6.40)
10°C/min T.P.: 1h	200°C	1650.6 (5.60)	945.37 (3.21)	0.0102 (0.0018)	101.41 (16.81)
10°C/min T.P.: 1h	400°C	411.6 (82.84)	235.79 (47.45)	0.0067 (0.002)	40.66 (9.07)

T.P.: Time period in which the specimens were kept at the target temperature.

In agreement with the results already observed from TRC's, preheating the "naked" basalt textile up to 75 and 150°C resulted in an improved mechanical performance (tensile strength and elastic modulus). Table 6 shows that tensile strength (σ_{FAB}) at the target temperatures of 75 and 150°C increased respectively 13% and 49% relative to the fabric tested at room temperature. Similarly, the elastic modulus increased 23% and 31% for temperatures of 75 and 150°C, respectively. In this temperature range (75 to 150°C), the polymer coating changes from visco-elastic to plastic [8] (as discussed before in section 6.1.1), while impregnating the internal contact zones of the yarns, thereby improving the interface regions between filaments and matrix. After cooling, the co-polymer returned back to the original (visco-elastic, stiffer) condition. This mechanism allows for a more uniform stress distribution between the impregnated filaments, improving the tensile performance of the yarns and, thus, of the whole fabric.

As was also observed in the TRC specimens, for temperatures higher than 150°C, a gradual loss of the fabric mechanical strength was observed (Figure 10). The mechanical parameters obtained at 400°C were significantly impaired, compared to those obtained at room temperature. The elastic modulus also decreased with increasing temperature, however, this behavior was observed only for temperatures higher than 200°C. The residual tensile strength and elastic modulus at 400°C were respectively 65% and 32% of the results obtained at room temperature. Such behavior reflects not only changes in the structure of basalt filaments, but also the final step of the degradation process of the polymer coating present in the fabric [8] (as shown by SEM and discussed in section 6.1.4). Both the loss of tensile strength and elastic modulus of basalt textile exposed to high temperature contribute to the contrast between the hot and residual response of TRC's. However, it is believed that the magnitude of this contribution, in the hot

testing condition, is considerably smaller than the effect caused by the softening of the polymer coating during these tests.

7. Conclusions

- All basalt TRC's tested in both conditions, hot and residual, exhibited strain hardening behavior, excluding only the TRC tested at 400°C under hot condition.
- Preheating the basalt fabric TRC reinforced specimens up to 150°C showed an increased tensile strength development. This trend is attributed to the polymer coating behavior, which change from a visco-elastic to a plastic stage at higher temperatures, and upon cooling, to a visco-elastic stage, while improving the stress distribution between the filaments. This behavior has been confirmed by mechanical tests combined with SEM observation. The altered behavior was clearly reflected by the TRC stress–strain curves performed in the residual condition.
- TRC tensile strength was severely impaired after 200°C. Such tendency was attributed to dehydration of the main hydrated products, loss of strength of the basalt fabric and thermal decomposition of the coatings.
- TRCs exposed and tested in hot conditions show a progressive loss of the load-bearing capacity. With increasing temperature, a significant reduction of the tensile strength, elastic modulus and strain capacity is observed. Values for the ultimate tensile strength obtained in hot conditions were, on average, about 50% lower than the residual ones. This detrimental effect was attributed mainly to the inefficiency of reinforcement generated by the coating's softening under high temperatures. Besides this, similar as observed in the residual tests, the loss of TRC load-bearing capacity is further enhanced

by the matrix dehydration and conversion reactions as observed from the thermogravimetry and X-ray diffraction analysis.

Acknowledgements

The authors gratefully acknowledge the Brazilian Agency CNPq for its partial financial support and Kerneos (France) for supplying the cement, superplasticizer and aggregates.

[1] V. Mechtcherine, Novel cement-based composites for the strengthening and repair of concrete structures, *Constr. Build. Mater.* 41 (2013) 365–373. doi:10.1016/j.conbuildmat.2012.11.117.

[2] C. Soranakom, B. Mobasher, Geometrical and mechanical aspects of fabric bonding and pullout in cement composites, *Mater. Struct.* 42 (2009) 765–777. doi:10.1617/s11527-008-9422-6.

[3] M. Krüger, H.W. Reinhardt. In: Wolfgang Brameshuber, editor. Chapter 6: Fire resistance. Report 36: Textile Reinforced Concrete - State-of-the-Art Report of RILEM Technical Committee 201-TRC, Bagnaux: Rilem publications S.A.R.L, (2006) 83-218.

[4] F.D.A. Silva, M. Butler, S. Hempel, R.D. Toledo Filho, V. Mechtcherine, Effects of elevated temperatures on the interface properties of carbon textile-reinforced concrete, *Cem. Concr. Compos.* 48 (2014) 26–34. doi:10.1016/j.cemconcomp.2014.01.007.

[5] H.W. Reinhardt, On the biaxial testing and strength of coated fabrics - Paper demonstrates that improved specimens allow the measurement of the true biaxial breaking strength, *Exp. Mech.* 16 (1976) 71–74. doi:10.1007/BF02328607.

[6] D.A.S. Rambo, F. de Andrade Silva, R.D. Toledo Filho, O.F.M. Gomes, Effect of elevated temperatures on the mechanical behavior of basalt textile reinforced refractory concrete, *Mater. Des.* 65 (2015) 24–33. doi:10.1016/j.matdes.2014.08.060.

[7] I. Colombo, M. Colombo, A. Magri¹, G. Zani¹, M. di Prisco. Textile Reinforced Mortar at High Temperatures. *App. Mech. and Mater.* 82 (2011) 202-207.

[8] Z.P. Bazant, M.F. Kaplan. Concrete at High Temperatures. Material Properties and Mathematical Models. *Conc. Des. and Constr. Ser. England: Longman Group*(1996).

[9] L. Phan, N. Carino, Effects of test conditions and mixture proportions on behavior of high-strength concrete exposed to high temperatures, *ACI Mater. J.* 99 (2002) 54–66. <http://fire.nist.gov/bfrlpubs/build02/PDF/b02024.pdf>.

[10] P. Bamonte, P.G. Gambarova, A study on the mechanical properties of self-compacting concrete at high temperature and after cooling, *Mater. Struct.* 45 (2012) 1375-1387.

[11] J. Soro, A. Smith, C. Gault, Processing by tape casting and mechanical behaviour of aluminous cement-based matrix alumina fibers composites, *J. Eur. Ceram. Soc.* 27 (2007) 1469–1474. doi:10.1016/j.jeurceramsoc.2006.05.077.

[12] G. I. Colombo. Multilayer precast façade panel: Structural optimization for energy retrofitting. PhD Thesis. Department of Civil and Environmental Engineering. Doctoral School in Structural, Earthquake and Geotechnical Engineering (2015).

[13] F. De Larrard. Concrete mixture proportioning: a scientific approach. London: E&FN SPON (1999).

[14] T. Sedran. Rhéologie et rhéométrie des bétons: application aux bétons autonivelants. Doctoral dissertation. Ecole Nationale des Ponts et Chaussées (1999).

[15] U. Köckritz, P. Offermann, F. Jesse, M. Curbach. Influence of textile manufacturing technology on load bearing behavior of textile reinforced concrete. In: Proceedings of the 13th International Tech textile-Symposium (2005).

[16] M.D.M. Innocenti, F.A.Cardoso, M.M.Akyiوشي, V.C. Pandolfelli. Drying Stages during heating of high-alumina. Ultra-low-cement refractory castables. *J. of the Am. Ceram. Soc.* 86 (2003)1146–1148.

[17] J. Bensted. Calcium aluminate cements. In *Struct and Perform of Cem* (Bensted J and Barnes P (eds)). Spon, London, UK (2002)114–140.

[18] C. Gosselin, E. Gallucci, K. Scrivener, Influence of self heating and Li₂SO₄ addition on the microstructural development of calcium aluminate cement, *Cem. Concr. Res.* 40 (2010) 1555–1570. doi:10.1016/j.cemconres.2010.06.012.f

[19] N. Ukrainczyk, Effect of polycarboxylate superplasticiser on properties of calcium aluminate cement mortar. *Adv. Cem. Res.* (2015) 27(7) 388–398. <http://dx.doi.org/10.1680/adcr.14.00022>

[20] K. Watanabe, M.R. Bangi, T. Horiguchi, The effect of testing conditions (hot and residual) on fracture toughness of fiber reinforced high-strength concrete subjected to high temperatures, *Cem. Concr. Res.* 51 (2013) 6–13. doi:10.1016/j.cemconres.2013.04.003.

Artigo D – Rambo DAS, Yao Y, Silva FA, Toledo RD and Mobasher B. Experimental investigation and modelling of the temperature effects on the tensile behavior of textile reinforced refractory concretes. Submitted to Cement and Concrete Composites (2016). Pending review.

**Experimental investigation and modelling of the temperature effects on the tensile behavior
of textile reinforced refractory concretes**

Dimas Alan Strauss Rambo^a, Yiming Yao^b, Flávio de Andrade Silva^{c*}, Romildo Dias Toledo
Filho^a and Barzin Mobasher^b

^a Department of Civil Engineering, COPPE, Universidade Federal do Rio de Janeiro, P.O. Box
68506, CEP 21941-972, Rio de Janeiro – RJ, Brazil.

^b School of Sustainable Engineering and the Built Environment, Arizona State University,
Tempe, AZ, USA

^c Department of Civil Engineering, Pontifícia Universidade Católica do Rio de Janeiro (PUC-
Rio), Rua Marques de São Vicente 225, 22451-900 - Rio de Janeiro - RJ, Brazil

November 2015

*Corresponding author: e-mail: dimasrambo@gmail.com, Tel: +55 (21) 2562-8493 ext. 48. Fax: +55 (21) 2562-8484.

Abstract

In the present work the post-heating residual strength of a basalt textile refractory composite submitted to tensile loading was investigated. The composites were produced as a laminate material using basalt bi-directional fabric layers as reinforcement. High alumina cement was used in the matrix composition which was designed using the compressible packing method. A series of uniaxial tensile tests were performed after a preheating process at temperatures ranging from 25 to 1000°C. The mechanical performance and cracking mechanisms were discussed and compared to that obtained at room temperature. Image analysis by means of digital image correlation (DIC) method was used to obtain the evolution of crack width which was subsequently correlated with the stress response for all target temperatures. Scanning electron microscopy (SEM) was used to investigate the damage processes in the fiber–matrix interfaces after exposure to high temperatures. A finite difference model developed earlier by the authors was used to model the strain-hardening behavior and the crack spacing of the TRC. The obtained results indicated that due to the coating decomposition the reliability of basalt TRC can only be guaranteed from room temperature to 150 °C.

Keyword: mechanical properties, elevated temperatures, textile reinforced refractory concrete, basalt fiber, finite difference model, digital image correlation.

1.0 Introduction

There is a growing interest in the use of fabrics as the main reinforcement in cement based composites. The 2- D and 3-D nature of fabrics shows a significant improvement over 1-D straight or deformed fibers in the development of mechanical bond [1]. Textile reinforced concrete (TRC) presents both strain and deflection hardening behavior and are commonly used in applications where large energy absorption and strain capacity are required [2]. Among different types of possible reinforcements, basalt textiles offer interesting opportunities for TRC's with relation to strength, strain capacity, elastic modulus and cost. Depending on the application, the TRC can be subjected to combined thermo-chemo-hygro-mechanical effects, which cause structural changes in both matrix and reinforcement. Thus, thermally treated TRC's may present mechanical behavior and cracking pattern very distinct in relation to those obtained at room temperature in regular conditions [3]. In certain cases, very fine cracks are formed immediately after the end of the elastic region in the stress-strain curves. Given the fineness of these cracks, it is almost impossible to observe the nature of crack formation and also to measure important parameters such as crack width and crack spacing, using conventional devices such as LVDT, extensometer and strain gages. Digital Image Correlation (DIC) is a non-contacting optical full field deformation measurement approach that can better address the complex behavior of this class of materials. The DIC technique was developed by Sutton et al. [4,5,6] and Bruck et al. [7] and has been widely applied in structural engineering [8,9,10,11]. Nevertheless, works on the use of DIC in addressing deformations in textile reinforced composites are very limited [12,13,14].

Simply analytical formulations for modeling tension-stiffening behavior of concrete composites have been developed in the past by several groups, normally, to predict the behavior of OPC matrices reinforced with conventional rebars [15,16]. Gupta and Maestrini [15], for example, assumed a bilinear bond stress-slip curve (linear in the initial stage of cracking and constant at the later stages) for modelling both strain-hardening and strain-softening relations of reinforced concrete bars. The model was able to well represent the composites stress-strain relations in both cases, however, the authors pointed out the need for other kind of models taking concepts of fracture mechanics into account. Soranakom and Mobasher [17] proposed a more sophisticated method for modeling tension stiffening responses based on nonlinear finite difference method. The studied method considers not only the matrix and reinforcement stress-strain relation, but also parameters related to interfacial characteristics and damage parameters. The validation of this model was verified recently in several composites using different types of reinforcement [18,19,20] and will be adopted in this study to the case of temperature effect in textile refractory composites reinforced with basalt fibers.

The aim of this article is to investigate the effect of elevated temperatures on the mechanical properties of a textile refractory composite reinforced with basalt fabric submitted to tensile loading. At first, the refractory composites were produced with a cementitious matrix, made of calcium aluminate aggregates and high alumina cement (HAC), reinforced with basalt fabrics. The composites were tested under tensile load after being submitted to different temperatures regime ranging from 25 to 1000°C. Scanning electron microscopy (SEM) was used to study the damage processes in the fiber-matrix interfaces after exposure to high temperatures. DIC was used to investigate

the cracking behavior and full field distribution of tensile strain. Moreover, a finite difference model developed based on the tension stiffening behavior was used to simulate the experimental results. The assumption and mechanisms employed in the model were verified by DIC observation.

2.0 Materials and Processing

2.1 Refractory Concrete Matrix

The matrix used in this research (compressive strength of about 45 MPa) was designed following the compressible packing model (CPM) routine [21,22] and then adapted to the rheology necessary to produce laminated TRCs. As a result of the small diameter of the continuous filaments and the small distance between the reinforcement textile layers, the maximum aggregate diameter had to be less than 1.18 mm. The materials used in the TRC composition included calcium aluminate cement (Secar 51) with alumina content of about 50%, synthetic calcium aluminate aggregates (with an alumina content of about 40%) with diameter ranging from 0.001 mm to 1.18 mm and polycarboxilate superplasticizer in powder. The water/cementitious material ratio of the refractory concrete was 0.35. Table 1 gives the composition of the concrete matrix.

Table 1 – Mix composition.

Composition	
Calcium aluminate aggregate (kg/m ³)	1416.2
Cement (kg/m ³)	750
Superplasticizer (kg/m ³)	4.87
Viscosity modifier agent - VMA (kg/m ³)	0.562
Water (kg/m ³)	262.6
Superplasticizer content (%)	0.65
Water/cementitious material ratio	0.35

2.2 The basalt fabric

A basalt textile commercialized by the Zhejiang GBF Basalt Fiber Co. Ltd., China, was used as reinforcement for the TRC specimens. The basalt textile was produced with a styrene-acrylic latex coating (43g/m²). The warp as well as the weft were formed by about 800 monofilaments with average diameter of 13μm. Table 2 presents the properties of coated basalt textile.

Table 2 – Properties of the basalt fabric.

Density (g/cm ³)	2.70
Melting point (°C)	1350
Warp wire spacing (mm)	5
Type of coating	styrene-acrylic latex
Coating content (g/m ²)	43
Specific surface weight (g/m ²)	250

2.3 Matrix processing and composite manufacturing

The refractory concretes were produced in a room with controlled temperature of 24°C ± 1°C using a planetary mixer (previously moisturized) of 5 liters capacity. The cementitious materials were homogenized by dry mixing for 60s prior to the addition of water. The mixture was blended for 5 min. The viscosity modifier agent type Rheomac UW 410 (VMA) was added after 4 min of mixing. Rectangular plates measuring 400 mm x 250 mm x 13 mm (length x width x thickness) were produced for direct tensile tests using a lamination technique. For the production of the plates, the concrete mixtures were placed in the acrylic molds. The process started with a thin concrete layer placed on the bottom of the surface mold. The second phase consisted on positioning the first mesh of basalt textile reinforcement over the fresh concrete. The basalt fabric

was then pressed and smoothed in order to regularize and align the surface of the layer. After the second phase, the procedure was repeated until reaching the desired number of fabric layers. In this study 5 fabric layers equally spaced (volume fraction: 2.98%) were used as reinforcement in the TRC, however, samples without fabric layers were also produced. Manual vibration was applied to the samples. After 7 days in a cure chamber, the rectangular plates were cut, resulting in 4 specimens of 400 mm x 60 mm x 13 mm (length x width x thickness). The determination of the cross-sectional area was performed by the average of four measurements (width and thickness) at four different points of each sample.

2.4 The heating regime

An electric oven with radiant heating (metal alloy type Kanthal "A1" in alumina tubes) internally protected by perforated ceramic plates was used to heat the TRC specimens up to 75, 150, 200, 300, 400, 600 and 1000°C at a heating rate of 10°C/min. The temperature levels were kept constant for 60 min after the target temperature was reached. The furnace was then cooled down naturally before the specimens were removed in order to prevent thermal shock while the rate of cooling was not controlled. Experiments on control specimens stored at room temperature were also carried out.

2.5 Mechanical Testing

The direct tensile tests on the TRC plates and on the fabric samples were performed using a Shimadzu universal testing machine model AGX – 100 kN and controlled by the actuator displacement at a rate of 0.4 mm/min. For the composites, the force was transferred to the specimens via rotatable steel plates screwed to the TRC plates. Four rectangular shaped specimens measuring 400mm x 60mm x 13mm (length x width x

thickness) were tested using a gage length of 200mm with fixed–hinged boundary conditions for each temperature. Deformation of TRC’s was measured using two LVDT’s. The tensile load and actuator displacement were recorded. The material parameters obtained from experiments include the tensile load, stress and strain at bend-over point (BOP), ultimate load, strength and strain at peak, as well as the modulus at different stages. The stress was obtained by dividing the load by the nominal area of the specimen cross section.

The DIC technique was coupled to the tensile tests and carried out by selecting an area of interest (AOI), which was further divided into equally spaced virtual grid as shown in Fig. 1a.

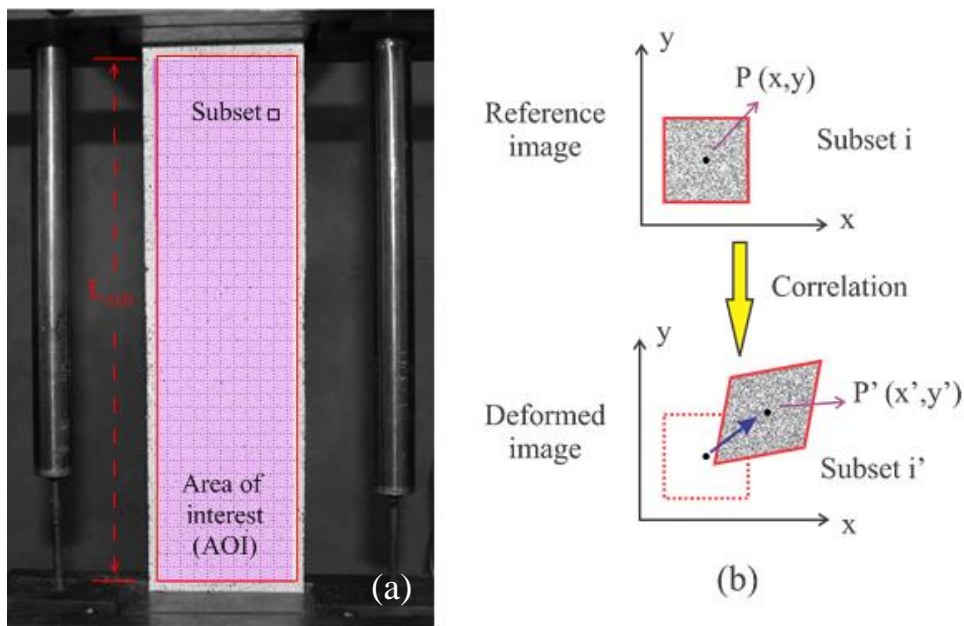


Fig. 1 - (a) Schematic presentation of a reference subset before deformation and the corresponding target subset after deformation; (b) area of interest (AOI) and subset in a reference image.

The displacements are computed at each point of the virtual grids to obtain full-field deformation. The imposed red square is the subset (a set of pixels) for tracking the movement of its center point $P(x,y)$ from the reference image (before deformation) to deformed images $P'(x', y')$ (Fig. 1b). The tracking of subset is conducted using selected correlation function such as cross-correlation (CC) and normalized cross-correlation (NCC) [23, 24]. Subsequently, the strain fields can be derived by smoothing and differentiating the displacement fields [25]. A commercial software Vic-2D 2009 developed by Correlated Solutions, Inc. was used to conduct image analysis.

2.6 Materials characterization

Before and after the heating process, the fiber–matrix interfaces were investigated using a scanning electron microscope (SEM) FEI Quanta 400. The TRC samples were sectioned in specimens with dimensions of 20 x 20 mm (length x width). The samples were coated with 20 nm of gold to become conductive and suitable for conventional SEM analysis. The SEM was operated using 25 kV of acceleration tension and about 30 mm of working distance.

3.0 Results and discussion

Based on the results, the produced laminated TRC showed to be strongly affected by thermal processing when submitted to a tensile loading. Fig. 2 presents representative curves obtained for the TRC tested under direct tensile loading after being submitted to the different heating regimes investigated in the present work. The results of evaluation of all curves are given in Table 3. A strain-hardening behavior was observed for the

TRCs in the majority of the target temperatures, excluding 600°C and 1000°C which presented, respectively, strain-softening and brittle behavior. As shown in Fig. 2, the strain-hardening responses of TRCs presents 3 distinct stages, with one stage prior and two stages after the BOP. The stage I corresponds to the elastic-linear range where both matrix and fiber behave linearly. The post BOP stage is characterized by the formation of distributed cracking (stage II). After the initiation of cracks in the matrix, the load-carrying capacity of TRC does not reduce since the cracks are bridged by the fabrics. Immediately after the initiation of the first matrix crack, other matrix cracks also propagate throughout the specimen at approximately regular intervals (related to the fabric geometry and the fiber-matrix interface). In this phase, as the applied strain increases, more cracks form culminating in a multiple cracking pattern along the sample. The stage III, is characterized by a crack-widening phase, leading to a stretching and pull out of the fabric and, posterior, failure of the composite. The positive influence of preheating the specimens up to 75°C and 150°C on the mechanical performance of TRC was clearly noticeable along the entire course of the stress–strain curves, but mainly with relation to the cracking strength at the BOP. This behavior was more pronounced for the temperature of 150°C where the TRC showed σ_{BOP} about 92% greater than the TRC tested at room temperature. With relation to the ultimate tensile strength (σ_{UTS}), the contribution of the preheating process up to 75°C and 150°C was not so significant, generating increases of, respectively, 10.7% and 13.4%. For temperatures greater than 150°C, the stress level at the BOP and the ultimate tensile strength decreased gradually with increasing temperature. This decrease was accompanied by a significant reduction of the elastic modulus for 200°C. The TRC heated to 200°C showed a multiple cracking pattern (see item 4.0), similar to the TRC

heated to 150°C, however significant signs of strength deterioration were noticed for this temperature and above.

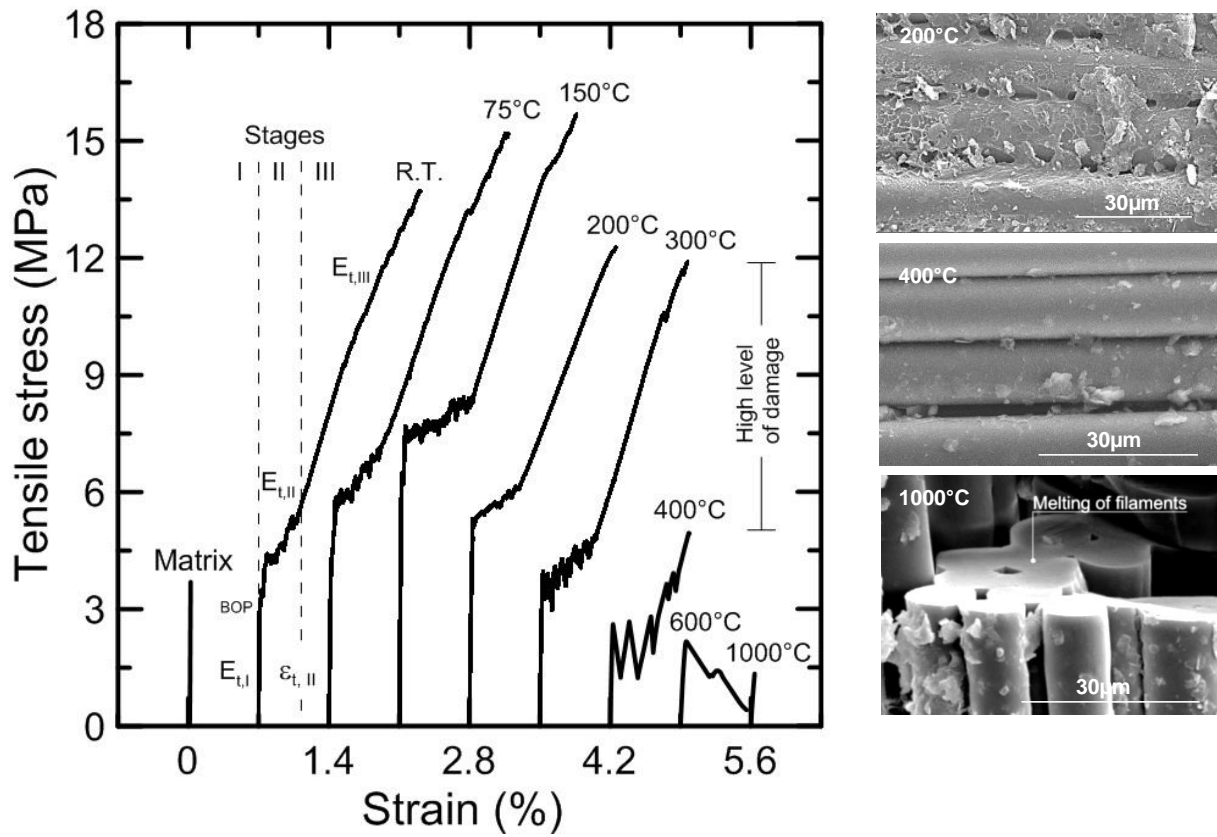


Fig. 2 - Influence of temperature on the tensile behavior of basalt TRC's obtained from the specimens tested at room temperature and after heating processes at 75°C, 150°C, 200°C, 300°C, 400°C, 600°C and 1000°C.

Table 3 – Average results of the direct tensile test performed on the basalt TRC.
Standard deviation values are presented in parentheses.

Heating rate	Target temperature	First crack values				Post crack values					
		P _{BOP} (kN)	σ _{BOP} (MPa)	ε _{BOP,I} (%)	E _{L,I} (GPa)	P _{UTS} (kN)	σ _{UTS} (MPa)	E _{L,II} (GPa)	E _{L,III} (GPa)	ε _{L,II} (%)	ε _{UTS,III} (%)
-	25°C*	2.85 (0.65)	3.45 (0.78)	0.011 (0.0006)	34.64 (2.55)	11.13 (0.38)	13.49 (0.39)	0.45 (0.13)	0.67 (0.01)	0.42 (0.05)	1.58 (0.11)
10°C/min T.P.: 1h	75°C	3.73 (0.45)	4.85 (0.58)	0.021 (0.0005)	28.57 (2.79)	11.48 (0.48)	14.94 (0.55)	0.31 (0.08)	0.79 (0.11)	0.71 (0.20)	1.66 (0.08)
10°C/min T.P.: 1h	150°C	5.10 (0.13)	6.65 (0.22)	0.024 (0.0024)	31.63 (0.67)	11.74 (0.58)	15.30 (0.58)	0.12 (0.10)	0.73 (0.03)	0.62 (0.14)	1.64 (0.11)
10°C/min T.P.: 1h	200°C	4.19 (0.74)	5.09 (0.92)	0.036 (0.0634)	23.82 (5.37)	10.22 (0.97)	12.40 (1.18)	0.15 (0.06)	0.64 (0.03)	0.39 (0.09)	1.50 (0.21)
10°C/min T.P.: 1h	300°C	3.47 (0.33)	4.31 (0.44)	0.033 (0.0048)	20.52 (1.68)	9.64 (0.56)	11.97 (0.65)	0.19 (0.05)	0.75 (0.06)	0.50 (0.10)	1.59 (0.07)
10°C/min T.P.: 1h	400°C	1.87 (0.13)	2.42 (0.17)	0.025 (0.0025)	10.93 (1.83)	3.79 (0.41)	4.98 (0.55)	0.36 (0.19)	0.90 (0.33)	0.47 (0.05)	0.68 (0.11)
10°C/min T.P.: 1h	600°C	1.56 (0.10)	1.98 (0.16)	0.044 (0.0032)	5.37 (1.41)	-	-	-	-	-	-
10°C/min T.P.: 1h	1000°C	1.10 (0.30)	1.33 (0.36)	0.037 (0.0274)	3.96 (0.39)	-	-	-	-	-	-

T.P.: Time period in which the specimens were kept at the target temperature.

*Room temperature.

Earlier studies with the same refractory matrix using thermo-gravimetric analysis showed that the loss in strength during this range (150°C to 200°C), can be explained by the end of the dehydration of metastable CAH₁₀, C₂AH₈, and by the start of dehydration of the stables AH₃ and C₃AH₆ phases [3]. Severe strength loss was observed from 300°C to 400°C. In comparison with the TRC heated at 300°C the decrease in the ultimate tensile strength (σ_{UTS}) for TRC heated at 400°C was 58%. With relation to the tensile strength at the BOP, the reduction was about 43%. For temperatures greater than 400°C the specimens failed abruptly and large cracks occurred (see item 4.0). Studies [26,27] have shown that the tensile strength of basalt fibers, as well as similar fibers (S-Glass fibers, E-Glass fibers, carbon fibers), decrease rapidly at temperatures greater than 400°C. As a consequence, the thermo-mechanical behavior of the TRC was largely affected at this temperature and above. As reported previously, the TRC heated at 600°C showed a strain softening behavior. At this temperature, the minor crack-bridging action of the fibers [3] could be neglected if compared to the results at the

lower target temperatures. The composite heated at 1000°C, however, showed a fragile type of failure. This brittle behavior is attributed, in part, to the melting of the basalt filaments (see Fig. 2) detected by SEM analyses. The average tensile strength for the composite heated at 1000°C at the first crack was 1.33 MPa, 38.5% of the σ_{BOP} at room temperature. There was no visible concrete spalling for any one of the temperatures investigated (75, 150, 200, 300, 400, 600 and 1000°C). This can be attributed to the small thickness of the samples and to the presence of the textile reinforcement.

3.1 Microstructural characterization

A microstructural investigation using the SEM was carried out to confirm the damage process on the TRC previously discussed. Fig. 2 shows fiber–matrix interface micrographs of the basalt yarns after exposure to 200°C, 400°C and 1000°C. At 75°C the styrene-acrylic latex coating starts to transform from visco-elastic to plastic, thus, impregnating more strongly the matrix and the internal filaments. The polymer is not decomposed at certain temperature and the styrene-acrylic latex becomes visco-elastic again and stiffer after cooling. The penetration of coating in the yarn, in this case due to the heating regime, makes pronounced changes in the composite behavior. This occurs because the filaments are stressed more equally, taking part in the load support and, consequently, increasing the tensile stress. The first signs of degradation of the polymer started to appear at 200°C (Fig. 2) when the polymer takes the form of thin-films or scales deposited over the filaments. As a result of the less amount of coating between the fibers and in the fiber–matrix interfaces, significant strength losses were observed. When the temperature increases to 400°C, it is possible to verify that the polymer was

entirely lost. As a consequence, the tensile behavior of the TRC changes which is characterized by a reduced crack-widening phase and a sudden drop in the load carrying capacity of the composite. Fig. 2 shows the micrograph of a basalt yarn highlighting the melting of fibers caused by the heating up to 1000°C.

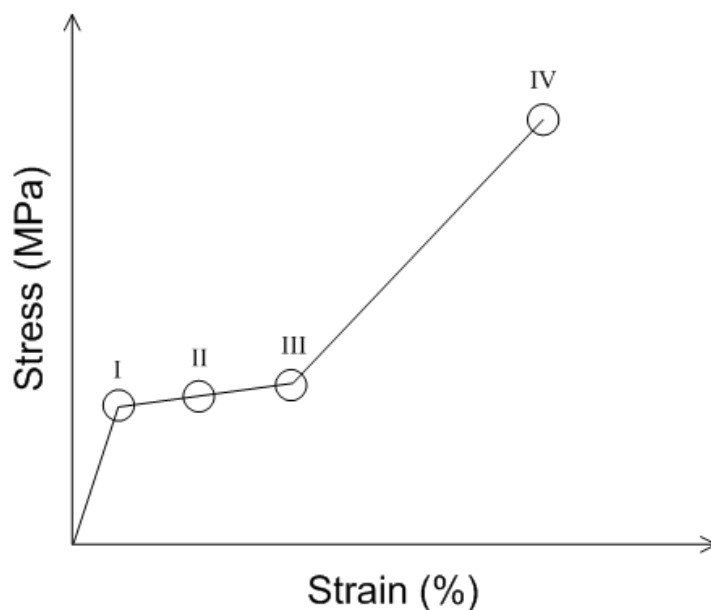
4.0 Analysis of Cracks and Localized Damage Using DIC

4.1 Quantification of the Strain Fields

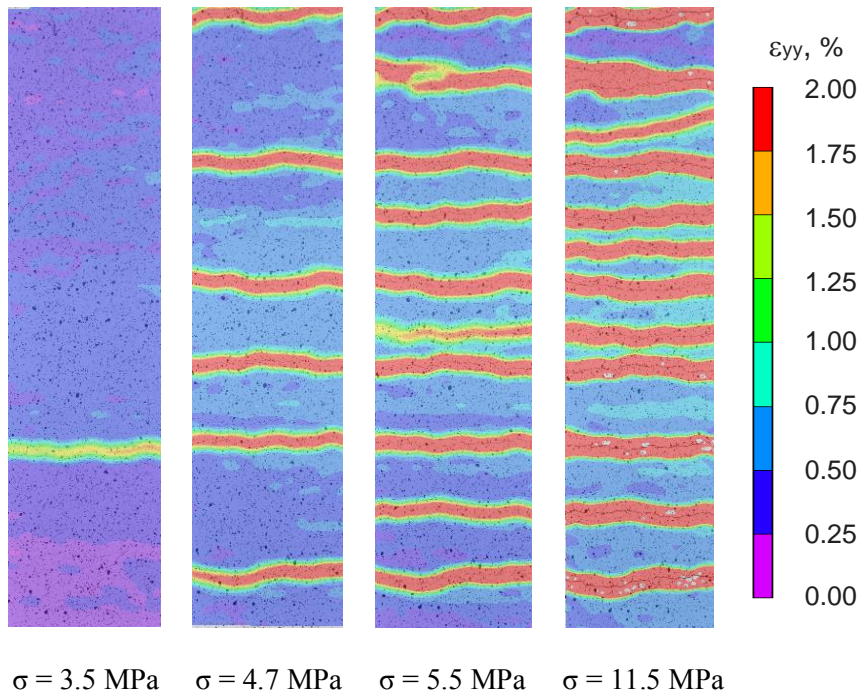
The longitudinal strain (ϵ_{yy}) fields of the TRC exposed to 25°C, 200°C and 400°C are shown in Fig. 3. The strain state at the sample face are shown at the right side using a color code where the purple color represents very low strain values and red is 2.0% indicating significant localization. The strain fields showed in the Fig. 3 were collected from four different points in the stress strain curves of the TRC: initial phase of the multiple cracking baseline “I”, center of the plateau of multiple cracking “II”, initial phase of the localization of cracks “III” and at the point where the composite reached the ultimate tensile strength (see Fig. 3a). A multiple cracking pattern is observed for all samples submitted to the residual tensile tests at 25°C, 200°C and 400°C. Tensile strain concentrates in the vicinity of the crack while the far-field is uniformly deformed. Through Fig. 3b and c it is possible to verify that the heating-cooling regimes at 200°C and 400°C dramatically change the sample failure mode. In comparison with the TRC tested at room temperature the composite preheated up to 200°C presented larger amount of cracks. As reported before, this behavior occurs due to the viscoelastic-plastic changes on the already degraded coating. After cooling, the newly generated polymer interlocks change the interface mechanisms of the TRC, increasing the bond

between the fibers and matrix. As the tensile stress rises to 4.5 MPa (initial phase of the multiple cracking baseline “I”), several bands in blue are formed indicating the initiation of matrix cracking. After reached this plateau, cracking formation is maintained, culminating in the point “III”, where the localization of cracks begins. The strain map of entire AOI revealed by DIC at 200°C, exhibited a distinct behavior characterized by smaller cracks (many shear lag zones). The red bands (localization of cracks), were observed clearly only at the “IV” zone. Fig. 3d shows the strain map of a TRC specimen preheated at 400°C. The pattern of cracks for 400°C was similar to that obtained at room temperature with relation to the extent of strain localization bands. However, as a result of damage evolution in the matrix and fabric, as well as the complete loss of the polymer coating, lower amount of cracks were observed at 400°C. The absence of deformation (purple color) in the uniform sections between cracks at 400°C (Fig. 3) indicates that tensile forces are being transferred predominantly by the textile reinforcement.

(a)



(b) 25°C



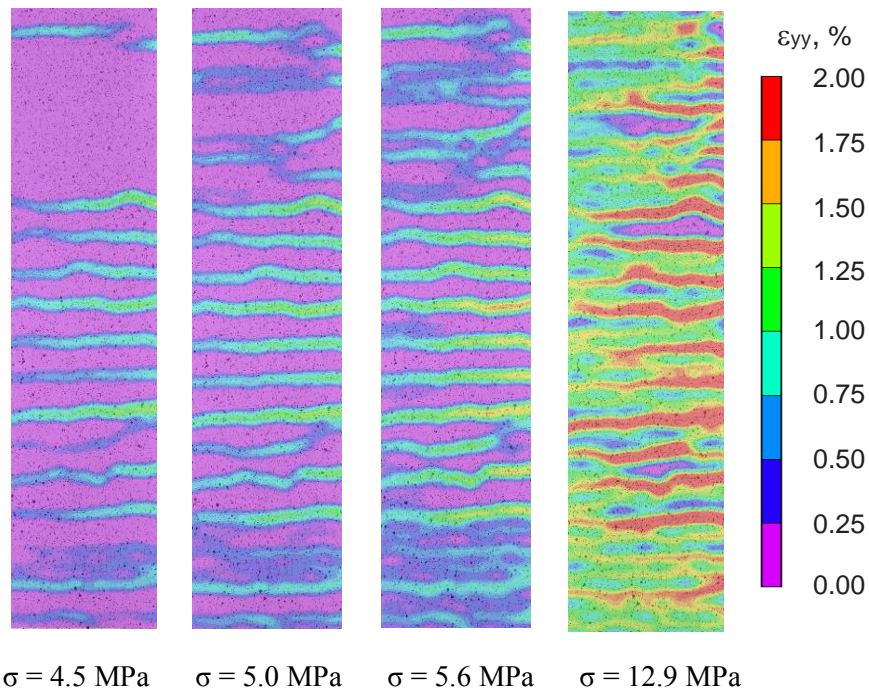
$\sigma = 3.5$ MPa

$\sigma = 4.7$ MPa

$\sigma = 5.5$ MPa

$\sigma = 11.5$ MPa

(c) 200°C



$\sigma = 4.5$ MPa

$\sigma = 5.0$ MPa

$\sigma = 5.6$ MPa

$\sigma = 12.9$ MPa

(d) 400°C

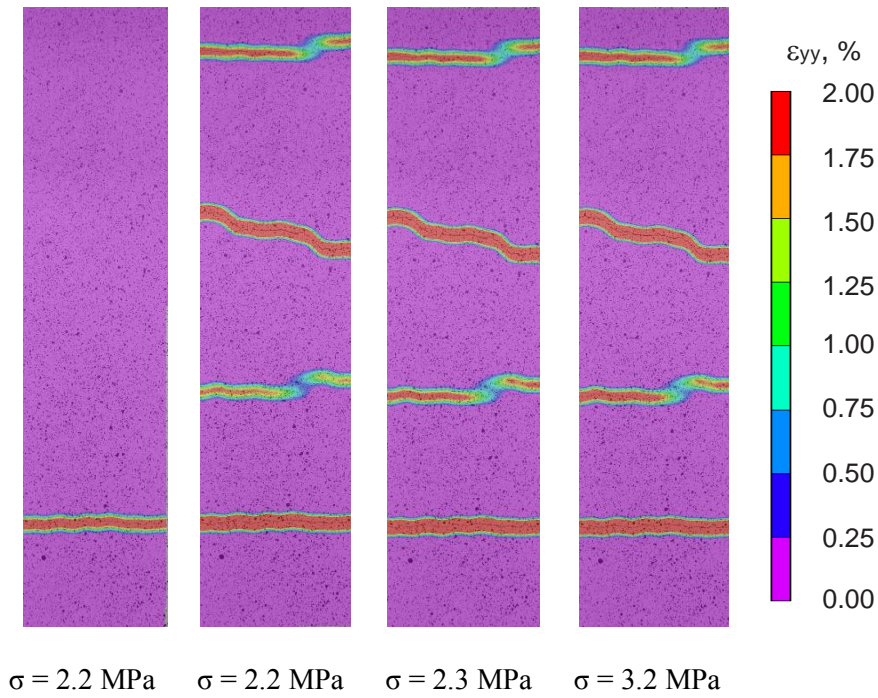


Fig. 3 - Strain fields (ϵ_{yy}) obtained by DIC. (a) Points of stress-strain curve where the strain fields were collected for temperatures of: (b) 25°C, (c) 200°C and (d) 400°C.

Fig. 4a and b show the distributions of longitudinal displacement and strain at an intermediate stress level, for the sample tested at room temperature. The discontinuities observed in the displacement map indicate the transverse cracks as the crack opening leads to sudden change in the displacement values. The location and width of the certain crack is therefore represented by the coordinates and the vertical amplitude of the discontinuity. Fig. 5a shows a 2D repetition of the displacement distributions with increasing stresses. The deformation and associated slope of uncracked segment are marginal compared to those at a crack, which explain the pattern of strain distribution shown in Fig. 3.

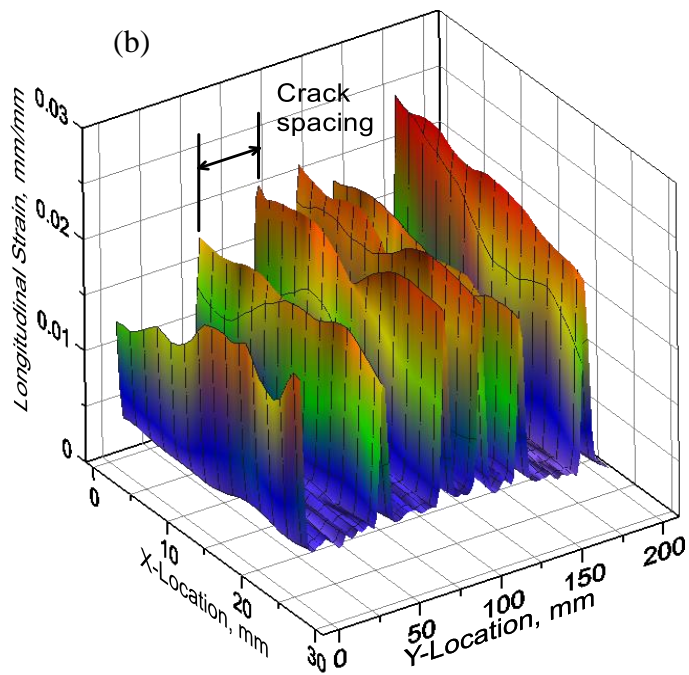
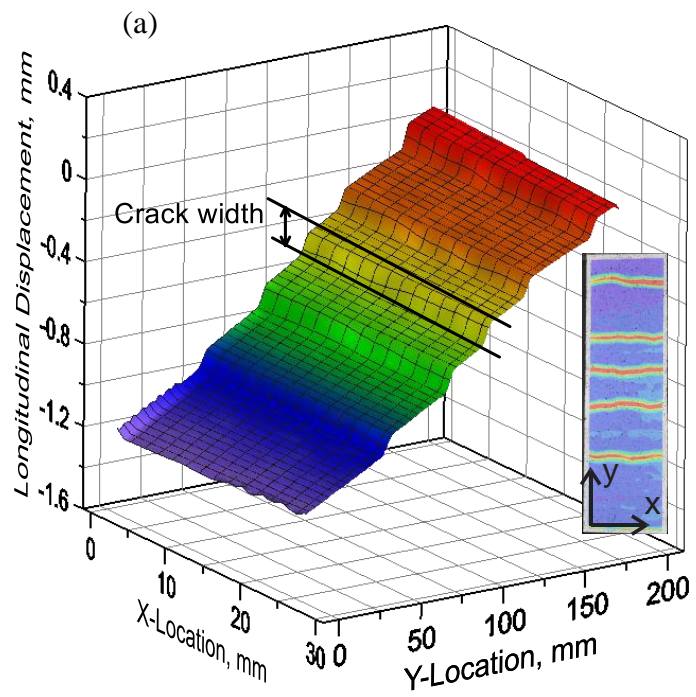


Fig. 4 – Crack width and crack location for the TRC tested at room temperature ($\sigma = 4.6$ MPa).

The widths of multiple cracks are measured, averaged, and subsequently correlated to the stress responses from experiment, as shown in Fig. 5.

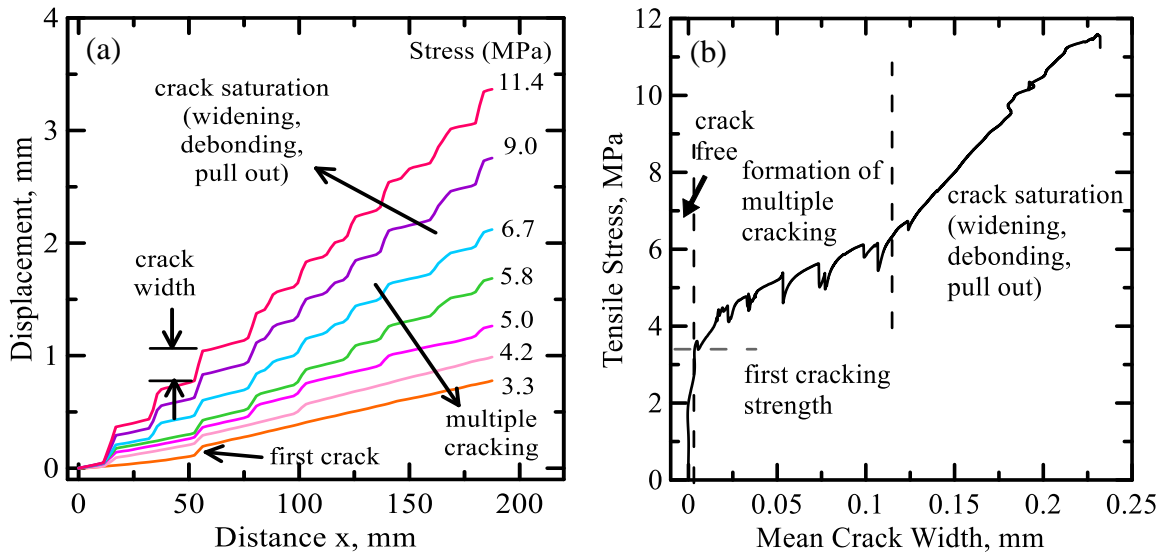


Fig. 5 – Correlation between displacement distribution and stress level for the TRC tested at room temperature.

As shown in Fig. 6, it is possible to observe three different zones in the cracking pattern revealed by DIC for 25°C: (A) the localization zone in red where the transverse crack is located and the majority of the load is carried by the textile phase; (B) the shear lag zone in green/blue where the slip between fiber and matrix cannot be ignored and the bond stress follows a shear lag pattern; (C) the uniform zone where no crack is formed and the slip is negligible. The fiber stress variation along the length reaches a maximum level in the bridge zone (A) and minimum value at the “perfectly bonded” zone (C). The distance is normalized with respect to the length of AOI (in this case $L_{AOI} = 200$ mm) and different zones are identified by the dashed lines. The behavior at zones A, B and C, can be modeled as an σ - ω relationship, non-linear bond stress-slip relationship, and with a linear stress-strain relationship, respectively. These mechanical behaviors are integrated in a finite difference model which will be introduced in next session. In

addition to these constitutive responses, crack spacing (s) and the width of debonding zone (h_D) were measured from the DIC data. The debonding zone is referred to as the combination of localization zone and shear lag zone where the fiber and matrix starts to debond and pull out.

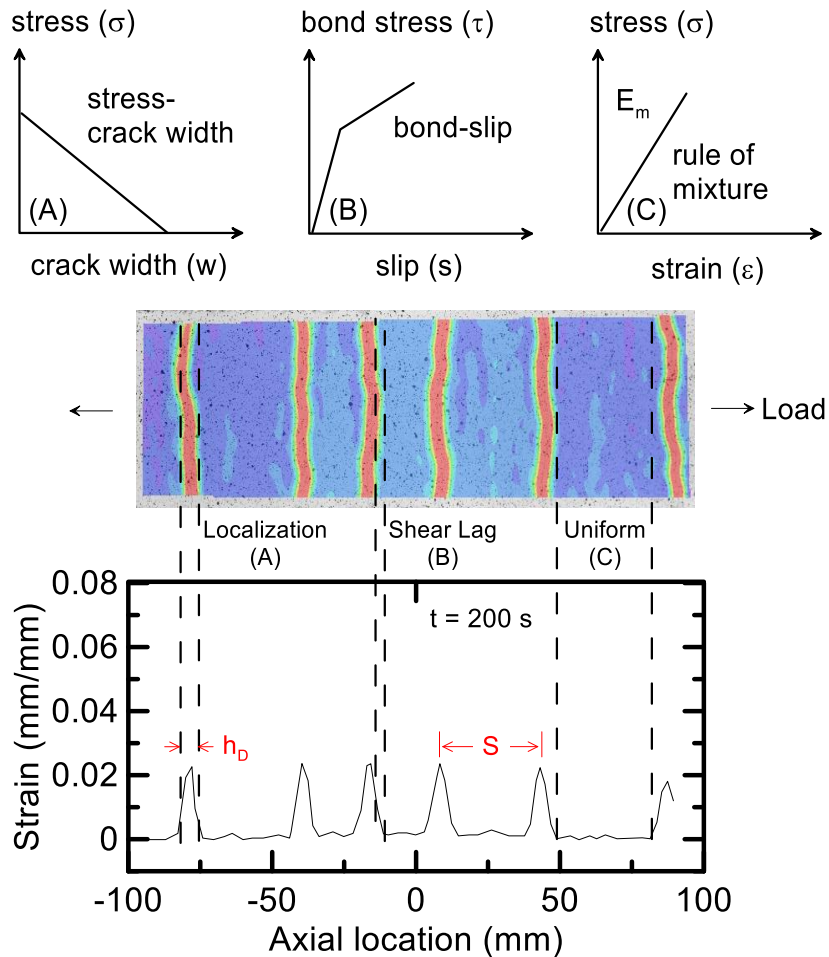


Fig. 6 - Identification of three zones: localization, shear lag, and uniform strain and corresponding modelling approaches.

Quantified distribution of tensile strains along the axial location of the specimens are extracted from DIC analysis and illustrated Fig. 7. The evolutions of strain distribution as a function of time/stress are characterized by six sub-images, where the first sub-image indicates the first cracking and the last one corresponds to the ultimate state.

Similar to the observations in strain maps, tensile strain localizes at the cracks and the far fields are under uniform deformation. However, the excessively high strain values at the peaks may not be reliable as the strain field loses its continuity across the cracks. The width of debonding zone (h_D) for the temperatures of 25°C, 200°C and 400°C are measured as 9.6mm, 6.3mm and 10.6mm, respectively. Previous study [12] showed that the width of debonding zone is related to the bonding characteristics such that higher bond strength corresponds to smaller zone width. The smallest h_D exhibited by the specimen at 200°C indicates the highest bond strength among the three which is caused by the polymer interlocks. On the other hand, the largest width at 400°C is associated with the complete loss of polymer coating at this temperature which reduces the bond strength. The crack spacing responses will be presented in the next section of modelling.

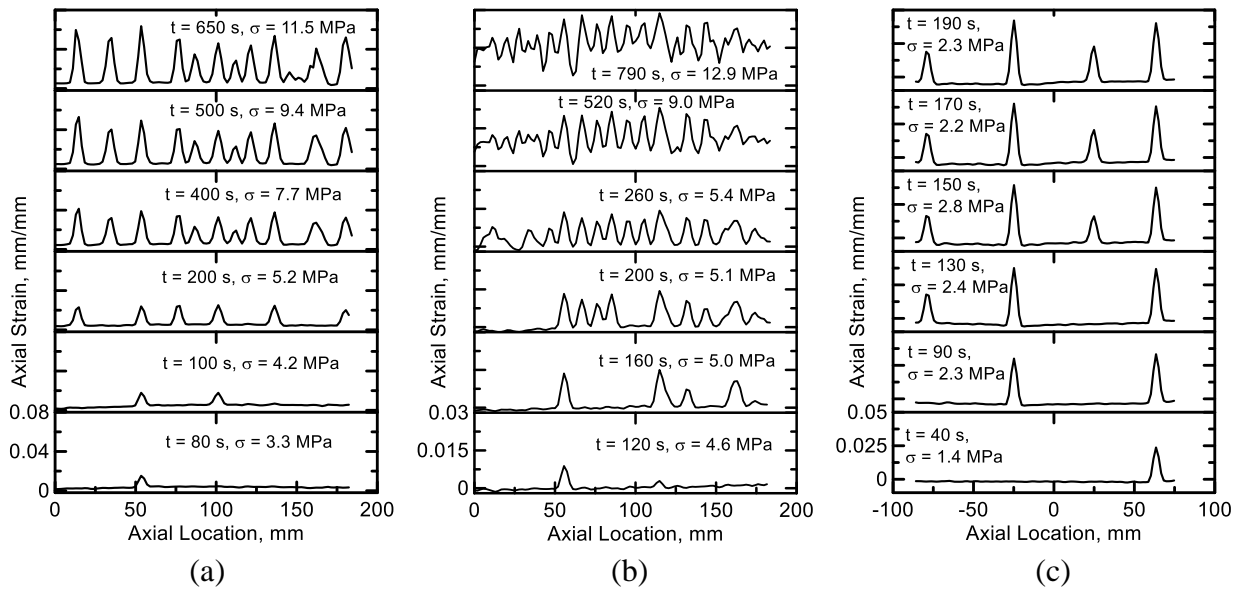


Fig. 7 - Axial strain vs. axial location obtained by DIC for temperatures: (a) 25°C, (b) 200°C and (c) 400°C.

4.2 Finite difference model

A finite difference method developed by Soranakom and Mobasher [1,17,19] was used to model the tension hardening behavior in TRC. A tension specimen is idealized as a series of 1-D segments consisting of fiber, matrix, and interface elements. The matrix is treated as brittle with no strain-softening response. One end of the sample is fixed and an increasing load is applied at the other end such that as the cracking stress of the matrix is exceeded and it cracks, however the load is now carried by the longitudinal yarns through the interface elements. The individual pullout segments continue to transfer the load back and forth between the yarns and matrix. In nonlinear analysis, an iterative solution algorithm is used to enforce material constitutive laws and obtain load-deformations. Once the slip distributions are solved and corresponding stress and strain responses are identified, results are added to represent the overall tensile response.

A numerical base model having a gage length of 200 mm and grip length of 100 mm at each end was simulated and the material responses were used as baseline for subsequent parametric studies. The 400 mm length was discretized into 201 nodes of equal spacing. The representative volume was consisted of 60 longitudinal yarns (yarn area = 0.194 mm²) and matrix phase of cross sectional area of 780 mm² (60 x 13 mm², Vf = 1.5%). The maximum interfacial bond strength $\tau_{\max_base} = 5.5$ MPa was selected as a base model while parametric study will be conducted on this parameter. The stochastic crack pattern was used with the mean matrix strength of 3.5 MPa and standard deviation of 0.1 MPa. Maximum spring force SF_{\max} was held constant as 6 N. The ultimate yarn strength σ_{yu} was set to 4.84 GPa while the elastic modulus is 89 GPa.

The observed decrease in post cracking stiffness with rising temperature from experimental results can be modeled as the degradation in the interfacial bonding characteristics. Fig. 8 shows the base fiber/matrix bond-slip model and variations to investigate its effect on numerical responses.

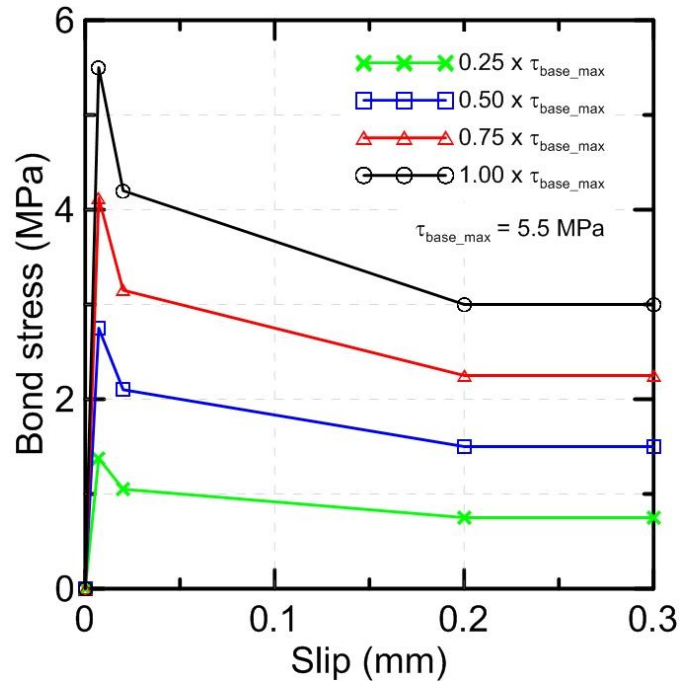


Fig. 8 - Bond-slip model for parametric study.

Fig. 9 shows the composite tensile stress–strain response of the base model as affected by the bond strength. Decrease in bond strength from 1 to 0.25 marginally decreases the postcrack stiffness.

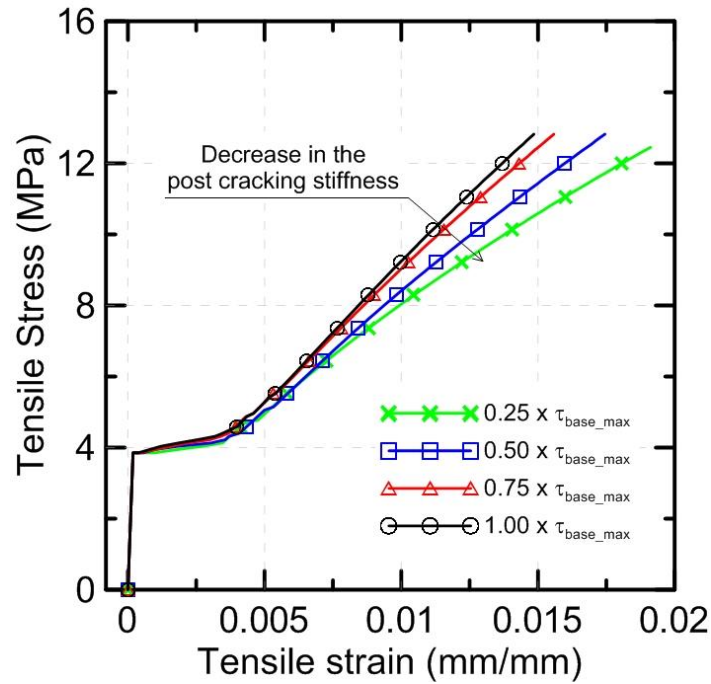


Fig. 9 - Composite stress-strain responses due to variation of bond strength.

This stiffening due to higher bond strength is caused by the intact matrix between two parallel cracks carrying more load. Fig. 10 shows the effect of decreasing bond strength on the saturation crack spacing. Decreasing the magnitude of bond strength causes a flatter slope of the bond-slip model which proportionally decreases the force transfer rate (Force/Length) to the matrix. As the bond strength decreases more development length is required to achieve the cracking strength which results in larger final crack spacing, which agrees with the trend of experimental observation above 150°C.

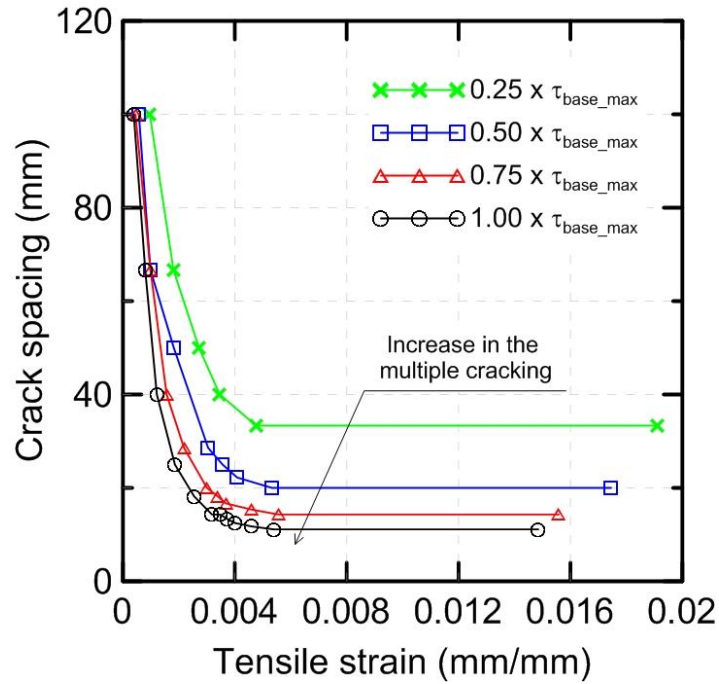


Fig. 10 - Crack spacing versus tensile strain responses with different bond strengths.

The numerical simulations have been carried on 5-layer TRC specimens at several temperatures, and the composite stress-strain responses are compared in Fig. 11. The material parameters for the model are summarized in Table 4.

As post-crack responses were not observed for the TRC's tested at 600°C and 1000°C, numerical simulations were not conducted. As shown in the Fig. 11, the model was able to simulate the experimental responses accurately up to the peak in three stages. Significant degradation in the mechanical performance can be observed when the temperature is above 200°C, indicating the reliability of basalt TRC from room temperature to 150°C.

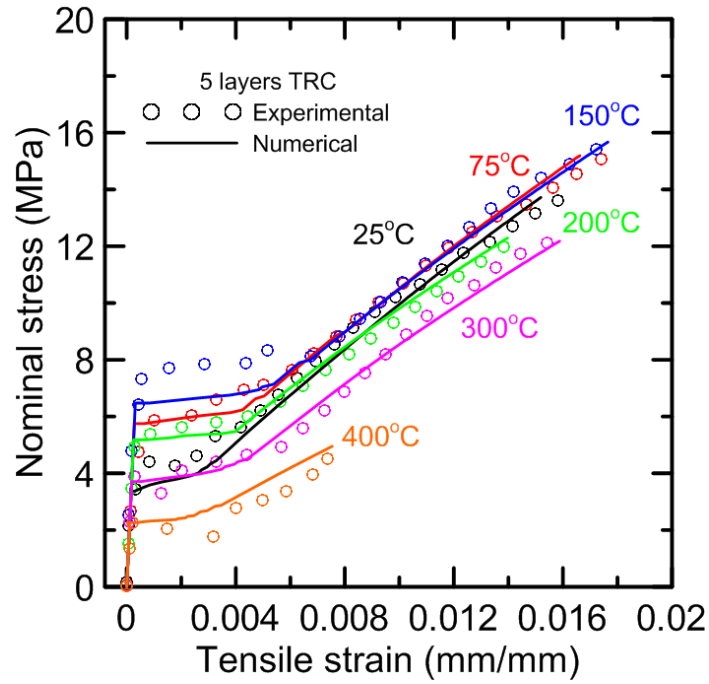


Fig. 11 - Comparison of experimental and numerical 5-layer TRC stress-strain responses at varying temperatures.

Table 4 – Model parameters.

Temperature (°C)	Peak Load (N)	Matrix Cracking Strength (MPa)	Elastic Modulus of Matrix (GPa)	Coefficient of efficiency	Bond Strength (MPa)	Max Spring Force (N)
25	10700	3.5	34	0.75	2.9	
75	11851	4.9	29	0.75	4.6	
150	12226	6.7	32	0.75	4.3	
200	9588	5.1	24	0.75	4.3	6.0
300	9503	4.3	21	0.75	2.5	
400	3862	2.4	11	0.65	1.8	

Fig. 12 compares the experimental and simulated crack spacing versus strain responses of the specimens tested at 25, 200 and 400°C. The smaller crack spacing values observed at 200°C compared to that at room temperature is modelled by a higher bond strength (see Table 4), which is in accordance with the polymer interlock formed under certain temperature. On the other hand, the bond strength used for the specimen at 400°C is below half of the strength for 200°C, which can be related to the complete loss

of polymer coating. Much less transvers cracks are formed due to the inability of the interfaces in transferring sufficient load to form more cracks.

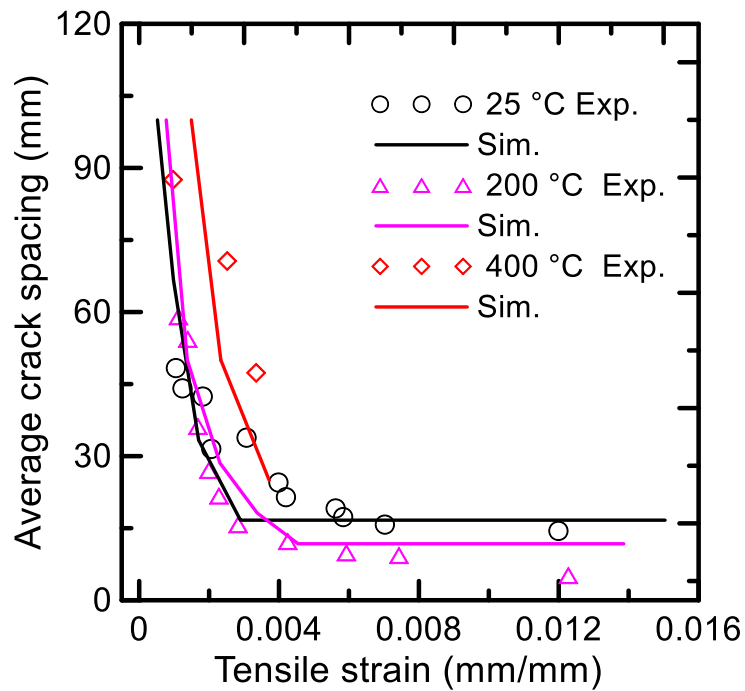


Fig. 12 - Comparison of experimental and numerical crack spacing-strain responses at temperatures of 25, 200 and 400 °C.

In addition, the stress-crack width responses obtained from DIC is also compared with the simulation as shown in Fig. 13, which further validates the rationality and accuracy of the finite difference model, as well as strengthens the connections among experimental observation, DIC measurement and numerical modelling.

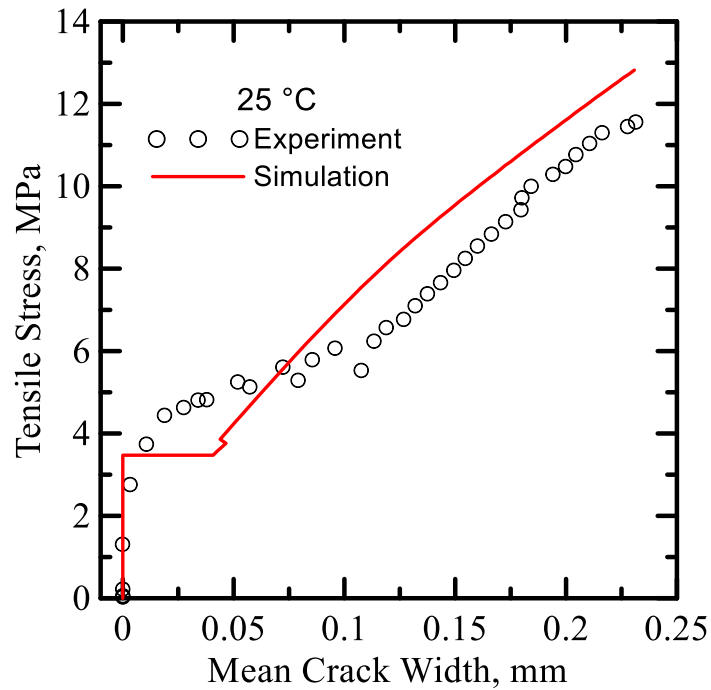


Fig. 13 - Comparison of experimental and numerical stress-crack width responses at room temperature.

5.0 Conclusions

Residual direct tensile tests of a textile refractory composite were conducted using servo-hydraulic testing machine. Crack distribution parameters based on digital image correlation (DIC) method were measured and a finite difference method was used to model the tension hardening behavior of TRCs. The following conclusions can be drawn from the present work:

- An increase in tensile strength and strain capacity with rising temperature was observed for the TRC specimens preheated up to 150°C. Up to this temperature level, the matrix-polymer interlocking mechanism helps to create a high bond between filaments and matrix. Furthermore, the yarn strength is impacted by the penetration of coating which, after cooled, promotes a better load redistribution between the filaments.

- Above 150°C, a clear drop in the tensile performance was observed, due to the coating's thermal decomposition (starting between 150°C and 200°C) and to the dehydration process of the refractory matrix. After the exposure to temperatures of 600°C and 1000°C the behavior of TRC's becomes brittle, presenting tensile strength smaller than at room temperature.
- The DIC measurements of the TRC strain fields presented non-uniform distribution of longitudinal strain consisting of three main zones: localization, shear lag and uniform strain based on the shear lag theory. Based on the full field distributions of tensile strain, multiple important parameters including width of debonding zone, crack spacing and crack width were directly measured.
- A tension stiffening model was able to predict the experimental responses by addressing the mechanical behaviors of matrix, fiber and interfaces. Increase in the bonding strength resulted in a finer crack pattern which is confirmed with the experimental and DIC observations.

[1] Soranakom C, Mobasher B. Geometrical and mechanical aspects of fabric bonding and pullout in cement composites. *Mater Struct* 2009;42:765–77. doi:10.1617/s11527-008-9422-6

[2] Mobasher B. *Mechanics of Fiber and Textile Reinforced Cement Composites*. CRC Press — Taylor and Francis Group 2012: 451.

[3] Rambo DAS, de Andrade Silva F, Toledo Filho RD, da Fonseca Martins Gomes O. Effect of elevated temperatures on the mechanical behavior of basalt textile reinforced refractory concrete. *Mater Des* 2015;65:24–33. doi:10.1016/j.matdes.2014.08.060.

-
- [4] Sutton M, Wolters W, Peters W, Ranson W, McNeill S. Determination of displacements using an improved digital correlation method. *Image Vis Comput* 1983;1:133–9. doi:10.1016/0262-8856(83)90064-1.
- [5] Sutton M, Mingqi C, Peters W, Chao Y, McNeill S. Application of an optimized digital correlation method to planar deformation analysis. *Image Vis Comput* 1986;4:143–50. doi:10.1016/0262-8856(86)90057-0.
- [6] Sutton M a., Turner JL, Bruck H a., Chae T a. Full-field representation of discretely sampled surface deformation for displacement and strain analysis. *Exp Mech* 1991;31:168–77. doi:10.1007/BF02327571.
- [7] Bruck H a., McNeill SR, Sutton M a., Peters WH. Digital image correlation using Newton-Raphson method of partial differential correction. *Exp Mech* 1989;29:261–7. doi:10.1007/BF02321405.
- [8] Ghiassi B, Xavier J, Oliveira D V., Lourenço PB. Application of digital image correlation in investigating the bond between FRP and masonry. *Compos Struct* 2013;106:340–9. doi:10.1016/j.compstruct.2013.06.024.
- [9] Giancane S, Panella FW, Nobile R, Dattoma V. Fatigue damage evolution of fiber reinforced composites with digital image correlation analysis. *Procedia Eng* 2010;2:1307–15. doi:10.1016/j.proeng.2010.03.142.
- [10] Hild F, Roux S, Guerrero N, Marante ME, Flórez-López J. Calibration of constitutive models of steel beams subject to local buckling by using digital image correlation. *Eur J Mech - A/Solids* 2011;30:1–10. doi:10.1016/j.euromechsol.2010.09.007.
- [11] Vijaya Kumar RL, Bhat MR, Murthy CRL. Evaluation of kissing bond in composite adhesive lap joints using digital image correlation: Preliminary studies. *Int J Adhes Adhes* 2013;42:60–8. doi:10.1016/j.ijadhadh.2013.01.004.

-
- [12] Yao Y, Silva FA, Butler M, Mechtcherine V, Mobasher B. Tension stiffening in textile-reinforced concrete under high speed tensile loads. *Cement and Concrete Composites* 2015;44:49-61. <http://dx.doi.org/10.1016/j.cemconcomp.2015.07.009>
- [13] Tetta ZC, Koutas LN, Bournas DA. Textile-reinforced mortar (TRM) versus fiber-reinforced polymers (FRP) in shear strengthening of concrete beams. *Compos Part B Eng* 2015;77:338–48. doi:10.1016/j.compositesb.2015.03.055.
- [14] Dey V, Zani G, Colombo M, Di Prisco M, Mobasher B. Flexural impact response of textile-reinforced aerated concrete sandwich panels. *Materials and Design* 2015; 86: 187–197. doi:10.1016/j.matdes.2015.07.004
- [15] Gupta AK, Maestrini SR. Tension-Stiffness Model for Reinforced Concrete Bars. *J Struct Eng* 1990;116:769–90. doi:10.1061/(ASCE)0733-9445(1990)116:3(769).
- [16] Bažant ZP, Oh BH. Deformation of progressively cracking reinforced concrete beams. *ACI J* 1984;81:268–78.
- [17] Soranakom C, Mobasher B. Modeling of tension stiffening in reinforced cement composites: Part I. Theoretical modeling. *Mater Struct* 2010;43:1217–30. doi:10.1617/s11527-010-9594-8.
- [18] Silva FDA, Mobasher B, Soranakom C, Filho RDT. Effect of fiber shape and morphology on interfacial bond and cracking behaviors of sisal fiber cement based composites. *Cem Concr Compos* 2011;33:814–23. doi:10.1016/j.cemconcomp.2011.05.003.
- [19] Soranakom C, Mobasher B. Modeling of tension stiffening in reinforced cement composites: part II - simulations vs. experimental results. *Mater Struct* 2010;43:1231-43. doi: 10.1617/s11527-010-9593-9

-
- [20] Yao, Y., Bonakdar, A., Faber, J., Gries, T., & Mobasher, B. Distributed cracking mechanisms in textile-reinforced concrete under high speed tensile tests. *Materials and Structures*, 2015. doi:10.1617/s11527-015-0685-4.
- [21] De Larrard F. *Concrete mixture proportioning: a scientific approach*. London. E&FN SPON. 1999.
- [22] Sedran T. *Rhéologie et rhéométrie des bétons: application aux bétons autonivelants*. Doctoral dissertation. Ecole Nationale des Ponts et Chaussées 1999:484.
- [23] Pan B, Qian K, Xie H, Asundi A. Two-dimensional digital image correlation for in-plane displacement and strain measurement: a review. *Meas Sci Technol* 2009;20:062001. doi:10.1088/0957-0233/20/6/062001.
- [24] Gao G, Yao W, Xia K, Li Z. Investigation of the rate dependence of fracture propagation in rocks using digital image correlation (DIC) method. *Eng Fract Mech* 2015;138:146–55. doi:10.1016/j.engfracmech.2015.02.021.
- [25] Bruck H a., McNeill SR, Sutton M a., Peters WH. Digital image correlation using Newton-Raphson method of partial differential correction. *Exp Mech* 1989;29:261–7. doi:10.1007/BF02321405.
- [26] Feih S, Boiocchi E, Kandare E, Mathys Z, Gibson AG and Mouritz AP. Strength degradation of glass and carbon fibres at high temperature. *Journal of Materials Science* 2008; 44(2):392-400. doi: 10.1007/s10853-008-3140-x
- [27] Krüger M, Reinhardt HW. In: Wolfgang Brameshuber, editor. *Fire resistance. Report 36: textile reinforced concrete – state-of-the-art report of RILEM technical committee 201-TRC*. Bagneux: Rilem publications S.A.R.L; 2006. p. 83–218. Chapter 6.

Artigo E – Rambo DAS, Silva FA, Toledo RD and Gomes OFM. Effect of elevated temperatures on the in-situ tensile strength of coated and uncoated carbon textile reinforced refractory composites. Submitted to Construction and Building Materials (2015). Pending review.

**Effect of elevated temperatures on the in-situ tensile strength of coated and uncoated
carbon textile reinforced refractory composites**

Dimas Alan Strauss Rambo^{a*}, Flávio de Andrade Silva^b, Romildo Dias Toledo Filho^c and Otávio
da Fonseca Martins Gomes^d

^{a,c}Civil Engineering Department, COPPE, Universidade Federal do Rio de Janeiro, P.O. Box
68506, CEP 21941-972, Rio de Janeiro – RJ, Brazil.

^b Civil Engineering Department, Pontifícia Universidade Católica do Rio de Janeiro (PUC-Rio),
Rua Marques de São Vicente 225, 22451-900 - Rio de Janeiro –RJ, Brazil.

^d Centre for Mineral Technology (CETEM), Av. Pedro Calmon 900, CEP 21941-908, Rio de
Janeiro – RJ, Brazil.

October 2015

*Corresponding author: e-mail: dimasrambo@gmail.com, Tel: +55(21) 3938-8215 ext. 204. Fax: +55 (21) 3938-8484.

Abstract

This work presents the results of an experimental investigation on the mechanical behavior of coated and uncoated carbon textile reinforced concrete (TRC) submitted to in-situ direct tensile tests (hot condition). Targeted constant temperatures considered were in the range of 25 to 600°C, in view of the main dehydration processes occurred in the used refractory matrix as well as the oxidation of the carbon fiber. Thermogravimetry and X-ray diffraction analysis were used to study the matrix phase changes as a function of temperature. Scanning electron microscopy (SEM) was performed in order to understand the effects caused by the presence of coating and by the carbon oxidation in the fiber–matrix interfaces. Given the effectiveness of the uncoated fabric embedment in the refractory matrix and the thermal stability of carbon fibers, the uncoated TRC exposed to 400°C was able to maintain the same load carrying capacity obtained at room temperature, while the strain capacity increased approximately by one order. In the coated TRC, the increase of temperature affected the fiber-matrix interfacial microstructure leading to a clear trend of tensile strength reduction.

Keyword: in-situ high temperature strength, textile reinforced refractory concrete, carbon fiber, calcium aluminate cement, high temperatures.

1. Introduction

Extensive efforts have been done to include TRC as a construction material into the market. However, there are still open aspects related to the material performance that need to be addressed and understood. One of these gaps recently highlighted in the 3rd International Conference on Textile Reinforced Concrete, deals with the mechanical performance of TRC under elevated temperatures [1] and fire conditions [2]. If little is known about the thermo-mechanical performance of Portland Cement TRC, even less is known about TRC performance using refractory concrete as a matrix [3, 4].

Refractory matrices are suitable for applications where elevated temperatures are expected. Furthermore, high alumina cements, used typically in refractory matrices, has alkali content typically less than 0.5% of its weight [5]. At this concentration the risk of alkali attack, common to carbon, basalt, glass and natural fibers, decreases substantially. Taking advantage of these properties, several researches in the past used aluminous cements to produce fiber reinforced composites (specially using glass fibers) [6].

The response of refractory concrete when submitted to elevated temperatures depends on the thermo-hygro-chemo-mechanical properties of the concrete determined by the cementitious and aggregate composite multi-scale structure, as well as boundary conditions such as humidity, heating rate, exposure time and presence of gases [7,8,9]. In concrete reinforced with fabrics or fibers, the mechanical response is also dependent on the reinforcement properties such as thermal expansion and melting point and its transitional interaction with the concrete matrix during the heating regime. In most cases, coatings are applied to textile fabrics, in order to modify their characteristics with relation to mechanical anchorage and durability. However, when exposed to

moderated or elevated temperatures, some types of coatings may change the fibers chemical and mechanical properties, leading to a reduced bond performance with the CAC [3].

A limited number of scientific researches have studied the temperature effect on textile reinforced composites [3,4 ,10,11]. Rambo et al [4] performed residual and in-situ tensile test on refractory TRC reinforced with coated basalt fabrics. According to the authors, a much more aggressive loss of the load-carrying capacity was observed in the in-situ condition. With increasing temperature in in-situ conditions, a significant reduction in tensile strength, elastic modulus and strain capacity was observed. Ultimate tensile strength values obtained under in-situ conditions were, on average, about 2 times lower than the residual ones. Such detrimental effect occurred in part due to the visco-elastic/plastic changes of the polymer with temperature as well as the pore pressures that combined with thermal cracking reduced the mechanical performance of the TRC in the in-situ condition.

Silva et al. [8], performed residual tensile test on TRC reinforced with coated carbon fibers, heated up to 600°C. The results showed that when heating the polymer coated carbon fibers TRC under temperatures up to 150°C a polymer-based interlocking mechanism between the filaments and matrix is revealed. This mechanism resulted in a significant increase in the maximum pullout load.

Colombo [10] showed the applicability of TRC's (reinforced with AR-glass fabric) on sandwich panels with the purpose of saving energy in new and existing buildings (energy retrofitting). In this study the durability of TRC when exposed to freezing-thawing cycles was investigated. According to the authors, curing conditions, both cooling and heating, may affect matrix shrinkage, and consequently the bond phenomenon in the composite material. In relation to the

freeze-thaw cycles, mechanical performances of TRC's are directly related to their self-healing and late hydration capacity since matrix cracking occurs during thermal cycles.

Taking advantage of the carbon thermal stability, Maluk et al. [12] evaluated the fire resistance of five large-scale concrete elements (OPC matrix) prestressed with carbon fiber reinforced polymer (CFRP) tendons simultaneously in a single standard floor furnace test. The authors showed that the fire resistance of CFRP prestressed elements is influenced by the occurrence of heat-induced concrete spalling or, by the loss of mechanical anchorage (as a result of the softening process of the resin). The loss of anchorage appeared to begin when the temperature at the lower edge of a central CFRP tendon at midspan reached around 310°C.

In this context, the aim of this article is to investigate the effect of elevated temperatures on the mechanical properties of a textile refractory composite reinforced with coated and uncoated carbon fabrics submitted to tensile loading under in-situ testing condition. The refractory composites were produced with a cementitious matrix, made of synthetic calcium aluminate aggregates and calcium aluminate cement (CAC), and then reinforced with carbon fabrics. The in-situ tests (hot condition) were performed after 1h of exposure at the target temperatures (25 to 600°C), without cooling process (common in residual tests). Micro-structural analyses using a scanning electron microscope (SEM) were carried out to evaluate the degradation of the fiber-matrix interface in both composites. Thermo-gravimetric analysis (TGA) and powder X-ray diffraction (XRD) were used to investigate the matrix and fibers degradation as well as their correlation with the TRC mechanical properties.

2. Materials and methods

a. Refractory Concrete Matrix

The matrix used in this research was designed using the compressible packing method (CPM) [13,14] to achieve a compressive strength of about 45MPa and adequate rheology to produce laminated TRC's. The materials used in the TRC composition were a calcium aluminate cement (Secar 51 from Kerneos Inc.) with an alumina content of about 51%, a synthetic calcium aluminate aggregate (Alag from Kerneos Inc. with an alumina content of about 40%) with diameters ranging from 0.001mm to 1.18mm and a polycarboxilate superplasticizer in powder (Peramin CONPAC 500 from Kerneos Inc.). The water/cementitious mass ratio of the refractory concrete was 0.35. Table 1 gives the composition of the concrete matrix.

Table 5 – Mix composition.

Composition	
Dense aggregate (kg/m ³)	1416.2
Cement (kg/m ³)	750
Superplasticizer (kg/m ³)	4.87
Viscosity modifier agent - VMA (kg/m ³)	0.562
Water (kg/m ³)	262.6
Superplasticizer content (%)	0.65
Water/cementitious material ratio	0.35

b. The carbon fabrics

Two types of carbon fabrics (coated and uncoated), commercialized by Toho Tenax, Europe, were used as reinforcement for the TRC specimens. The warp as well as the weft, in both fabrics, is formed by about 11900 monofilaments with an average diameter of 6.29 μm (see item 4).

Table 2 presents the properties of the used carbon textiles.

Table 6 – Properties of the carbon fabrics.

Features	Uncoated Fabric	Coated Fabric
Warp wire spacing (mm)**	7.2	7.2
Stitching yarn**	polypropylene	polypropylene
Filament diameter (μm)*	6.29	6.29
Type of coating**	none	epoxy based coating

*Determined by authors (see item 4)

**Manufacturer data

c. Matrix processing and composite manufacturing

The refractory concretes were produced in a temperature controlled room of $24^{\circ}\text{C} \pm 1^{\circ}\text{C}$ using a planetary mixer (moisturized in advance) of 5 liters capacity. The cementitious materials were homogenized by dry mixing for 60s prior to water addition. The mixture was blended for 5 minutes. The viscosity modifier agent type Rheomac UW 410 (VMA) was added after 4 minutes of mixing. Rectangular plates measuring 400 mm x 250 mm x 13 mm (length x width x thickness) were produced for direct tensile tests using a lamination technique. For the plate production, concrete was poured in acrylic molds. The process started with a thin concrete layer placed at the bottom of the mould. The second phase was the placement of the first fabric of carbon textile reinforcement over the fresh concrete. The carbon fabric was then pressed and smoothed in order to regularize and align the surface of the layer. After the second phase, the procedure was repeated until reaching the desired number of fabric layers. In this study two equally spaced fabric layers were used as reinforcement in the TRC's, resulting in a fiber volume fraction of 1.92%. A manual vibration was applied to the samples. After 7 days, the rectangular plates were de-moulded and cut, resulting in 4 specimens of 400 mm x 60 mm x 13 mm (length x width x thickness). The applied stress was obtained by dividing the load by the nominal area of

the specimen's cross section. The cross-sectional area was determined from the average of four measurements (width and thickness) at four different locations of each sample.

3. Testing condition and heating regime

a. In-situ strength

The TRC specimens tested in direct tension at “in-situ” condition were performed at 25°C, 200°C, 400°C and 600°C. The heating regime applied to the specimens (at an age of 7 days) is presented in the Fig. 1.

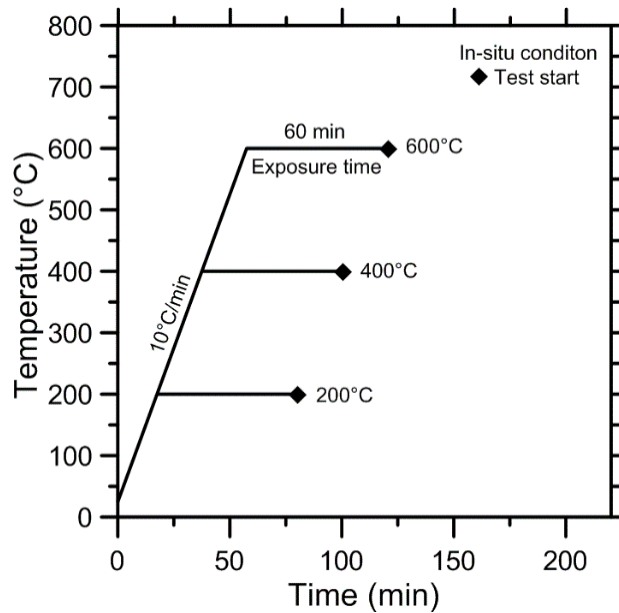


Fig. 1 – Heating regime applied to the refractory TRC's.

A Shimadzu universal testing machine coupled to an electric furnace with a radiant heating unit was used to perform the tensile tests up to 600°C (Fig. 2).

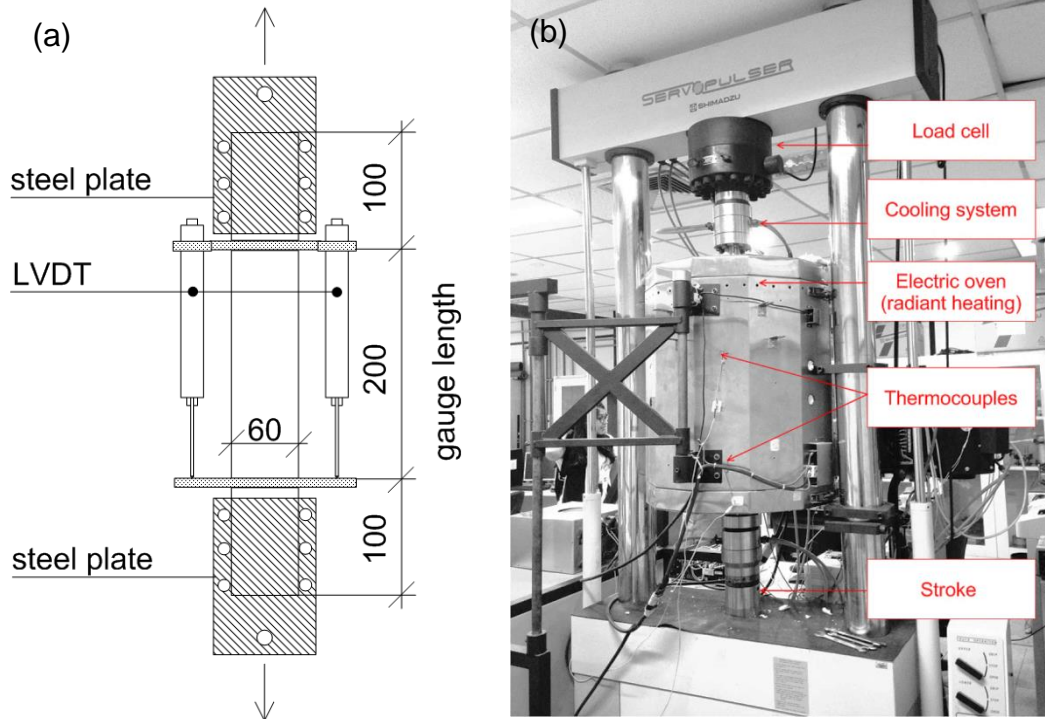


Fig. 2 – Direct tensile test set up for the TRC (a) and In-situ testing condition (b). Measurements in millimeters.

The actuator displacement rate was 0.4 mm/min. For all target temperatures between 25°C and 600°C, the strain measurements were done using LVDT's for high temperatures (maximum working temperature of 700°C). All samples were subject to a heating rate of 10°C/min in the furnace. Temperature levels were kept constant for 60 min at each target temperature before the beginning of loading. The tensile force was applied to the specimens using rotatable steel plates screwed at both outer ends of the TRC plates. Four rectangular shaped specimens measuring 400mm x 60mm x 13mm (length x width x thickness) were tested for each temperature range and testing condition, using a gage length of 200 mm with fixed-hinged boundary conditions. The laminated composites were tested in the warp direction.

4. Image acquisition

a. Determining the cross sectional area of the yarns

To enable a precise determination of the real fiber volume fraction used to reinforce the TRC's, the cross-sectional area of the carbon yarns was measured by image analysis. The samples of carbon yarns were cold embedded in epoxy resin to form cylindrical blocks of 30 mm diameter and about 30 mm height. These blocks were ground and polished with diamond suspensions down to 1 μm in an automatic polishing machine following the traditional metallographic sample preparation. Then, the cross-sections were covered with evaporated carbon to make them conductive and suitable for conventional SEM analysis. A SEM FEI Quanta 400 was used to acquire back-scattered electron images (8 bit, 1024 x 884 pixels, 1.67 $\mu\text{m}/\text{pixel}$) from polished cross-sections of individual yarns (Fig. 3a). This kind of image presents atomic number contrast [15] and consequently allows the discrimination among fibers, coatings, and the epoxy resin.

b. Image analysis

The image analysis was performed through an automatic routine implemented as a script in the Zeiss Axiovision software. Fig. 3 presents a sample image obtained in the SEM (Fig. 3a), in which an entire yarn section can be seen close to the center, some images that arise from routine intermediate steps (Fig. 2b-e), and the resulting image from which the yarn and its fibers were measured (Fig. 2f). The critical image analysis step is the segmentation. The aim of segmentation is to distinguish the relevant components of the image in order to recognize and measure them. In the present case, these components are yarns and their composing fibers. The routine starts by segmenting fibers. It is carried out through intensity thresholding using the Otsu [16] automatic method. The resulting binary image (Fig. 3b) shows white fibers surrounded by a black background. The segmentation of yarns is made from the binary image of fibers (Fig. 3b)

employing a sequence of image processing operations [17]. The binary image of fibers passes through a morphological closing (cross structuring element, 5 times) and a binary fill operation in order to connect them (Fig. 3c). Following, partial imaged yarns that touch image edges are removed, as well as, spurious fibers and noise that are eliminated by their sizes. Therefore, the resulting image presents one segmented yarn (Fig. 3d). The binary intersection of the latter image and the binary image of fibers returns the fibers of the segmented yarn (Fig. 3e). Fig. 3f presents a pseudo-color composition of Fig. 3d and Fig. 3e showing the segmented yarn and its fibers. Once the yarn and its fibers were segmented, measurements of the yarn area and the area fraction of fibers are automatically obtained. The average result for the warp yarns was 0.45 mm^2 obtained from 5 independent measurements. The calculated fiber volume used to reinforce the carbon TRC's (2 layers) was 1.92%.

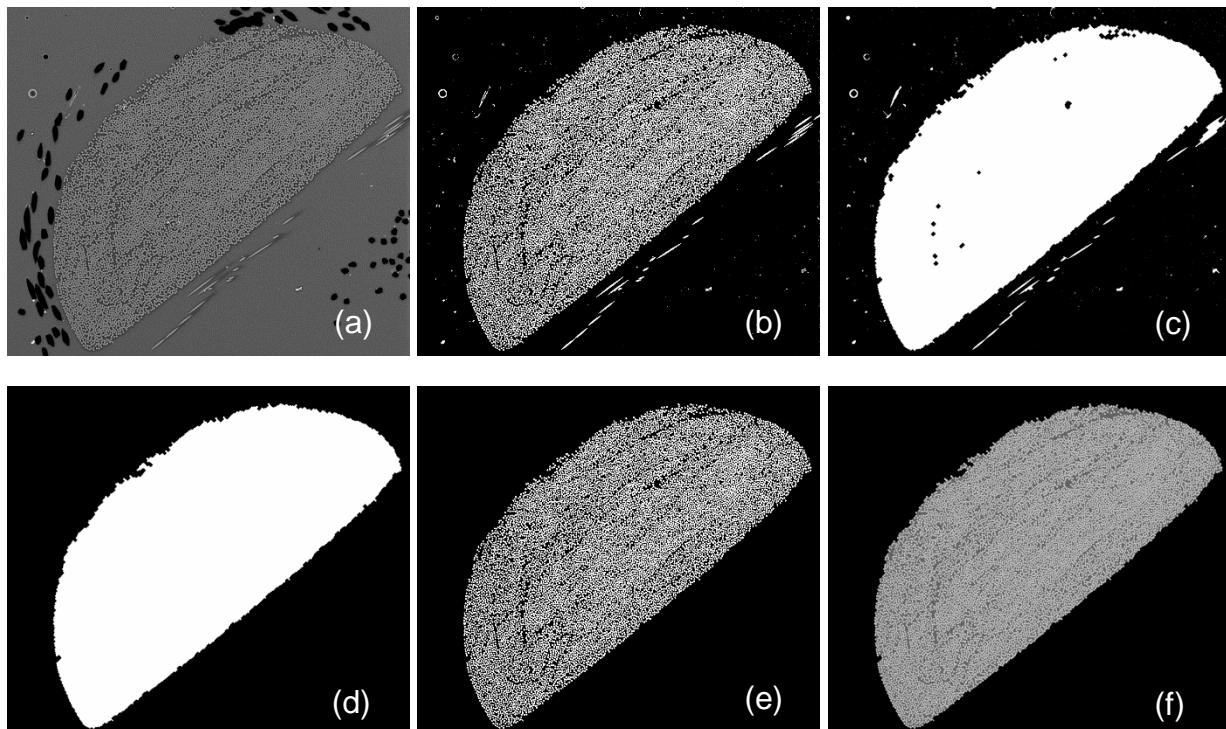


Fig. 3 – Image analysis: (a) SEM back-scattered electron image; (b) binary image of fibers; (c) joining fibers; (d) segmented yarn; (e) fibers of segmented yarn; (f) segmented yarn and its fibers.

5. Materials characterization

Before and after heating, fiber–matrix interfaces were investigated using a SEM FEI Quanta 400. For this, TRC samples were sectioned in specimens with dimensions of 20 x 20 mm (length x width). The samples were coated with about 20 nm gold to become conductive and suitable for conventional SEM analysis. The SEM was operated using 25 kV of accelerated tension and about 30 mm of working distance. TG analyses were carried out using crushed fragments of the samples tested under tensile loading. After testing, the extracted samples, were placed in plastic bags to avoid contact with moisture. Samples of about 10 mg were collected and analyzed. The thermal analyses were performed in a TA Instruments, SDT Q600 model TGA/DTA/DSC simultaneous apparatus with temperatures ranging between 35 and 1000°C using 100 mL/min of nitrogen flow. In order to eliminate the residual non-bounded free water, an isothermal step at 35°C during 1 hour was applied before the analyses. The reference material and sample pans were platinum. The TG analyses of the uncoated carbon fibers were carried out in the same way as used for concrete samples. However, using atmospheres of nitrogen and synthetic air. The refractory concretes and also de carbon fibers were analyzed by X-ray diffraction (XRD) with a 2θ value between 3 to 55° with a Brucker D8 Advance instrument using a step of 0.02° and a $\text{CuK}\alpha_{1,2}$ radiation. In order to enable a qualitative analysis, matrix samples were prepared using crushed matrix material with particle sizes less than 75 μm . The analyzes were performed with samples stored at room temperature and preheated up to 200°C, 400°C and 600°C (key temperatures in the dehydration process of the used refractory concrete).

6. Discussion and analyses

a. Influence of temperature on uncoated carbon TRC in-situ tensile behavior

Fig. 4 shows representative stress–strain curves obtained from the in-situ tensile tests at 25°C, 200°C, 400°C and 600°C performed on TRC specimens, reinforced with 2 bi-directional uncoated carbon fabric layers. Results obtained from the specimens tested at 7 days of age are given in Table 7. All values represent the average of three TRC test specimens. The TRC under consideration presents a typical non-linear tensile stress-strain curve composed by three main stages: At first, a linear branch where the material reveal its elastic behavior and which ends at the bend-over point (BOP). In the second phase, the matrix tensile strength is reached and a non-linear response start to appear. This behavior is a result of multiple-cracking of the matrix and the redistribution of efforts by the reinforcement. Immediately after the initiation of the first matrix crack, other cracks also propagate throughout the specimen at approximately regular intervals (related to the fabric geometry and the fiber-matrix interface). Since several cracks are formed, there is an increase in the measured total strain. In the third phase, normally, no further cracks occur and only the contribution of the textile is visible, culminating in the ultimate tensile strength (UTS). The tensile performance of TRC specimens turned out to be strongly affected by temperature when submitted to in-situ tests. A strain-hardening behavior was observed for the uncoated carbon TRC's at all targeted temperature up to 400°C. Test results revealed decrease of 8.7% on the σ_{BOP} of the TRC heated up to 200°C, in comparison with the TRC tested at room temperature. On the other hand, for the ultimate tensile strength (σ_{UTS}), there was an increase of 21.6%. With relation to the strain capacity (ϵ_{UTS}), the increase achieved about 61%.

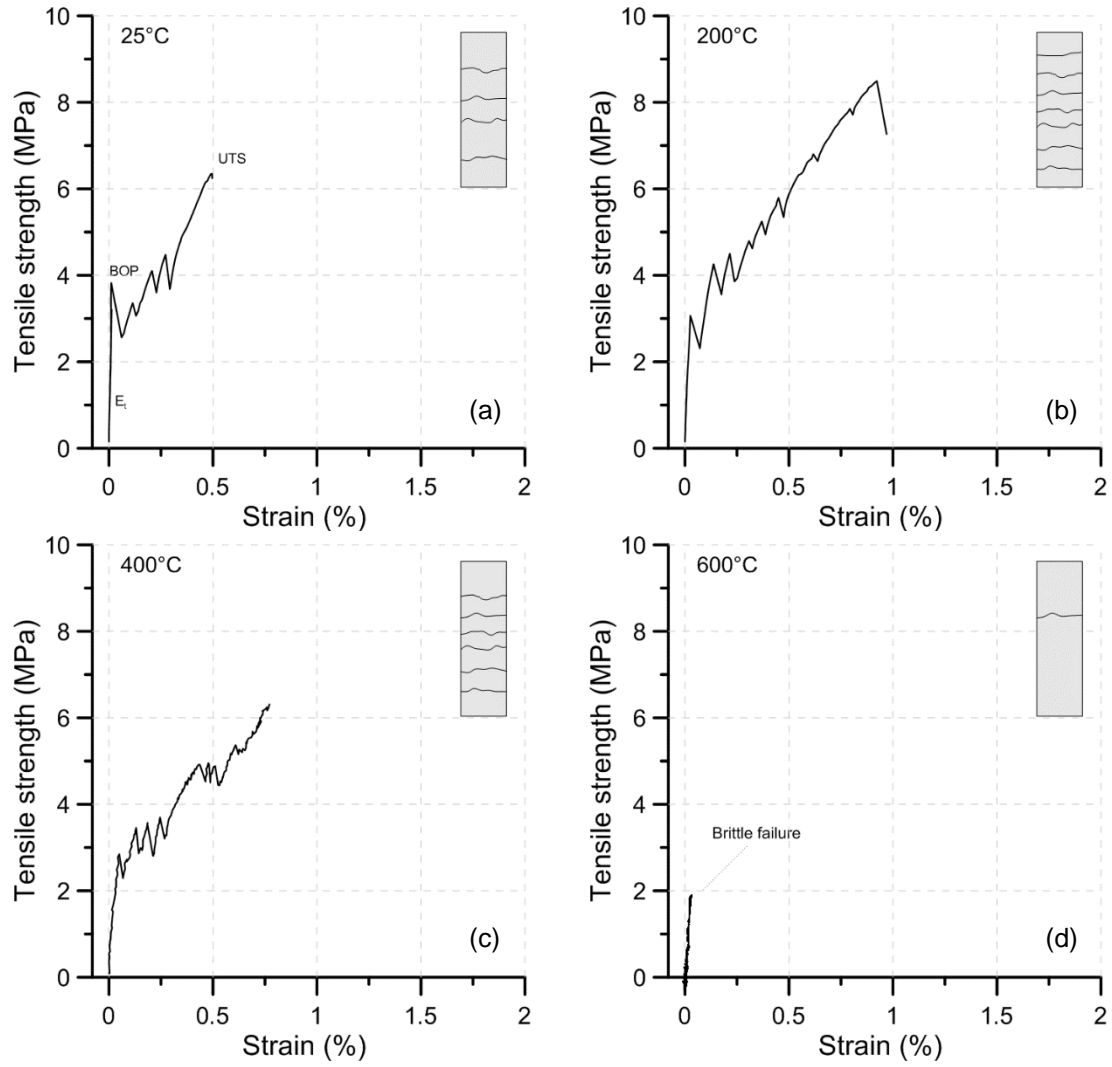


Fig. 4 – Influence of temperature on the in-situ tensile strength of laminated TRC's reinforced with 2 uncoated carbon layers. Stress-strain curves for (a) room temperature, (b) 200°C, (c) 400°C and (d) 600°C.

Table 7 – Average results of the in-situ tensile test performed on the uncoated carbon TRC.
Standard deviation values are presented in parentheses.

Heating Rate	Target Temperature	First crack values			Post crack values	
		σ_{BOP} (MPa)	ϵ_{BOP} (%)	E_t (GPa)	σ_{UTS} (MPa)	ϵ_{UTS} (%)
-	25°C	3.77 (0.27)	0.0139 (0.0029)	24.72 (5.20)	6.51 (0.37)	0.54 (0.17)
10°C/min T.P.: 1h	200°C	3.44 (1.09)	0.0275 (0.0008)	12.89 (3.57)	7.92 (0.96)	0.87 (0.20)
10°C/min T.P.: 1h	400°C	3.15 (0.57)	0.0512 (0.0044)	5.45 (0.23)	7.06 (0.68)	1.05 (0.39)
10°C/min T.P.: 1h	600°C	2.11 (0.73)	0.0291 (0.0051)	5.46 (2.86)	-	-

T.P.: Time period in which the specimens were kept at the target temperature.

This positive influence on the σ_{UTS} and ϵ_{UTS} values (see Fig. 5) is associated, in part, with the increase on the mechanical anchorage of the carbon yarns given by the matrix shrinkage at 200°C [18]. Similar behavior was reported by other authors in the past, using different types of fibers [19,18]. With relation to the reinforcement, the temperature of 200°C is not able to degrade severely the carbon fiber strength [20]. At this temperature the behavior of the textile reinforcement was still effective in limiting the crack propagation thus increasing the load capacity of the TRC. Due to the decrease on matrix stiffness and the shrinkage, the number of cracks formed in the uncoated carbon TRC at 200°C was more pronounced than at room temperature. As reported by Park [21], carbon fibers show a small negative coefficient of thermal expansion in the fiber direction and large positive coefficient in the opposed direction. This property may be advantageous to the case of TRC, given that the fabric yarns can work as prestressing bars into the composite in the longitudinal direction at the same time that increase interface contact with the cementitious matrix. With relation to the elastic modulus, the composite tested at 200°C presented elastic modulus 47.85% lower than the TRC tested at room temperature.

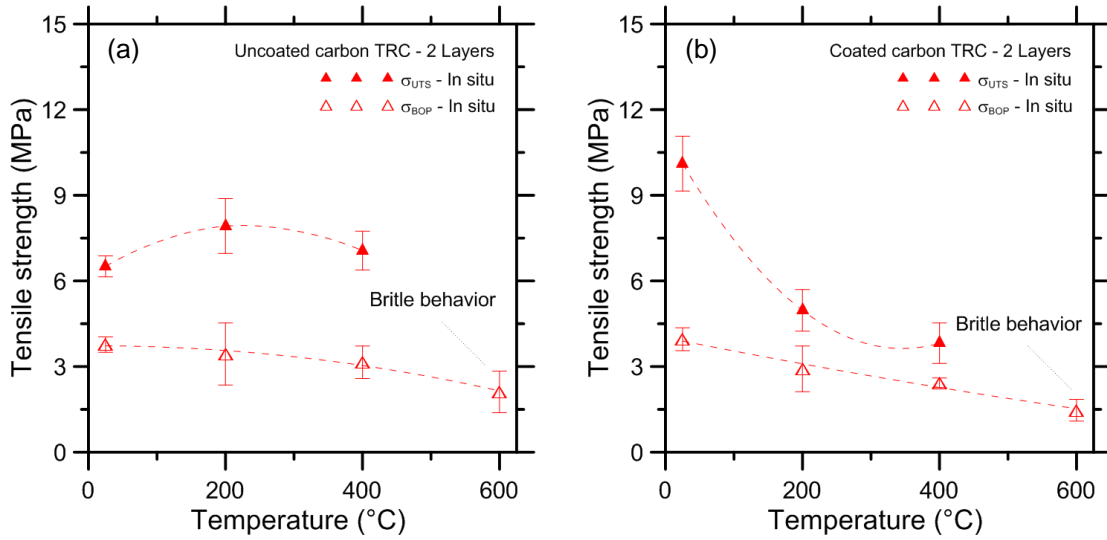


Fig. 5 – Comparative of tensile response in both carbon TRC's: (a) Uncoated and (b) coated.

The degradation of E_t at 200°C can be explained observing the TG studies showed in Fig. 6a. Between 25°C and 200°C the investigated matrix suffers several changes: evaporation of free water, loss of structural water of the AH_x gel, dehydration of metastable CAH_{10} ($CaO \cdot Al_2O_3 \cdot 10H_2O$) and C_2AH_8 ($2CaO \cdot Al_2O_3 \cdot 8H_2O$) and finally, initiation of dehydration of stable AH_3 ($Al_2O_3 \cdot 3H_2O$) and C_3AH_6 ($3CaO \cdot Al_2O_3 \cdot 6H_2O$) phases.

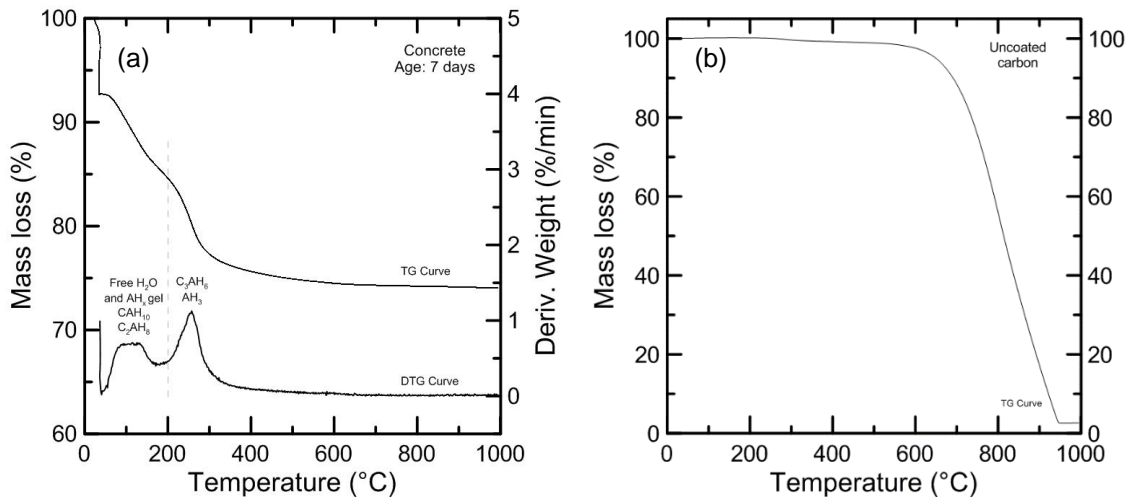


Fig. 6 – Thermal analysis of the refractory concrete at 7 days of age (nitrogen flow) and of the uncoated fibers on initial sample mass basis (synthetic air).

As shown in Fig. 7a CAH_{10} and C_2AH_8 phases were not detected by XRD at 200°C and above, confirming total dehydration of both phases. Since the evolution of modulus of cement based materials during hydration is related to the growth of solid volume and to the degree of connectivity of the solids, the loss of chemically-bound water due to the dehydration process up to 200°C reduced substantially the E_t value. Given the effectiveness of the uncoated fabric embedment in the refractory matrix, the specimens exposed to 400°C showed no reduction on the ultimate tensile strength if compared to the specimens tested at room temperature. As reported by Soranakom et al. [22], in the case of uncoated fabrics, the paste infiltration as well as the dense structure formed surrounding the yarn can reduce the potential of debonding at the interface zone. On the other hand, the strain capacity of the specimens heated up to 400°C increased approximately by one order. This behavior occurs because the composite heated up to 400°C presents large crack widths [3]. Thus, even forming lower amount of cracks compared to the TRC tested at room temperature, the ultimate strain at 400°C was the highest among all uncoated composites. It is important to remember that this energy absorption capacity is essential for providing damage tolerance in applications where elevated temperatures are expected (i.e: tunnel lining, fire barriers, cooling towers and encapsulation elements).

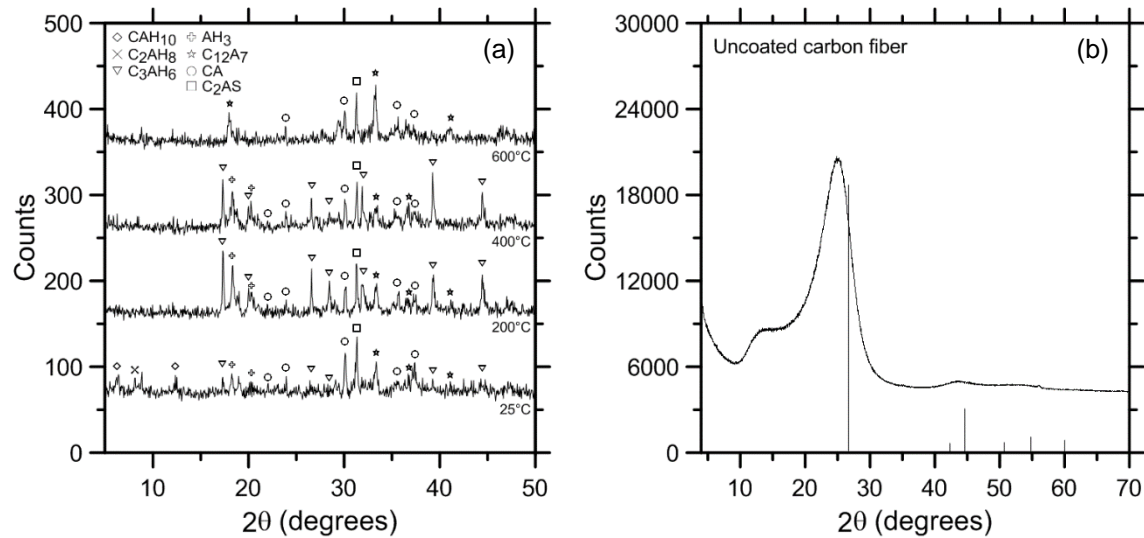


Fig. 7 – XRD profiles for the refractory concrete (25°C, 200°C, 400°C and 600°C) (a) and for the uncoated carbon fiber (b). The vertical bars in the Fig. 7 (b) show the graphite peak positions.

As shown in Fig. 8, at 400°C the internal filaments slip when the TRC is loaded. Thus, the smaller the interfilament friction the smaller the TRC load carrying capacity. As reported by Feih et al. [20], a considerable reduction in tensile strength of the carbon fibers may occur for moderated temperatures (~450°C). This explains, in part, the reduction of 10.8% in the ultimate tensile strength of the composite at 400°C in comparison with 200°C. At this temperature, not only the carbon fiber is partially degraded but also the stable hydrates C_3AH_6 and AH_3 .

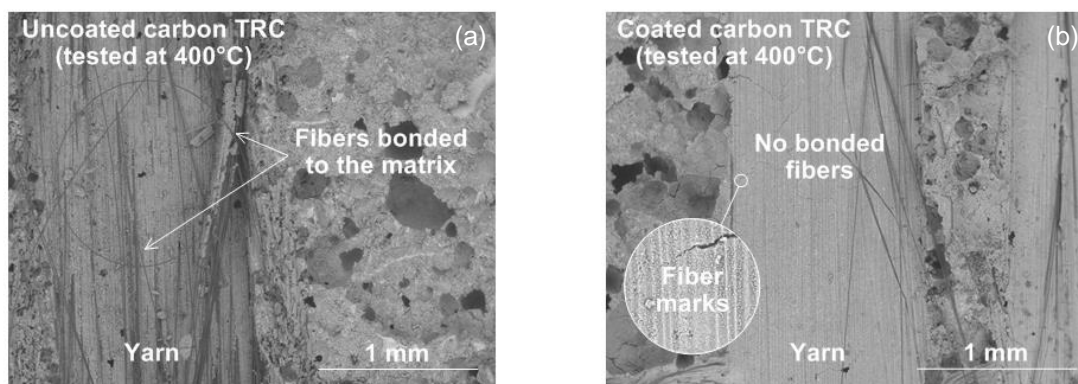


Fig. 8 – Bonding characteristics in fractured samples extracted from uncoated and coated carbon TRC's exposed to 400°C.

As can be seen in the thermo-gravimetric analyses (Fig. 6a), at 400°C, the long term hydrates C_3AH_6 and AH_3 were completely dehydrated. However, it is still possible to observe traces of both hydrates at the XRD patterns at 400°C. This behavior was well discussed by Rambo et al. [4], and refers to the dissolution and re-precipitation processes, which occur in the in situ test, during the conversion of metastable hydration products (CAH_{10} , AH_x and C_2AH_8) to stable ones (C_3AH_6 and AH_3). Conversion reactions are accompanied by a consecutive increase in material porosity and, consequently, loss of strength and elastic modulus. The E_t values obtained under in-situ tension at 400°C were, on average, about 5 times lower than at room temperature. As reported by Feih [20], the elastic modulus of carbon fibers is expected to remain constant up to 450°C, although reduction in cross sectional area can occur. At 600°C, the specimens exhibited a brittle behavior, reaching only 2.11 MPa of strength. This behavior is explained by different factors among which is necessary to highlight the oxidation of carbon fibers. As there are no hydrated products between 400°C and 600°C, the main deteriorating agent responsible for the decrease of the TRC tensile strength is the fiber oxidation. The TG curves of the uncoated carbon fibers are shown in Fig. 6b. The carbon fibers are stable during their initial heating from 28 to 450°C. At this range the weight remains approximately 99%. However, beyond 488°C a significant drop on carbon fiber mass occur due to the carbon oxidation which result in the formation of carbon monoxide (CO) and carbon dioxide (CO₂). The oxidized process ends around 950°C where fibers are converted in gases. After oxidization, the diameter of the fibers exposed to 600°C were reduced and several surface flaws were detected. The details of the fiber surfaces are shown in Fig. 9.

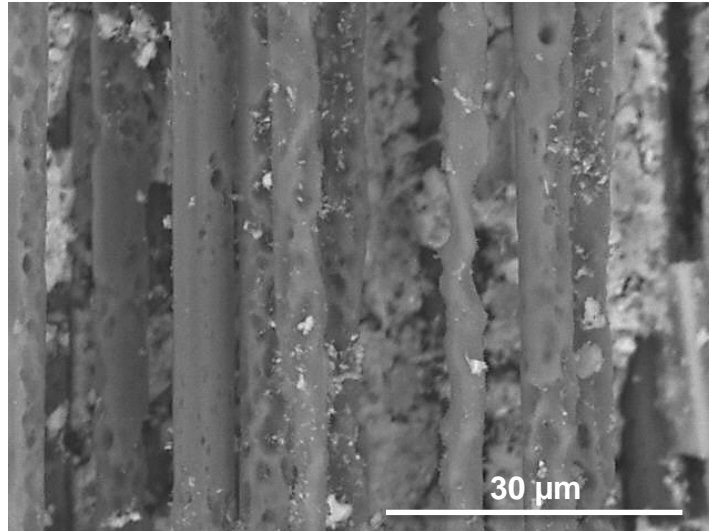


Fig. 9 – Detailed view of the carbon fibers after being submitted to in-situ tensile test at 600°C.

Similar behavior was reported by Rallini et al. [23], in carbon fibers subjected to fire tests during 2 minutes. The deformed shape of the carbon fibers result from the tensile efforts as well as the uneven oxidation process occurred during the in-situ test. As reported by YIN et al. [24] the mechanical strength of the fibers falls as the fiber dimension decreases. Furthermore, once a strong interfacial debonding process occurs due to carbon oxidation, a significant drop on the TRC mechanical performance occurred at 600°C.

6.1. Influence of temperature on coated carbon TRC tensile behavior

The effect of elevated temperatures on the coated carbon TRC tensile strength is shown in Fig. 10. Results obtained from the specimens tested at 7 days of age are given in Table 8. All values represent the average of three TRC test specimens. As well as in the uncoated carbon TRC, a strain-hardening behavior is clearly observed in the stress-strain curves up to 400°C. Although, not impregnated by matrix, coated carbon TRC presented higher tensile strength compared to the uncoated TRC at room temperature (Fig. 10a). This behavior occurs due to the coating's

impregnation which acts mechanically activating equally part of the filaments present in the carbon yarns. In the uncoated case, however, outer filaments are preferably tensioned.

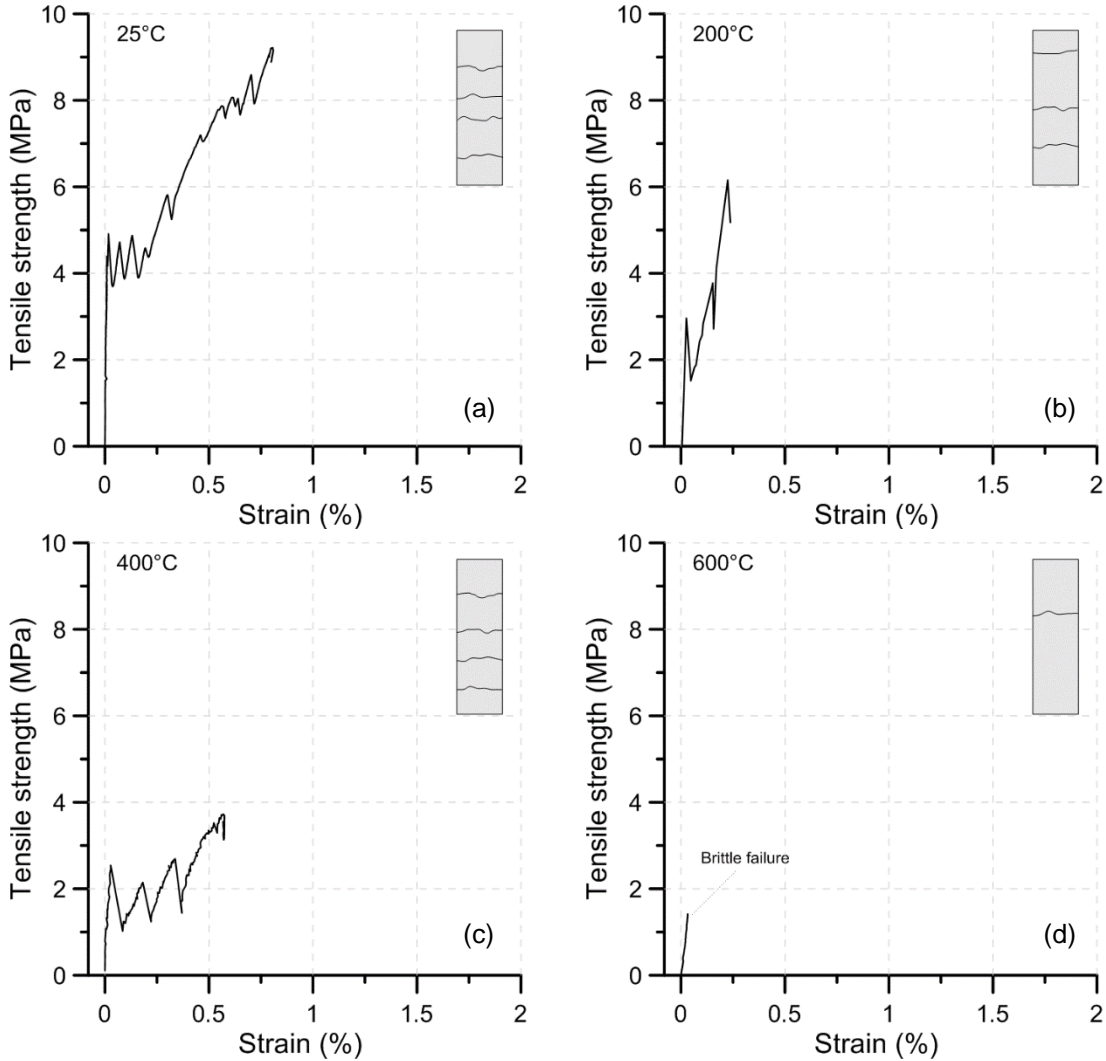


Fig. 10 – Influence of temperature on the in-situ tensile strength of laminated TRC’s reinforced with 2 coated carbon layers. Stress-strain curves for (a) room temperature, (b) 200°C, (c) 400°C and (d) 600°C.

Table 8 – Average results of the in-situ tensile test performed on the coated carbon TRC.
Standard deviation values are presented in parentheses.

Heating Rate	Target temperature	First crack values			Post crack values	
		σ_{BOP} (MPa)	ϵ_{BOP} (%)	E_t (GPa)	σ_{UTS} (MPa)	ϵ_{UTS} (%)
-	25°C	3.96 (0.40)	0.0136 (0.0049)	28.32 (3.85)	10.11 (0.96)	0.87 (0.15)
10°C/min T.P.: 1h	200°C	2.92 (0.80)	0.0152 (0.0049)	15.61 (3.34)	4.97 (0.73)	0.27 (0.17)
10°C/min T.P.: 1h	400°C	2.43 (0.17)	0.0378 (0.0053)	6.50 (0.54)	3.82 (0.71)	0.48 (0.12)
10°C/min T.P.: 1h	600°C	1.47 (0.38)	0.0334 (0.0006)	4.61 (0.94)	-	-

T.P.: Time period in which the specimens were kept at the target temperature.

Despite the better performance at 25°C, a clear trend of tensile strength reduction could be observed in the coated TRC's with rising temperature (Fig. 5). In relation to the ultimate tensile strength (σ_{UTS}) obtained at room temperature, the decreases induced by the in-situ regime in the coated carbon TRC were, respectively, 50.8%, 62.2% and 85.4% for temperatures of 200°C, 400°C and 600°C. Through Table 7 and Table 8 it is possible to verify that the σ_{UTS} values obtained for the uncoated carbon TRC under imposed temperature (200°C and 400°C) were, on average, about 1.7 times greater than that obtained for the coated ones. The relation was not computed for 600°C given the absence of post-cracking response. In comparison with the results obtained at room temperature, the decrease in the elastic modulus for the temperatures of 200°C, 400°C and 600°C were 44.8%, 77% and 83.7%, respectively. The decreases were very similar to those obtained for uncoated TRC's. This reduction in mechanical parameters is related to changes in the refractory matrix structure (see item a). The main aspect to be considered in these composites, is the presence of coating which affect considerably the load carrying capacity of TRC even under moderate temperatures. This is because generally in the in-situ condition epoxy based coatings, including heat-resistant ones, start to decompose at temperatures between 200°C and 400°C [25]. As the epoxy coating cannot act as a thermal barrier, the carbon yarns

experience loss of adhesional resistance. For example, compared to the uncoated carbon TRC tested at 200°C, the coated carbon TRC presented lower strain-hardening behavior and reduced load carrying capacity. The response of the coated carbon TRC exposed to 200°C allowed the composite to reach 0.27% of strain. In contrast, the uncoated carbon TRC, presented strain capacity of 0.87% when tested at the same condition. As shown in Fig. 8b the bond between the coated carbon yarns and the concrete is inferior compared to uncoated yarns (Fig. 8a). Although uncoated yarns undergo slip during loading, external filaments remain attached to the matrix favoring adhesional and frictional bond between fibers and matrix. As well as in the uncoated case, only at 600°C the coated TRC's lost the strain hardening behavior. This was explained by the rapid decomposition of carbon fibers at ~488°C, related before. During the heating process, high pore pressure within the matrix structure can lead to micro cracking or even spalling. However, no spalling was observed in the TRC specimens, including those heated up to 600°C.

6.1.1 Microstructural characterization

Coated carbon TRC tensile behavior

A microstructural investigation using SEM was carried out to confirm the damage process on the TRC's tested in the in-situ condition. Fig. 11 shows SEM micrographs of the fiber-matrix interface with the carbon yarns in its natural condition (25°C) and after exposure to the studied temperatures (200°C, 400°C and 600°C). When the temperature increase up to 200°C the epoxy based coating starts to decompose. The plastic condition acquired during heating disables the coating with respect to transfer stresses, which results in decreased tensile performance of the composite. Once the temperature of 200°C is not able to decompose the polymer, during SEM investigations, the coating presents itself stiffer and visco-elastic again (see Fig.11b). It is known that incompatibility between cement and aggregates creates internal stresses, microcracks and

weakens in the refractory concrete when exposed to high temperatures. However, given that the calcium aluminate clinker, used as aggregate in this study, has a strong compatibility with calcium aluminate cement, it is believed that the cracking of the matrix for temperatures up to 200°C is practically irrelevant compared to the effect caused by the coating's changes during testing. At 400°C the coating (Fig. 11c) as well as the stitching yarns are no longer visible. As a result of the decomposition of coating significant strength losses were observed. Although mechanically affected by moderate temperature [20], carbon fiber presented smooth outer surfaces and circular cross-sections at 400°C. The brittle behavior at 600°C can be explained by the decomposition of carbon fibers that can be easily seen in the SEM images (Fig. 9).

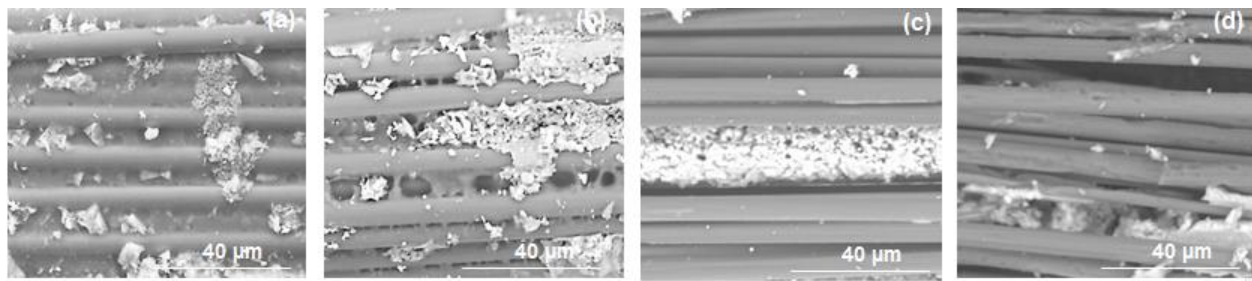


Fig. 11 – Coated carbon–fiber–matrix interface (a) at room temperature and after exposure to (b) 200°C, (c) 400°C and (d) 600°C.

Uncoated carbon TRC tensile behavior

In the case of uncoated carbon TRC, it was possible to see signs of composite degradation only at 400°C and 600°C (see Fig. 12c). At 400°C, it was observed thermal cracking in the refractory matrix, while carbon fibers kept their cylindrical shape and smooth surface. It's important to remember that the SEM observation was done at room temperature, after cooling. Thus, it is probable that, when at the target temperature, the cracks had different dimensions (length and

width). As shown in Fig. 12d, at 600°C the fibers were compromised by the oxidation process which resulted in surface flaws, rupture and decrease of the fiber cross sectional area.

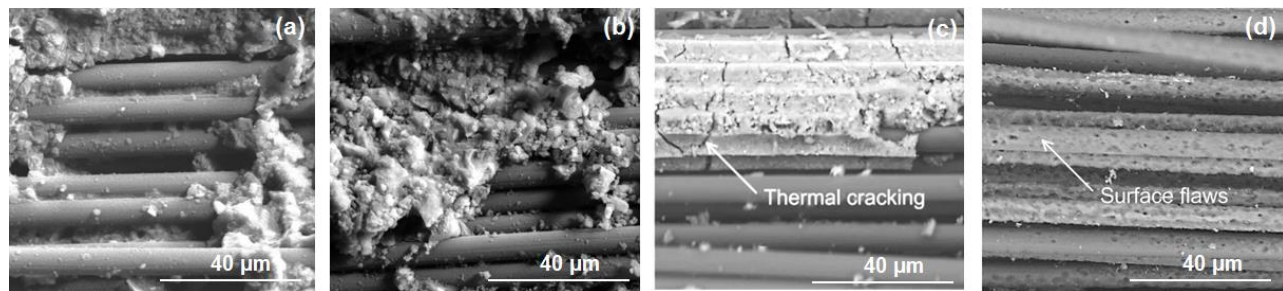


Fig. 12 – Uncoated carbon–fiber–matrix interface (a) at room temperature and after exposure to (b) 200°C, (c) 400°C and (d) 600°C.

7. Conclusions

- The coated and uncoated carbon TRC's submitted to in-situ direct tensile test proposed in this study exhibited strain-hardening behavior and multiple cracking up to 400°C.
- Given the effectiveness of the uncoated fabric embedment in the refractory matrix and the thermal stability of carbon fibers, the uncoated TRC exposed to 400°C showed load carrying capacity very close to the specimens tested at room temperature, while the strain capacity increased approximately by one order. Such performance provides to the carbon TRC advantages in relation to ordinary and unreinforced refractory concretes in terms of structural safety, damage tolerance and maintenance.
- Since the coating transforms to plastic state and decompose under low and moderated temperatures, respectively, a clear trend of tensile strength reduction could be observed in the coated carbon TRC's. Besides the coating's changes, other reasons were attributed to the distinct behavior between coated and uncoated TRC's: 1) the irreversible shrinkage of the hardened paste that can improve the bond between the fibers and the matrix in the uncoated case, and 2) matrix

infiltration in the uncoated yarns that establish a direct interface with the fibers, favoring adhesional and frictional bond between matrix and reinforcement.

- Tensile strength losses in the TRC agree well with the results obtained from the thermogravimetry and X-ray diffraction analysis of the matrix and fiber.

Acknowledgements

The authors gratefully acknowledge the Brazilian Agency CNPq for its partial financial support and Kerneos (France) for supplying the cement, superplasticizer and aggregate.

[1] Rambo DAS, Silva FA, Toledo RD. Textile reinforced refractory concrete at high temperature: Mechanical properties under uniaxial tensile loading. 11th International Symposium on Ferrocement and 3rd ICTRC International Conference on Textile Reinforced Concrete, 2015, Aachen. In: Proceedings of the 11th International Symposium on Ferrocement and 3rd ICTRC International Conference on Textile Reinforced Concrete. Bagnus: RILEM Publications S.A.R.L., 2015. p. 63-69.

[2] Colombo I, Colombo M, Magri A, Zani G, di Prisco M. Textile Reinforced Mortar at High Temperatures. 2011; 82:202-207.

[3] Rambo DAS, Silva FA, Toledo RD, Gomes OFM. Effect of elevated temperatures on the mechanical behavior of basalt textile reinforced refractory concrete. Mater and Des 2015;65: 24–33.

[4] Rambo DAS, Silva FA, Toledo RD, Ukrainczyk N and Koenders E. Effect of elevated temperatures on in-situ and post-heating residual strength of basalt textile reinforced CAC composites. 11th International Symposium on Ferrocement and 3rd ICTRC International Conference on Textile Reinforced Concrete, 2015, Aachen. In: Proceedings of the 11th International Symposium on Ferrocement and 3rd ICTRC International Conference on Textile Reinforced Concrete. Bagnus: RILEM Publications S.A.R.L., 2015. p. 80-95.

-
- [5] Lea's. Chapter 13 - Calcium Aluminate Cements. In: Peter C. Hewlett, Butterworth-Heinemann editor. Chemistry of Cement and Concrete, 4th ed. Oxford, 2003. p. 713-782.
- [6] Fibre-Reinforced Cement Composites. Technical Report 51.067. Conc Soc, London; 1973.
- [7] Krüger M, Reinhardt HW. In: Wolfgang Brameshuber, editor. Chapter 6: Fire resistance. Report 36: Textile Reinforced Concrete - State-of-the-Art Report of RILEM Technical Committee 201-TRC, Bagnaux: Rilem publications S.A.R.L, 2006. p.83-218.
- [8] Silva FA, Butler M, Hempel S, Toledo RD, Mechtcherine V. Effects of elevated temperatures on the interface properties of carbon textile-reinforced concrete. *Cem & Conc Compos* 2014;48:26–34.
- [9] Reinhardt HW. On the Biaxial Testing and Strength of Coated Fabrics. *Exp Mech* 1976;16:71-74.
- [10] Colombo G I. Multilayer precast façade panel: Structural optimization for energy retrofitting. PhD Thesis. Department of Civil and Environmental Engineering. Doctoral School in Structural, Earthquake and Geotechnical Engineering. Politecnico de Milano, 2015. p.228.
- [11] Krüger M, Reinhardt HW. In: Wolfgang Brameshuber, editor. Chapter 6 - Fire resistance. Report 36: textile reinforced concrete – state-of-the-art report of RILEMtechnical committee 201-TRC. Bagnaux: Rilem publications S.A.R.L, 2006. p. 83–218.
- [12] Maluk C, Terrasi GP, Bisby L, Stutz A, Hugi E. Fire resistance tests on thin CFRP prestressed concrete slabs. *Constr and Build Mat* 2015;101:558–571.
- [13] De Larrard F. Concrete mixture proportioning: a scientific approach. London. E&FN SPON. 1999.
- [14] Sedran T. Rhéologie et rhéométrie des bétons: application aux bétons autonivelants. Doctoral dissertation. Ecole Nationale des Ponts et Chaussées, 1999. p.484.

-
- [15] Goldstein J, Newbury DE, Joy DC, Lyman CE, Echilin P, Lifshin E, Sawyer L, Michael JR. Scanning Electron Microscopy and X-ray Microanalysis, 3rd edition. Springer, New York, 2003. p.689.
- [16] Otsu N. Threshold selection method from gray-level histograms. IEEE Trans Syst, Man, and Cyber 1979;9(1):62–66.
- [17] Gonzalez RC, Woods RE. Digital Image Processing, 2nd edition. Prentice-Hall, Upper Saddle River, 2002. p.793.
- [18] Bazant ZP, Kaplan MF. Concrete at High Temperatures. Material Properties and Mathematical Models. Conc Des and Constr Ser, England: Longman Group, 1996.
- [19] Innocenti MDM, Cardoso FA, Akyioshi MM and Pandolfelli VC. Drying Stages during heating of high-alumina. Ultra-low-cement refractory castables. J of the Am Ceram Soc 2003;86:1146–8.
- [20] Feih S, Boiocchi E, Kandare E, Mathys Z, Gibson AG, Mouritz AP. Strength degradation of glass and carbon fibres at high temperature. J of Mat Sci 2008; 44(2):392-400.
- [21] Park SJ. Carbon fibers. Springer Series in Materials Science. 2014.
- [22] Soranakom C, Mobasher B. Geometrical and mechanical aspects of fabric bonding and pullout in cement composites. Mat and Struct 2009; 42: 765-777.
- [23] Rallini M, Natali M, Kenny JM, Torre L. Effect of boron carbide nanoparticles on the fire reaction and fire resistance of carbon fiber/epoxy composites. Poly 2013;54(19):5154–5165.
- [24] Yin Y, Binner JGP, Cross TE, Marshall SJ. The oxidation behaviour of carbon fibres. J of Mat Sci 1994; 29(8):2250-2254.
- [25] Yuan H, Lu C, Zhang S, Wu G. Preparation and characterization of a polyimide coating on the surface of carbon fibers. New Carbon Mat 2015;30(2):115-121.

